SYNTHESIS-STRUCTURE–PROCESSING-PROPERTY RELATIOSHIPS IN POLYMER NANOCOMPOSITES

A THESIS
SUBMITTED TO THE
UNIVERSITY OF PUNE
FOR THE DEGREE OF
DOCTOR OF PHILOSOPHY
(IN CHEMISTRY)

BY

GIRISH GALGALI
CHEMICAL ENGINEERING DIVISION
NATIONAL CHEMICAL LABORATORY
PUNE 411008, INDIA

MAY 2003

CERTIFICATE

Certified that the work incorporated in the thesis "**SYNTHESIS-STRUCTURE-PROCESSING–PROPERTY RELATIONSHIPS IN POLYMER NANOCOMPOSITES"**, submitted by Mr. Girish Galgali was carried out by the candidate under my supervision. Such material as has been obtained from other sources has been duly acknowledged in the thesis.

(Dr. Ashish K. Lele)
Research Guide
Chemical Engineering Division
National Chemical Laboratory,
Pune-411008.

ACKNOWLDEMENTS

I would like to express my gratitude to Dr. Ashish Lele for his invaluable guidance. I thank him for teaching me the skills of presenting, writing the technical matters and to help me in analyzing the data. He has not just guided me in the scientific problems, but has always taken extra efforts to shape my approach towards research. He always has been a perfectionist and a good critic to bring this thesis in its present form. I learnt a great deal from interacting with him. Finally, I would like to thank him for his patience with me.

It is my honour to acknowledge Dr. S. Sivaram, Director NCL, who introduced me to this esteemed institute in very early days of my career, and for giving me an opportunity to work in NCL. I would like to acknowledge Dr. M. G. Kulkarni, Head, Polymer Science and Engineering Division and Dr. B. D. kulkarni, Head, Chemical Engineering Division for their cooperation.

I would like to thank Dr. Premnath, Dr. Guruswamy and Dr. C. Ramesh for many useful discussions, for their encouragement and valuable suggestions. I would also like to thank Dr. Badiger, Dr. Suresh, Dr. Wadgaonkar, Mrs. Deepa Dhobale and Dr. Mohan Bhadbhade for their kind cooperation.

I would also like to express my debt and gratitude to many of colleagues and friends. It is my pleasure to thank the *PPCites* namely Shyni, Yogesh, Abhijeet, Prashant Leena and Nivedita. It was a wonderful experience to work with them. Many thanks are

TABLE OF CONTENTS

ABSTRACT

The work presented in this thesis is focused on understanding the linkages between the microstructure, processing and properties of polyolefin nanoclay composites.

Polymer nanocomposites are hybrid materials comprising of inorganic components that have nano-dimensions. In contrast to the traditional fillers, nano-fillers such as nano dimensional layered clays are found to be effective even at as low as 5-wt % loading. This happens because of two reasons: (a) Nano-sized clays have dramatically higher surface area compared to their macro-size counterparts like china clay or talc, and (b) the presence of mobile cations on the surface of the clay allows for organic modification of the surface, which can render the clays hydrophobic thereby increasing their potential to mix well in a polymer matrix. Polymer nanoclay composites show significantly higher modulus, thermal stability and barrier properties without increasing weight and in some cases, without affecting the optical clarity.

A nanoclay consists of two dimensional nanometer thick platelets that are stacked up in layers separated about 1 nm apart. Organo-clays have layer spacings (galleries) of upto 4 nm. Based on the state of dispersion of the clay in the polymer matrix, nanocomposites are classified as *intercalated composites* (in which polymer chains reside in between the silicate layers, while preserving the ordered layered structure to some extent) and *exfoliated composites* (in which polymer chains completely delaminate the clay layers). It is generally observed that the best enhancement in thermo-mechanical properties are achieved for exfoliated nanocomposites and so the ultimate goal of manufacturing strategies of polymer nanoclay composites is to achieve ideal exfoliation. The three main strategies for synthesis of nanoclay composites are (i) i*n-situ polymerization*, wherein the monomer is allowed to intercalate in between the clay layers and then polymerized, (ii) s*olution intercalation*, wherein the polymer chains are allowed to diffuse in between the clay layers from a solution, and (iii) *melt intercalation*, where-in the composite is formed at temperature above the softening point of the polymer by the combined action of mechanical shear and diffusion. Of these the melt intercalation route is commercially the most attractive option but does not necessarily result in an ideal exfoliated microstructure.

Polymer nanocomposites ultimately have to undergo many processing operations such as extrusion and injection molding either during their manufacture by melt intercalation or during shaping operations for the manufacturing of a product. During these operations the nanocomposite melt flows through complex geometries and experiences different stress fields. The microstructure of the final product is dictated to a large extent by the processing conditions. Moreover, the microstructure in turn determines the flow properties of the melt. The work presented in this thesis attempts to understand the structure-processing-property relations in polyolefin nanocomposites in a semi quantitative manner.

Polypropylene (PP)–layered silicate nanocomposites were prepared by melt compounding PP and organically modified montmorillonite in the presence or absence of a compatibilizer viz., a high MFI PP-co-maleic anhydride. The hybrid materials were characterized using Transmission Electron microscopy (TEM) and high temperature WAXD. Rheological measurements in shear mode included creep and stress ramp studies using a controlled stress rheometer (Bohlin, CVO-50), step strain and oscillatory studies using a controlled rate rheometer (Rheometric Scientific, ARES) and high shear measurements using a capillary rheometer (Ceast, Rheovis).

Creep resistance of compatibilized hybrids was found to be significantly higher than that of uncompatibilized hybrids and also increased with annealing time. The creep data together with the micro-structural investigation indicated a small amount of exfoliation from the edges of the clay crystallites during extrusion and annealing. The zero-shear viscosity of the compatibilized nanocomposites was at least three orders of magnitude higher than that of matrix resin and the uncompatibilized hybrids. Importantly, the large increase in zero-shear viscosity was not accompanied with any increase in the flow activation energy compared to the matrix polymer. It is concluded that (a) at low stresses the hybrids exhibit a Newtonian response of high viscosity, (b) presence of confined chains between galleries, if any, do not significantly contribute to the rheological response, and (c) the high viscosity of the molten nanocomposite originates from large frictional interactions of the clay crystallites, which form a percolating network.

At high stresses the compatibilized hybrids showed an apparent ‘yield’ behavior, which is an indirect suggestion for breakage of the network by incipient flow-induced

alignment of the clay crystallites. A direct evidence for orientation under shear was obtained from a novel in-situ rheo-x ray technique. The rheo-x ray data allowed for quantitative measurements of orientation as a function of shear stress after the yield transition. It was found that the clay tactoids oriented quite easily by shear and achieved an average orientation function value of ~ 0.85 at high stresses. Orientation relaxation after shear revealed an interesting behavior in that the presence of the compatibilizer accelerated the orientation relaxation of the clay tactoids.

The flow-induced orientation and orientation relaxation results are relevant to both processing and product properties of PLS nanocomposites. To complete the story of microstructure-flow-property linkages the effect of clay orientation on the tensile modulus of extruded products was also studied. Tapes of PP-nanoclay composites were extruded through a slit die under different shear stresses using a capillary rheometer. Clay orientation was measured from 2D diffraction patterns obtained by using an image plate. The tensile modulus of the tapes was measured using an Instron UTM. In the range of extrusion speeds tested in this study, both the tensile modulus and the clay orientation were initially found to increase with piston speed and then saturated at higher speeds. Thus, quantification of the dependence of modulus on clay orientation was possible.

Rheological measurements were also made on polyethylene nanocomposites that were prepared by in-situ polymerization of ethylene using a metallocene catalyst that was heterogenized on montmorillonite by a novel strategy (Saptarshi Ray, Ph.D. thesis, Univ. of Pune, 2003). This study has helped to understand some of the differences in the rheology of intercalated and exfoliated nanocomposites.

LIST OF FIGURES

LIST OF TABLES

also due to my friends Ganapathi, Shailesh, Sachin, Suhas, Grace, Samir, Chandru, Mohan, Rohan, Nitin, Kalpesh, Raghu, Yuwaraj, Harsha, Namrata, Vipin, Sai, Jawahar, Amogh, Shubhangi, Aarati, Smitha, Bhoje, Malli, Uma, Jayant, Rajendra, Priya, and Madhuri. I would like to thank all NCL staff in particular Rajesh, Dinadyalan, Dhupe, Borkar and Shukla for their cooperation. Thanks are also due to Mr. Saptarshi Ray for providing PE nanocomposite samples.

I greatly acknowledge the financial assistance from Council of Scientific and Industrial Research (CSIR) for providing a research fellowship for carrying out the doctoral work.

Chapter 1 Introduction

This thesis is concerned with the study of structure-processing-property linkages in a new class of hybrid materials known as polymer nanoclay composites. We begin the thesis with a brief introduction to polymer nanoclay composites. The purpose of this chapter is to describe the context of the work, the overall objectives of the study and the structure of the thesis.

1.1. Polymer composites

Polymer composites are prepared by mixing polymers with inorganic materials such as reinforcing fibers (e.g., glass, carbon, aramid etc.) and particulate solids (e.g., talc, carbon black, calcium carbonate, mica etc.). Such composites exhibit physical properties synergistically derived from both the organic and inorganic components, for example, they show superior mechanical properties and higher heat deflection temperature compared to the pristine polymers while maintaining processibilty. [1] Fiber reinforced polymer (FRP) composites were first developed in the 1940's mainly for military applications. Polymer composites since then have replaced metals and have found applications in diverse areas like construction, electronics and consumer products.

However, the improvement in properties is typically achieved at the expense of optical clarity and surface gloss, and often results in increased part weight. This is because conventional reinforcing agents and fillers are required to be added at a higher loading level (typically >10-wt%) in order to achieve significant improvement in the properties. The replacement of traditional composites with a new class of more effective composites that use nano fillers is today an active field of industrial and academic research.

1.2. Polymer nanocomposites

In recent years the advances in synthesis techniques and the ability to characterize materials on atomic scale has lead to a growing interest in nanometer-size materials.

Polymer nanocomposites combine these two concepts, i.e., composites and nano-sized materials.

Polymer nanocomposites are materials containing inorganic components that have nano-dimensions. Nano fillers can be classified as

1. Symmetric nanoparticles e.g. cadmium sulphate
2. Asymmetric 2-dimensional nanofillers e.g. layered nanoclays
3. Asymmetric 1- dimensional nanofillers e.g. carbon tubes

In this thesis the discussion is restricted to polymer nanocomposites made by dispersing two-dimensional layered nanoclays into polymer matrices. In this thesis, such nanocomposites are called as polymer layered silicates (PLS) nanocomposites, polymer nanoclay composites or hybrids. In contrast to the traditional fillers, nano-fillers are found to be effective even at as low as 5-wt% loading. Nano-sized clays have dramatically higher surface area compared to their macro-size counterparts like china clay or talc. This allows them to interact effectively with the polymer matrix even at lower concentrations. As a result, polymer nanoclay composites show significantly higher modulus, thermal stability and barrier properties without much increase in the specific gravity and sometimes retaining the optical clarity to a great extent. As a result the composites made by mixing layered nanoclays in polymer matrices are attracting increasing attention commercially.

In the late 1980's the Toyota Motor Company commercialized a timing belt cover made from nylon-6/ nanoclay composites for one of its car models. Since then efforts are on to commercialize these materials for various applications ranging from automobile parts to packaging materials. For instance, General Motors and Montell U.S.A have jointly developed thermoplastic olefin (TPO) clay composites for exterior automotive applications. Eastman chemical and Nanocor are jointly developing nanocomposites of polyethylene terephthalate (PET) and other packaging materials like polyethylene (PE). [2-4]

According to a report by Bins and Associates, Sheboygan, U.S.A, a leading market-research firm, the usage of polymer clay nanocomposites in automotive applications is expected to be about 10,000 - 25,000 metric tonnes by 2005 in North America alone, with very high annual growth. By 2010, the market for nanocomposites

could be in the order of millions of tonnes annually in North America alone and is valued at over US$4 billion.

A nanoclay consists of two-dimensional nanometer thick platelets that are stacked up as layers about one nanometer apart. Polymer nanoclay composites are formed by either polymerizing a monomer in the presence of the clay (in-situ polymerization) or by allowing the polymer to diffuse in between the clay platelets from a solution or a melt (solution or melt intercalation). Often shear is used to disperse the clay platelets into the polymer matrix. Nanocomposites in which the clay layers are completely delaminated and are dispersed in the polymer matrix are said to be exfoliated nanocomposites. Intercalated nanocomposites are those in which the polymer chains reside in between the clay galleries, while preserving the layered structure. Exfoliated nanoclay composites show the best enhancements in properties and are typically obtained by smart in-situ polymerization techniques. However, melt intercalation is a preferred route as it utilizes existing compounding equipment such as twin-screw extruders to prepare the nanocomposites.

Polymer nanoclay composites are melt processed to form the final products. During melt processing the materials flow through complex geometries and experience shear and elongational stresses. The microstructure of the nanoclay composites determines its flow behaviour and the flow in turn, modifies the microstructure. Finally the microstructure so developed during melt processing determines the solid-state properties of the final product. The performance of the product, as gauged by the ultimate user, is determined by the properties.

Thus, the understanding of the links between the microstructure, the flow properties of the melt and the solid-state properties is critical to the successful development of polymer nanoclay composite products. The overall objective of this work is to try to quantify the structure-processing-property linkages in polymer nanoclay composites.

1.3. Structure of the thesis

The work presented in this thesis is concerned with polyolefin nanoclay composites and the various chapters are so structured as to bring forth the structure-processing-property relationships in these nanocomposites.

Chapter 2 provides the necessary background relevant to the contents of the thesis. It discusses the various types of nanoclays, their classification and chemical structure. The various procedures for the synthesis of nanocomposites and the applications of these materials are described. Next, the experimental techniques used to study the microstructure of polymer nanoclay composite materials are discussed. Finally, a brief introduction is provided for the rheology of complex fluids, in particular the rheology of viscoelastic fluids, viscoplastic fluids and filled systems.

Chapter 3 provides a detailed literature search on polymeric nanocomposites. It outlines the contribution of various researchers towards synthesis, characterization, processing and rheology of polymer layered silicate nanocomposite materials. Both theoretical and experimental works are described.

Chapter 4 presents the objectives of this work. Chapter 5 describes the experimental methods and materials used for this study. The materials studied in this work are intercalated polypropylene (PP) nanocomposites, and intercalated and exfoliated polyethylene (PE) nanocomposites, which were synthesized both by melt intercalation and in-situ polymerization.

Chapter 6 reports the experimental investigation of the microstructure of the as-prepared nanocomposites using x-ray diffraction, transmission electron microscopy and optical microscopy techniques.

In Chapter 7, the linear rheological studies of PP nanocomposites are reported. It describes the rheological behaviour in creep, step-shear strain and oscillatory shear experiments. The effect of clay loading and molecular weight of the matrix on the rheological response of the composites are also discussed.

Chapter 8 focuses on the non-linear rheology of PP nanocomposites. It presents the apparent yield like behaviour observed in such materials. Visco-plastic models for yield behaviour are also discussed. In-situ measurements on the orientations of clay

tactoids under steady shear and of relaxation of the orientation on cessation of shear using a novel rheo x-ray technique are described. In chapter 9 the effect of the orientation of clay tactoids on the solid-state properties of these composite are studied. Chapter 9 also summarizes the microstructure-rheology-solid property links for PP nanocomposites based on the results described in chapters 6, 7, 8, and 9.

Chapter 10 describes PE nanocomposites prepared by in-situ polymerization. It describes the rheological response of these materials. The overall conclusions of the work described in this thesis are summarized in chapter 11 followed by recommendations for future work.

Reference List:

1. Manson, J. A.; Sperling, L. H. *Polymer Blends and composites* Plenum Press, N.Y. **1976.**
2. Garces, J. M.; Moll, D. J.; Bicerano, J.; Fibiger, R.; McLeod, D. G. *Adv. Mater.* **2000,** *12* (23), 1835-1839.
3. Giannelis, E. P. *Adv. Mater.***1996***, 8* (1), 29-35.
4. LeBaron, P. C.; Wang, Z.; Pinnavaia, T. J. *Appl. Clay Sci.* **1999,** *15* (1-2), 11-29.

Chapter 2 Background

This chapter presents some background material that is relevant to the contents of the thesis. The first part of the chapter describes the various types of nanoclays, their classification and chemical structure. Further, the synthesis and applications of polymer nanoclay composites are also described. In the latter part of the chapter a brief introduction to conventional experimental techniques used for studying the microstructure of polymer nanoclay composite materials is provided. This includes x-ray diffraction, optical microscopy and transmission electron microscopy (TEM). Finally, a more detailed discussion on the rheology of complex fluids, in particular the rheology of filled systems, is provided.

2.1. Clays

2.1.1. Phyllosilicates-structure and classification

Clays are ubiquitous minerals, which constitute a large part of the sediments, rocks and soils. Recent advances in polymer nanocomposites have rekindled interest in the smectite or phyllosilicates group of clays. [1-4] Phyllosilicates are aluminosilicates, which are found as large mineralogical deposits. They are also commonly known as layered silicates since their structural framework consists of Al octahedral and Si tetrahedral layers, joined together in varying proportions and stacked top of each other.

Aluminosilicate condensates in 2:1 ratio of tetrahedral Si sheets with an octahedral Al sheet are called as 2:1 phyllosilicates. Coupling of only one Si sheet to one Al sheet gives rise to 1:1 phyllosilicates called as kaolinite. In many phyllosilicates either Al^{3+} or Si^{4+} ions are isomorphically substituted partially by lower valency metal cations of similar sizes like $Mg^{2+}$and Fe^{2+}. The type of the cation occupying the tetrahedral and octahedral sites is dependent on the ionic size and coordination rather than the valency. Phyllosilicates are categorized broadly depending on the type and location of these substituted lower valency cations as 1) *Trioctahedral*, in which all Al^{3+} in the octahedral sites are substituted by lower valency cations, e.g., three Mg^{2+}cations replace two Al^{3+},

and 2) *Dioctahedral*, in which two-thirds of the Al ions are substituted by the lower valence cations. [1] Various groups of naturally occurring phyllosilicates are listed in Table 2.1.

Table 2.1. Classification of Phyllosilicates

Mineral Group (Type)		Structural formula	Formula unit charge	Series
Kaolinite(1:1)		$Al_2Si_20_5(OH)_4$	0	Dioctahedral
Serpentine(1:1)		$Mg_3Si_20_5(OH)_4$	0	Trioctahedral
Pyro-phyllite (2:1)	Pyrophyllite	$Al_4Si_8O_{20}(OH)_4$	0	Dioctahedral
	Talc	$Mg_6Si_8O_{20}(OH)_4$	0	Trioctahedral
Smectite (2:1)	Montmori-llonite	$Na_{0.2}Ca_{0.1}Al_2Si_4O_{10}(OH)_2(H_2O)_{10}$	~ 0.25-0.6	Dioctahedral
	Saponite	$Ca_{0.1}Na_{0.1}Mg_{2.25}Fe^{2+}_{0.75}Si_3AlO_{10}(OH)_2\,4(H_2O)$	~ 0.25-0.6	Trioctahedral
	Vermicullite	$Mg_{1.8}Fe^{2+}_{0.9}Al_{4.3}SiO_{10}(OH)_2{\cdot}4(H_2O)$	~0.6-0.9	Dioctahedral
	Illite	$K_{0.6}(H_3O)_{0.4}Al_{1.3}Mg_{0.3}Fe^{2+}_{0.1}Si_{3.5}O_{10}(OH)_2(H_2O)$	~0.9	Dioctahedral
Mica (2:1)	Muscovite	$KAl_3Si_3O_{10}(OH)_2$	~1.0	Dioctahedral
	Phlogopite	$KMg_3AlSi_3O_{10}(OH)_2$	~1.0	Trioctahedral

The isomorphic substitution gives rise to a deficiency of positive charge. This deficiency is balanced by the sorption of external cations such as alkaline earth ions (e.g., Ca^{2+}) or alkali metal ions (e.g., Na^{+}). The unit cell of smectite clay comprises of eight silica tetrahedrons and six alumina octahedrons. [4] The charge per unit cell ranges from ~ 0 to ~ 2 depending on the extent of the type and the extent of the substitution. Apart

from the external cations balancing the charge deficiencies, water is also present in the interlamellar space. It may associate with the cations, forming hydration shells around them. [4,1]

The deficiency of positive charge on the layers of smectites is intermediate between the end member mica and the starting pyrophyllite groups of phyllosilicates. The externally sorbed mobile hydrated cations, which balance the positive charge deficiency, can be replaced with other cations by simple ion exchange methods. [4,1] The ability to exchange cations, usually referred to as the Cation Exchange Capacity (CEC), distinguishes smectites from other phyllosillicates, which do not have any ion exchange ability. These cations can be exchanged with suitable organic cations to make silicate surface more organophilic. [5,6]

2.1.2. Smectite Clays

2.1.2.1. Montmorillonite

Montmorillonite is the most widely used clay for making polymer nanocomposites. This dioctahedral 2:1 phyllosilicate has silica tetrahedrons having oxygen and hydroxyl ions tetrahedrally arranged around central Si atoms. The base of the tetrahedron is made up of oxygen atoms while the hydroxyl group makes up the tip of the tetrahedron and is fused with the aluminum octahedron. The aluminum octahedral sheet has Al^{3+} ion octahedrally coordinated to the hydroxyl groups. [5,6] Two third of the Al^{3+} ions are substituted by lower valency cations such as Mg^{2+} and Fe^{2+} in octahedral sites as shown in Figure 2.1.

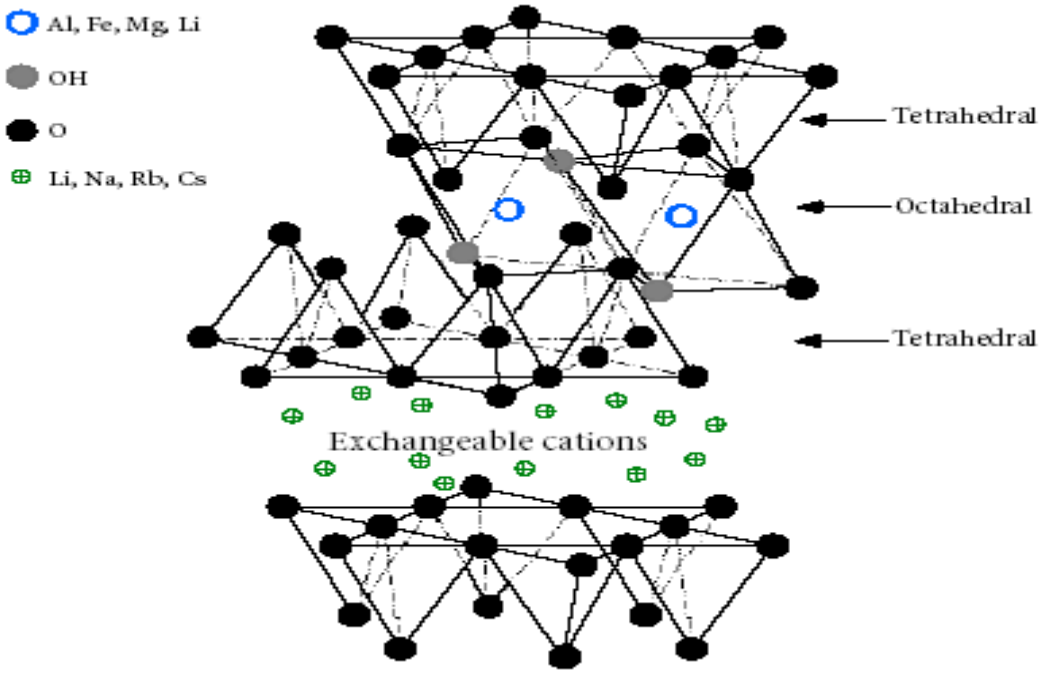

Figure 2.1. Structure of montmorillonite [5]

Montmorillonite is further classified in different chemical varieties depending on the isomorphic substitution as: 1) *Bentonite*, where Al^{3+} is substituted for Si^{4+}, and 2) *Nontronite*, in which Fe^{2+} substitutes Al^{3+}. [1,2] Montmorillonites have a highly asymmetric structure, in which each two dimensional aluminosilicate platelet or clay layer is about 0.95 - 1.3 nm thick and about 500 - 1000 nm in lateral dimensions. For nanoclays an aspect ratio may be defined as D/t, where D is the average platelet diameter and t is the thickness of either individual platelet or a stack of platelets [called as tactoids], as shown in Figure 2.2 (a). For montmorillonite, the aspect ratios are as high as 1000 for individual platelets and 300-500 for tactoids. The clay is white-pale yellow in color. An interlamellar space or *gallery* of about ~ 1 nm separates these platelets. Consequently montmorillonite has a large surface area of about 700 - 800 m^2/g. It has a high CEC of 70 - 150 meq/100g for a comparatively lower isomorphic substitution of ~ 0.25 - 0.6. The successive layers in montmorillonite are more randomly stacked compared to pyrophyllites. [7] These structural features endow montmorillonite with peculiar swelling properties and allow a wide range of moieties to be intercalated. For the study reported in this thesis, organically modified montmorillonites were used for making

polyolefin nanocomposites. A transmission electron microscope image (TEM) of montmorillonite is shown in Figure 2.2 (b).

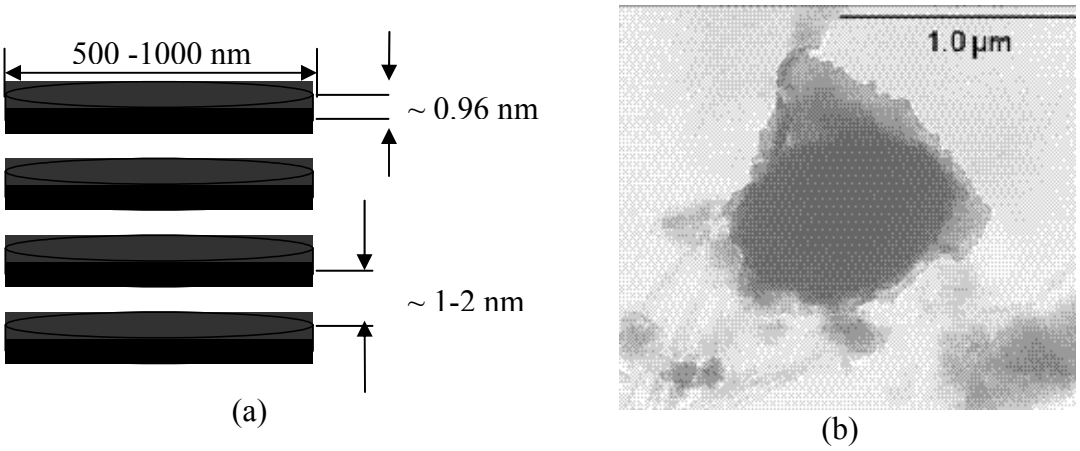

Figure 2.2. (a) Schematic of a montmorillonite tactoid (b) Transmission Electron Micrograph (TEM) of montmorillonite [8]

2.1.2.2. Other nano clays

Apart from montmorillonite, other types of layered silicates both naturally occurring (e.g., vermiculite) and synthetic clays (e.g., hectorite, Trade name: Laponite RD, manufactured by Rockwood additives Ltd.) have been used for making polyolefin nanoclay composites. [9-11] Tjong et. al. have used vermiculites for preparing polypropylene (PP) nanocomposites. [10] Vermiculite is a dioctahedral smectite clay. The Al^{3+} and Si^{4+} ions are partially substituted by Fe^{2+} and Mg^{2+} respectively. The extent of this isomorphic substitution is greater compared to montmorillonite, and much of this substitution occurs in the Si tetrahedral sheet.

Tudor et. al. have prepared PP-nanocomposites, using Laponite RD {structural formula: $(Na_{0.46}Mg_{5.45}L_{0.46}Si_8(OH)_4O_{20})$} by in-situ polymerization method. [11] They envisaged these clays to support the polymerization catalyst. The basic unit structure consists of a magnesium oxide octahedral layer sandwiched between two tetrahedral silica layers. The CEC of about 60 – 70 meq/100g arises from isomorphic substitution of Li^{+} for Mg^{2+}. [9]

Except for a few such examples, organically modified montmorillonite is the most commonly used clay in commercial polyolefin nanocomposites due to its easy availability and lower cost.

2.1.3. Advantages of layered silicates

Any physical mixture of a polymer and an inorganic material (such as clay) does not form a nanocomposite. Conventional polymer composites that are prepared by reinforcing a polymer matrix with inorganic materials like reinforcing fibers and minerals have poor interaction between the organic and the inorganic components, which leads to separation into discrete phases. Therefore the inorganic fillers are required to be added in higher concentrations to achieve enhancements in the thermomechanical properties of the polymer. [5,6,12] Table 2.2 shows a comparison of the physical properties of nanocomposites and conventional composites of polyamide.

Table 2.2. Comparison of physical properties of Nylon nanocomposites and conventional composites

	Pristine polymer	**3-5% Organo clay**	**30% Mineral**	**30% Glass fiber**
Tensile Strength, Psi	7250	11800	8000	23000
Flexural Modulus, Psi* 100	120	500	650	1000
Notched Izod impact Strength	1.2	1.2	1.6	1.8
Heat Distortion Temperature, ^{0}C	66	110	120	194
Specific gravity	1.3	1.14	1.36	1.35
Source: RTP Co.				

It is observed that in contrast to conventional composites, significant property enhancement is still achieved at much lower filler loading for nanoclays. Importantly, this is achieved with negligible increase in the weight of the part.

The reasons for the greater effectiveness of the nanoclays are two-fold. First, the nanoclays can be dispersed to the level of individual platelets. This nano scale dispersion of silicates provides very high surface area for polymer clay interaction. [12,5] Second, the lamellar surfaces of the nanoclays can be modified through an ion exchange reaction to make them compatible with the polymer matrix. Layered silicates in the pristine state are highly hydrophilic. However, the interlayer cations like Na^{+}, Ca^{2+} can be exchanged with various organic cations like alkylammonium cations and cationic surfactants. The cationic head of the modifier molecule preferentially resides on the clay surface and the aliphatic tail radiates away from the surface. The organic cations lower the surface energy of the silicate surface, and make it compatible with the polymer matrix. Furthermore, the organic modifier may contain various functional groups, which can interact with the polymer matrix. It may also expand the interlayer galleries to an extent that facilitates the intercalation of polymer chains. The equilibrium gallery distance depends on the CEC of silicate and the chain length of the modifier. Thus organosilicates are more compatible with polymer matrix. These two advantages namely, the high surface area and the ability to render it hydrophobic, are interrelated in a sense, as for a given matrix, the surface area is determined by the dispersion of the clay, which in turn depends on the interaction between clay and polymer. [12,5,6]

In addition to the above-mentioned advantages nanoclays offer other interesting features. For instance, polymer nanoclay composites can potentially form optically clear films under certain conditions. [13] This is possible for the instance in the case of exfoliated composites wherein the clay platelets are oriented with their surface normal parallel to the direction of incident light. Under these circumstances the nanocomposites will not scatter light, because the thickness of the platelets is less than the wavelength of the visible radiation. Another interesting feature of nanoclays is that the inter gallery distance (~ 2-3 nm) of the organo clays approximately matches the typical persistence length of flexible polymers, thus making the diffusion of polymer chains more easy.

Incorporation of nano-clays is believed to increase the barrier properties by creating additional '*tortuous path*' that impedes the diffusion of gas or solvent molecules while passing through the matrix resin as shown in the Figure 2.3. [14,15]

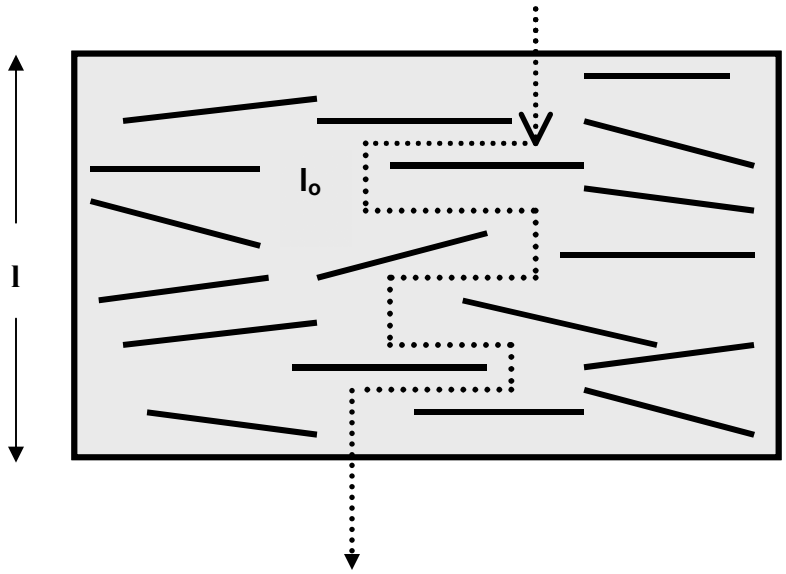

Figure 2.3. Schematic of diffusion barrier by silicate platelets (lo>>l) [14]

To sum up, polymer nanoclay composites exhibit unique thermomechanical, barrier and optical properties not shared by conventional filled composites.

2.2. Synthesis of polymer nanoclay composites

Polymer nanoclay composites can be synthesized by four methods:

1. **Sol-gel process:** The sol-gel process involves hydrolysis and polycondensation of metal alkoxides {M $(OR)_n$} in aqueous acid or base, to form an inorganic gel network in an organic polymer matrix as shown in e. q. 2.1 and 2.2. [16,17]

$$\text{Si-OR} + H_2O \xrightarrow{H^- / OH^+} \text{Si-OH} + \text{R-OH} \qquad (2.1)$$

$$\text{Si-OH} + \text{HO-Si} \xrightarrow{H^- / OH^+} \text{Si- O- Si} + H_2O \qquad (2.2)$$

Most of the efforts in this method have been concentrated on metal organic alkoxides, especially tetraethyl orthosilicate (TEOS) and tetramethyl orthosilicate

(TMOS), since they can form an oxide network in an organic matrix. [16] The mild conditions allow for the incorporation of an organic matrix in the inorganic network. Polymethylmethacrylate (PMMA) nanocomposites are reported to be synthesized by the sol-gel method. [17]

However, composites synthesized by this method are found to be very difficult to process, because often initially soluble polymers phase-separate once the gelation begins. Also, the choice of suitable solvent-polymer pairs further limits the applicability of this method. [18]

2. In-situ Polymerization: In this method, first the nano dimensional clay is dispersed in the monomer, which is then polymerized. The monomer may be intercalated with the help of a suitable solvent and then polymerized as illustrated in the schematic in Figure 2.4. Polycaprolactone [19] and nylon [20] nanocomposites are commonly synthesized by the intercalation of monomer.

In-situ polymerization of monomer very often produces nearly exfoliated nanocomposites. However, commercialization of this method would require separate production lines or major changes in the existing production facilities to suit the heterogeneous polymerization of monomer in the presence of clay. Such factors limit the commercialization of this method. [6]

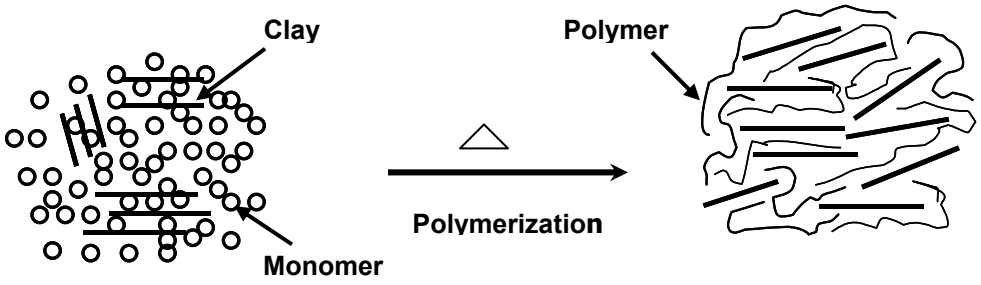

Figure 2.4. Schematic of nanocomposite synthesis by in-situ polymerization

3. Solution Intercalation: In this method the polymer is dissolved in an appropriate solvent, in which the nano-clay is dispersed. Intercalation of polymer chains into the clay galleries occurs from solution. The operating temperatures are typically low.

Nanocomposites of polymers like polyethylene oxide [21] and polylactide [22] have been synthesized by this method.

This method can be useful for few polymers, for which suitable solvents are available. This route is also preferred for polymers that require high processing temperature at which the organoclay may degrade. Apart from the limited choice of suitable solvents, factors like the cost of the solvents and the recovery of the solvent, would further restrict the commercial viability of this method. [5]

4. Melt Intercalation: This method involves the mixing of polymer with clay above the polymer glass transition or melt temperature. At higher temperatures polymer chains are sufficiently mobile to diffuse into the galleries of the clay. [23-27] Vaia et. al. have shown that intercalation can be improved with conventional processing techniques. Twin-screw extrusion has been found to be effective for the dispersion of silicate layers. [23,26] Cho et. al. found that an organoclay, if compatible with the polymer, may even exfoliate during extrusion due to shear. The dispersion of clay depends on the parameters like residence time, level of shear, etc. [24]

Melt intercalation is an environmentally friendly technique, as it does not require any solvent. It is also commercially attractive due to its compatibility with existing processing techniques. However, the resulting morphology of the nanocomposite is often an intercalated microstructure rather than the preferred exfoliated state.

Apart from the four main techniques listed above, a few other techniques for the preparation of polymer nanocomposites include sonication [28] and miceller intercalation. [29]

2.3. Morphologies of polymer nanocomposites

In general, the microstructures of polymer-layered silicate nanocomposites are classified in two idealized morphologies viz., intercalated and exfoliated. [5,6,30,31]

In an immiscible composite or an unmixed system the polymer does not penetrate inside the galleries between the clay layers and hence the pristine gallery distance is maintained in the composite. In intercalated structures however, polymer chains penetrate

inside the galleries and effectively expand the silicate layers. [31] Such structures consist of ordered, alternating polymer–silicate layers with repeat distance of a few nanometers. The equilibrium gallery height is determined by entropic and energetic factors. When the gallery distance, (h) is less than the radius of gyration, (R_0), of the polymer chains, the configurational entropic penalty of polymer chain confinement may be compensated by increased conformational freedom of the tethered surfactant chain. When $h > R_0$, the entropy is change is almost zero. [30]

An ideal exfoliated state refers to a structure, where the polymer extensively penetrates in the silicate galleries so as to completely delaminate the layered structure. In the exfoliated state the average gallery height is determined by clay loading. This class of microstructure can be further classified based on the relative change in the separation between platelets with silicate volume fraction. Low silicate loadings result in *disordered exfoliated* nanocomposites in which single clay platelets are randomly suspended in the polymer matrix and are typically separated by an average distance of > 10 nm. Above a critical clay loading, the platelets start arranging in an ordered fashion and this is called the *ordered exfoliated nanocomposites,* as shown in Figure 2.5. [31]

However, real nanoclay composites exhibit morphologies, which are combinations of these idealized morphologies.

The state of dispersion of clay in polymer is in general dictated by the polymer-silicate interactions, aspect ratio of silicate, method of manufacturing (melt, solution, in-situ polymerization) and possible orientation of layers during processing.

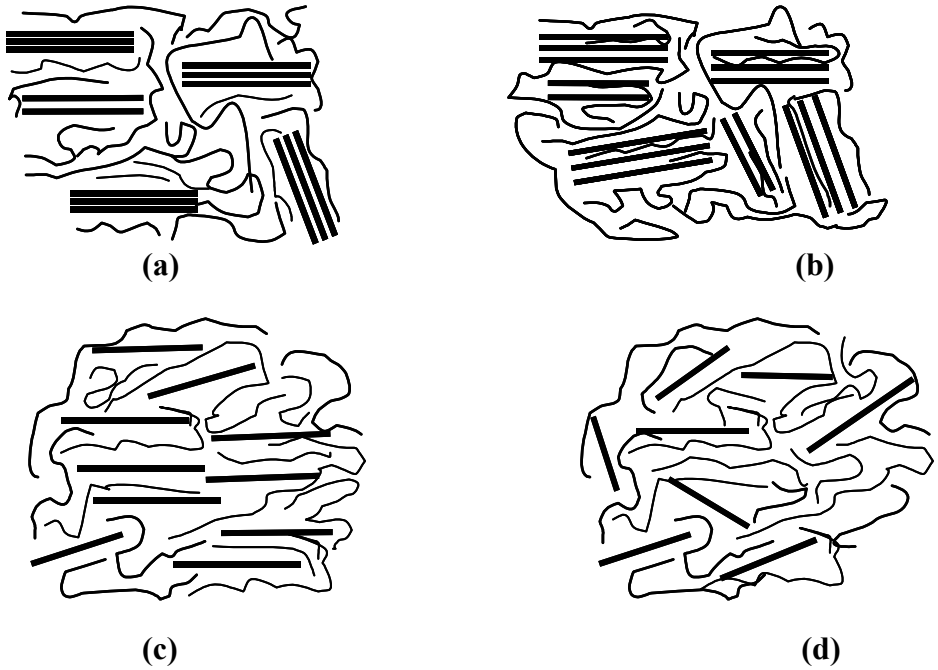

Figure 2.5. Schematic of various morphologies of composites
(a) immiscible composite (b) intercalated nanocomposite
(c) ordered exfoliated and (d) disordered exfoliated nanocomposite

2.4. Applications of polymer nanocomposites

Polymer nanoclay composites caught the attention of the technologist after nylon nanocomposite made a market debut in Toyota Motor Company's car model in the late 1980's. Since then nanocomposites are gradually gaining acceptance in mainstream polymer industry finding applications in automotive to packaging sectors. [6,7,12,32]

Polymer nanoclay composites have huge potential as they can achieve the same properties, e.g., increased tensile strength, improved heat deflection temperature and impact strength, with typically 3 – 5 wt% of the filler compared to 30-wt% for conventional composites, as shown in Table 2.2. Such improvements in the thermo-mechanical properties make nanocomposites a potential candidate for many automotive products such as mirror housings, door handles, engine covers and timing belt covers. General industrial applications currently being considered include usage as impellers and blades for vacuum cleaners, power tool housings, etc. [12]

Nanocomposites offer 25% weight reduction over conventional composites and as much as 80% over steel. Reduced weight helps to increase fuel efficiency. Further, such improvements can be achieved with very little increase in fabrication cost and material cost. General Motors and Montell have jointly developed olefin (TPO) clay nanocomposite for an exterior step assist for the 2002 Astra and Safari vans. Mitsubishi used a nanocomposite in the engine cover for its GDI engines. [12]

A recent study in UBE Industries revealed significant reductions in diffusive fuel loss through polyamide–6/66 polymers by using nanoclay as filler. This is due to the enhanced barrier properties of polymer nanoclay composites as discussed earlier in section 2.1.3. As a result, considerable interest is now being shown in these materials as both fuel tank and fuel line components for cars. [33]

Honeywell Inc. claims that incorporation of just 2 % nano-clays improves the oxygen barrier (OTR) three times than that of pristine nylon 6 films. [33] Owing to the excellent barrier properties, nanocomposite films can be used in food packaging like pet foods, boil-in bags and vacuum packs. Bayer and Nanocor are aiming nylon 6 nanocomposites cast film for multi-layer packaging, protective films for medical and corrosion-prone items.

Kabelwerk Eupen of Belgium claims to be on the way to commercialize EVA nanocomposites for wire and cable compounds. [33] Calorimeter tests for these materials show decline in heat release at relatively low (3 - 5 wt%) loadings. Nano-EVAs also exhibit superior mechanical properties, chemical resistance and thermal stability. Showa Denko of Japan recently started commercial production of nylon 66 nanocomposites. They show improved flame retardancy and rigidity. [33] Table 2.3 lists the current suppliers of polymer nanoclay composites.

In addition to these already commercialized nanocomposites various industries and academic research groups are investigating nanocomposites of other polymers like polycarbonate, biodegradable polylactic acid (PLA) and polyaniline. It will not be a surprise to see many of them in the market soon.

Table 2.3. List of nanocomposite suppliers and targeted applications

Supplier & Tradename	Matrix Resin	Target Application
Bayer AG (Durethan LPDU)	Nylon 6	Barrier films
Clariant	PP	Packaging
Creanova (Vestamid)	Nylon 12	Electrically conductive
GE Plastics (Noryl GTX)	PPO/Nylon	Automotive painted parts
Honeywell (Aegis)	Nylon 6, Barrier Nylon	Multi-purpose bottles and film
Hyperion	PETG, PBT, PPS, PC, PP	Electrically conductive
Kabelwerk Eupen of Belgium	EVA	Wire & cable
Nanocor (Imperm)	Nylon 6, PP Nylon MDX6	Multi-purpose molding PET beer bottles
Polymeric Supply	Unsaturated polyester	Marine, transportation
RTP	Nylon 6, PP	Multi-purpose, electrically conductive
Showa Denko (Systemer)	Nylon 6, Acetal	Flame retardance, Multi-purpose
Ube (Ecobesta)	Nylon 6, 12, Nylon 6, 66	Multi-purpose Auto fuel systems
Unitika	Nylon 6	Multi-purpose
Yantai Haili Ind., Commerce of China	UHMWPE	Earthquake-resistant pipe
Source: Bins & Associates, Sheyboygan, U.S.A..		

2.5. Experimental characterization techniques

Analytical techniques like x-ray diffraction (XRD), optical microscopy (OPM) and transmission electron microscopy (TEM) are very often used to elucidate the structure of polymer nanoclay composites.

2.5.1. X-ray Diffraction (XRD)

X-ray diffraction (XRD) is a non-destructive analytical technique for identification and quantitative determination of long-range order in various crystalline compounds. X-rays are electromagnetic radiation generated when an electron beam accelerated through a high voltage field hits a metal, which acts as an anode. The wavelength (λ) of x-rays is characteristic of the target anode material used and is given by [34,35]

$$\lambda = \frac{hc}{E} \tag{2.3}$$

where, h is the Planck's constant, c is the velocity of light and E is the energy of the photon.

The wavelength of x-ray is comparable to the size of atoms, therefore they can be effectively used to measure the structural arrangement of atoms in materials. In laboratory instruments x-rays are produced in tubes having copper (Cu) or molybedenum (Mo) anodes, which emit x-rays corresponding to wavelengths of 1.54 Å and 0.8 Å, respectively. In recent years synchrotron facilities have been widely used for x-ray diffraction measurements. Electrons or positrons travelling at near light speed in a circular storage ring are used to produce synchrotron radiation. These radiations are thousands to millions of times more intense than laboratory x-ray tubes, and are very useful for structural investigations at very low incident x-ray angles. [34]

X-rays interact with electrons in atoms. When x-rays collide with electrons, some x-rays from the incident beam are deflected away from the incident direction. If the wavelengths of these scattered x-rays remain unchanged, the process is called an *elastic scattering (Thompson Scattering*) in that only momentum is transferred during collision.

[34] These are the x-rays that are measured in diffraction experiments. They carry information about the electron distribution in materials. On the other hand, during *inelastic collision (Compton Scattering),* x-rays transfer some of their energy to the electrons and so the scattered x-rays will have different wavelength than the incident x-rays.

X-rays diffracted from different atoms interfere with each other. If the atoms are arranged in a periodic fashion, as in the case of crystals, the peaks in the interference pattern will correspond to the distribution of atoms. The peaks in an x-ray diffraction pattern are directly related to the atomic distances by Bragg's law [34,35]

$$n\lambda = 2d\sin\theta \tag{2.4}$$

where, λ is the wavelength of x-ray, d is the inter-planar distance, θ is the scattering angle and n an integer representing the order of the diffraction peak, as shown in Figure 2.6.

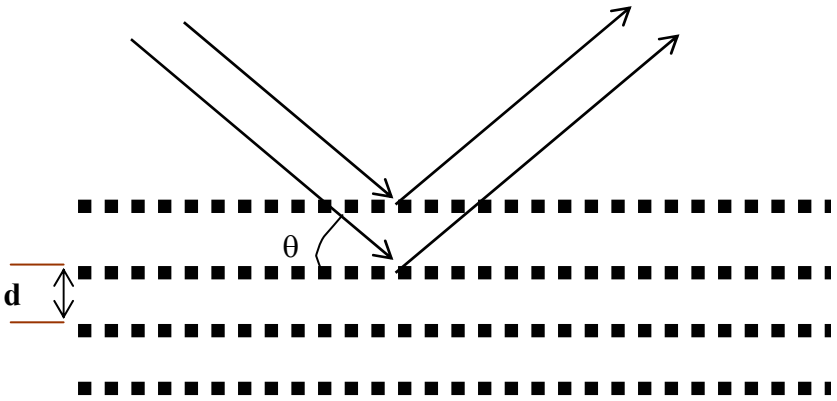

Figure 2.6. Schematic for Bragg's law

X-ray diffraction data can be collected by using either reflection or transmission geometry as shown in Figure 2.7. In the reflection mode, x-rays scattered or reflected from the sample are detected as shown in Figure 2.7 (a). The reflected x-rays interfere with each other such that in the diffractogram, intense peaks are obtained at corresponding d values, according to the Bragg's law.

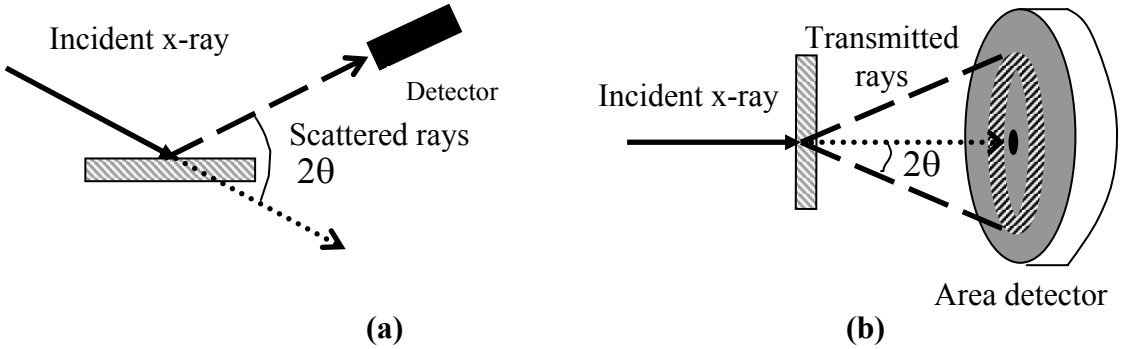

Figure 2.7. Schematic of x-ray diffraction geometries (a) reflection mode (b) transmission mode

The peak position, intensity, and shape provide important information about the long-range order in the material. For example, the apparent crystal size (L) can be quantitatively calculated by Scherrer's formula. [34]

$$L = \frac{0.9\lambda}{\beta_0 \cos\theta} \tag{2.5}$$

where, β_0 is the half width of the crystalline peak in radians

In the transmission mode, an area detector detects the x-rays transmitted through the sample. A circular cone of transmitted rays is incident on the detector, giving a circular ring like pattern as shown in the Figure 2.7 (b). The radius of the circular ring corresponds to the inter-planar distance. The intensity along the circumference of the circle gives the intensity along the azimuthal angle (χ), which gives information about orientation of the scattering entities in the sample. XRD can be very effectively used for intercalated composites, containing silicate layers arranged in a periodic spacing of a few nanometers. However, XRD has limited use in completely disordered exfoliated state, where the layered structure is completely lost. The x-ray diffraction technique has been extensively used to investigate the structure of polyolefin-nanoclay composites in this thesis.

2.5.2. Optical Microscopy (OPM)

Optical microscopy is a technique in which visible light transmitted through the bulk of or reflected from the surface of a sample is collected and magnified to enable visualization of the structural features in the sample. [34] In this thesis we will be concerned with observing cross-polarized light transmitted through the sample. When light passes through any material, it interacts with the molecules of the material. Depending upon these interactions, light is partly absorbed, partly transmitted and partly reflected. These interactions often slightly reduce the velocity of light passing through it. The extent of reduction in velocity of light can be measured as the *refractive index*.

In general, the optical character of any specimen can be described by three orthogonal refractive indices, (n_1, n_2, n_3). The three indices would be equal for an unoriented sample, while the refractive indices parallel and perpendicular to the direction of orientation would be different for an orientated sample. The birefringence may be expressed as [34]

$$\Delta n = n_1 - n_2 \tag{2.6}$$

Thus the magnitude of Δn measured using an optical microscope depends on the degree of orientation and the optical anisotropy of the material. Birefrigent structures up to a few microns (~1-4 microns) can be studied by using optical microscopy. Thus polymer crystalline entities such as spheurlites and primary clay particles can be observed by OPM.

A schematic of an optical microscope is illustrated in Figure 2.8. As shown in the schematic, light is first passed through a polarizer, which allows the rays vibrating in only one direction to pass through. Polarized light is then passed through the sample followed by an analyzer before reaching the observer. [34]

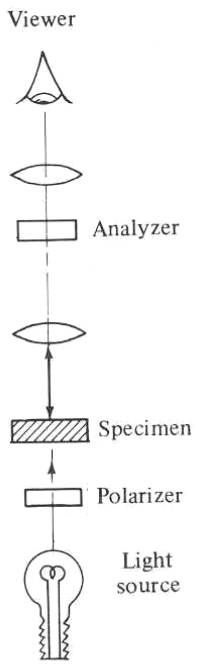

Figure 2.8. Schematic of optical microscope

2.5.3. Transmission Electron Microscopy (TEM)

Conventional optical microscopes can investigate structure to the resolution of few micrometers. But much higher resolution is required to study the fine structural details of the polymer nanoclay composites. A transmission electron microscope (TEM) is used to observe the fine scale structure. [34] A TEM functions exactly as its optical counterpart except that it uses a focused beam of electrons instead of visible light to "image" the specimen and gain insight about the structure and composition.

The four basic operations involved are [34]: 1) A stream of electrons is formed and accelerated towards the specimen using a positive electrical potential, 2) This stream is confined and focused using a metal aperture and *magnetic lenses* into a thin, monochromatic beam, (magnetic lenses are circular electro-magnets capable of projecting a precise circular magnetic field in a specified region) 3) The focused beam is impinged on the sample by a magnetic lens, 4) The energetic electrons then interact with the irradiated sample. These interactions and effects are detected and transformed into an image. A schematic of a TEM is illustrated in Figure 2.9.

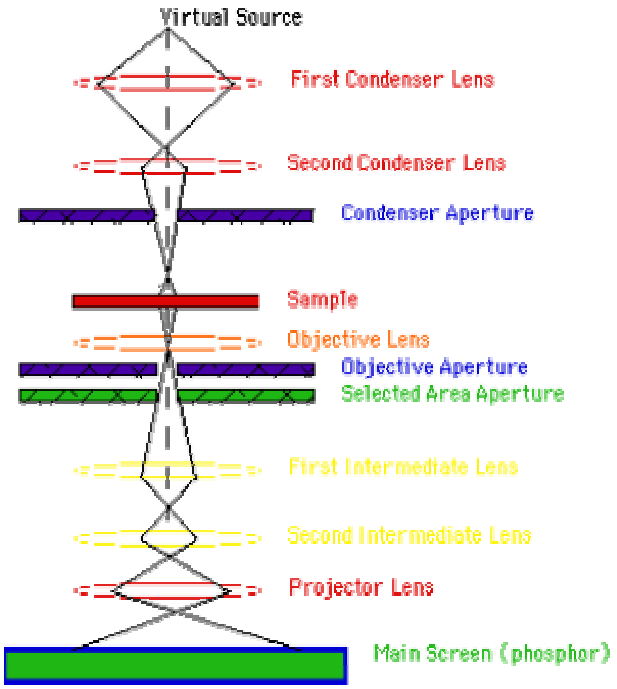

Figure 2.9. Schematic of transmission electron microscope (TEM)

In the present work TEM has been used occasionally to directly observe the state of dispersion of clay in the polymer matrix. A TEM of polypropylene nanocomposites is illustrated in Figure 2.10

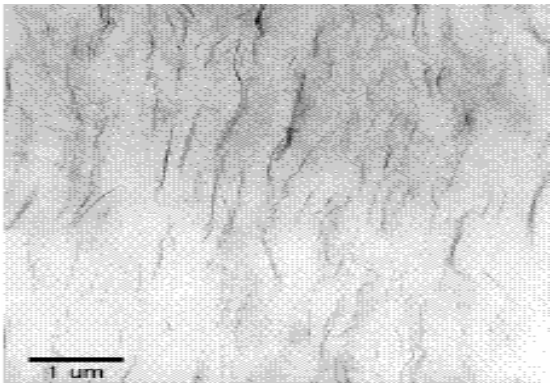

Figure 2.10. TEM of polypropylene nanoclay composites [12]

2.6. Rheology

2.6.1. General introduction

The term 'Rheology' means the study of deformation and flow of matter. The science of rheology deals with the study of stress - deformation relationships of materials that are more complex in behavior than ordinary liquids and solids. [36-41]

Consider the case of simple shear deformation, where the material is sheared in between two parallel plates, held distance (h) apart, with the lower plate stationary and the upper plate moving with velocity (V), exerting shear force (F) on area (A), and displacing the material by a finite distance (∇) in time (dt) as illustrated in Figure 2.11.

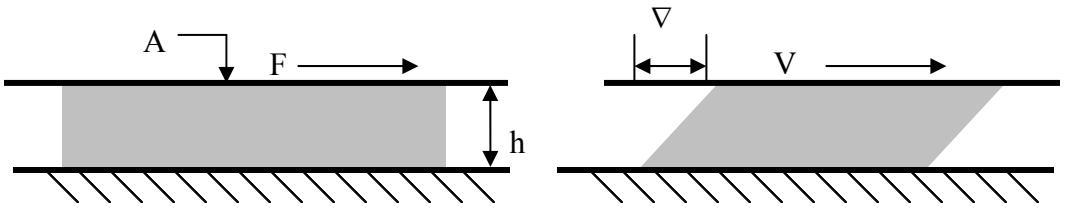

Figure 2.11. Simple shear deformation of material

Then, shear stress (σ), shear rate ($\dot{\gamma}$) are defined as

$$\left.\begin{aligned} &\text{Shear stress } (\sigma) = F/A = \text{Force/Area} \quad (\text{dyne/cm}^2) \\ &\text{Shear Strain } (\gamma) = \nabla/h = \text{Displacement/spacing} \quad (\text{dimensionless}) \\ &\text{Shear rate } (\dot{\gamma}) = (d\nabla/dt)/h \quad (s^{-1}) \end{aligned}\right\} \qquad (2.7)$$

Hookean solid: For a perfectly Hookean elastic solid, the applied stress (σ) is proportional to the strain (γ). [36]

$$\sigma = G\gamma \qquad (2.8)$$

where, the proportionality constant, G is called as the shear modulus. The modulus of the material is a measure of its stiffness or ability to resist the deformation.

Newtonian liquid: For a perfectly viscous liquid, the applied stress (σ) is proportional to the strain rate ($\dot{\gamma}$)

$$\sigma = \eta\dot{\gamma} \qquad (2.9)$$

where, η is the coefficient of viscosity. A liquid is said to be Newtonian if the viscosity does not depend upon the strain rate.

Hookean solids and Newtonian liquids are idealized cases representing perfectly elastic and viscous materials, respectively. A perfectly elastic material stores all the deformational energy and regains its original shape after the deforming forces are removed, while a perfectly viscous material dissipates all the deformational energy through flow. In reality however, the response of all materials, especially those of complex fluids such as polymers, to the applied deformation is a combination of both viscous and elastic behavior. Such combined behavior is termed as *viscoelastic behaviour*. [37]

2.6.2. Linear viscoelasticity

Linear viscoelasticity refers to the behaviour of complex fluids which can be expressed as a linear combination of a Newtonian viscous and a Hookean elastic response Thus, the modulus and viscosity of the material remains constant over the range of deformation or stresses applied. The stress in a viscoelastic fluid depends on not only the present deformation but also on the history of deformation. A fading memory function, which is typically an exponential decay, describes how much of the past deformation contributes to the present stress state. [38,40] A viscoelastic fluid has a characteristic time scale over which the stress relaxes. A dimensionless number, the Deborah number (D_e) may be defined as the ratio of the material relaxation time (λ) to process time (t_p).

$$D_e = \frac{\lambda}{t_p} \tag{2.10}$$

For a steady state process a similar dimensionless number viz., the Weissenberg number (W_e), may be defined as,

$$W_e = \lambda \dot{\gamma} \tag{2.11}$$

where, $\dot{\gamma}$ is the steady rate deformation rate. At short times, i.e., large D_e or W_e, the material response is elastic, while at long times, i.e., small D_e or W_e, the material response is viscous.

Typically linear viscoelastic behaviour is exhibited over a limited range of small deformation or stress. Several linear viscoelastic material functions, which quantify the response of the fluid, can be obtained from rheological experiments. Those that are used in this work are described in the following:

Stress relaxation after step strain: In this experiment, a small strain (γ_o) is instantaneously imposed on the material and held constant, while the stress (σ) is measured as a function of time. Typical response of a Hookean elastic solid, a Newtonian viscous liquid and a linear viscoelastic fluid are shown in Figure 2.12. (b). [40]

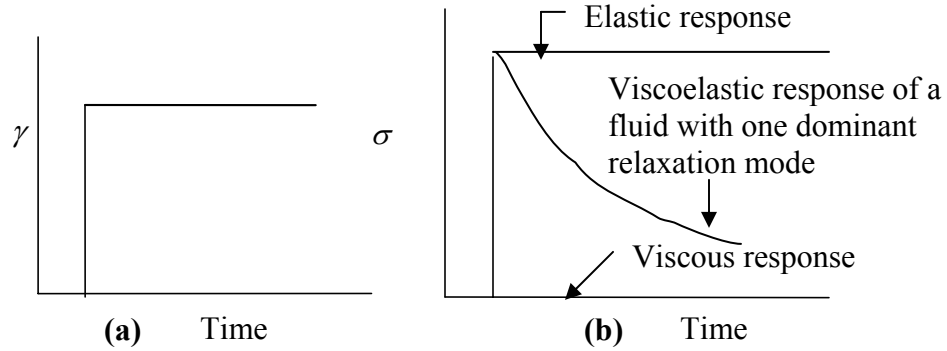

Figure 2.12. Stress relaxation experiment a) step in shear strain with time b) typical response of viscous, elastic, viscoelastic materials

When γ_0 is small, then stress relaxation modulus $G(t)$ is defined as

$$G(t) = \sigma(t)/\gamma_0 \tag{2.12}$$

Creep Experiment: In a shear creep experiment, a constant shear stress (σ_0) is imposed and the shear strain $\gamma(t)$ is monitored as a function of time. For polymeric liquids the strain rapidly increases initially like an elastic solid and then continues to increase more slowly with time until at long times a linear increase with time (i.e., constant $\dot{\gamma}$) is observed. Creep behaviour of typical polymer is shown in Figure 2.13. [37]

Data usually is expressed in terms of the creep compliance, $J(t)$ given as

$$J(t) = \gamma(t)/\sigma_0 \tag{2.13}$$

As indicated in the figure steady state creep compliance (J_e^0) is defined by the extrapolation of the limiting slope to t = 0. For a Newtonian liquid (J_e^0) would be zero. A

non-zero value for J_e^0 is clear indication of viscoelastic nature. [38] An ideal Hookean solid will not creep or flow under stress with time and for Newtonian liquid creep compliance will vary linearly with time. [40]

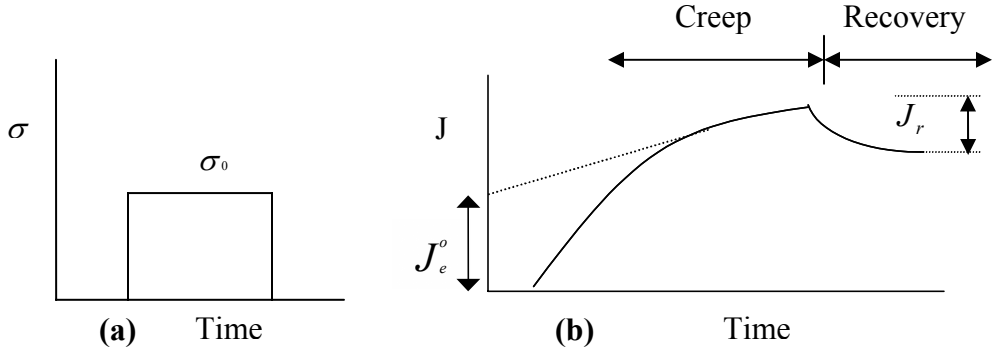

Figure 2.13. Creep experiment a) stress with time b) compliance with time

The slope of the compliance curve at long time gives the inverse of zero shear viscosity (η_0). At long times the creep compliance can be written as [37,39,40]

$$J(t) = J_e^o + \frac{t}{\eta_0} \tag{2.14}$$

Another type of experiment often done in conjunction with creep is *creep recovery,* which is the measurement of the recoil of strain after the stress is removed. Recoverable creep compliance is given as [35]

$$J_r = \frac{\gamma_r(t)}{\sigma_0} \tag{2.15}$$

where, σ_0 is the stress before recovery starts.

Oscillatory experiments: An oscillatory shear experiment is the most commonly used method for determing the linear visocelastic properties of polymers. In a typical oscillatory shear experiment a sinusodally varying small amplitude stress or strain is applied to the sample, and the response, i.e., either sinusodally varying strain or stress, respectively, is measured. This kind of deformation is achieved in parallel plate or cone-plate geomerties (discussed in the next section) by rotating the cone or the plate about its axis.The strain oscillates sinusoidally as given by

$$\gamma(t) = \gamma_o \sin(\omega\, t) \tag{2.16}$$

where, ω is the frequency of oscillations. For viscoelastic materials the response is qualitatively illustrated in the Figure 2.14. [36]

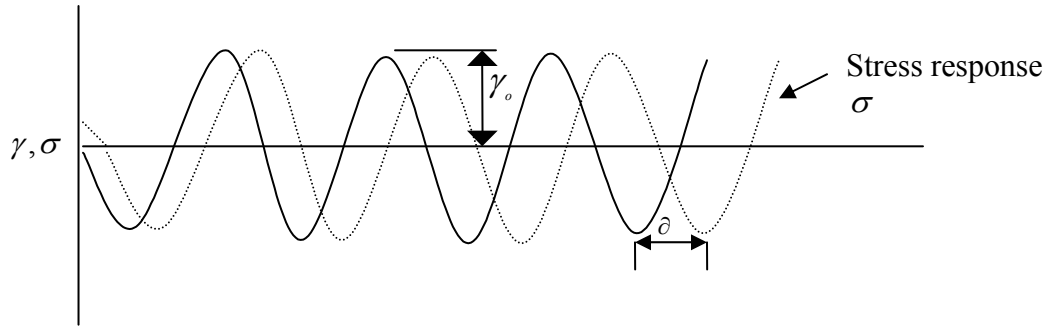

Figure 2.14. Oscillatory shear strain, shear stress in small amplitude oscillatory shear

The strain amplitude (γ_o) is so chosen as to ensure that the material deformation is in the linear viscoelastic regime. For an elastic solid, since the stress is directly proportional to the strain, it will be *in phase* with the applied strain. In case of viscous liquids the stress response is *out of phase* with the applied strain. The polymer response is typically in between these two limits as illustrated in Figure 2.14 with some phase shift (∂). In general, the sinusoidally varying stress can be represented as [36,41]

$$\sigma(t) = \gamma_o[G'(\omega)\sin(\omega t) + G''(\omega)\cos(\omega t)] \tag{2.17}$$

where, the term $G'(\omega)$ is *in phase with the strain* (γ) and is called the *storage modulus.* It represents the stored elastic energy. The term $G''(\omega)$ is in phase with the rate of strain ($\dot{\gamma}$) and is called the *loss modulus*. It represents the viscous dissipation of stored energy. The ratio G''/G' is called the *loss tangent* (tan ∂). A higher value (>>1) of loss tangent indicates liquid like response of the material and lower value (<<1) indicates a solid like behavior. The complex modulus (G^*) is given as

$$G^* \equiv G' + iG'' \tag{2.18}$$

where, G' is the real part and G'' is the imaginary part. Similarly, a complex viscosity is defined as

$$\eta^* \equiv \eta' + i\eta'' \tag{2.19}$$

where, η' is the real part and η'' is the imaginary part.

Figure 2.15 shows a schematic variation of the complex modulus (G^*) with frequency (ω) for a flexible, entangled polymer melt.

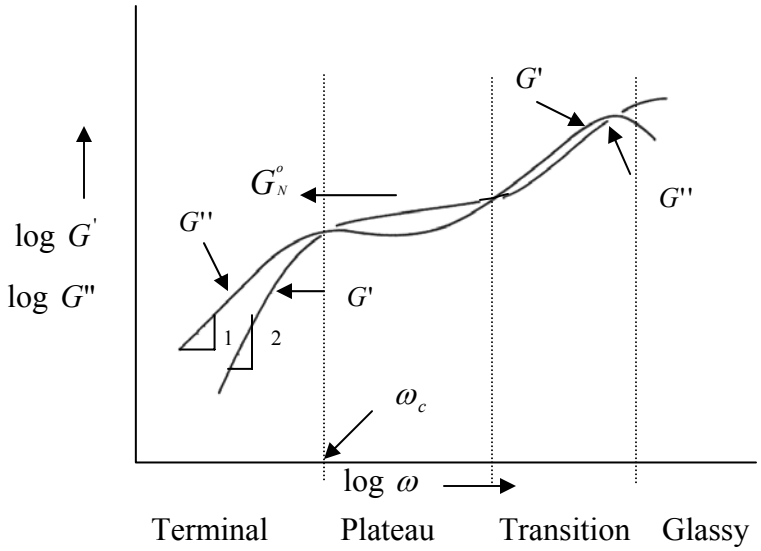

Figure 2.15. Schematic of complex modulus variation as a function of frequency for a typical polymer [39]

At low frequencies, i.e., in the terminal region of relaxation, the material response is mainly liquid-like and $G" > G'$ in this region. The slopes of $G"$ and G' are 1 and 2, respectively. Both $G"$ and G' increase in this region till a crossover point at some frequency (ω_c). [39] The reciprocal of crossover frequency gives the characteristic relaxation time of the material. In the terminal regime $G^{'}$ and $G^{"}$ data can be fit to a multimode Maxwell model given by [36]

$$G^{'} = \sum_i \frac{g_i(\omega\lambda_i)^2}{1+(\omega\lambda_i)^2},\ G" = \sum_i \frac{g_i(\omega\lambda_i)}{1+(\omega\lambda_i)^2} \tag{2.20}$$

where, g_i and λ_i are the modulus and relaxation time of mode *i*.

After crossover, at intermediate frequencies, i.e., in the plateau region, G' reaches a constant value ($G' \approx G_N^o$). The *plateau modulus* (G_N^o) is independent of the molecular weight and depends only on the chemical nature of the polymer. Correspondingly in this region $G"$ passes through a minimum.

Both $G"$ and G' increase again at higher frequencies. At such higher frequencies or small time scales only the response of small parts of the polymers (i.e., few monomeric

units) can be probed. The glassy modulus (G_g) measured at much higher frequency is of the same order of magnitude for all polymers ($G_g \sim 10^9$ Pa). [39]

Time-temperature superposition: The viscoelastic material functions are strong functions of temperature. Also, the $G(t)$, G' and G'' span many orders of magnitude in time or frequency scale. No single experiment can cover the entire span. Fortunately most of the polymeric melts obey the principle of time-temperature superposition. Consequently a change in temperature shifts the viscoelastic functions along the time (or frequency) scales without changing their shapes. [34,37]

Thus, from e. q. 2.20 and neglecting the weak temperature dependence of g_{ig}, $G^{'}(T) = G'(T_o)$ if

$$[\omega\lambda]_T = [\omega\lambda]_{To} \tag{2.21}$$

The dependence of the relaxation time on temperature is given by either the WLF e. q.

$$\ln a_T = \ln \frac{\lambda(T)}{\lambda(T_o)} = \frac{-C_1(T - T_o)}{C_2 + T - T_o} \tag{2.22}$$

or by the Arrhenius e. q.

$$\ln a_T = \ln \frac{\lambda(T)}{\lambda(T_o)} = \frac{\Delta E_a}{R}\left(\frac{1}{T} - \frac{1}{T_0}\right) \tag{2.23}$$

where, E_a is the flow activation energy and a_T is called the horizontal shift factor. Thus we get,

$$\ln \omega_T = \ln \omega_{To} + \ln a_T \tag{2.24}$$

which implies a horizontal shift by an amount $\ln a_T$ on $\ln\ \omega$ axis.

2.6.3. Non-Linear viscoelasticity

At high strains the viscoelastic response of polymeric fluids deviates from linearity. The non-linear response is typically caused by orientation of the microstructure (e.g., chain orientation). Usually $G(t)$, G' and G'' decrease with increasing strain. A dynamic amplitude sweep test is done to delineate the linear and non-linear viscoelastic regimes. Figure 2.16 shows a schematic of a strain amplitude sweep test.

In the non-linear regime the relaxation modulus $G(t)$ becomes a function of time and strain. Equation. 2.12 is then modified to

$$G_{nl}(t,\gamma) = \sigma(t,\gamma)/\gamma_o = G(t)h(\gamma) \tag{2.25}$$

where, $G(t)$ is the relaxation modulus in the linear regime (e. q. 2.12) and $h(\gamma)$ is called the damping function. Equation 2.25 shows an important property of viscoelastic fluids viz., time-strain factorability, which is observed for polymer melts above a certain time scale.

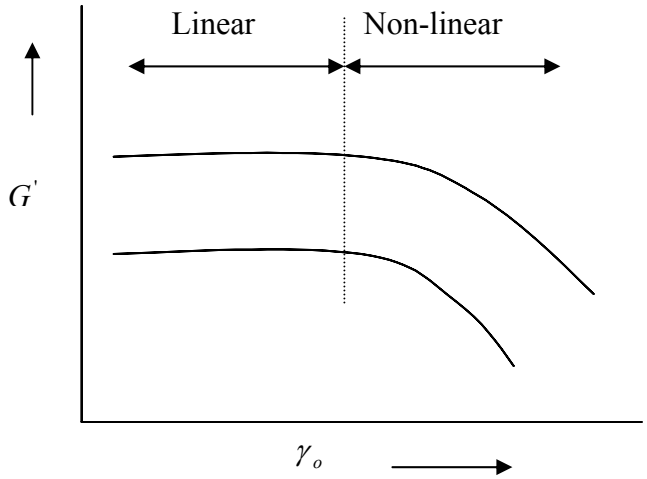

Figure 2.16. Schematic of a strain amplitude sweep

Steady shear: In this experiment, a constant shear rate is applied and steady shear stress and normal stresses are measured. Measurements are typically made over a wide range of shear rates to study shear rate dependence of the sample. At low shear rates a Newtonian plateau is seen, whereas the viscosity often decreases with increasing shear rates at high shear, as illustrated in Figure 2.17. The shear thinning or thickening response can be described by a simple empirical inelastic constitutive model viz. the power law equation given by

$$\eta_{app} = m\gamma^{n-1} \tag{2.26}$$

where, η_{app} is the apparent viscosity, n is power law index and m is the consistency index. The material is shear thinning when $n < 1$ and shear thickening when $n > 1$.

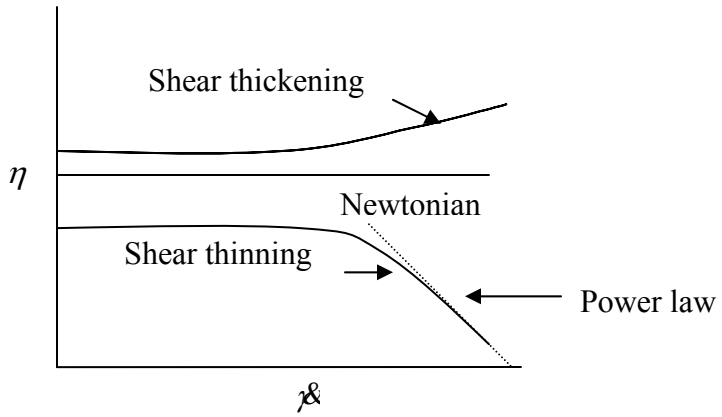

Figure 2.17. Viscosity dependence of Newtonian and Non-Newtonian materials

Cox-Merz rule: Generally for many polymer melts and solutions, the shear viscosity as a function of shear rate, $\eta(\dot{\gamma})$, is almost identical to the complex viscosity as a function of frequency. [35]

$$\eta(\dot{\gamma}) = \eta^*(\omega), \text{ for } \dot{\gamma} = \omega \tag{2.27}$$

This is the empirical Cox-Merz rule and is frequently used to estimate shear-viscosity curves from linear viscoelastic data. However fluids having complex structure such as liquid crystalline polymers do not obey this law.

Plastic behaviour: Certain materials show no deformation up to certain level of stress, referred to as the yield stress. Above the yield stress the material flows readily, as illustrated in the Figure 2.18. [37]

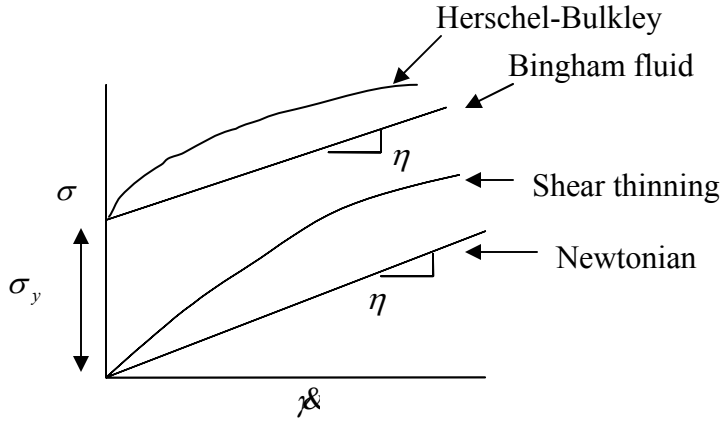

Figure 2.18. Various flow models of Newtonian and Non-Newtonian materials

Various flow models have been proposed to explain the viscoplastic behaviour of such fluids. [38]

Bingham model:

$$\sigma = \sigma_y + \eta\dot{\gamma} \tag{2.28}$$

Herschel-Bulkely:

$$\text{(HB-1) } \sigma = G_o\gamma \text{ for } \sigma < \sigma_y \quad ; \text{(HB-2) } \sigma = \sigma_y + m\dot{\gamma}^n \text{ for } \sigma > \sigma_y \tag{2.29}$$

Casson Model:

$$\dot{\gamma} = 0 \text{ for } \sigma < \sigma_y ; \ \sigma^{1/2} = \sigma_y^{1/2} + (\eta\dot{\gamma})^{1/2} \text{ for } \sigma > \sigma_y \tag{2.30}$$

Papanastasiou's modification: [38]

$$\sigma = \left\{\eta + \frac{\sigma_y\left(1 - \exp(-a\dot{\gamma})\right)}{\dot{\gamma}}\right\}\dot{\gamma} \tag{2.31}$$

The above models qualitatively predict the plastic behaviour of the material. These models will be discussed in more detail in chapter 8.

2.6.4. Rheometers and test geometries

The rheological characterization reported in this thesis has been performed using both stress-controlled and strain-controlled rheometers. A stress-controlled rheometer consists of a constant torque motor. [36-41] The software converts the applied value of torque to a shear stress, and by monitoring the change of strain as a function of time the shear rate is obtained. The strain-controlled rheometer consists of a constant speed motor with a torque detection system. The software converts the measured torque to shear stress value.

Test geometries: Parallel plate geometry is used for the melt rheological experiments at lower shear rates. The material is held in between two parallel plates as shown in the schematic in Figure 2.19. [36]

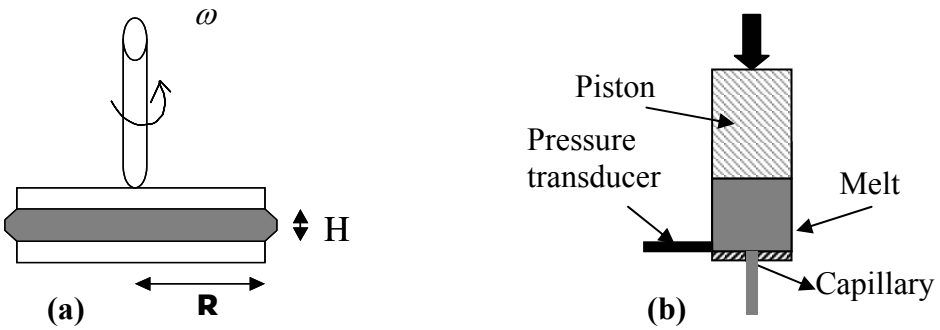

Figure 2.19. Schematic of a) parallel plate geometry b) capillary rheometer

One of the discs is rotated with an angular velocity (ω). The shear rate ($\dot{\gamma}$) is given by

$$\dot{\gamma} = \frac{\omega R}{H} \tag{2.32}$$

where, R is the radius of the plate.

The viscosity (η) is given as

$$\eta = \frac{2\pi R^3}{\dot{\gamma}_R}\left[3 + \frac{d\ln(T/2\pi R^3)}{d\ln\dot{\gamma}_R}\right] \tag{2.33}$$

where, $\dot{\gamma}_R$ is the shear rate at the edge of plate.

A small quantity of sample is required for the analysis. The parallel plate geometry can be used only over a limited range of shear rates. For higher shear rates, a capillary rheometer is used. In this rheometer the melt in the barrel is forced through a capillary by a piston moving with a velocity (V) as shown in the schematic in Figure 2.19 (b).

The shear stress at the wall (τ_w) is given by

$$\tau_w = \frac{\Delta P R}{2L} \tag{2.34}$$

where, ΔP is the pressure drop across the capillary, R is the radius of capillary and L is length of the capillary. The shear rate at wall ($\dot{\gamma}_w$) is given by the *Weissenberg - Rabinowitsch* equation as [38]

$$\dot{\gamma}_w = \frac{1}{\tau_w^2}\frac{d}{d\tau_w}\left[\tau_w^3 \frac{Q}{\pi R^3}\right] \tag{2.35}$$

where, Q is the flow rate of the material. The apparent viscosity η_{app} is then calculated from e. q. (2.9).

2.6.5. Rheology of filled polymers

The low shear viscosity of a dilute suspension is given by the Einstein equation as [40]

$$\eta_o = \eta_{os}(1 + K_E\phi) \tag{2.36}$$

where, η_{os} is viscosity of the matrix fluid, η_0 is the viscosity of the suspension, ϕ is the volume fraction of the suspended rigid particles and K_E is the Einstein coefficient which is 2.5 for spherical particles. This equation holds for very low filler loading ($\phi \le 0.03$). When the filler loading increases, the filler particles get close enough that the drag on one of them is influenced by a second nearby particle. The particles are then said to experience *hydrodynamic interactions*. The viscosity of a suspension of spherical particles at higher filler loading ($\phi \le 0.10$) is given by [40]

$$\frac{\eta_o}{\eta_{os}} = 1 + 2.5\phi + 6.2\phi^2 \tag{2.37}$$

At still higher filler concentration, the viscosity of the suspension increases dramatically with the filler loading and may be modeled by an exponential function as shown in the Figure 2.20. [40]

$$\eta_o = \eta_{0s}\exp(\phi) \tag{2.38}$$

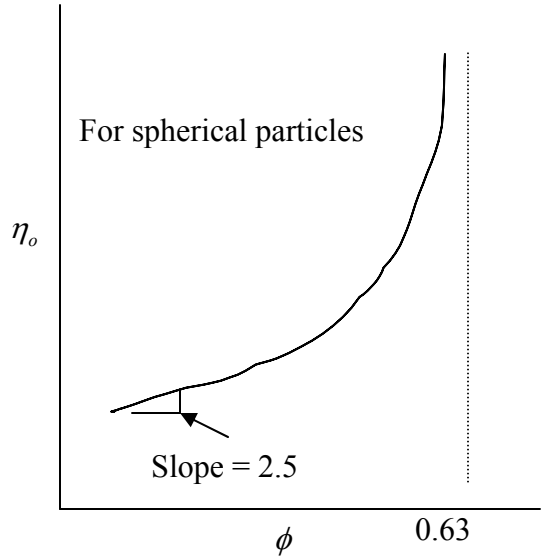

Figure 2.20. Zero shear viscosity variation with filler concentration

These relations are valid for affine deformation. At higher shear rates, the suspensions may exhibit shear-thinning behaviour. Then a dimensionless shear rate, or *Peclet number* (P_e) may be defined as [40]

$$P_e \equiv \frac{\eta_{os}\dot{\gamma}a^3}{k_B T} \propto \dot{\gamma}t_D \tag{2.39}$$

where, the time (t_D) for a particle to diffuse a distance equal to its radius (a) is given as

$$t_D \approx \frac{6\pi\eta_{os}a^3}{k_B T} \tag{2.40}$$

k_B is the Boltzmann constant and T is the absolute temperature.

Asymmetric filler particles like clay particles used in this study can be oriented in the flow direction. Orientation relaxation of individual particles under quiescent conditions is expected to occur by Brownian motion, given as [40]

$$\frac{\partial f}{\partial t} = \Theta\frac{\partial^2 f}{\partial \phi^2} \tag{2.41}$$

where, $f(\phi,t)$ is the fraction of particles oriented at an angle (ϕ) at time (t), and (Θ) is the rotational diffusion coefficient. From e. q. (2.40) the orientation is expected to decay in an exponential manner given by

$$f = f_0 e^{-t\Theta} \tag{2.42}$$

For an ellipsoidal particle the rotational diffusivity is related to particle dimensions and to matrix viscosity (η_{matrix}) by [42]

$$\Theta = \frac{3k_B T}{16\pi\eta_{matrix} a^3}\left[2\ln\left(\frac{2a}{b}-1\right)\right] \tag{2.43}$$

where, a and b are the major and minor axes of the ellipsoidal particle. For such asymmetric particles the Peclet number may be defined as

$$P_e = \frac{\dot{\gamma}}{\Theta} \tag{2.44}$$

2.6.6. Mechanical behaviour of semicrystalline polymers

This discussion of mechanical properties is restricted to only tensile properties of semicrystalline polymers in the context of the work reported in chapter 9 of this thesis. The schematic of stress-strain curve for a typical semicrystalline is shown in the Figure 2.21 along with different stages of ductile deformation of a tensile specimen. [43]

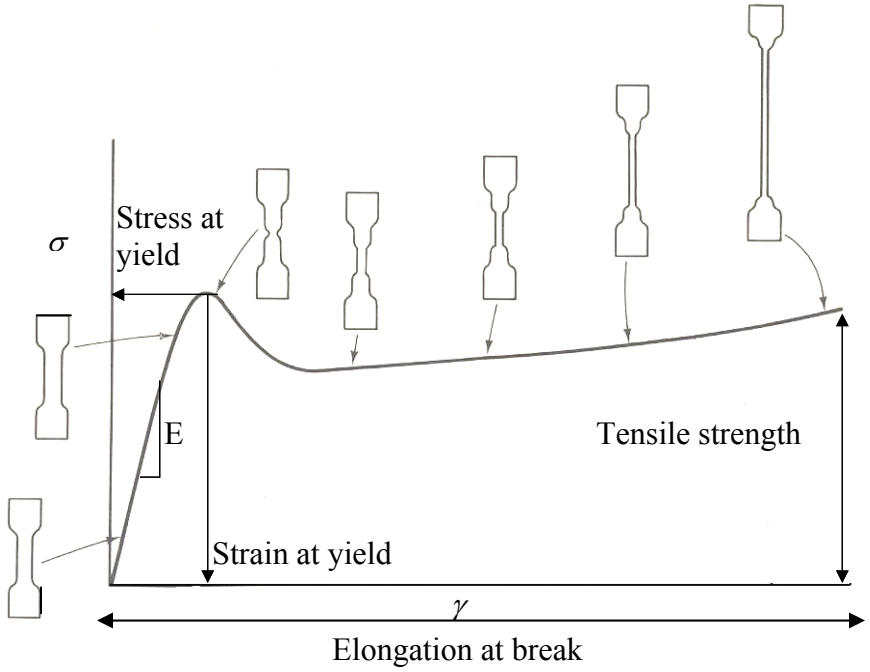

Figure 2.21. Schematic of the mechanical behaviour of the semicrystalline polymer

Initially the stress (σ) increases linearly with strain (γ), and the slope of this linear part of the graph gives the Young's modulus (E) of the sample. After a critical stress the material yields; the stress passes through a maximum and then slightly decreases. The yield stress corresponds to the beginning of the process of necking in the gauge length. Necking continues with elongation in the sample and in this region the stress increases only slightly with increasing strain. The upsweep in the curve is called as strain hardening. At still higher strain the specimen finally breaks. The area under the curve is called the toughness of the sample. Some polymers exhibit brittle fracture, i.e., the tensile sample breaks at the maximum applied load, without necking.

Reference List:

1. Pinnavaia, T. J. *Science* **1983,** *220*(4595), 365-371.
2. Theng, B. K. G. *Developments in Soil Science, Vol. 9: Formation and Properties of Clay-Polymer Complexes Elsevier Publications,* **1979**.
3. Theng, B. K. G. *Chem.N.Z.* **1980,** *44*(5), 194-199.
4. Brindley, G. W.; Brown, G. *Crystal Structures of Clay minerals and Their X-ray identification*; Mineralogical Society, London, **1980**
5. Giannelis, E. P.; Krishnamoorti, R.; Manias, E. *Adv. Polym. Sci.* **1999,** *138*, 107-147.
6. Giannelis, E. P. *Adv. Mater.* **1996,** *8*(1), 29-35.
7. LeBaron, P. C.; Wang, Z.; Pinnavaia, T. J. *Appl. Clay Sci.* **1999,** *15*(1), 11-29.
8. Polyak, V. J.; Guven, N. *Journal of Cave and Karst studies* **2000,** *62*(2), 120-126.
9. Carrado, K. A. *Appl.Clay Sci.* **2000,** *17*(1), 1-23.
10. Tjong, S. C.; Meng, Y. Z.; Hay, A. S. *Chem. Mater.* **2002,** *14*(1), 44-51.

11. Tudor, J.; Willington, L.; O'Hare, D.; Royan, B. *Chem. Comm.* **1996,** (17), 2031-2032.

12. Garces, J. M.; Moll, D. J.; Bicerano, J.; Fibiger, R.; McLeod, D. G. *Adv. Mater.* **2000,** *12*(23), 1835-1839.
13. Dietsche, F.; Thomann, Y.; Thomann, R.; Mulhaupt, R. *J. Appl. Polym. Sci.* **2000,** *75,* 396-406.
14. Yano, K.; Usuki, A.; Okada, A.; Kurauchi, T.; Kamigaito, O. *J. Polym. Sci. Part A: Polym. Chem.* **1993,** *31*(10), 2493-2498.
15. Yano, K.; Usuki, A.; Okada, A. *J. Polym. Sci. Part A: Polym. Chem.* **1997,** *35*(11), 2289-2294.
16. Ellsworth, M. W.; Novak, B. M. *J. Am. Chem. Soc.* **1991,** *113*(7), 2756-2758.
17. Huang, Z. H.; Qiu, K. Y. *Polymer* **1997,** *38*(3), 521-526.
18. Rodrigues, D. E.; Risch, B. G.; Wilkes, G. L. *Chem. Mater.* **1997,** *9*(12), 2709-2719.
19. Messersmith, P. B.; Giannelis, E. P. *Chem. Mater.* **1993,** *5*(8), 1064-1066.
20. Usuki, A.; Kojima, Y.; Kawasumi, M.; Okada, A.; Fukushima, Y.; Kurauchi, T.; Kamigaito, O. *J Mater. Res.* **1993,** *8*(5), 1179-1184.
21. Ogata, N.; Kawakage, S.; Ogihara, T. *Polymer* **1997,** *38*(20), 5115-5118.
22. Ogata, N.; Jimenez, G.; Kawai, H.; Ogihara, T. *J. Polym. Sci. Part B: Polym. Phys.* **1997,** *35*(2), 389-396.
23. Vaia, R. A.; Jandt, K. D.; Kramer, E. J.; Giannelis, E. P. *Macromolecules* **1995,** *28* (24), 8080-8085.
24. Cho, J. W.; Paul, D. R. *Polymer* **2000,** *42*(3), 1083-1094.
25. Dennis, H. R.; Hunter, D. L.; Chang, D.; Kim, S.; White, J. L.; Cho, J. W.; Paul, D. R. *Polymer* **2001,** *42*(23), 9513-9522.
26. Vaia, R. A.; Jandt, K. D.; Kramer, E. J.; Giannelis, E. P. *Chem. Mater.* **1996,** *8*(11), 2628-2635.
27. Vaia, R. A.; Giannelis, E. P. *Macromolecules* **1997,** *30*(25), 8000-8009.
28. Ryu, J. G. *Macromol. Res* **2002,** *10,* 187-193.
29. Hou, S. S.; Schmidt-Rohr, K. *Chem. Mater*. **2003,** *15*(10), 1938-1940.
30. Balazs, A. C.; Singh, C.; Zhulina, E.; Lyatskaya, Y. *Acc.Chem.Res.* **1999,** *32*(8), 651-657.

31. Vaia, R. A.; Lincoln, D.; Wang, Z. G.; Hsiao, B. S. *Polym. Mater. Sci. Eng.* **2000,** *82* 257-258.
32. Dagani, R. *Chem. Eng. News* **1999,** *77*(23), 25-37.
33. John DeGaspari *Prospecting Paydirt*; John DeGaspari, Ed., *The American Society of Mechanical Engineers*: **2001**.
34. Klugg, H. P.; Alexander, L. E. *X-ray diffraction procedures;* John Wiley & Sons: U.S.A, **1974**.
35. Moore, D.; Reynolds, R. Jr. *X-ray diffraction and identification and analysis of clay minerals of clay minerals;* second Ed.; Oxford University Press, U. K., **1997**.
36. Bird, B. R.; Armstrong, R. C.; Hasseger, O. *Dynamics of Polymeric Liquids Vol.1: Fluid Mechanics;* John Wiley: N.Y., **1977**.
37. Barnes, H. A.; Hutton, J. F.; Walters, K. *An Introduction to Rheology;* Elsevier Publications, U. K., **1989**.
38. Macosko, C. W. *Rheology principles Measurements, and Applications;* Wiley-VCH Inc., N. Y., **1994.**
39. Collyer, A. A.; Clegg, D. W. *Rheological measurements;* second ed.; Chapman and Hall publication, U.K., **1995**.
40. Larson, R. G. *The structure and rheology of complex fluids;* Oxford University Press: U.K., **1999**.
41. Morrison, F. A. *Understanding Rheology;* Oxford University Press: U.K., **2001**.
42. Alexander, A. F.; Johnson, P. *Colloid Science*; Oxford University Press: U.K., **1949**.
43. Schultz, J. *Polymer Materials Science;* Prentice Hall. Inc. N.Y., **1974**.

Chapter 3 Literature

This chapter presents a survey of the contribution of various researches towards synthesis, characterization, processing and rheology of polymer layered silicate (PLS) nanocomposite materials. The purpose of the chapter is not to summarize all of the literature in this area, which is growing at an enormous rate. Rather, the discussion is restricted to only those topics that are of immediate relevance to the work described in this thesis. This survey includes only the literature published in various scientific journals. A compilation and discussion of the nearly 400 patents filed in last three decades for the various commercially important PLS nanocomposites, is out of the scope of this thesis.

3.1. Synthesis of PLS nanocomposites

The synthesis of polymers such as polystyrene [1,2] and polyacrylic acid [3] in the interlayer spacing of montmorillonite has been reported as early as in the 1960's. The technological potential of these materials was realized after the pioneering efforts of the research group in Toyota Motor Co.

PLS nanocomposites can be synthesized by in-situ polymerization, solution blending and melt intercalation as discussed in chapter 2. Usuki et. al. reported the synthesis of nylon 6-clay hybrid by in-situ polymerization of ε-caprolactum in the interlayer layer space of montmorillonite, the surface of which was modified by ω-amino acid. [4] The carboxyl acid end group of the amino acid initiated the polymerization of ε-caprolactum. TEM and XRD analysis of these hybrids showed an exfoliated microstructure. Polymers like polyε-caprolactone (PCL), [5] polycarbonate (PC), [6,7] epoxy, [8-11] polyethylene (PE), [12-14] polypropylene (PP), [13,15,16] polyethylene terephathalate (PET), [17] polydimethyl siloxane (PDMS), [18] polyamide [19-22] and polyimide [23] have also been reported to give exfoliated hybrids by in-situ polymerization of the respective monomers in the interlayer spacing of the clays. Thus it may be inferred that in-situ polymerization often leads to exfoliated nanocomposites. However, the exact reason behind this phenomenon remains elusive. There are extensive

reports of exfoliated nanocomposites synthesized by in-situ polymerization method where the catalyst is anchored on the clay surface. PLS nanocomposites synthesized by this route has a portion of polymer chains tethered to the clay surface. [12,24-27] In this case monomers diffuse into the clay gallery to react chemically at this growth site; the growing polymer chain physically pushes the platelets apart by volume expansion to cause exfoliation.

PE nanocomposites have been synthesized by using a wide range of catalysts like Zircocene based metallocene catalysts, [24,15] Ziegler-Natta Titanium based catalysts [27,26] and late transition metal based catalysts like Palladium (Pd), and Nickel (Ni). [28,12] Various types of clays like Flurohectorite, [28] montmorillonite [26] and Seiolite-palgorskite [27] have been used as the clay support. Jin et. al. reported synthesis of PE nanoclay composites using Ti-based Ziegler-Natta catalyst, anchored to the silicate layers of montmorillonite. [26] The montmorillonite surface was modified using intercalation agents containing hydroxyl groups. Heinemann et. al. synthesized HDPE, LLDPE and LDPE nanoclay composites by both melt extrusion and in-situ homo and copolymerization of ethylene, in the presence of methylaluminoxane (MAO) activated metallocene catalyst and late transition metal based catalyst like Ni and Pd and found that PLS-nanocomposite prepared by in-situ polymerization are better exfoliated. [12]

PLS nanocomposites can also be synthesized by using the sol-gel method, as discussed in chapter 2. Polymethylmethacrylate (PMMA) nanocomposites are commonly synthesized by the sol-gel method. [29-32] Seckin et. al. synthesized PPMA nanoclay composite using bentonite clay. FTIR and XRD analysis showed that the polymer was linked to clay via hydrogen bonding. [30] Huang et. al. synthesized PLS nanocomposites by using different functionalized viz., trialkoxysilyl, hydroxyl and unfunctionalized methyl acrylic polymers by the sol-gel method. [32] The trialkoxysilyl functionalized PMMA was found to be best suited, since it exhibited maximum property improvement.

Polymer clay hybrids can be synthesized by solution blending (i.e., intercalation of polymer from solution). PLS nanocomposites based on polymers like PCL, [33] polylactide (PLA), [34] polyethylene oxide (PEO), [35] syndiotactic-polystyrene (s-PS), [36] PMMA [37] and PE [38] have been synthesized by solution blending. Jeon et. al have reported the synthesis of HDPE nanoclay composites by solution blending. [38]

TEM analysis revealed the formation of intercalated nanocomposites. However, the presence of fairly large clay tactoids indicated very poor dispersion of clay in the polymer matrix.

PLS nanocomposites of polymers like PEO, [39] polystyrene (PS) [40] and PMMA [41-43] have been synthesized by conventional techniques like emulsion and suspension polymerization. For example, Noh et. al. reported on the synthesis of PS nanocomposite synthesis by emulsion polymerization using Na^{+}-montmorillonite, which demonstrated fine dispersion of clay in the polymer matrix and improved mechanical properties. [40]

Giannelis et. al. proposed the more versatile and environmental friendly method for nanocomposite synthesis namely, melt intercalation, which involves melt mixing the polymer and clay. [44] Vaia et. al. found improved intercalation through the aid of conventional processing techniques like extrusion. [45-47] Cho et. al. have shown twin-screw extrusion to be more effective for exfoliation and dispersion of the clay layers compared to single screw extrusion due to more extensive shear. Furthermore, for optimally compatibilized polymer-organoclay systems twin-screw extrusion leads to composite properties comparable to those produced by in-situ polymerization. [48] Fornes et. al. have suggested that during melt compounding the shear stress, dictates the final morphology of the hybrid. [49,50] It was suggested that in the initial stages of extrusion the stress would break up the organoclay particles into smaller tactoids. Further during the extrusion, individual platelets of these tactoids would be peeled apart by combined effect of shear and diffusion of polymer chains in the gallery as illustrated in the Figure 3.1.

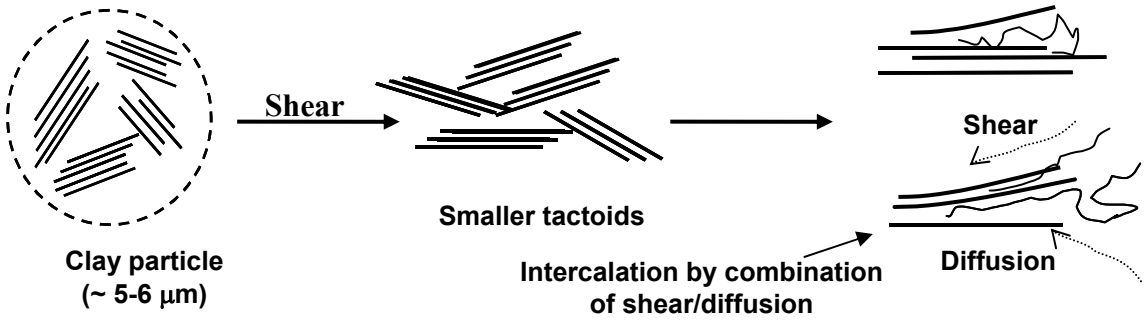

Figure 3.1. Stepwise mechanism of clay exfoliation during the melt mixing of nanocomposites

Dennis et. al. have reported on the effects of the melt processing conditions on the exfoliation of PLS nanocomposites. [51] They observed that factors like the residence time in the extruder and the intensity of shear play a crucial role in determining the dispersion of clay in the polymer matrix. They found that the degree of clay dispersion was maximized by the backmixing in a co-rotating twin-screw extruder. [51]

PLS nanocomposites of almost all commercially important polymers like PS, [43] Nylon, [49-51] PE, [52] PP, [53,54] PCL, [55,56] polybutylene terephathalate (PBT), [57] Ethylene vinyl alcohol (EVOH) [58] and PC [10] can be manufactured by melt intercalation. PLS nanocomposites of polymers like PEO, [39,47] PMMA, [41-43,37] PCL [52,33] and Nylon [49,50,20,21] can be prepared by more than one method based on the availability of suitable polymer-solvent pair and processibility issues.

In the case of many commercially important polymers, the solution intercalation or the in-situ polymerization techniques are difficult to implement on an industrial scale, because a suitable solvent–polymer system is not always available and also an additional step of solvent removal is involved. [59,60] Ecofriendly and cost-effective melt intercalation shifts the synthesis of the nanocomposites down stream to the polymer processing industry.

Vaia et. al. have shown that the d spacing in PEO/Na^+ montmorillonite hybrids prepared by melt intercalation at 80^{o}C matches with those of the PEO hybrids prepared by solution intercalation. [47] Thus under suitably chosen processing conditions the morphology of hybrids obtained by melt intercalation can be comparable with that in hybrids prepared by other synthetic routes.

Organic modifiers play a crucial role in the synthesis of PLS nanocomposites. Layered silicates, montmorillonite in particular, are hydrophilic in the pristine form. The clay surface can be rendered organophilic by exchanging the mobile Na^+ with suitable cationic surfactants. Such organoclays have lower surface energy compared to pristine clay and are more compatible with the polymer matrix. [44,45] Vaia et. al. found that PS does not intercalate in pristine Na^+-montmorillonite, however the intercalation does take place with organosilicates. [45] Usuki et. al. synthesized nylon-6 nanocomposite using the Na^+ - montmorillonite modified with various ω-amino acids $\{H_3N^+(CH_2)_{n-1}COOH,\ n = 2\text{-}8,\ 11,\ 12 \text{ and } 18\}$. [22] XRD results showed that amino

acids were stretched with longitudinal axes perpendicular to the silicate layer in the interlayer gallery. Among the different amino acids used, 12-aminolauric acid was found to be the most appropriate modifier for nylon nanocomposites.

The hybrids of polymers like nylon [49,50] and PS [44,45] can be prepared by melt intercalation with organosilicate. However, for non-polar polymers like PP [53,54, 61-68] and PE [52] very often an additional compatibilizer is required. The backbone of the compatibilizer is typically miscible with the polymer matrix, while the polar group interacts with silicates as illustrated in the Figure 3.2. Polyethylene grafted with maleic anhydride (PE-g-MA) [52] and polypropylene grafted with maleic anhydride (PP-g-MA) [53] respectively, are widely used for making PE and PP nanocomposites by melt intercalation. Kawasumi et. al. suggested that PP-g-MA could intercalate in the interlayer space through hydrogen bonding with polar OH group of silicates. [53] Addition of such modifiers may help to enhance certain desired properties of the hybrids. For instance, Liu et. al. have shown that addition of PP-g-MA in nylon-6 PLS nanocomposite further reduces the water absorption of the composite. [69]

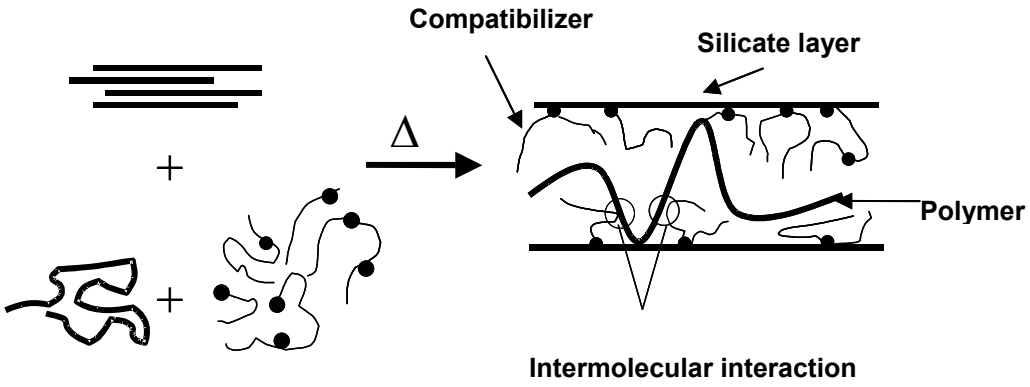

Figure 3.2. Schematic of compatibilizer action with clay and polymer

Functionalization of the polymer matrix can also aid the synthesis of nanoclay composites by melt intercalation. Chisholm et. al. have prepared PBT nanocomposites by sodium sulfonate functionalization ($-SO_3Na$) of PBT, which helps to achieve better exfoliation compared to pristine PBT. [57] The exfoliation does increase with concentration of ($-SO_3Na$) group and so do the mechanical properties.

The addition of modifier and clay has been reported to enhance the rate of crystallization of PLS nanocomposites. [64,70,71] Ma et. al. observed isothermal

crystallization of PP nanocomposites and reported that the crystallinity of PP-nanocomposites decreased with increasing clay concentration. On the other hand, the crystallization rate increased dramatically with clay content. [70] Similarly Maiti et. al. found that clay acts as a nucleating agent and observed reduction in the spherulite dimensions with increasing clay content. [71] Kodigre et. al. found that the PP nanocomposites could be crystallized at higher temperature than pristine PP. They also reported significantly different crystalline morphology of PP at high temp (T = 122^{o}C). [64]

Apart from the synthesis of homopolymer PLS nanocomposites, the intercalation of copolymers like polystyrene-acrylonitrile, [72] Acrylonitrile-Butadiene-Styrene (ABS) [73] and polystyrene-polyisoprene (PS-PI) block copolymers [74-76] has also been studied. Ren et. al. reported that while pristine polyisoprene (PI) could not be intercalated into organoclay, the same could be achieved by copolymerising PI with PS. [76]

Apart from the three main methods of synthesis mentioned above the PLS nanocomposites can also be synthesized by different methods like ultasonication, [77] photo-polymerization [78] and UV curing. [79]

Thus PLS nanocomposites have been synthesized by many different methods. Generally the surface of the clay is suitably tailored to facilitate the clay-polymer interaction. All the efforts in the synthesis of these materials are focused on finding ways to delaminate the layered structure of silicates, which is critically required for maximum property enhancement. [80-82]

3.2. Characterization and properties of PLS nanocomposites

As discussed in chapter 2, the state of dispersion of clay in PLS nanocomposites may be classified in two idealized class of morphologies: (1) *Intercalated,* in which the polymer expands the interlayer distance resulting in an ordered, alternating multilayered polymer - clay layer structure, and (2) E*xfoliated*, where the polymer chains completely delaminate the layered clay structure. However, real nanocomposites exhibit morphologies, which are combinations of these two idealized cases as discussed in several researches summarized below. [83-85]

Transmission electron microscopy (TEM), scanning electron microscopy (SEM) and x-ray diffraction (XRD) are techniques that are often used to directly quantify the structure of PLS nanocomposites. [86] XRD is the most obvious technique to study the periodic structure of clays in case of intercalated PLS nanocomposites. However, XRD cannot be used very effectively for exfoliated PLS nanocomposite systems. In addition to XRD, TEM can be used effectively to characterize the hybrid structure. Figure 2.10 shows TEM of PP - nanoclay composite. [82] The dark lines in the micrograph are the silicate layers, dispersed in the polymer matrix. The separated dark lines correspond to the exfoliated clay, while the small clustered dark lines are for the intercalated clay tactoids. Thus the two idealized morphologies coexist in the PLS nanocomposites.

XRD has also been extensively used to study polymorphism in PLS nanocomposites, and the effect of clay on polymorphism. [87-91] It has been reported that clay induces the γ phase of nylon-6 in nylon-6/PLS nanocomposites. [89,90] Similarly for nylon-66 PLS nanocomposites, the γ phase of nylon-66 is favored and the crystalline phase transition was lowered by 20^{o}C. [87,88] Tseng et. al. reported that in s-PS nanocomposites, in the presence of clay facilitated the formation of β phase of s-PS. [91]

Spectroscopic techniques like Fourier Transform Infrared spectroscopy (FTIR) [92] and Nuclear magnetic resonance (NMR) [93-95] are also being employed to probe the interlayer structure of the clay.

Analytical techniques like differential scanning calorimetric (DSC), dynamical mechanical analysis (DMA) and thermogravemetric analysis (TGA) can provide indirect but useful evidence of structural attributes. For instance, Vaia et. al. have used DSC to study the kinetics of PEO/clay hybrid formation. [47] Pristine PEO is a crystalline material. At time t = 0 hr, it showed a distinct endotherm corresponding to the crystalline PEO. However, as the intercalation progressed, more and more PEO chains were intercalated and consequently the area of the endotherm corresponding to the crystalline PEO reduced. At time t = 6 hrs, this transition had largely vanished, indicating that all of the PEO had intercalated. Similarly for PS-nanocomposites, Vaia et. al. have shown that the DSC thermograms of pristine PS, physical mixture of PS - organoclay and intercalated PS – organoclay are qualitatively different. [46] Both the pristine polymer

and the physical mixture of PS with organoclay exhibited characteristic glass transition at 96^{o}C, while the intercalated hybrid did not show any such transition. These results complimented the results obtained by high temperature x-ray analysis, which showed that with annealing time the clay peak shifted to higher d spacing.

PLS Nanocomposites exhibit improved thermo mechanical properties, reduced gas permeability and improved solvent resistance. [86] Kojima et. al. have shown that the modulus of nylon-6 PLS nanocomposite increases by 100%, impact strength by 25%, flexural modulus by 100% and heat distortion temperature (HDT) increases by 125%. These improvements in the properties were achieved by the addition of just 4.5 wt% of clay. [21] Usuki et. al. have tested the mechanical properties of nylon-6 clay hybrid using four different types of clays viz., montmorillonite, aconite and synthetic clays like limonite and mica. These clays were modified using 12-aminolauric acid. [22] They found that the mechanical properties for the hybrid synthesized by using montmorillonite were superior to other clay hybrids. Using NMR measurements they attributed this property enhancement to greater ion bonding between the montmorillonite and nylon-6 as compared to that in the other the types of clays. [12,93] Lan et. al. have shown that exfoliated epoxy clay nanocomposites have higher modulus than the intercalated epoxy clay composites. [80]

Fornes et. al. studied the structure, mechanical properties and rheological properties of nylon-6 PLS nanocomposites prepared from nylons of three different molecular weights by melt intercalation. [49,50] The mechanical properties enhanced with increasing molecular weight. These results were in agreement with TEM results, which showed greater extent of exfoliation with increasing molecular weight. The PLS nanocomposites based on lower molecular weight polymer had significant amounts of intercalated clay tactoids. Akkapeddi et. al. compared the barrier and mechanical properties of cast and biaxially oriented nylon nanoclay composites films. [96,97] The biaxially oriented composite film showed markedly improved properties compared to the cast films.

Thus the mechanical property enhancement was found to be dependent on many factors such as the concentration and aspect ratio of the silicate layers, [20] interactions between clay and polymer [97] and orientation of clay and polymer. [98,99]

Yano et. al. have shown that incorporation of nano-clays in polyimide matrix increases the barrier properties by creating additional '*tortuous path*' that impedes the diffusion of gas or solvent molecules while passing through the matrix resin as shown in the Figure 2.3. [100] Interestingly, Merkel et. al. have shown that dispersion of nanoparticles of fumed silica increases the permeability of glassly amorphous poly(4-methyl-2-pentyne) membranes due to disruption of chain packing and a subsequent increase in the free volume. [101]

3.3. Thermodynamics of PLS nanocomposites

Vaia et. al. proposed a mean-field, lattice-based model of polymer melt intercalation in organically–modified layered silicates (OLS). In general, an interplay of entropic and energetic factors determines the outcome of polymer intercalation. The entropic penalty of polymer chain confinement is compensated by the increased conformational freedom of the surfactant, when the layers are separated. When the total entropy change is small, small changes in the internal energy of the system will determine whether the intercalation is thermodynamically possible.

However, exfoliation requires complete layer separation [i.e., interlayer distance (h) > radius of gyration of polymer chain (R_0)]. This requires very favourable polymer-OLS interactions to overcome the polymer - polymer and clay - clay interaction. [102,103] Thus, the dispersion of OLS in polymer matrix requires sufficiently favourable enthalpic contribution to overcome any entropic penalties. Favourable enthalpy of mixing is achieved when the polymer - OLS interactions are more compared to surfactant - OLS interactions. [102-106] For polar polymers like nylons an alkylammonium surfactant (most commonly used organic modifier) is sufficient to offer the excess enthalpy, required for the formation of PLS nanocomposite. However, this is not true for the non - polar polymers like PP. There are two ways to promote nanocomposite formation in these cases:

1. Improve the interactions between the polymer and the OLS: The most convenient way to achieve this is to *functionalize* the polymer matrix by polar or polarizable groups like the anhydride group. [53,64,62]

2. Decrease the interaction between the surfactant and OLS, which effectively makes the polymer-OLS interaction dominant. Manias et. al have claimed to reduce the alkylammonium surfactant-montmorillonite interaction by fluorinating the surfactant. [61]

3.4. Rheology of PLS nanocomposites

Rheology of PLS nanocomposites is important because on the one hand it relates to the microstructure of the nanocomposite and on the other, it provides information about the processibility of the material. Rheology is highly sensitive to the microstructure and can be effectively used as a characterization tool that complements the traditional methods of structure determination like XRD and TEM.

Linear viscoelastic properties: The linear viscoelastic properties of several intercalated and exfoliated nanocomposites such as those made from polystyrene-polyisoprene (PS-PI) block copolymer, [74-76,107-109] PCL, [110-112] polyamide, [113,114] PS, [115-117] PDMS [94] and polypropylene (PP) [62,66,67,118] have been studied.

The characteristic rheological signatures of PLS nanocomposites in the linear region, in the above-mentioned reports can be summarized as:

1. A solid-like response ($G', G'' \rightarrow \omega^0$) at very low frequency above a certain clay loading. [75]

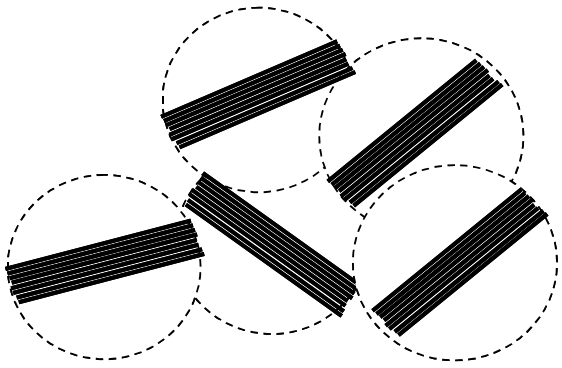

Figure 3.3. Schematic of percolating network formed by clay tactoids

2. Dynamic data ($G', G'' vs\ \omega$) can be shifted by the time-temperature superposition even for the PLS nanocomposites to obtain master curves. The temperature dependence of the frequency shift factors (a_T) is comparable to that of the pristine polymer matrix. The values of frequency shift factors (a_T) are found to be independent of silicate loading. [75] This indicates that the fraction of polymer chains tethered to the clay surfaces are not responsible for solid-like behaviour exhibited by PLS nanocomposites. [75]

Ren et. al. attributed the solid-like behaviour to the existence of a percolating network of the clay tactoids. [75] Such a percolation network is formed even at very low clay concentration, due to the anisotropy of the tactoids. A three dimensional network is formed when the clay tactoids are close enough to interact hydrodynamically with each other, as illustrated in the Figure 3.3. Ren et. al. have related the weight fraction of layered silicates at percolation ($w_{sil,per}$) to the average number of silicate layers per tactoid (n_{per}) as [75]

$$n_{per} \equiv \frac{4}{3\phi_{per}} \left[\frac{w_{sil,per}\rho_{org}}{w_{sil,per}\rho_{org} + (1 - w_{sil,per})\rho_{sil}} \right] \frac{R_h}{h_{sil}} \tag{3.1}$$

where, ρ_{org} and ρ_{sil} are the densities of the organic phase (i.e., polymer matrix) and silicates, respectively. R_h, h_{sil} are the hydrodynamic radius and the thickness of the layered silicate, respectively and ϕ_{per} is the volume fraction at percolation threshold for of spheres in 3-D space reported to be ~ 0.30. [75]

Krishnamoorti et. al. reported the dynamic and steady state flow of PDMS nanocomposites, containing 8 - 15 wt% clay. [94] At low shear rates, they observed viscosity enhancement, which increased monotonically with increasing silicate loading. Furthermore at the lower shear rates, where a Newtonian plateau was observed for the PDMS matrix, the nanocomposite exhibited shear thinning.

Lee et. al. showed that hydrogen bonding between the polymer and silicate can have dramatic effects on the rheology of PLS nanocomposites. [74] Nanocomposite of polystyrene-block-hydroxylated polyisoprene (SIOH diblock) and polystyrene-block-polyisoprene (SI diblock) with clay were prepared. It was observed that PLS

nanocomposites using SIOH diblock showed increase in the G^* and η^* with temperature, while G^* and η^* decreased with increasing temperature for PLS nanocomposites based on SI diblock. FTIR analysis suggested that the Si-OH – nanocomposite had hydrogen bonding even at higher temperature, which might be contributing to the observed increase in the modulus. [74]

Krishnamoorti et. al. have also reported the solid-like behaviour at low oscillatory frequencies for end-tethered polymer chains in polyε-caprolactone nanocomposites. [110] Hoffmann et. al. showed that tethering has an effect on the degree of dispersion and rheology of PLS nanocomposites. [116] Two types of PS based nanoclay composites were prepared. The first containing phenyl ethylamine as a modifier was of intercalated type, while the second, containing amine terminated - PS tethered to the clay surface was of exfoliated nature. The plots of $G^{'}$ vs. shifted frequency (ωa_T) of both PS and intercalated PLS nanocomposites nearly superposed on each other, while the exfoliated nanocomposites showed a significantly higher $G^{'}$ compared to matrix polymer, particularly at the lower frequencies. [116]

Non-linear rheological properties: The strain amplitude sensitivity of PP [62,66,67] and PS - PI copolymer [74-76,107-109] nanoclay composites have been reported. [119] It was observed that G' and $G^{"}$ begins to decrease at strain amplitudes significantly smaller than those for the pristine polymer matrix. Additionally, the strain amplitude defining the onset of softening decreased with increasing silicate loading.

PLS nanocomposites exhibit significant decrease in the viscoelastic moduli under large amplitude oscillatory shear. Kim et. al. reported the ability of large amplitude oscillatory shear to orient short glass fibers in glass reinforced polymer composites. [120] PLS nanocomposites show similar orientation when an external shear field is applied. PLS nanocomposites demonstrate liquid-like behaviour, under the application of large amplitude oscillatory shear, even in the cases where the silicate loading is well above the percolation threshold. [75]

Krishnamoorti et. al. reported the nonlinear dynamic response of end-tethered polyε-caprolactone nanocomposites to large amplitude oscillatory shear. [112] PLS nanocomposites exhibit shear thinning at higher shear rates, however, these materials

exhibited a strain hardening beyond certain critical strain amplitude. This critical strain amplitude was found to be a function of silicate loading. The observed strain hardening was attributed to the stretching of the tethered polymer chains beyond a critical displacement and is considered unique to the high surface grafting density melt - brush systems. [112]

Krishnamoorti et. al. reported that at higher shear rates, the viscosity of the hybrids is comparable to the matrix viscosity, [109] suggesting that the application of shear flow aligns the clay tactoids, which is reminiscent of conventional filled composites [120] and highly filled clay suspensions. [121,122]

The elasticity, as measured by the first normal stress difference, when compared at constant shear stress was found to be independent of silicate loading and was the same as that of the polymer matrix. This unique combination of matrix like viscosity and elasticity for the PLS nanocomposites is ascribed to the alignment of the clay tactoids in the flow direction resulting in a minimal contribution by the clay tactoids to both viscosity and the elasticity of the hybrids. [109]

The empirical Cox-Merz rule (e. q. 2.20), which is obeyed by the polymer matrix, fails for PLS nanocomposites and especially for the case of hybrids with silicate loading greater than percolation threshold, as reported by Krishanmoorti et. al. [109] and Fornes et. al. [49,50] Typically, the complex viscosity (η^*) measured in the linear viscoelastic regime in the case of PLS nanocomposites, exceeds the steady shear viscosity [$\eta(\dot{\gamma})$]. Furthermore, a comparison of the steady shear viscosity $\eta(\dot{\gamma})$ with aligned state viscosity (η^*_{al}) shows that $\eta(\dot{\gamma}) \geq \eta^*_{al}$. These results indicated that even at low shear rates, the application of steady shear results in at least some alignment of the silicate layers.

Failures of the Cox-Merz rule have been observed in other systems like polymer-polymer blends, [123] particle filled polymers, [124] liquid crystalline polymers, [125] and fiber reinforced polymer composites. [120,126] Nakajima et. al. observed for rubber composite filled with particulate carbon black that $\eta(\dot{\gamma})$ obtained by capillary rheometry was significantly lower than the η^* obtained by dynamic measurements. This was ascribed to the strain hardening in dynamic measurements. [124] Bailey et. al. demonstrated that glass reinforced nylon-6 and polypropylene composites do not obey

Cox-Merz rule due to significant fiber orientation in capillary under high shear rates. [126]

Solomon et. al. studied the linear and non-linear rheological properties of PP nanocomposites by using flow reversal experiments. [62,118] The transient flow reversal stress response exhibited a stress overshoot, the magnitude of which was found to increase with the quiescent annealing time between the flow reversals. The stress overshoot varied linearly with the concentration of clay and scaled with the strain. These results indicate that microstructure of PLS nanocomposite evolved with annealing time and that the rheological measurements were sensitive to these changes.

3.5. Yield behaviour of filled systems

The existence of structured fluid was intensely debated a decade ago, mainly due to the confusion over the precise definition of yield stress. [127-134] It was originally accepted that the yield stress of a solid is a stress from which if the applied stress were increased, the deforming solid would exhibit liquid-like behaviour i.e., continual deformation. Similarly in the context of structured fluids and liquids, it was understood that as the stress is decreased below the yield stress a solid-like behaviour is observed i.e., no continual deformation. [127]

However, with the increase in sophistication of experimental capabilities, it became clear firstly for solids and then for structured fluids that, although there is a small range of applied stress over which the viscosities change dramatically, which is usually referred to as the *apparent yield stress,* these materials show slow but continual steady deformation when stressed for a very long time even below yield stress level. [131-134] Thus yield behaviour of materials was understood to be a time dependent phenomenon.

The shear thinning, shear thickening, and apparent yield behaviour for filled suspensions and conventional polymer composites has been very well reported. [128-131] Krishnamoorti et. al. indicated the presence of an apparent yield stress for the PLS - nanocomposites. [109] They studied the shear rate dependence of steady shear viscosity for PS-PI nanocomposites, as a function of clay loading. The viscosity of PLS nanocomposites showed divergence with increasing silicate loading. The divergence was

significant above the percolation threshold and was considered as being indicative of the existence of a finite yield stress for these materials.

3.6. Flow orientation of PLS nanocomposites

The silicate layers can be oriented in response to an externally applied force field. [109, 110, 135] Zhang et. al. investigated the shear-induced morphological changes for PP nanocomposites by TEM and XRD analysis. [136] The intercalated structure changed to exfoliated under shear, due to the orientation of silicate clay platelets. The silicate layers were found to be oriented under shear while the polymer chains remained unoriented. This ability to orient the clay appears to control the viscoelastic properties of such materials. [109,110] Recent studies have demonstrated that along with the exfoliation, orientation of the clay platelets plays a crucial role in determining the property enhancement in PLS nanocomposites. [98,99,137-146] The three dimensional (3-D) orientation of clay platelets and unit cells in polymers in PLS nanocomposite have also been studied. [138-142] The orientation of silicate layers in PLS nanocomposites has been studied using various techniques like XRD, TEM, SAXS and SANS. [137-146]

Kojima et. al. have characterized the orientation of silicate layers in nylon-6 nanocomposites using XRD and TEM. [137] In an injection-molded bar they found three different regions of orientations as a function of depth. At the center of the sample, where the shear forces are minimal, the silicate layers and polymer crystallites were found to be randomly oriented with the chain axes of the polymer crystallites always perpendicular to the silicate layers. Near the surface, where the shear stress would be very high the silicate layers and chain axes of the polymer crystallites were parallel to the bar surface. In the intermediate shear region, the clay layers, may due to their asymmetric nature, still orient parallel to the bar surface, but the chain axes of the polymer crystallites were perpendicular to the silicate layers. [137] Varlot et. al. also demonstrated that the polymer lamellae grow on the silicate sheet with chain axes parallel to the silicate layer. [138]

Rheological characterization coupled with other structural characterization offers a useful tool to directly investigate the rheology-microstructure linkages in the materials. Ex-situ analysis of clay orientation in PP-nanocomposites under biaxial and uniaxial

extensional flow has been reported recently. [140,141] Okamoto et. al. observed strain induced hardening in an elongational flow for PP nanocomposite foam. [141] The strain hardening and time dependent shear thickening was attributed to the perpendicular alignment of the silicate layers in the stretching direction. [140] The TEM analysis showed that, the biaxial flow-induced alignment of clay particles along the cell boundaries, enhances the modulus of the foam. [141]

Several in-situ techniques like Rheo-SAXS, [142] Rheo-SANS, [143-148] Rheo-NMR, [149,150] Rheo-optics [151,152] and Rheo-WAXD [153] and have been used to investigate the flow-induced micro structural evolution in other structured fluids.

The effect of high strain on the crystallization of end-tethered nylon-6 nanocomposite was studied by Medalling-Rodriguez et. al. using rheo-SAXS analysis. They found that the silicate layers and the polymer chains are oriented in the flow direction even at relatively low shear and at temperatures just above the melting point. [142] The shear-induced orientation was found to increase with time. The clay platelets were found to be oriented even after cessation of shear, and this orientation remains stable for relatively longer times in the molten state. Typical time resolved SAXS study shows that for the end tethered nylon nanocomposites the relaxation period is around 12 min (at T = 240^{o}C, $\dot{\gamma}$ = 60 s^{-1}). The slow relaxation of clay is ascribed to the tethered polymer chains, which are expected to have extended relaxation time. [142] Schmidt et. al. studied shear orientation in aqueous solutions of PEO nanocomposites using flow birefringence and SANS. [143-148] It was found that the clay platelets were oriented in the flow direction with their surface normal perpendicular to the flow direction. They also reported that the randomization of the oriented silicate layers upon cessation of flow was much faster than that described by Brownian motion.

Recently Somwangthanaroj et. al. studied early stage quiescent and flow-induced crystallization kinetics of intercalated polypropylene nanocomposites by in situ rheo-optics. [152] They observed that crystallization kinetics of intercalated polypropylene nanocomposites, prepared with PP-g-MA as a compatibilizer, differs significantly from that of pure polypropylene. The use of PP-g-MA as a compatibilizer contributed to the retardation of the quiescent isothermal crystallization kinetics of the intercalated nanocomposites compared to the pristine polypropylene. However, the application of

shear-flow accelerated the crystallization kinetics of the intercalated PLS nanocomposites under conditions at which the polypropylene showed no flow-induced effects.

Several references on the rheology and flow-induced orientation of PLS nanocomposites cited in this chapter are contemporary to the work reported in this thesis in chapter 7-9 and will be discussed in that context in more detail later in the thesis.

Reference List:

1. Blumstein, A. *J.Polym.Sci.A* **1965,** *3,* 2653-2664.
2. Friendlander, H. Z.; Frick, C. R. *J. Polym. Sci .B* **1964,** *2,* 475-479.
3. Solomon, D. H. *J. Appl. Polym. Sci.* **1968,** *12,* 1253-1262.
4. Usuki, A.; Kojima, Y.; Kawasumi, M.; Okada, A.; Fukushima, Y.; Kurauchi, T.; Kamigaito, O. *J. Mater .Res.* **1993,** *8*(5), 1179-1184.
5. Messersmith, P. B.; Giannelis, E. P. *Chem. Mater.* **1993,** *5*(8), 1064-1066.
6. Huang, X.; Lewis, S.; Brittain, W. J.; Vaia, R. A. *Macromolecules* **2000,** *33*(6), 2000-2004.
7. Huang, X.; Lewis, S.; Brittain, W. J.; Vaia, R. A. *Polym. Prepr.* **2000,** *41*(1), 589-590.
8. Lan, T.; Pinnavaia, T. J. *Chem. Mater.* **1994,** *6*(12), 2216-2219.
9. Ryu, J. G.; Park, G. R.; Lyu, S. G.; Rhew, J. H.; Sur, G. S. *Polymer (Korea)* **1998,** *22* (2), 328-334.
10. Lan, T.; Kaviratna, P. D.; Pinnavaia, T. J. *Polym. Mater. Sci. Eng.* **1994,** *71*, 527-528.
11. Lan, T.; Wang, Z.; Shi, H.; Pinnavaia, T. J. *Polym. Mater. Sci. Eng.* **1995,** *73,* 296-297.
12. Heinemann, J.; Reichert, P.; Thomann, R.; Mulhaupt, R. *Macromol. Rapid Commun.* **1999,** *20*(8), 423-430.
13. Tudor, J.; Willington, L.; O'Hare, D.; Royan, B. *Chem. Commun.* **1996,** 17, 2031-2032.
14. Rong, J.; Li, H.; Jing, Z.; Hong, X.; Sheng, M. *J. Appl .Polym. Sci.* **2001,** *82*(8), 1829-1837.

15. Weiss, K.; Wirth-Pfeifer, C.; Hofmann, M.; Botzenhardt, S.; Lang, H.; Bruning, K.; Meichel, E. *J. Mol. Cata. A: Chemical* **2002,** *182-183,* 143-149.
16. Ma, J.; Qi, Z.; Hu, Y. *J. Appl. Polym. Sci.* **2001,** *82*(14), 3611-3617.
17. Ke, Y.; Long, C.; Qi, Z. *J. Appl. Polym. Sci.* **1999,** *71*(7), 1139-1146.
18. Burnside, S. D.; Giannelis, E. P. *Chem. Mater.* **1995,** *7*(9), 1597-1600.
19. Yang, F.; Ou, Y.; Yu, Z. *J. Appl. Polym. Sci.* **1998,** *69*(2), 355-361.
20. Kojima, Y.; Usuki, A.; Kawasumi, M.; Okada, A.; Kurauchi, T.; Kamigaito, O. *J. Polym. Sci. Part A: Polym. Chem.,* **1993,***31*(7), 1755-1758.
21. Kojima, Y.; Usuki, A.; Kawasumi, M.; Okada, A.; Kurauchi, T.; Kamigaito, O. *J. Polym. Sci. Part A: Polym. Chem.,* **1993,** *31*(4), 983-986.
22. Usuki, A.; Kawasumi, M.; Kojima, Y.; Okada, A.; Kurauchi, T.; Kamigaito, O. *J. Mater. Res.* **1993,** *8*(5), 1174-1178.
23. Yano, K.; Usuki, A.; Okada, A.; Kurauchi, T.; Kamigaito, O. *J. Polym. Sci. Part A: Polym. Chem.* **1993,** *31*(10), 2493-2498.
24. Liu, C.; Tang, T.; Zhao, Z.; Huang, B. *J. Polym. Sci. Part A: Polym. Chem.* **2002,** *40* (5), 1892-1898.
25. Weimer, M. W.; Chen, H.; Giannelis, E. P.; Sogah, D. Y. *J. Am. Chem. Soc.* **1999,** *121*(7), 1615-1616.
26. Jin, Y. H.; Park, H. J.; Im, S. S.; Kwak, S. Y.; Kwak, S. *Macromol. Rapid Commun.* **2002,** *23*(2), 135-140.
27. Rong, J.; Jing, Z.; Li, H.; Sheng, M. *Macromol. Rapid Commun.* **2001,** *22*(5), 329-334.
28. Bergman, J. S.; Chen, H.; Giannelis, E. P.; Thomas, M. G.; Coates, G. W. *Chem. Commun.* **1999,** *21,* 2179-2180.
29. Lemmon, J. P.; Wu, J.; Lerner, M. M. in Hybrid Organic-Inorganic Composites. ACS Symp. Series, 585 Mark, J. E.; Lee, C. Y. C.; Bianconi, P. A.; Eds. *ACS: Washington* D.C. **1995**.
30. Seckin, T. *J. Mater. Chem* **1997,** *7*(2), 265-269.
31. Ellsworth, M. W.; Novak, B. M. *J. Am. Chem. Soc.* **1991,** *113*(7), 2756-2758.
32. Huang, Z. H.; Qiu, K. Y. *Polymer* **1997,** *38*(3*)*, 521-526; Huang, X. Y. *Macromolecules* **2001,** *34*(10), 3255-3260.

33. Jimenez, G.; Ogata, N.; Kawai, H.; Ogihara, T. *J. Appl. Polym. Sci.* **1997,** *64*(11), 2211-2220.
34. Ogata, N.; Kawakage, S.; Ogihara, T. *Polymer* **1997,** *38*(20), 5115-5118.
35. Ogata, N.; Jimenez, G.; Kawai, H.; Ogihara, T. *J. Polym. Sci. Part B: Polym. Phys.* **1997,** *35*(2), 389-396.
36. Tseng, C. R.; Wu, J. Y.; Lee, H. Y.; Chang, F. C. *Polymer* **2001,** *42*(25), 10063-10070.
37. Tabtiang, A. *Polym.-Plast. Technol. Eng* **2000,** *39,* 293-303.
38. Jeon, H. G.; Jung, H. T.; Lee, S. W.; Hudson, S. D. *Polym. Bull. (Berlin)* **1998,** *41*(1), 107-113.
39. Wu, J.; Lerner, M. M. *Chem. Mater.* **1993,** *5*(6), 835-838.
40. Noh, M. W.; Lee, D. C. *Polym. Bull. (Berlin)* **1999,** *42*(5), 619-626.
41. Huang, X.; Brittain, W. J. *Polym. Prepr.* **2000,** *41*(1), 521-522.
42. Choi, Y. S. *Macromolecules* **2001,** *34*(26), 8978-8985.
43. Huang, X. Y. *Macromolecules* **2001,** *34*(10), 3255-3260.
44. Giannelis, E. P. *Adv. Mater.* **1996,** *8*(1), 29-35.
45. Vaia, R. A.; Jandt, K. D.; Kramer, E. J.; Giannelis, E. P. *Chem. Mater.* **1996,** *8*(11), 2628-2635.
46. Vaia, R. A.; Jandt, K. D.; Kramer, E. J.; Giannelis, E. P. *Macromolecules* **1995,** *28*(24), 8080-8085.
47. Vaia, R. A.; Vasudevan, S.; Krawiec, W.; Scanlon, L. G.; Giannelis, E. P. *Adv. Mater.* **1995,** *7*(2), 154-156.
48. Cho, J. W.; Paul, D. R. *Polymer* **2000,** *42*(3), 1083-1094.
49. Fornes, T. D.; Yoon, P. J.; Keskkula, H.; Paul, D. R. *Polymer* **2001,** *42*(25), 9929-9940.
50. Fornes, T. D.; Yoon, P. J.; Paul, D. R. *Poly. Mater. Sci. Eng.* **2002,** *87,* 104-105.
51. Dennis, H. R.; Hunter, D. L.; Chang, D.; Kim, S.; White, J. L.; Cho, J. W.; Paul, D. R. *Polymer* **2001,** *42*(23), 9513-9522.
52. Koo, C. M.; Ham, H. T.; Kim, S. O.; Wang, K. H.; Chung, I. J.; Kim, D. C.; Zin, W. C. *Macromolecules* **2002,** *35*(13), 5116-5122.

53. Kawasumi, M.; Hasegawa, N.; Kato, M.; Usuki, A.; Okada, A. *Macromolecules* **1997,** *30*(20), 6333-6338.
54. Kurokawa, Y.; Yasuda, H.; Oya, A. *J. Mater. Sci. Lett.* **1996,** *15*(17), 1481-1483.
55. Di.Y.; Iannace, S.; Dimaio, E.; Nicolais, L. *J. Polym. Sci. Part .B: Polym. Phy.* **2003,** *41*(7), 670-678.
56. Lepoittevin, B.; Devalckenaere, M.; Pantoustier, N.; Alexandre, M.; Kubies, D.; Calberg, C.; Jerome, R.; Dubois, P. *Polymer* **2002,** *43*(14), 4017-4023.
57. Chisholm, B. J.; Moore, R. B.; Barber, G.; Khouri, F.; Hempstead, A.; Larsen, M.; Olson, E.; Kelley, J.; Balch, G.; Caraher, J. *Macromolecules* **2002,** *35*(14), 5508-5516.
58. Artzi, N. *Polym. Comp.* **2001,** *22,* 710-720.
59. Zeng, C. C. *Macromolecules* **2001,** *34*(12), 4098-4103.
60. Wang, D. Y. *Chem. Mat.* **2002,** *14*(9), 3837-3843.
61. Manias, E.; Touny, A.; Wu, L.; Strawhecker, K.; Lu, B.; Chung, T. C. *Chem. Mater.* **2001,** *13*(10), 3516-3523.
62. Solomon, M. J.; Almusallam, A. S.; Seefeldt, K. F.; Somwangthanaroj, A.; Varadan, P. *Macromolecules* **2001,** *34*(6), 1864-1872.
63. Kato, M.; Usuki, A.; Okada, A. *J. Appl. Polym. Sci.* **1997,** *66*(9), 1781-1785.
64. Kodgire, P.; Kalgaonkar, R.; Hambir, S.; Bulakh, N.; Jog, J. P. *J. Appl. Polym. Sci.* **2001,** *81*(7), 1786-1792.
65. Hambir, S.; Bulakh, N.; Kodgire, P.; Kalgaonkar, R.; Jog, J. P. *J. Polym. Sci. Part B: Polym. Phy.* **2001,** *39*(4), 446-450.
66. Reichert, P.; Hoffmann, B.; Bock, T.; Thomann, R.; Mulhaupt, R.; Friedrich, C. *Macromol. Rapid Commun.* **2001,** *22*(7), 519-523.
67. Reichert, P.; Nitz, H.; Klinke, S.; Brandsch, R.; Thomann, R.; Mulhaupt, R. *Macromol. Mater. Eng.* **2000,** *275*, 8-17.
68. Kurokawa, Y.; Yasuda, H.; Kashiwagi, M.; Oyo, A. *J. Mater. Sci. Lett.* **1997,** *16*(20), 1670-1672.
69. Liu, X.; Wu, Q.; Berglund, L. A.; Fan, J.; Qi, Z. *Polymer* **2001,** *42*(19), 8235-8239.
70. Ma, J.; Shimin, Z.; zongneng, Q.; Ge, L.; Youliang, H. *J. Appl. Polym. Sci.* **2002,** *83*(9), 1978-1985.

71. Maiti, P.; Nam, P. H.; Okamoto, M.; Hasegawa, N.; Usuki, A. *Macromolecules* **2002,** *35*(6), 2042-2049.
72. Noh, M. H.; Jang, L. W.; Lee, D. C. *J. Appl. Polym. Sci.* **1999,** *74*(1), 179-188.
73. Jang, L. W.; Kang,C. M.; Lee, D. C. *J. Polym. Sci., Part B: Polym. Phy.* **2001**, *39*(6), 719-727.
74. Lee, K. M.; Han, C. D. *Macromolecules* **2003,** *36*(3), 804-815
75. Ren, J.; Silva, A. S.; Krishnamoorti, R. *Macromolecules* **2000,** *33*(10), 3739-3746.
76. Ren, J.; Krishnamoorti, R. *Polym. Mater. Sci. Eng.* **2000,** *82,* 264-265.
77. Ryu, J. G. *Macromol. Res.* **2002,** *10,* 187-193.
78. Wang, H. M. *Polym. Int.* **2002,** *51,* 7-11.
79. Decker, C. *J. Mater. Sci.* **2002,** *37,*4821-4828.
80. Lan, T.; Kaviratna, P. D.; Pinnavaia, T. J. *Chem. Mater.* **1995,** *7*(11), 2144-2150.
81. Krishanmoorti, R.; Silva, A. S. *Polymer-Clay Nanocomposites;* Pinnavaia, T. J. Beall, G. W. Eds. John Wiley and Sons. N.Y. **2000**.
82. Garces, J. M.; Moll, D. J.; Bicerano, J.; Fibiger, R.; McLeod, D. G. *Adv. Mater.* **2000,** *12*(23), 1835-1839.
83. Lincoln, D. M.; Vaia, R. A.; Wang, Z. G.; Hsiao, B. S.; Krishnamoorti, R. *Polymer* **2001,** *42*(25), 9975-9985.
84. Lincoln, D. M.; Vaia, R. A.; Wang, Z. G.; Hsiao, B. S. *Polymer* **2000,** *42*(4), 1621-1631.
85. Vaia,R. A.; Lincoln, D.; Wang, Z. G.; Hsiao, B. S. *Polym. Mater. Sci. Eng.* **2000**, *82*, 257-258.
86. Giannelis, E. P.; Krishnamoorti, R.; Manias, E. *Adv. Polym. Sci*. **1999**, *138*, 107-147.
87. Liu, X.; Wu, Q.; Berglund, L. A. *Polymer* **2002,** *43*(18), 4967-4972.
88. Liu, X.; Wu, Q. *Macromol. Mater. and Eng.* **2002,** *287*(3), 180-186.
89. Liu, X.; Wu, Q. *European Polymer Journal* **2002,** *38*(7), 1383-1389.
90. Kojima, Y.; Matsuoka, T.; Takahashi, H.; Kurauchi, T. *J. Mater. Sci. Lett.* **1993,** *12*(21), 1714-1715.
91. Tseng, C. R.; Lee, H. Y.; Chang, F. C. *J. Polym. Sci. Part B: Polym. Phy.* **2001,** *39*(17), 2097-2107.
92. Vaia, R. A.; Teukolsky, R. K.; Giannelis, E. P. *Chem. Mater.* **1994,** *6*(7), 1017-1022.

93. Usuki, A.; Kojima, Y.; Kawasumi, M.; Okada, A.; Kurauchi, T.; Kamigaito, O. *Polym. Prepr.* **1990,** *31*(2), 651-652.
94. Krishnamoorti, R.; Vaia, R. A.; Giannelis, E. P. *Chem. Mater.* **1996,** *8*(8), 1728-1734.
95. VanderHart, D. L.; Asano, A.; Gilman, J. W. *Chem. Mater.* **2001,** *13*(10), 3796-3809.
96. Akkapeddi, M. K. *SPE ANTECH.1999 proceedings* **1999,** *21*(4), 1619-1622.
97. Worley, D. C.; Akkapeddi, M. K.; Socci, E. P. "Deformation an orientation of polyamide 6 nanocomposite"; Honeywell Engineering Applications and Solutions, New technologies group: **2000**.
98. Kojima, Y.; Usuki, A.; Kawasumi, M.; Okada, A.; Kurauchi, T.; Kamigaito, O.; Kaji, K. *J. Polym. Sci***,** *Part B: Polym. Phys.* **1994,** *32*(4), 625-630.
99. Varlot, K.; Reynaud, E.; Kloppfer, M. H.; Vigier, G.; Varlet, J. *J. Polym. Sci. Part B: Polym. Phy.* **2001,** *39*(12), 1360-1370.
100. Yano, K.; Usuki, A.; Okada, A. *J. Polym. Sci.***,** *Part A: Polym. Chem.* **1997,** *35*(11), 2289-2294.
101. Merkel, T. C.; Freeman, B. D.; Spontak, R. J.; He. Z.; Pinned, I.; Me akin, P.; Hill, A. J. *Science* **2002,** *296*(5567), 519-522.
102. Vaia, R. A.; Giannelis, E. P. *Macromolecules* **1997,** *30*(25), 7990-7999.
103. Vaia, R. A.; Giannelis, E. P. *Macromolecules* **1997,** *30*(25), 8000-8009.
104. Ginzburg, V. V.; Balazs, A. C. *Macromolecules* **1999,** *32*(17), 5681-5688.
105. Balazs, A. C.; Singh, C.; Zhulina, E.; Lyatskaya, Y. *Acc. Chem. Res.* **1999,** *32*(8), 651-657.
106. Lyatskaya, Y.; Balazs, A. C. *Macromolecules* **1998,** *31*(19), 6676-6680.
107. Mitchell, C. A.; Krishnamoorti, R. *ACS Symposium Series* **2002,** *804*, 159-175.
108. Mitchell, C. A.; Krishnamoorti, R. *J. Polym. Sci. Part B: Polym. Phy.* **2002,** *40*(14), 1434-1443.
109. Krishnamoorti, R.; Ren, J.; Silva, A. S. *J. Chem. Phy.* **2001,** *114*(11), 4968-4973.
110. Krishnamoorti, R.; Giannelis, E. P. *Macromolecules* **1997,** *30*(14), 4097-4102.
111. Krishanmoorti, R.; Giannelis, E. P. *Polym. Mater. Sci. Eng.* **1996,** *75, 46-47.*
112. Krishnamoorti, R.; Giannelis, E. P. *Langmuir* **2001,** *17*(5), 1448-1452.
113. Utracki, L. A.; Lyngaae-Jorgensen, J. *Rheologica Acta* **2002,** *41,* 394-407.

114. Hoffmann, B.; Kressler, J.; Stoppelmann, G.; Friedrich, C.; Kim, G. M. *Colloid Polym. Sci.* **2000,** *278*(7), 629-636.

115. Hoffmann, B.; Dietrich, C.; Friedrich, C. *Polym. Mater. Sci. Eng.* **2000,** *82,* 243-244.

116. Hoffmann, B.; Dietrich, C.; Thomann, R.; Friedrich, C.; Mullhaupt, R. *Macromol. Rapid Commun.* **2000,** *21*(1), 57-61.

117. Lim, Y. T.; Park, O. O. *Rheologica Acta* **2001,** *40*(3), 220-229.

118. Solomon, M. J.; Lu, Q. *Current Opinion in Colloid & Interface Science* **2001,** *6*(5,6), 430-437.

119. Krishnamoorti, R.; Yurekli, K. *Current Opinion in Colloid & Interface Science* **2001,** *6*(5,6), 464-470.

120. Kim, J. K.; Song, J. H. *J. Rheol.* **1997,** *41*(5), 1061-1085.

121. Zhong, Y.; Wang, S. Q. *J. Rheol.* **2003,** *47*(2), 483-495.

122. Dzuy, N. Q.; Boger, D. V. *J. Rheol.* **1983,** *27*(4), 321-349

123. Han, J. H.; Feng, C. C.; Li, D. J.; Han, C. D. *Polymer* **1995,** *36,* 2451-2462.

124. Nakajima, N.; Bowermann, H. H.; Collins, W. A. *J. Appl. Polym. Sci.* **1977,** *21,* 3063-3075.

125. Kim, S. S.; Han, C. D. *Polymer* **1994**, *35*(1), 95-103.

126. Bailey, R. S.; Bellamy, A. M.; Groves, D. J.; Stocks, D. M.; Young, R. C. *Theor. Appl. Rheol.* **1992,** *2,* 838-840.

127. Macosko, C. W. *Rheology principles, Measurements, and Applications*; Wiley-VCH Inc., N.Y., **1994**.

128. Jeffrey, D. J.; Acrivos, A. *AIchE J.* **1976,** *22,* 417-432.

129. Astarita, G. *J. Rheol.* **1990,** *34*(3)*,* 275-277.

130. Hartnett, J. P.; Hu, R. Y. Z. *J. Rheol.* **1989,** *33*(4), 671-679.

131. Barnes, H. A. *The myth of yield stress fluids*; Emri, I. S. D.; Eds; Darmstadt, Germany, **1998**.

132. Roberts, G. P.; Barnes, H. A.; Carew, P. *CES* **2001,** *56,* 5617-5623.

133. Barnes, H. A. *J. Non Newtonian Fluid Mech.* **1999,** *81,* 133-178.

134. Barnes, H. A. *Appl. Rheol.* **1999,** *9*(6), 262-266.

135. Hornsby, P. R. *Adv. Poly. Sci* **1999,** *139,* 155-217.

136. Zhang, Q.; Wang, Y.; Fu Q. *J Polym. Sci. Part. B: Polym .Phy.* **2003,** *41,* 1-10.

137. Kojima, Y.; Usuki, A.; Kawasumi, M.; Okada, A.; Kurauchi, T.; Kamigaito, O.; Kaji, K. *J. Polym. Sci. Part B: Polym. Phys.* **1995,** *33*(7), 1039-1045.

138. Varlot, K.; Reynaud, E.; Vigier, G.; Varlet, J. *J. Polym. Sci. Part. B: Polym .Phy.* **2002,** *40*(3), 272-283.

139. Bafna, A.; Beaucage, G.; Mirabella, F.; Mehta, S. *Polymer* **2003,** *44*(4), 1103-1115.

140. Okamoto, M.; Nam, P. H.; Maiti, P.; Kotaka, T.; Hasegawa, N.; Usuki, A. *Nano Letters* **2001,** *1*(6), 295-298.

141. Okamoto, M.; Nam, P. H.; Maiti, P.; Kotaka, T.; Nakayama, T.; Takada, M.; Ohshima, M.; Usuki, A.; Hasegawa, N.; Okamoto, H. *Nano Letters* **2001,** *1*(9), 503-505.

142. Medellin-Rodriguez, F. J.; Burger, C.; Hsiao, B. S.; Chu, B.; Vaia, R.; Phillips, S. *Polymer* **2001,** *42*(21), 9015-9023.

143. Schmidt, G.; Nakatani, A. I.; Butler, P. D.; Karim, A.; Han, C. C. *Macromolecules* **2000,** *33*(20), 7219-7222.

144. Schmidt, G.; Nakatani, A. I.; Butler, P. D.; Ferreiro, V.; Karim, A.; Han, C. C. *Materials Research Society Symposium Proceedings* **2001,** *661-665.*

145. Schmidt, G.; Nakatani, A. I.; Han, C. C. *Rheologica Acta* **2002,** *41*(1-2), 45-54.

146. Schmidt, G.; Nakatani, A. I.; Butler, P. D.; Han, C. C. *Macromolecules* **2002,** *35*(12), 4725-4732.

147. Han, C.; Schmidt, G.; Nakatani, A. I.; Karim, A. *Polym. Prepr.* **2001,** *42*(1), 269-270.

148. Han, C. C.; Schmidt, G.; Nakatani, A. I.; Butler, P. D. *Polym. Mater. Sci. Eng.* **2001,** *85,* 219-220.

149. Arola, D. F.; Powell, R. L.; Barrall, G. A.; McCarthy, M. J. *J. Rheol.* **1999,** *43*(1)*,* 9-30.

150. Thiele, T. J.; Berrett, J. F.; Muller, S.; Schmidt, C. *J. Rheol.* **2001,** *45*(1)*,* 29-48.

151. Janeschitz-kreig, H. *Polymer Melt Rheology and Flow Birefringence;* Springer: Berlin, **1983**.

152. Somwangthanaroj, A.; Lee, C. E.; Solomon, M. J. *Macromolecules* **2003,** *36*(7), 2333-2342.

153. Sondergaard, K.; Lyngaae-Jorgensen, J. *Rheo-Physics of Multiphase Polymer Systems;* Technomic, Basel, **1995**.

Chapter 4 Objectives

As described in the earlier chapters, polymer nanoclay composites exhibit significant enhancement in thermomechanical properties. These property enhancements are attributed to the nanoscale dispersion of the clay in the polymer matrix. The maximum property enhancements are achieved for exfoliated nanocomposites, which are typically synthesized by in-situ polymerization of the monomer in the interlayer galleries. However, synthesis by melt mixing of polymer with clay is commercially a more viable alternative, as this method is compatible with the existing processing equipment. Under optimum processing conditions, melt intercalated polymer nanocomposites also exhibit properties comparable to those synthesized by in-situ polymerization route.

Ultimately polymer nanocomposites have to be melt processed, irrespective of the method of synthesis, to manufacture the final products. During melt processing the materials have to undergo several operations like extrusion, injection molding, etc. Here, the melt is made to flow through complex geometries, where it experiences shear and elongational stresses. The stress fields affect the microstructure of the composites, which in turn influences the flow behaviour of these materials. Thus, the interlinkages between flow behaviour and microstructure is critical to the understanding of processibility of PLS nanocomposites.

The microstructure so developed during melt processing would determine the solid-state properties of the final product. For instance, the highly asymmetric clay platelets can be easily oriented by flow during processing. Such orientation of the clay tactoids may affect the final solid-state properties. The performance of the product, as gauged by the end user is ultimately determined by the solid-state properties.

Thus, understanding the links between the microstructure, flow properties of the melt and solid-state properties is critical to the successful development of polymer nanoclay composite products, as shown schematically in Figure 4.1. The overall objective of the work reported in this thesis is to understand and quantify the structure-processing-property linkages in nanoclay composites.

The linkages between microstructure and flow were studied by performing several rheological measurements. In particular, the rheology at very low stresses was studied by performing creep measurements, while the evolution of microstructure at high stresses was studied by in-situ rheo-XRD measurements. The effect of structural evolution during flow on the solid-state properties was studied by producing solid tape samples under controlled processing history. Studies on the solid-state properties were restricted to tensile properties. In the entire work reported in this thesis the focus has been on the quantification of structure-processing-property links in PLS nanocomposites.

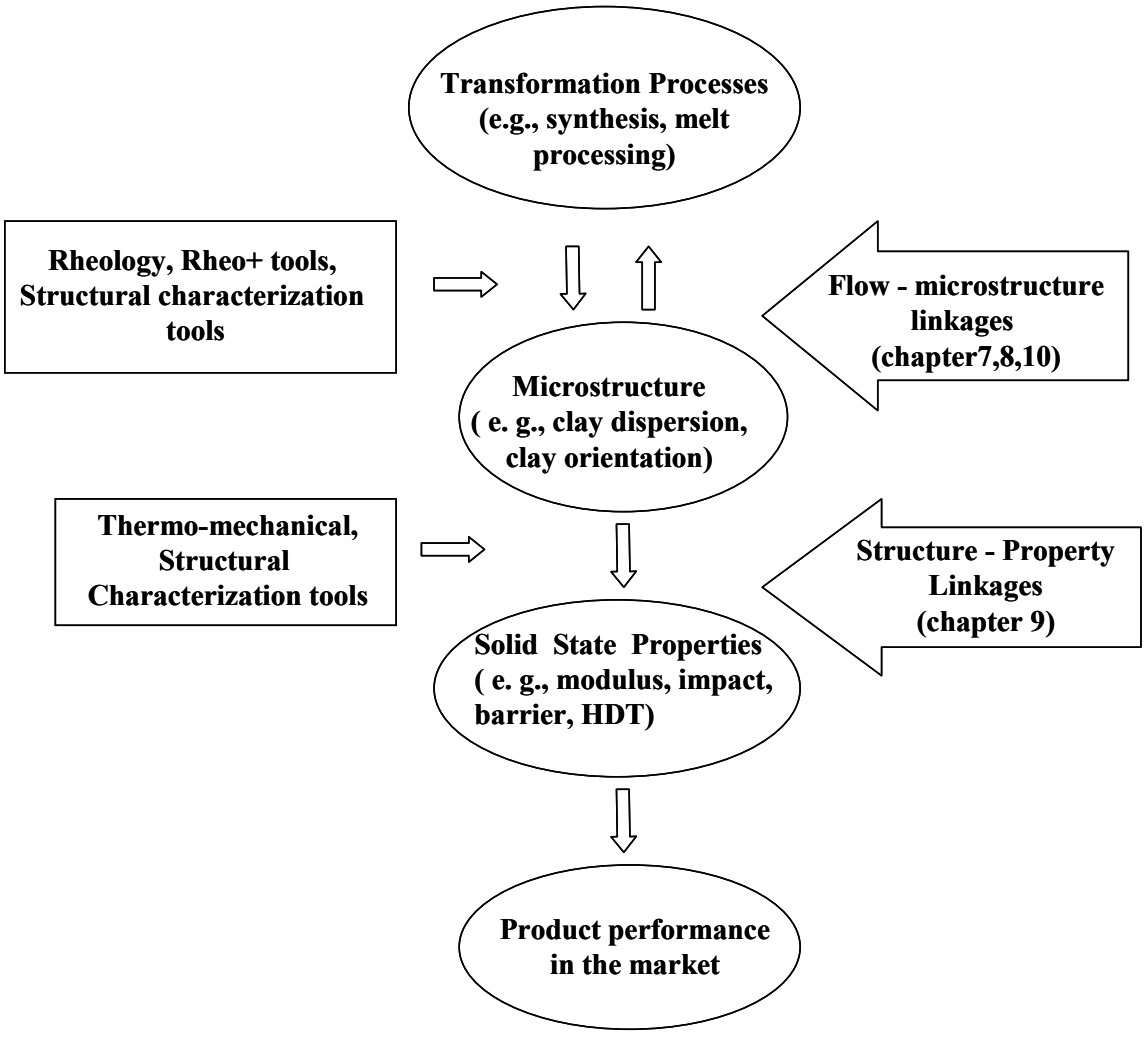

Figure 4.1. Schematic flow chart of microstructure-property-processing linkages

This chapter describes the experimental methods and materials used in this study. Specifically, the materials studied were intercalated polypropylene (PP) nanocomposites and intercalated and exfoliated polyethylene (PE) nanocomposites, which were synthesized both by melt intercalation and in-situ polymerization procedures.

5.1. Isotactic polypropylene nanoclay composites

5.1.1. Materials

Polypropylene (PP, grade-Montell KF6100) of MFI = 3 and M_w of approximately 300,000 was used as the matrix phase. Maleic anhydride grafted polypropylene (PP-MA, grade-Polybond 3200) of MFI = 140 was used as the compatibilizer in some cases. Accordingly, two types of nanoclay composites were prepared, viz., compatibilized (i.e., those containing the compatibilizer) and uncompatibilized (i.e., those without the compatibilizer)

The clays used were organically modified montmorillonite, (Closite 6A and Closite 20A) supplied by Southern Clay Products, Texas, U. S. A. Dimethyl dihydrogenatedtallow quaternary ammonium chloride (DMDHTMC) was exchanged with montmorillonite clay, to render the surface hydrophobic. The structure of DMDHTMC is shown in Figure 5.1.

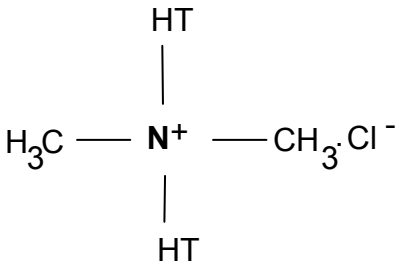

where, HT = hydrogenated tallow (~65% C18, ~30%C16, ~5%C14)

Figure 5.1. Structure of tallow based organic modifier

Closite 6A is more hydrophobic than Closite 20A. The modifier concentration and CEC of the clays are listed in the Table 5.1. All materials were dried at 80^{o}C before use.

Table 5.1. Typical physical properties of Closite clays [#]

	Modifier concentration (meq/100g)	% Wt. loss on ignition
Closite 6A	140	47
Closite 20A	95	38

Values supplied by Southern Clay Products, U.S.A

5.1.2. Method of preparation of iPP nanoclay composites

iPP and PP-MA were melt blended with DMDHTMC at 175-200^{o}C in a Bertsoff ZE-25 twin screw extruder having co-rotating and intermeshing 25 mm screws (L/D = 41) at 100 rpm. The residence time inside the extruder was approximately 2 minutes under the processing conditions used in this work. The compositions of the hybrids are shown in Table 5.2. The extruded strands were pelletized and dried under vacuum at 80^{o}C for 12 hrs.

5.1.3. Methods of characterization

Rheological characterization: Rheological measurements were performed on as-extruded and annealed samples using a Bohlin CVO-50 controlled stress rheometer and Rheometric scientific ARES strain controlled rheometer, fitted with 25 mm diameter parallel plates. All experiments were performed under a nitrogen blanket to minimize oxidative degradation of polypropylene. Sample discs (1 mm thick and 25 mm diameter) were prepared by compression molding of the extruded pellets at 200^{o}C followed by slow cooling for about 3 min.

Table 5.2. Compositions of iPP nanocomposites

Sample code	PP (wt%)	Clay (wt%)	PP-MA (wt%)
iPP3/3/0	97	3	0
iPP3/3/3	94	3	3
iPP3/0/3	97	0	3
iPP3/6/0	94	6	0
iPP3/6/6	88	6	6
iPP3/0/6	94	0	6
iPP3/9/0	91	9	0
iPP3/9/9	82	9	9
iPP3/0/9	91	0	9
iPP3/25/10	65	25	10
iPP3/25/0	75	25	0

Creep experiments in shear mode were performed at a small constant shear stress of 10 Pa (for 3% and 6% clay) and 50 Pa (for 9% clay) for a creep time of 180 s at 200^{o}C. In case of annealing studies, creep data was collected every 15 min. for a period of 3 hrs at 200^{o}C. In a few creep experiments the stress was gradually increased in a step-wise manner, while in some other experiments creep measurements were done after an initial pre-shearing of the samples. Dynamic strain sweep experiments were performed on ARES rate controlled rheometer at 200^{o}C, in the range of 0.01-100 % strains at a constant frequency of 10 rad/s to delineate the linear and non-linear regimes in the iPP nanocomposites. Further low amplitude oscillatory shear experiments were performed in the linear region of deformation on the Bohlin stress controlled rheometer over a frequency range of 0.01-75 Hz on as-extruded samples as well as on samples annealed at 200^{o}C.

WAXD: The x-ray diffraction experiments were performed using Rigaku Dmax 2500 diffractometer with Cu target. The system consisted of a rotating anode generator and wide angle powder goniometer fitted with a high temperature attachment. The generator

was operated at 40 kV and 150 mA. The sample holder was a copper block on which a thin film of the sample was formed by melt pressing the as-extruded sample just above its melting temperature. Initially the x-ray hot stage furnace was heated to 200^{o}C and then the sample was mounted on the furnace and allowed to equilibrate for 2 min. The temperature was maintained at 200^{o}C within ±0.5^{o}C during an annealing period, which was similar to that used during the rheological measurements. Samples were scanned at regular time intervals from $2\theta = 2^{o}$ to 10^{o} at the scan rate of 8^{o}/ min.

Optical Microscope: An Olympus Polarising optical Microscope (Model BX50) and a Mettler hot stage (FP 82H) were also used to monitor the hybrid morphology developed. A small piece of polymer hybrid (about 1 to 3 mg) was initially melt pressed between a microscopic slide and a cover slip. The slide with the sample was then placed in the hot stage and heated to 200^{o}C, where it was equilibrated for 60 s before shooting the picture.

TEM: The as-extruded pellets were sectioned into roughly 100 nm thin sections at –100^{o}C using a Reichert Ultracut FC-S ultramicrotome. TEM was done using a Philips 400T machine at 100 KV.

5.2. Metallocene sPP and metallocene iPP nanoclay composites

5.2.1. Materials

Two types of metallocene catalyzed matrix resins were used, one isotactic polypropylene resin (m-iPP) and three syndiotactic polypropylene resins (sPP) the details of which are listed in Table 5.3. Clay loadings ranged from 3-wt% to 9-wt%. A polypropylene-g-maleic anhydride copolymer (Polybond 3200, MFI=140) was used in some cases as a compatibilizer. Thus, both compatibilized and uncompatibilized hybrids were prepared. The molecular weights of polymers used are listed in Table 5.3.

Table 5.3. Molecular weight of the polymers

Polymer	Mw	Mw/Mn	MFI
sPP4	160 000[a]	4.5[a]	4[a]
sPP10	115 000[a]	3.6[a]	10[a]
sPP20	87 000[a]	3.4[a]	20[a]
PP-MA	122 700[b]	2.7[b]	140[a]
iPP27	160 000[a]	2.8[a]	27[a]

[a] Values supplied by the manufacturer.

[b] Values obtained by GPC analysis. The GPC analysis was done using Polylab GPC (model PLGPC220) equipped with refractive index (RI) detector. The analysis was carried out using 3 X mixed B type gel columns with 1,2,3 trichlorobenzene as a mobile phase 160^{o}C. The molecular weight and molecular weight distribution are reported with respect to polystyrene (PS) standard.

All nanocomposites were prepared by melt intercalation in a co-rotating Berstoff ZE-25 twin screw compounder having screws of 25 mm diameter and L/D = 41. Melt compounding was done at 190^{o}C (temperature profile of the screw increased from 150^{o}C at the feed to 190^{o}C near the die) and at screw speed of 200 rpm. The compounded melt was water quenched and pelletized. For some rheological measurements the pellets were compression molded into 25 mm diameter x 1 mm thick discs. Molding was carried out by compressing the pellets at 190^{o}C followed by slow cooling under pressure.

5.2.2. Method of preparation of sPP and m-iPP nanocomposites

Table 5.4. Samples used for rheological and rheo-XRD experiments

Sample code	Matrix polymer	Clay (wt%)	Compatibilizer (wt%)	Experiments*
Nanocomposites containing different clay loadings				
sPP20/3/3	sPP, MFI-20	3	3	C
sPP20/6/6	sPP, MFI-20	6	6	C
sPP20/9/9	sPP, MFI-20	9	9	DSS,DFS,SR,C,SS, rheo-XRD
sPP20/25/25	sPP, MFI-20	25	25	C
Matrix resins of different molecular weights				
sPP20/0/9	sPP, MFI-20	0	9	DSS,DFS,SR,C
sPP10/0/9	sPP, MFI-10	0	9	C
sPP4/0/9	sPP, MFI-4	0	9	C
sPP4/9/9	sPP, MFI-4	9	9	C
sPP4/9/0	sPP, MFI-4	9	0	C
Nanocomposites with matrix resins of different molecular weights				
sPP20/9/9	sPP, MFI-20	9	9	DSS,DFS,SR,C,SS, rheo-XRD
sPP20/9/0	sPP, MFI-20	9	0	DSS,DFS,SR,C,SS, rheo-XRD
sPP10/9/9	sPP, MFI-10	9	9	C
sPP10/9/0	sPP, MFI-10	9	0	C
iPP27/9/9	iPP, MFI-27	9	0	C
iPP27/9/9	iPP, MFI-27	9	9	C

*DSS: Dynamic strain sweep, DFS: Dynamic frequency sweep, SR: stress relaxation after step strain, C: creep, SS: steady shear

5.2.3. Methods of characterization

Rheological measurements were performed on all nanocomposite samples while the rheo-x-ray data was obtained only for the syndiotactic polypropylene due to limitation of the apparatus for reaching temperatures sufficient to completely melt the isotactic polypropylene.

Rheological measurements of sPP-nanocomposites: Rheological characterization of the sPP nanocomposites was carried out using three different types of rheometers viz., strain controlled rheometers (Rheometrics Scientific's ARES and RDS-II), stress controlled rheometer (Bohlin CVO-50) and capillary rheometers (Cambridge MultiPass Rheometer {MPR-III} and Ceast Rheovis 2100). [1] A 25 mm diameter parallel plate configuration was used in the RDS-II, ARES and the CVO-50 rheometers, while a 4 mm diameter x 10 mm length specially made Beryllium capillary was used in the MPR. The Beryllium capillaries were handled with great care in a hood. The rheological data obtained from the shorter Beryllium capillary may be subject to entry losses. Therefore a 1 mm diameter x 30 mm length capillary die was used in the Rheovis 2100 capillary rheometer to record better rheological data at high shear. All experiments on the parallel plate geometry were carried out under Nitrogen blanket to minimize thermo-oxidative degradation. In the capillary rheometers the sample was completely contained either between two reciprocating pistons in the MPR or between the piston and the die in the Rheovis 2100. Thus the sample was not exposed to air during the experiment. Experiments performed on the strain-controlled rheometer included dynamic strain sweep, small amplitude oscillatory shear and stress relaxation after step strain, while creep and stress ramp experiments were done using the stress controlled rheometer. The MPR was used to perform steady shear experiments in a 'multipass mode', which is explained in detail in chapter 8.

Linear rheology: The dynamic strain sweep test was carried out on three samples viz., the matrix polymer (sPP20/0/9), the uncompatibilized hybrid (sPP20/9/0) and the compatibilized (sPP20/9/9) hybrid on the ARES rheometer at 200^{o}C at a constant frequency of 10 rad/s in the strain range of 0.01-100%. Further, the small amplitude frequency sweep experiments were carried out using either the ARES or RDS-II

rheometer in the frequency range of 0.1-100 rad/s and in the temperature range of 170-210^{o}C, at 0.5% strain for the compatibilized hybrids and at 5% strain for the uncompatibilized and the matrix samples. The mastercurves were generated by shifting the frequency sweep data to 170^{o}C, using horizontal shift only.

Creep experiments were performed using the Bohlin CVO-50 stress controlled rheometer. In creep experiments, the samples were subjected to a constant stress of 10 Pa for a creep time of 180 s at 190^{o}C. In some creep experiments the compliance data was recorded at time intervals of 15 min after 180 s of creep time, for a total of 3 hrs annealing period.

Nonlinear rheology: The viscosity at higher stresses (i.e., the nonlinear response) was probed by performing stress ramp experiments on the Bohlin rheometer. Samples of sPP nanocomposites with different molecular weight and clay content were subjected to increasing stresses from 10 Pa –1500 Pa at 190^{o}C, as tabulated in the Table 5.5.

Steady shear experiments were performed on the compatibilized (sPP20/9/9) and the uncompatibilized (sPP20/9/0) hybrids in the 'multipass mode' at 190^{o}C using the MPR, as described in chapter 8.

Microstructure characterization: X-ray diffraction (XRD) was used as the main characterization technique for determining the microstructure of the nanocomposites. Transmission electron microscopy was used for iPP nanocomposites (see chapter 6, Fig. 6.9), but gave more qualitative results of the microstructure. Hence XRD was used as the principle technique and was found adequate for the purpose of this work. Two types of XRD apparatus were used:

(i) A Rigaku Dmax 2500 diffractometer with rotating anode generator and wide angle powder goniometer fitted with high temperature attachment was used as a preliminary characterization tool for the as-extruded samples.

(ii) The Cambridge MultiPass Rheometer (MPR) was used for in-situ rheo-XRD measurements on sPP nanocomposite melts during shearing. Figure 5.2 shows a schematic of the rheo-XRD apparatus.

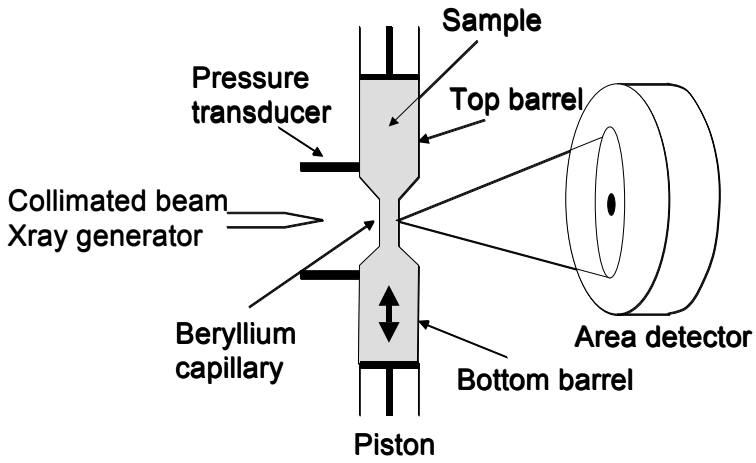

Figure 5.2. Schematic of Cambridge Multi Pass rheometer with an in situ XRD measurement

The MPR consists of two pistons, which are located one each in the top and bottom barrels. A fixed volume of sample is enclosed between the pistons, which is then pushed backwards and forwards by the reciprocating pistons through a central test section such as a capillary. The piston displacements and speeds are precision controlled using a servo hydraulic mechanism. A 4 mm diameter x 10 mm long capillary made from x-ray transparent beryllium was used as the central section in our experiments. The sample temperature was controlled to within ±0.5^{o}C by circulating heating oil in the jackets around the barrels and the test section. [1-3] Piston speeds used in this work ranged from 0.01–50 mm/s, which corresponded to apparent wall shear rates of 0.28–1406 s^{-1}. Experiments were performed at 190^{o}C. In a 'multipass' mode of operation the pistons were reciprocated at a set speed and for a set displacement with rest time between each stroke. Two pressure transducers located near the ends of the capillary measured the pressure drop across it during each stroke. The uncorrected wall shear stress was calculated from the measured steady state pressure drop (see Fig.8.10) as

$$\sigma_w = \frac{\Delta PR}{2L} \tag{5.1}$$

where R and L are the radius and length, respectively, of the capillary. The apparent wall shear rate was calculated by using the standard relations for Poiseuille flow namely,

$$\dot{\gamma}_{a,w} = \frac{4Q}{\pi R^3} \tag{5.2}$$

Here, $Q = (\pi/4) D_b^2 V_p$ is the flow rate, D_b is the barrel diameter and V_p is the piston velocity.

The MPR was located within an x-ray diffractometer cabinet such that the capillary was aligned in front of a collimated x-ray beam. The x-ray generator was operated at 45kV, 45mA. Various safety interlocks ensured minimum exposure to x-rays. Scattered x-rays from the sample were collected on an area detector. The distance between the sample and the detector can be varied and thus measurements in both wide and small angle modes can be made. All measurements in this work were made in wide-angle mode in the 2θ range of 1^o – 10^o. Thus, the MPR can be used to control temperature and shear rates while simultaneously allowing for in-situ WAXD measurements.

5.3. Mechanical properties of sPP nanocomposites

5.3.1. Materials

The sPP nanocomposites described in the section 5.2 were also used for studies on the solid-state properties. Thus, the nanocomposites were prepared by melt mixing metallocene catalyzed syndiotactic polypropylene supplied by Fina oil and chemical Co. U.S.A., with montmorillonite clay modified using dimethyl dehydrogenated tallow, (Trade name: Closite 20A, CEC=95 meq/100g) supplied by Southern Clay Products, U.S.A. and with isotactic polypropylene–g-maleic anhydride compatibilizer (MFI=140, Trade name: PB3200, M_w= 122700, maleic anhydride = 1wt%) supplied by Uniroyal Co. U.K.

5.3.2. Methods of preparation of sPP nanocomposites

The nanocomposite under investigation were prepared by melt compounding, in Berstoff ZE-25 twin screw extruder, under the conditions described in section 5.2.2. Some composites were also prepared without using the compatilibilizer. Sample composition and nomenclature used is shown in the Table.5.5.

Table 5.5. Composition of the sPP nanoclay composites

Sample code			Nano (wt%)	patibilizer (wt%)
sPP matrix				
MFI=4	MFI=10	MFI=20		
sPP4/9/9	sPP10/9/9	sPP20/9/9	9	9
sPP4/9/0	sPP10/9/0	sPP20/9/0	9	0
sPP4/0/9	sPP10/0/9	sPP20/0/9	0	9

The extruded nanocomposites were water quenched and pelletized. The pellets so prepared were then extruded into tapes using the rate controlled capillary rheometer (model: CEAST Rheovis 2100, supplied by CEAST S.P.A, Italy) equipped with a slit die (10 mm in length x 1 mm in thickness). Films were extruded at various the piston speeds at a temperature of 190^{o}C, and cool air was blown across the extruded tapes to facilitate solidification. Five different tape samples were produced using different piston speeds, as will be described in detail in chapter 9. In addition to the capillary extruded tapes, one film of compatibilized hybrid (sPP20/9/9) was prepared by compression molding at 190^{o}C.

5.3.3. Methods of characterization

Mechanical Testing: The mechanical properties of these tapes (15 cm long x 10 mm wide x 1 mm thick) were tested using an Instron 4204 Universal Testing Machine at a crosshead speed of 25 mm/min at room temperature. The results of these mechanical properties were discussed in detail in chapter 9.

Microstructure characterization: The x-ray diffraction data for the tape samples was collected from three different x-ray equipment.

(i) The clay orientation was measured using a Rigaku x-ray machine having a 'RUH3R' rotating anode x-ray generator and a 'RAXIS IV^{++}' image plate detector. Monochromatic x-rays (Cu Kα, λ=1.5418 Å) were produced at a voltage of 50 KV and

current of 100 mA with copper target as anode. The sample to detector distance was 75 mm. 2D diffraction images were recorded by exposing the sample to x-rays for 2 s, while applying 0.05° oscillations to the sample. Image collection was controlled by Windows NT workstation using the software 'crystal clear'. The images so obtained were further processed by Image pro-plus supplied by Media cybernetics U.S.A.

(ii) It was observed that over the time period required to collect the clay signals, the polymer patterns on the image plate were saturated. Therefore for measuring the characteristic polymer signals appearing at smaller d-values, a Bruker SMART APEX CCD Single Crystal x-ray Diffractometer, having a M_o Kα source was used for obtaining 2D x-ray diffraction patterns for the polymer chains. Cut tapes of suitable size were mounted on the goniometer and the still photographs recorded using monochromatic Mo K alpha (λ = 0.7107 Å) radiation at 50 kV and 30 mA x-ray power. The specimen to detector distance was kept at 60 mm. The specimen was exposed to the x-rays for 10 s.

(iii) Finally, x-ray diffraction experiments were also performed as a benchmark to measure the 2θ peak positions for the clay and the polymer crystallites using a Rigaku Dmax 2500 diffractometer consisting of a rotating anode generator with Copper Kα target operating at 40 kV and 150 mA and a wide angle powder goniometer.

Thermogravemetric analysis: Differential scanning calorimety (DSC) experiments were performed using Perkin Elmer DSC-7 under nitrogen atmosphere, to measure the degree of crystallinity in different samples.

The microstructure of the sPP tapes extruded at different piston speeds and the effect of this on the mechanical properties are discussed in detail in chapter 9.

5.4. Polyethylene (PE) nanocomposites

Polyethylene nanocomposites investigated in this thesis were supplied by Mr. Saptarshi Ray and were prepared by in-situ polymerization of ethylene gas in the presence of clay using a novel synthesis strategy developed by Saptarshi et. al. [4,5].

5.4.1. Materials

The clay used was Closite 20A procured from Southern Clay Products, USA. A late transition metal catalyst was used for the in-situ polymerization of ethylene to prepare the polyethylene nanocomposites (PENC). Details of the catalyst and synthesis procedures can be found in Saptarshi et. al. [4,5]. The catalyst is known to yield linear polymers. Two types of nanocomposites were used: one prepared by heterogenization of the catalyst i.e., adsorption of the catalyst on the clay by a novel strategy (series PENC-1 and PENC-3) [4,5] and the other in which the catalyst was used as such in the presence of suitably treated clay without heterogenization (PENC-2). In the former case, there is a significant chance of finding polyethylene chains end-tethered to the clay surface, while in the latter case the PE chains could be expected to at best intercalate within the clay galleries. Also, two series of PE nanocomposites were used, one containing approximately 1 wt% clay loading (PENC-1) and the other containing ~ 5 wt% clay loading (PENC-3). The PENC-2 contained 1-wt% clay. A pristine polyethylene was also synthesized using the catalyst and co-catalyst in the absence of clay.

Table 5.6 shows the molecular weight of the polyethylene matrix extracted from the nanocomposites. The numbers in brackets in the first column indicate the co-catalyst/catalyst ratio used for the synthesis of the nanocomposites. The data in the table suggests that the average molecular weight of the matrix resin increased with increase in the catalyst: co-catalyst ratio. Also, the molecular weight distribution of the polyethylene matrix resin is rather broad.

5.4.2. Methods of characterization

Rheological characterization: Dynamic strain sweep test was carried out using the ARES rheometer at 150^{o}C at constant frequency of 10 rad/s in the strain range of 0.01-100%. Further, small amplitude frequency sweep experiments were carried out using the ARES rheometer in the frequency range of 0.1-100 rad/s and in the temperature range of 150-230^{o}C, at 5% strain for the hybrids (PENC-1) synthesized using catalyst

heterogenized on the clay surface and for the pristine PE samples, and at 0.1% strain for the hybrids (PENC-2) synthesized using catalyst without heterogenization on the clay surface. The mastercurves were generated by shifting the data to 150^{o}C, using horizontal shift only.

Creep measurements are carried out using the Bohlin CVO-50 stress controlled rheometer; the samples were subjected to a constant stress of 50 Pa at 170^{o}C. The compliance data was recorded at time intervals of 15 min after 120 s of creep time, for total of 8 hrs annealing period.

XRD: A Rigaku Dmax 2500 diffractometer consisting of a rotating anode generator with Copper Kα target operating at 40 kV and 150 mA and a wide angle powder goniometer was used. Powdered polymer samples were filled in the sample holder and scanned from 2θ =2°-10°at the rate of 1°/min at room temperature.

GPC: The polymers were extracted in the hot 1,2,3, trichlorobenzene at 140^{o}C for 1 hr and then precipitated in methanol. The precipitates were filtered and dried. This entire process was repeated twice so as to avoid any amount of clay remaining in the polymers. The polymer fractions so obtained were used further for GPC analysis.

The GPC analysis was done using Polylab GPC (model PLGPC220) equipped with refractive index (RI) detector. The analysis was carried out using 3 X mixed B type gel columns with 1,2,3 trichlorobenzene as a mobile phase at 160^{o}C. The GPC results are listed in the Table 5.6. It is seen that the molecular weight of the polymer decreased with the increase in the clay loading. This might be due to the reduction in the catalyst activity due to heterogenization of the catalyst.

Table 5.6. Molecular weights of the PE nanocomposites

Sample code	M_w	M_w/M_n
Pristine PE	73,000[a]	35.9
PENC-1 (1600)	104,000[b]	27.7
PENC-1 (1000)	116,200[b]	26.6
PENC-1 (600)	266,200[b]	23.9
PENC-1 (200)	298,000[b]	23.9
PENC-2 (1600)	32,100[a]	23.96
PENC-3 (1600)	23,600[b]	39.5
PENC-3 (1000)	26,400[b]	38.9
PENC-3 (600)	62,900[b]	38.9
PENC-3 (200)	66,200[b]	52.5

[a] Values of molecular weights and molecular weight distribution are reported by using universal calibration methods using RI detector.

[b] Values of molecular weights and molecular weight distribution are reported by using triple detector. Data obtained from Saptarshi et. al. [4,5]

Reference List:

1. Mackley, M. R.; Marshall, R. T. J.; Smeulders, J. B. A. F. *J. Rheol.* **1995**, *39*(6), 1293-1309.
2. Mackley, M. R.; Moggridge, G. D.; Saquet, O. *J. Mater. Sci.* **2000**, *35(*20), 5247-5253.
3. Ranganathan, M.; Mackley, M. R.; Spiteller, P. J. H. *J. Rheol.* **1999**, 43(2), 443-451.
4. Saptarshi Ray Ph. D thesis to be submitted to University of Pune (Dept. of chemistry) 2003.
5. Saptarshi, R.; Sivaram, S. manuscript under preparation (2003).

Chapter 6 Microstructure of as-prepared nanocomposites

This chapter describes the structural investigations related to the microstructure of as- prepared sPP, iPP and PE nanocomposites using techniques like x-ray diffraction, transmission electron microscopy and optical microscopy. X-ray diffraction is used as the main technique to elucidate the microstructure of intercalated and exfoliated polymer nanocomposites in this study.

6.1. Isotactic polypropylene (iPP) nanocomposites

6.1.1. X-ray diffraction analysis

Figure 6.1 shows the x-ray diffraction patterns for the as-extruded the compatibilized (iPP3/9/9) and the uncompatibilized (iPP3/9/0) hybrids, at room temperature.

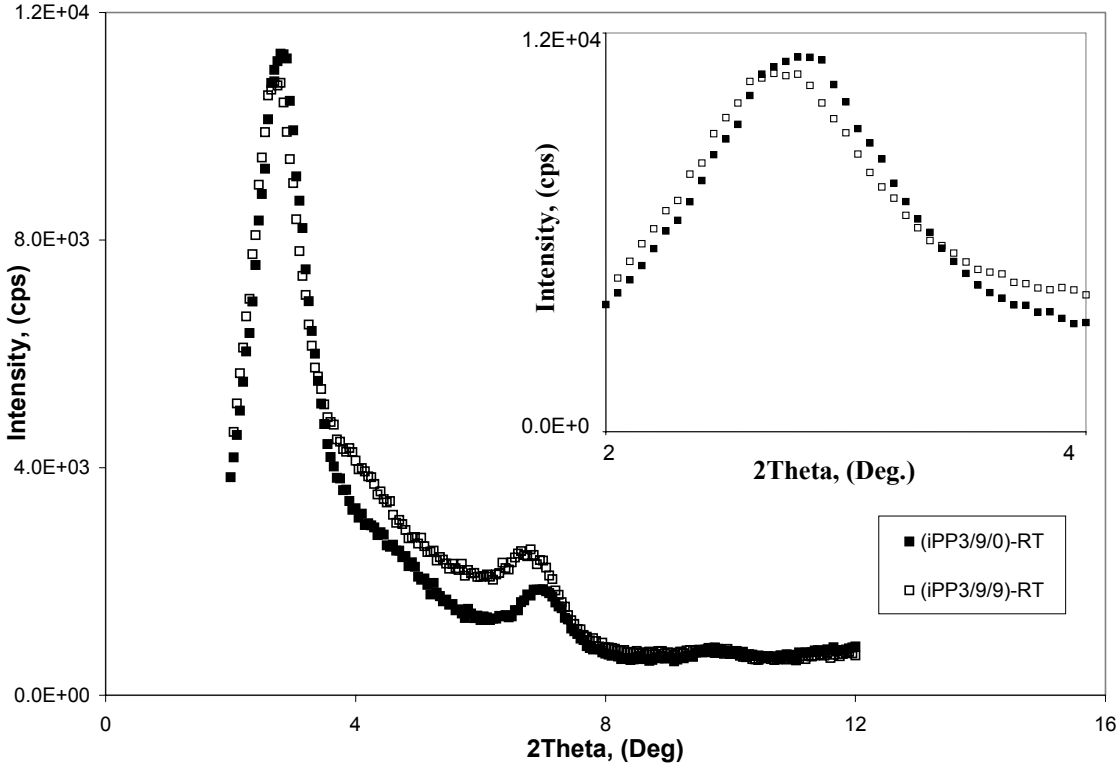

Figure 6.1. X-ray diffraction pattern of compatibilized (iPP3/9/9) and uncompatibilized (iPP3/9/0) hybrids

The inset shows the first clay peak in more detail. As it can be seen, the clay peak for the compatibilized hybrid (iPP3/9/9) is shifted to lower d spacing compared to the uncompatibilized hybrid (iPP3/9/0) hybrid. This indicates better intercalation in the presence of the compatibilizer.

High temperature x-ray analysis of clay and extruded iPP nanocomposites was performed. Figure 6.2 shows WAXD patterns for DMDHTMC clay (Closite6A) as a function of annealing time. The clay showed three distinct peaks at 2θ = 2.2°, 4.5° and 7.0° corresponding to the *d* spacing of 3.3 nm, 2.0 nm and 1.0 nm respectively. On annealing the clay at 200°C for 30 minutes, a distinct shift in the peaks towards the higher 2θ region and a decrease in peak intensities were observed. The peak shift towards higher 2θ values indicate a decrease in *d* spacing, which could be due to slow degradation of the organic modifier at the high annealing temperature resulting in gradual collapse of the gallery heights.

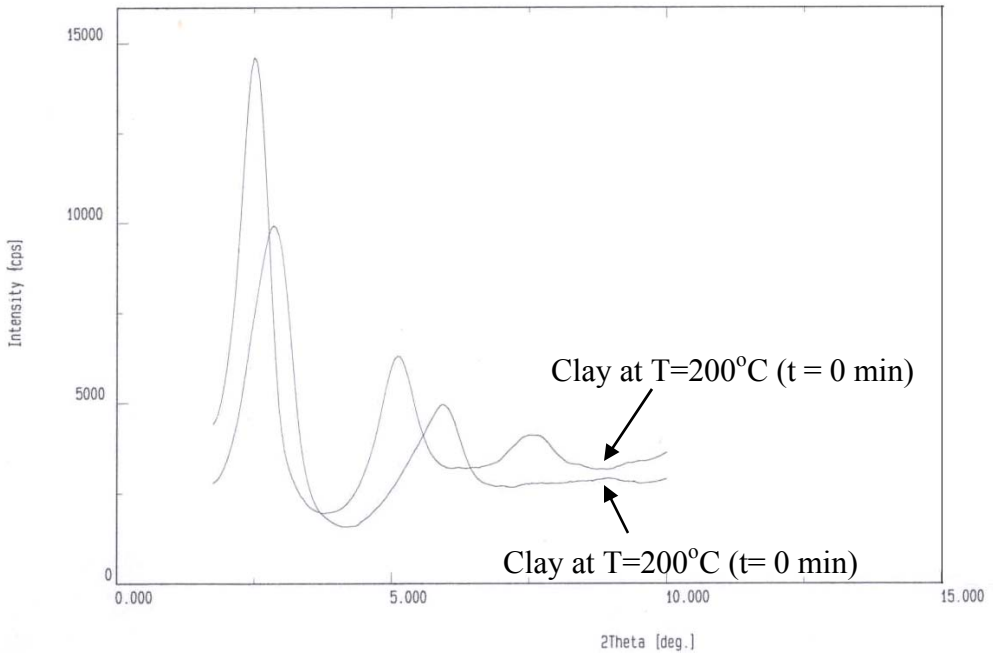

Figure 6.2. X-ray diffraction data for the clay during in-situ annealing at T = 200°C

An important point to be noted from the WAXD pattern of DMDHTMC is that the *d* spacing of 3.3 nm is already significantly higher than that of the unmodified Na^+ clay, which has a *d* spacing of about 1 nm. The large gallery heights in DMDHTMC are

conducive to intercalation of the polymer chains in between the silicate layers provided the interactions between the polymer and the clay are favourable.

The WAXD data for the compatibilized hybrid (iPP3/9/9) and the uncompatibilized hybrid (iPP3/9/0) are shown in Figure 6.3 and 6.4, respectively, as a function of annealing time. Semicrystalline isotactic polypropylene homopolymer does not show any peak in the 2θ region between 1^o and 10^o. Hence the peaks in the diffraction patterns in Figure 6.3 and Fig.6.4 are those arising from the clay alone. As seen in the figures, the clay peaks did not shift to lower 2θ region for either of the hybrids indicating no further increase in *d* spacing even if intercalation might have occurred. The shift towards higher 2θ values might be an indication of the degradation of the organic modifier. A decrease in the peak intensity accompanied by a broadening of the peaks can be clearly seen in the Figure 6.3. The WAXD data indicates that stacks of silicate layers (i.e., clay tactoids) are present in both the uncompatibilized (iPP3/9/0) and the compatibilized (iPP3/9/9) hybrids. Calculation based on Scherrer's formula (see e. q. 2.5) suggests a slight decrease in the clay tactoid size with annealing. Roughly 4-5 platelets in the clay tactoid at time (t= 0 min) decreased to about 3 platelets, after 3 hrs annealing. This decrease in the crystallite thickness in the compatibilized hybrid (iPP3/9/9) could be due to possible exfoliation of a few layers from the end of the stacks into the melt.

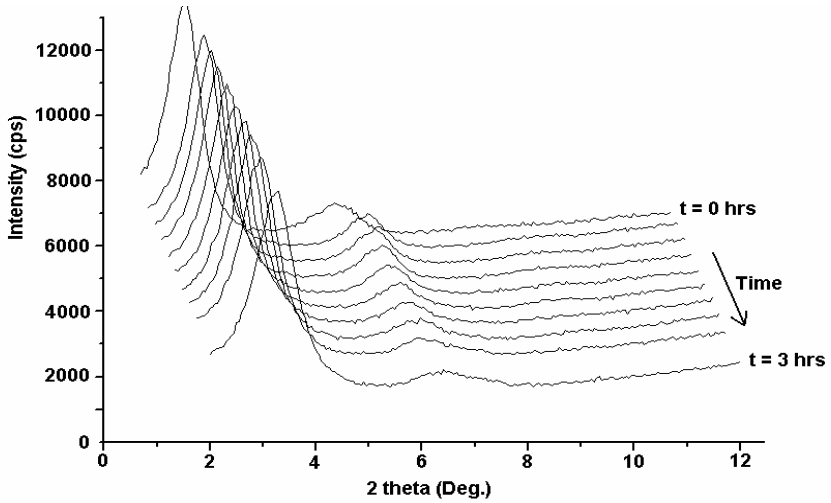

Figure 6.3. X-ray diffraction data for the compatibilized hybrid (iPP3/9/9) during in-situ annealing at T = 200^{o}C

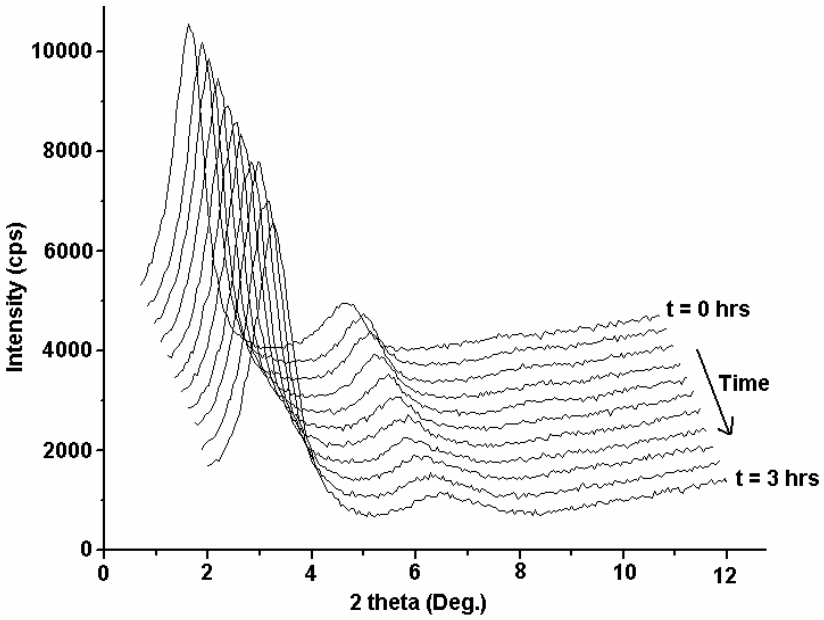

Figure 6.4. X-ray diffraction data for the uncompatibilized hybrid (iPP3/9/0) during in-situ annealing at T = 200^{o}C

The uncompatibilized hybrid (iPP3/9/0) also showed a similar decrease in peak intensity with annealing time. There is no distinct qualitative difference in the XRD patterns of the uncompatibilized (iPP3/9/0) and the compatibilized (iPP3/9/9) hybrids.

Thus it can be said that the WAXD data is rather inconclusive of subtle differences, if any, between the morphology of the compatibilized (iPP3/9/9) and that of the uncompatibilized (iPP3/9/0) hybrids.

6.1.2. Optical microscopy

Optical micrographs of the iPP nanocomposites for both the compatibilized (iPP3/9/9) and the uncompatibilized (iPP3/9/0) hybrids are shown in Figure 6.5. The optical micrographs of both the uncompatibilized and the compatibilized hybrids show agglomerates of primary particles of clay (~ 50–70 μm) dispersed in the polymer matrix.

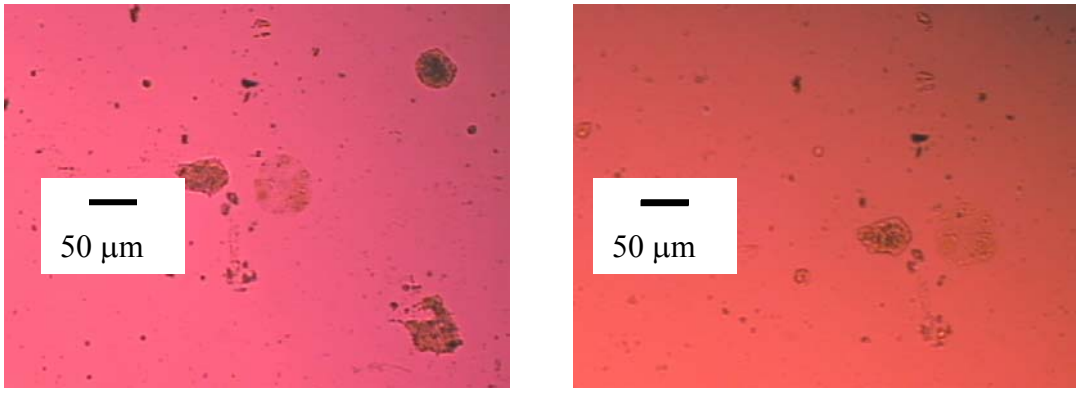

(a) **(b)**

Figure 6.5. Optical micrographs of (a) compatibilized hybrid (iPP3/9/9) (b) uncompatibilized hybrid (iPP3/9/0)

6.1.3. Transmission electron microscopy

Figure 6.6 shows the TEM of as–extruded compatibilized (iPP3/9/9) hybrid at a magnification of 46000 x. It is clear that the silicate layers forming the clay tactoids are dispersed within the polymer matrix. Also, the edges of the clay tactoids appeared to be better dispersed into the surrounding matrix.

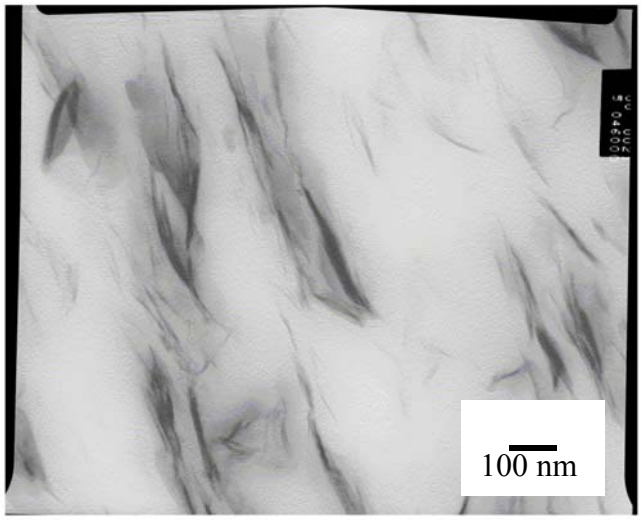

Figure 6.6. TEM image of as-extruded compatibilized hybrid (iPP3/9/9)

Thus, the as-extruded iPP nanocomposites show a hierarchy of morphologies. Primary particles of 50 –70 μm size are dispersed in the sample. At the same time the sample also contains dispersed clay tactoids, which are made up of stacks of 3-5 silicate layers on an average. The d spacing of the silicate layers is about 3.3 nm, which is the same as that for the clay itself. Annealing of the samples causes degradation of the organic modifier and consequent collapse of the galleries. There is also some edge exfoliation from the tactoids. However, there appears to be no distinct difference between the microstructure of the compatibilized and uncompatibilized hybrids.

6.2. Syndiotactic polypropylene (sPP) nanocomposites

6.2.1. X-ray diffraction analysis

Figure 6.7 shows the diffraction patterns at 190^{o}C for the organically modified clay, the uncompatibilized hybrid (sPP20/9/0) and the compatibilized hybrid (sPP20/9/9). The presence of a dominant peak indicates that the nanocomposites contain intercalated clay tactoids. The *d* spacing (gallery height) of the clay platelets in the tactoids was about 30 Å in the pure clay, about 32 Å in the uncompatibilized hybrid and about 34 Å in the

compatibilized hybrid. The inset shows more clearly that clay peak for the compatibilized hybrid is at a lower 2θ value.

Similar to the iPP nanocomposites, the slight increase in the gallery height for the compatibilized hybrid (sPP20/9/9) compared to the uncompatibilized (sPP20/9/0) hybrid shows better intercalation possibly due to the presence of the compatibilizer.

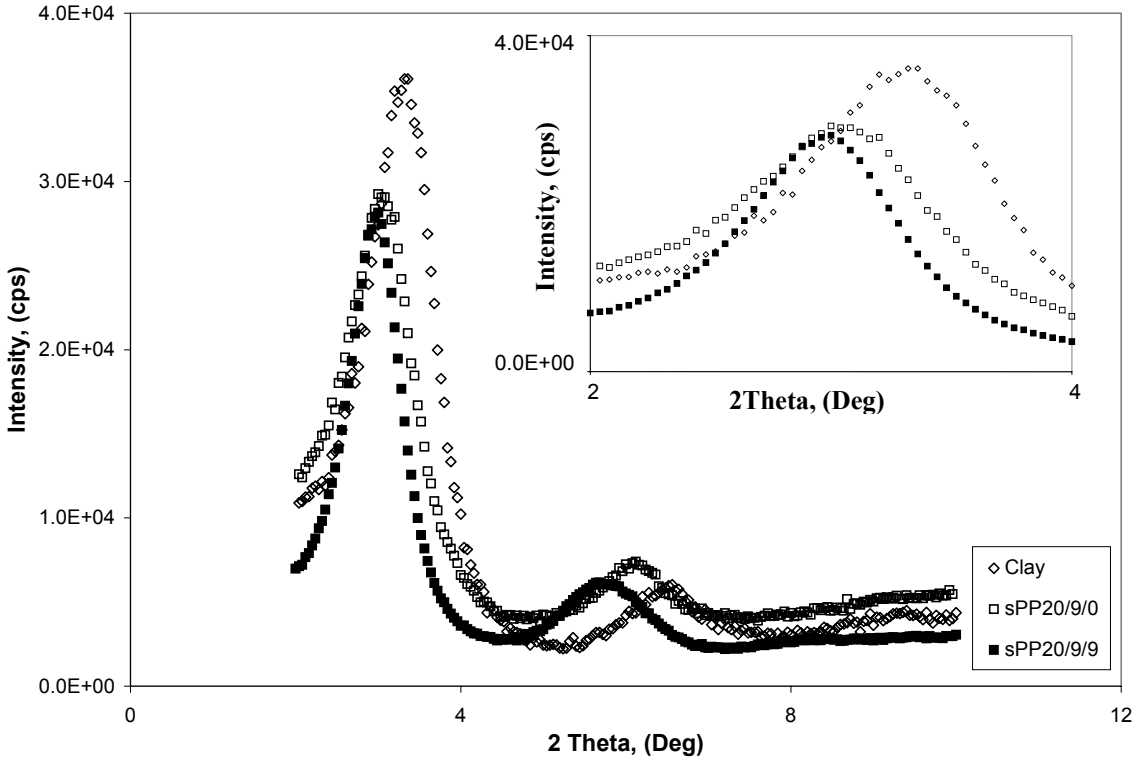

Figure 6.7. X-ray diffraction data for the clay (C20A), uncompatibilized hybrid (sPP20/9/0) and compatibilized hybrid (sPP20/9/9) at T = 190^{o}C

The Cambridge MultiPass Rheometer (MPR) was used for in-situ rheo-XRD measurements on sPP nanocomposite melts during shearing. The rheo x-ray experiments reported in this study have been used to study the microstructural changes occurring in the hybrid during flow. As described in the chapter 5.2, the MPR uses Be capillary aligned in front of a collimated beam of x-rays. The scattered x-rays transmitted from the sample were collected on the area detector. The data collected by the area detector of the MPR-XRD equipment was processed and analyzed to correct for warping, background scattering, smoothing and peak searching. The peak 2θ positions for pristine C20A clay

obtained from the Rigaku Dmax 2500 diffractometer was used as a one-point calibration for converting the diffraction ring data into intensity-2θ data.

Figure 6.8 shows the scattered x-ray intensity from the clay, the uncompatibilized hybrid (sPP20/9/0) and the compatibilized hybrid (sPP20/9/9) under quiescent conditions at 190^{o}C. The inset in the figure shows, as an example, the two-dimensional diffraction pattern of the compatibilized hybrid. The clay tactoids in the compatibilized nanocomposite have a slightly larger gallery height of 34 Å than that in the uncompatibilized sample or the clay (~30 Å). These peak positions are similar to those obtained from the Rigaku Dmax 2500 diffractometer shown in Fig. 6.5. The inset shows the 2D x-ray diffraction pattern of the compatibilized hybrid (sPP20/9/9). The diffraction rings corresponding to the peaks at $2\theta \sim 6^{o}$ were not easily visible on the area detector. This is because of the lower intensity source of the x-rays in the MPR-XRD equipment compared to the Rigaku machine. Thus, the peak 2θ positions obtained from the Rigaku diffractometer are expected to be more accurate. The MPR-XRD apparatus, on the other hand, was used specifically to obtain data on flow-induced orientation.

6.2.2. Optical microscopy

Cross polarized optical micrographs of the sPP nanocomposites for the compatibilized (sPP20/9/9) and the uncompatibilized (sPP20/9/0) hybrids are shown in Figure 6.9. The micrographs show that both the uncompatibilized and the compatibilized hybrids have agglomerates of primary particles of clay ~ 40–50 μm in size. It s believed that the agglomerates shown in Figure 6.9 and Figure 6.5 contain primary particles (~ 0.5 μm), which in turn contain several clay tactoids that are made of stacks of individual platelets.

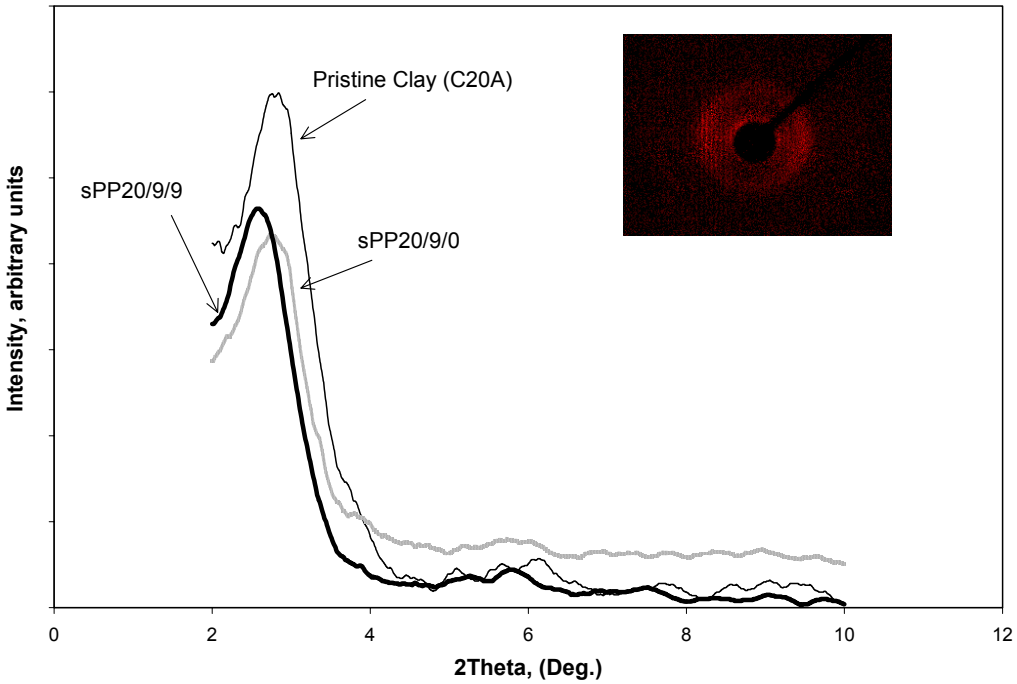

Figure 6.8. X-ray diffraction data for the clay (C20A), uncompatibilized (sPP20/9/0) and compatibilized (sPP20/9/9) hybrid at T = 190°C, in MPR rheo-XRD equipment under quiescent conditions

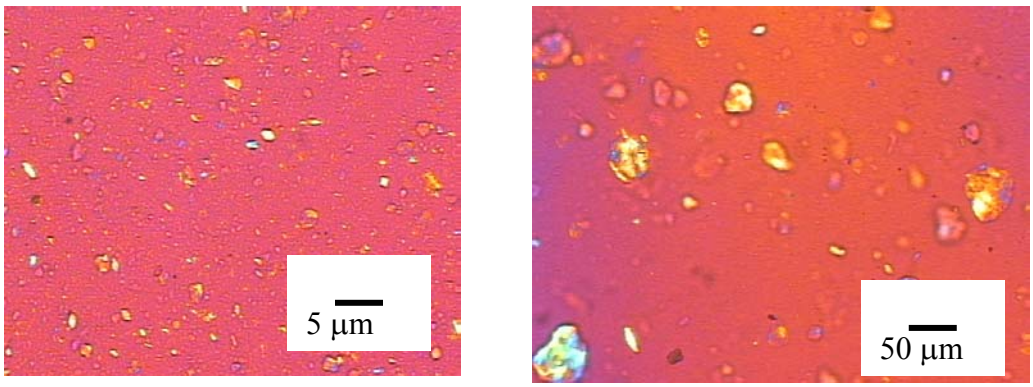

(a) **(b)**

Figure 6.9. Optical micrographs of (a) compatibilized hybrid (sPP20/9/9) (b) uncompatibilized hybrid (sPP20/9/0)

6.3. Polyethylene (PE) nanocomposites

6.3.1. X-ray diffraction analysis

PE nanocomposite were synthesized by in-situ polymerization of ethylene in the presence of a suitably modified clay (see chapter 5.3). The XRD data shown in figures 6.10 and 6.11 was kindly provided by Mr. Saptarshi Ray (see relevant references in chapter 5). Figure 6.10 shows the XRD patterns of the PE nanocomposites (PENC-1) series having ~ 1-wt% clay and made with catalyst heterogenized on the clay surface. The nanocomposites in this series were made using different catalyst: co-catalyst ratio (see Table 5.6). XRD data was acquired for 10 min to get sufficient signal from clay, since the clay concentration was low. As it can be seen from Figure 6.10, the PE nanocomposites appear almost completely exfoliated, at least to an extent determinable by WAXD. Figure 6.11 shows the XRD pattern of the PE nanocomposites (PENC-3) series, having ~ 5-6-wt% clay and made with catalyst heterogenized on the clay surface. Again, the nanocomposites in this series were made using different co-catalyst: catalyst ratio (see Table 5.6). The (PENC-3) nanocomposites were not as exfoliated as the (PENC-1) series, with the clay peaks evident in the XRD. However, the major clay peak is still not visible in the PENC-3 hybrids.

Thus under similar conditions of polymerization the extent of exfoliation was dependent on the clay concentration.

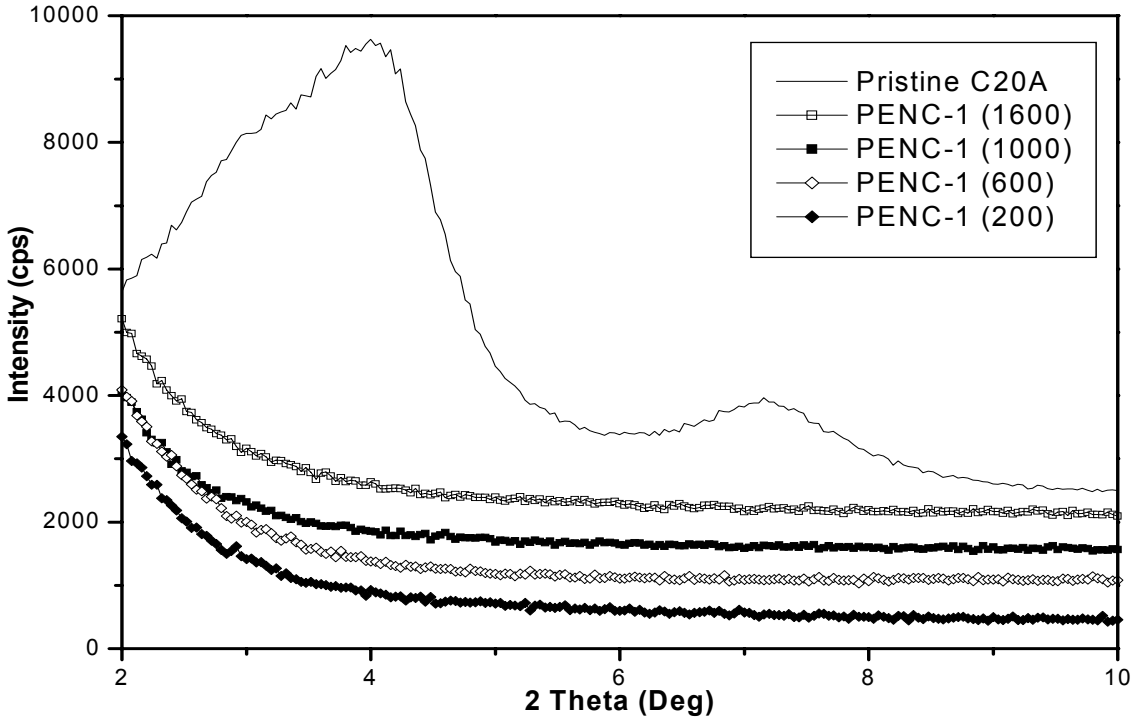

Figure 6.10. X-ray diffraction patterns of the (PENC-1) series and pristine clay

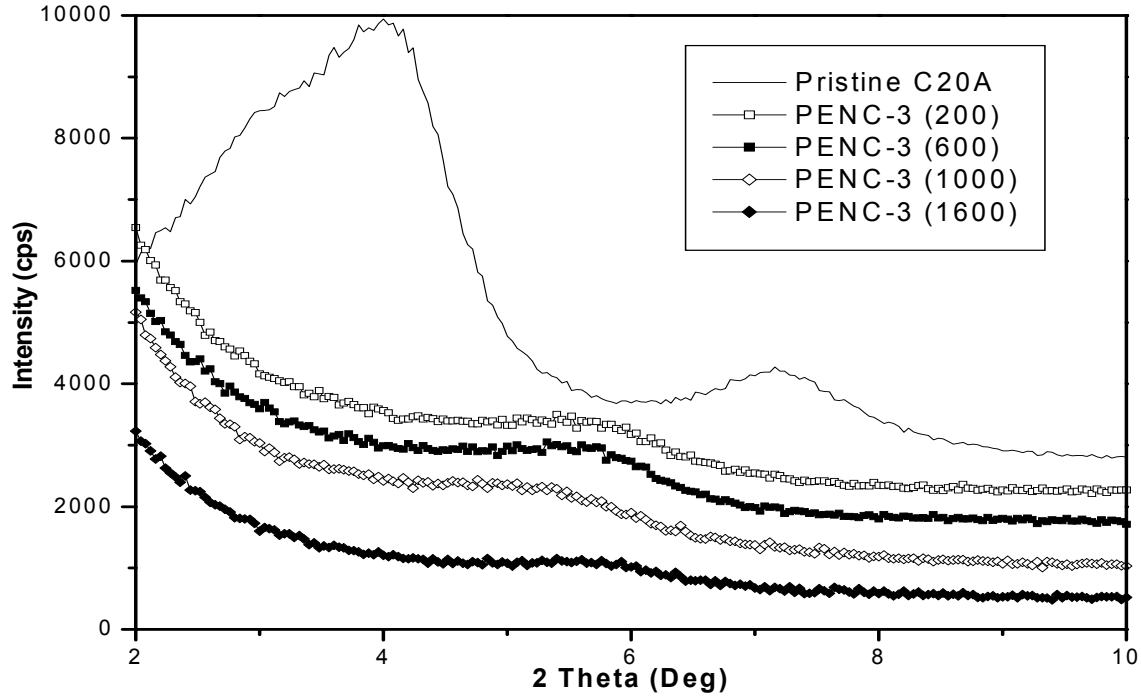

Figure 6.11. X-ray diffraction patterns of the (PENC-3) series and pristine clay

Interestingly, it can also be seen from Figure 6.11 that the peak intensity decreases and the peak width increases with the increase in co-catalyst: catalyst ratio for

the same clay concentration. This implies an increase in the extent of intercalation with increase in the co-catalyst: catalyst ratio. It may be noted that increasing this ratio decreases the average molecular weight of the polymer as mentioned earlier in chapter 5.

PE nanocomposites were also synthesized by in situ polymerization, wherein the catalyst was not heterogenized on the clay surface. Figure 6.12 shows a comparison of the XRD patterns for the PE nanocomposites synthesized with heterogenization and without heterogenization of the catalyst keeping other polymerization conditions identical.

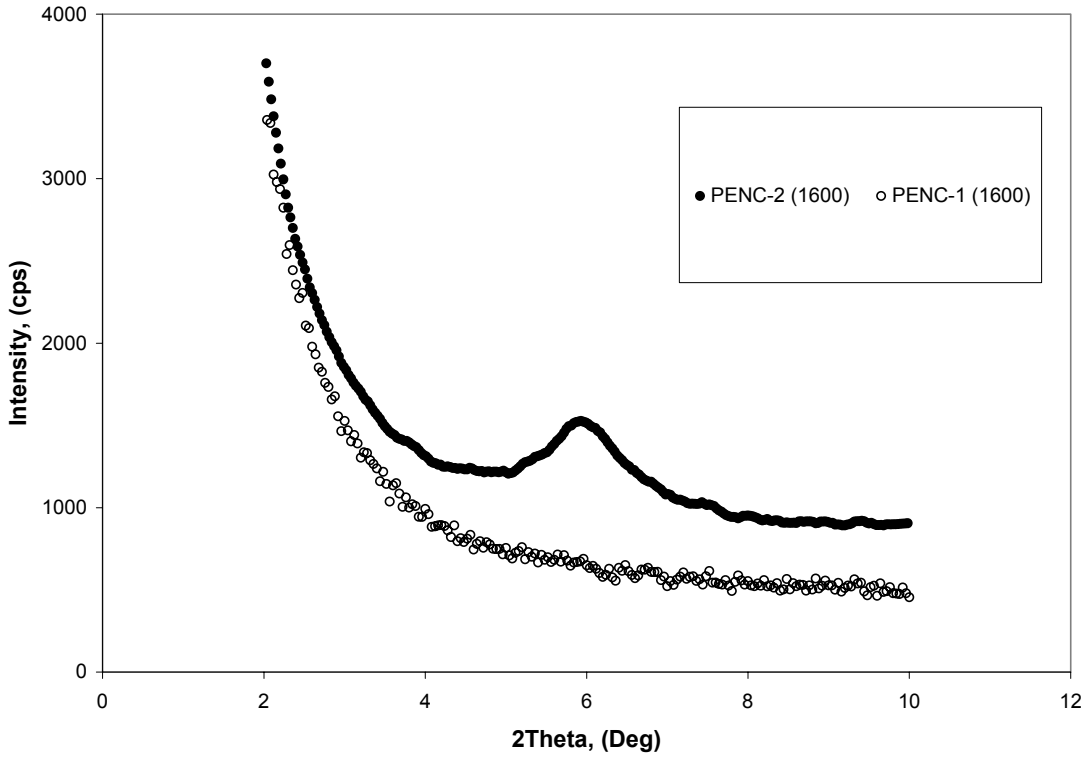

Figure 6.12. X-ray diffraction patterns of the PENC-1 (1600) and PENC-2 (1600)

As seen from the Figure 6.12, under similar conditions of polymerization, the nanocomposite prepared using the catalyst heterogenized on the clay surface [PENC-1 (1600)] were nearly exfoliated, while the nanocomposite synthesized without the heterogenization of the catalyst [PENC-2 (1600)] had remnants of intercalated microstructure.

Thus, the heterogenization of the catalyst on the clay surface played a very crucial role in determining the microstructure of the hybrid. As mentioned earlier in chapter 5, there is a strong possibility that the heterogenization of the catalyst would result in hybrids with polymer chains tethered to the clay surface, although no direct evidence for this has been presented here.

6.4. Summary

XRD, optical microscopy, and TEM suggest that the polypropylene hybrids investigated in this study were mainly intercalated hybrids, with clay tactoids having typically 3-4 clay platelets. The compatibilized hybrid showed slightly better intercalation compared to the uncompatibilized hybrids. The d spacing in the compatibilized and the uncompatibilized hybrids as indicated by WAXS are not significantly different. Even with the annealing times as high as 3 hrs the x-ray diffraction pattern of the compatibilized and the uncompatibilized hybrids did not show any significant difference. However, as we will see in the chapters 7 and 8, the rheological response of the compatibilized and the uncompatibilized hybrids are qualitative different.

The microstructure of the PE nanocomposites can be classified as being of nearly exfoliated type. However, subtle differences in the extent of exfoliation were observed as a function of clay loading and catalyst: co-catalyst ratio specifically, the PENC's containing higher clay loading and lower co-catalyst: catalyst ratio had more intercalated microstructure. At the same time molecular weight of the matrix resin was also determined by these parameters. It is not yet clear whether there is a definitive relation between the extent of exfoliation and resin molecular weight. These parameters affect the rheological response of PENC's as will be shown in chapter 10.

WAXD was found to be a sensitive technique to study the microstructure of the nanocomposites synthesized with and without heterogenization of the catalyst on the clay surface. It might be possible that some polymer chain will be tethered to the clay surface. The rheological response of these hybrids also is vastly different, as will be discussed in chapter 10.

Chapter 7 Linear rheology of PP nanocomposites

This chapter describes the linear viscoelastic behavior of isotactic and syndiotactic polypropylene (PP) nanocomposites in creep, step-shear strain and oscillatory shear experiments. The effect of clay loading and molecular weight of the matrix on the rheological response of the composites are discussed.

7.1. Isotactic polypropylene (iPP) nanocomposites

7.1.1. Linear rheology of iPP nanocomposites

The linear and nonlinear viscoelastic regions of the isotactic polypropylene matrix (iPP3/0/9), uncompatibilized hybrid (iPP3/9/0), and compatibilized hybrid (iPP3/9/9) were delineated by dynamic strain sweep experiment at 200^{o}C without any pre-annealing.

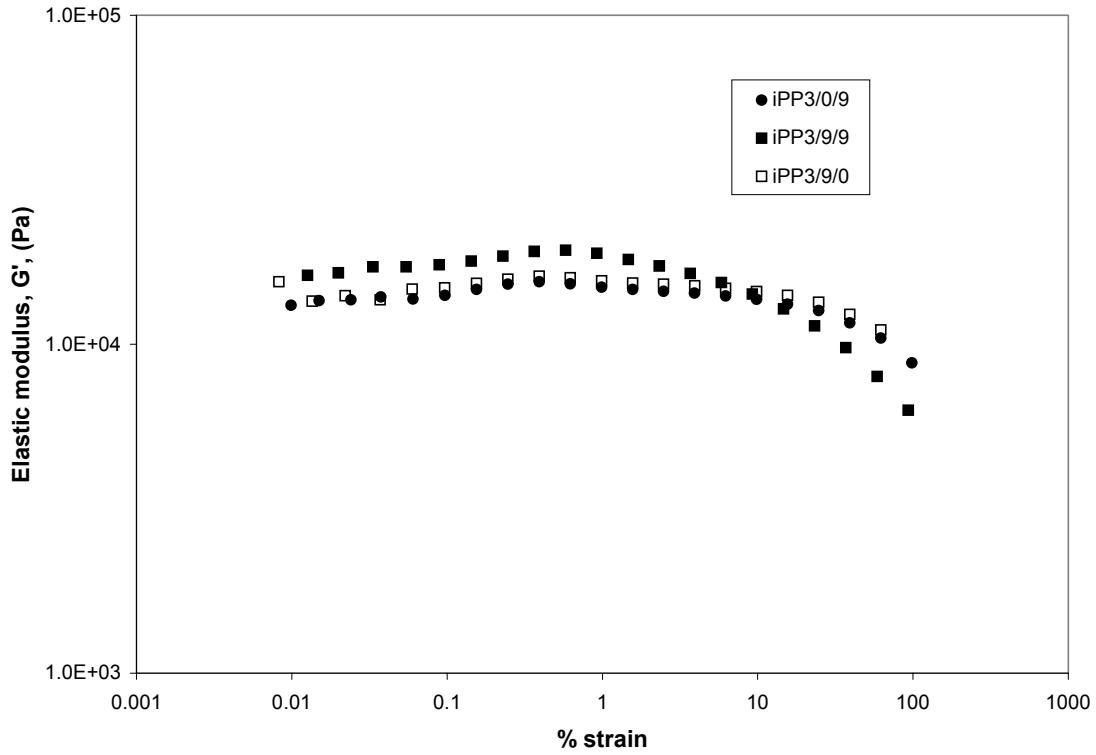

Figure 7.1. Dynamic strain sweep for iPP hybrids and matrix at T = 200^{o}C

As seen from the Figure 7.1, the non-linear regime starts at 10%, 10%, and 4% strain for the polymer matrix (iPP3/0/9), the uncompatibilized hybrid (iPP3/9/0) and the compatibilized (iPP3/9/9) hybrid, respectively. It is noteworthy that the non-linear regime starts at lower strain for the compatibilized hybrid sample compared to the matrix and the uncompatibilized sample. Further transient viscoelastic experiments were carried out below these strain limits to ensure linear response. Figure 7.2 shows the dynamic frequency sweep data for the polymer matrix (iPP3/0/9) and the uncompatibilized (iPP3/9/0) hybrid at 200^{o}C.

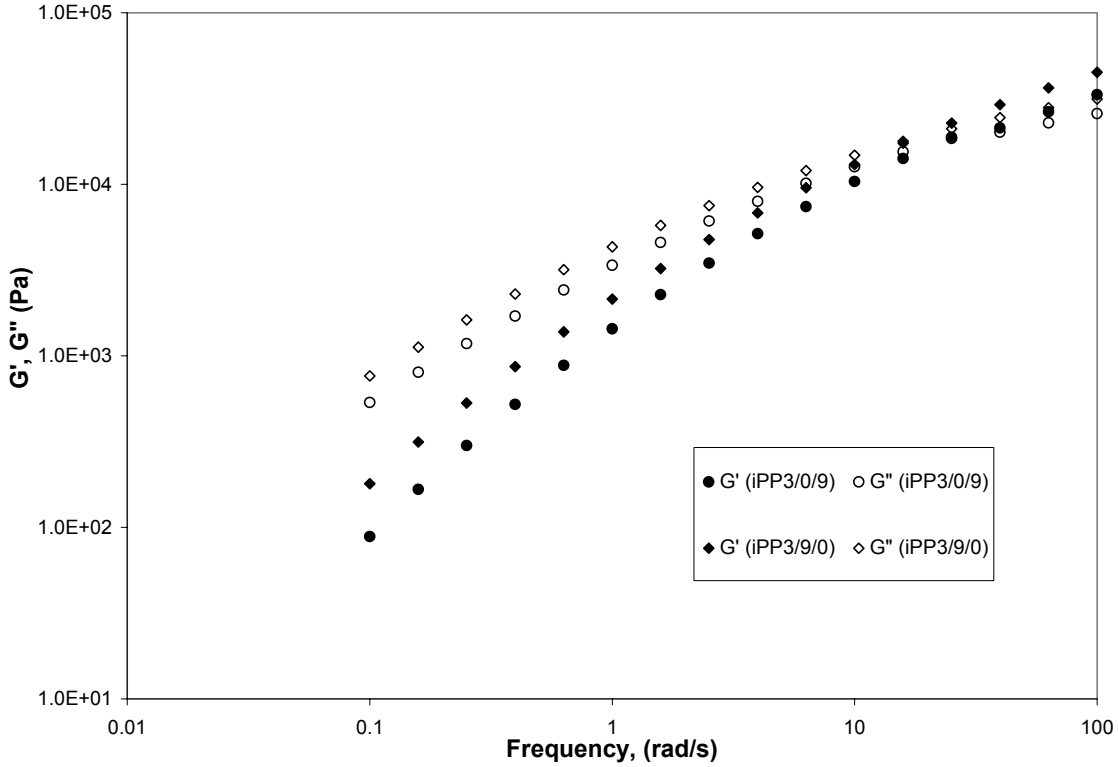

Figure 7.2. Dynamic frequency sweep for polypropylene matrix at T = 200^{o}C and γ_0 = 5%

The polymer matrix (iPP3/0/9) exhibits a classical viscoelastic behaviour viz., in the terminal region $G'' > G'$, and the slopes of G' and G'' were found to be 1.4 and 0.9, respectively. The values of the slopes of G' and G'' are expected to be 2.0 and 1.0 for monodisperse polymers and the deviation from these values may be attributed to the polydispersity of the commercial sample. For the uncompatibilized hybrid (iPP3/9/0) the corresponding values of the slopes of G' and G'' were 1.4 and 0.9 respectively. The

crossover frequencies are 15 and 25 rad/s, respectively, for the uncompatibilized hybrid (iPP3/9/0) and the polymer matrix (iPP3/0/9). Further, the G' and G'' for the uncompatibilized hybrid are not much higher than those for the matrix polymer. The compatibilized hybrid showed a distinctly different behaviour from the matrix polymer and the uncompatibilized hybrid (iPP3/9/9) as shown in the Figure 7.3. This highlights the crucial role played by the compatibilizer in the iPP nanocomposites.

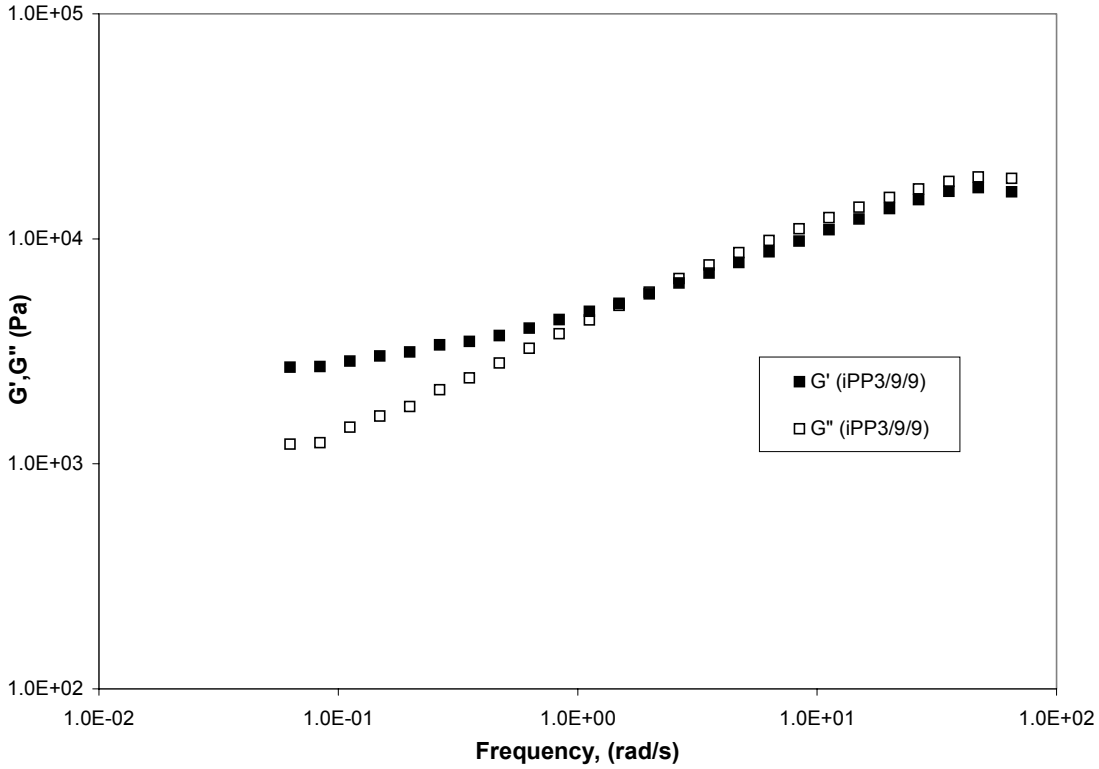

Figure 7.3. Dynamic sweep for compatibilized hybrid (iPP3/9/9) at T = 200°C, γ_0 = 0.5%

In contrast to the behaviour of the matrix or the uncompatibilized hybrids, for the compatibilized hybrid it was found that $G' > G''$ in the terminal regime and the terminal slopes of G' and G'' were much lower viz., 0.19 and 0.41, respectively. This implies weak frequency dependence, i.e., solid-like relaxation behaviour in the terminal regime. Also, the low frequency values of G' and G'' for the compatibilized hybrid were higher by almost by order of magnitude than those for the matrix and the uncompatibilized hybrids. With increase in frequency, the G'' crosses over G' so that over a range of intermediate frequency, $G'' > G'$ until a second crossover (not shown in the Fig. 7.3), after

which again $G' > G''$. The values of G' and G'' for the compatibilized hybrid at higher frequencies match with those for the polymer matrix and the uncompatibilized hybrid.

These trends indicate that for the compatibilized hybrid the viscoelastic response at the lower frequencies is dictated by the microstructure of the sample. However, at higher frequencies the polymer viscoelasticity dominates the response of the hybrid.

Complementary data in the time domain was obtained by performing stress relaxation experiments after a step shear strain. Based on the dynamic strain sweep data a step strain of 5 % was used for the uncompatibilized hybrid and the matrix polymer, while 0.5 % strain was used for the compatibilized hybrid to ensure linear viscoelastic regime. The uncompatibilized hybrid showed slightly higher modulus than the matrix, but apart from this the relaxation behaviour of both the uncompatibilized hybrid and the matrix were qualitatively similar. Both materials relaxed very rapidly. However, the relaxation behaviour of the compatibilized hybrid was different than the matrix and the uncompatibilized hybrid as shown in Figure 7.4. The relaxation modulus of compatibilized hybrid was only slightly higher than the matrix at short times but then relaxed much more slowly with time. The relaxation modulus G(t) seemed to reach a plateau values at t >300 s.

The above data suggests that the linear viscoelastic response of the compatibilized hybrid is significantly different than that of the matrix, while that of the uncompatibilized hybrid is similar to the response of the matrix. Large differences are particularly visible at low frequencies or at longer times. These results have motivated us to probe the microstructure of the hybrid under near quiescent conditions by performing creep experiments.

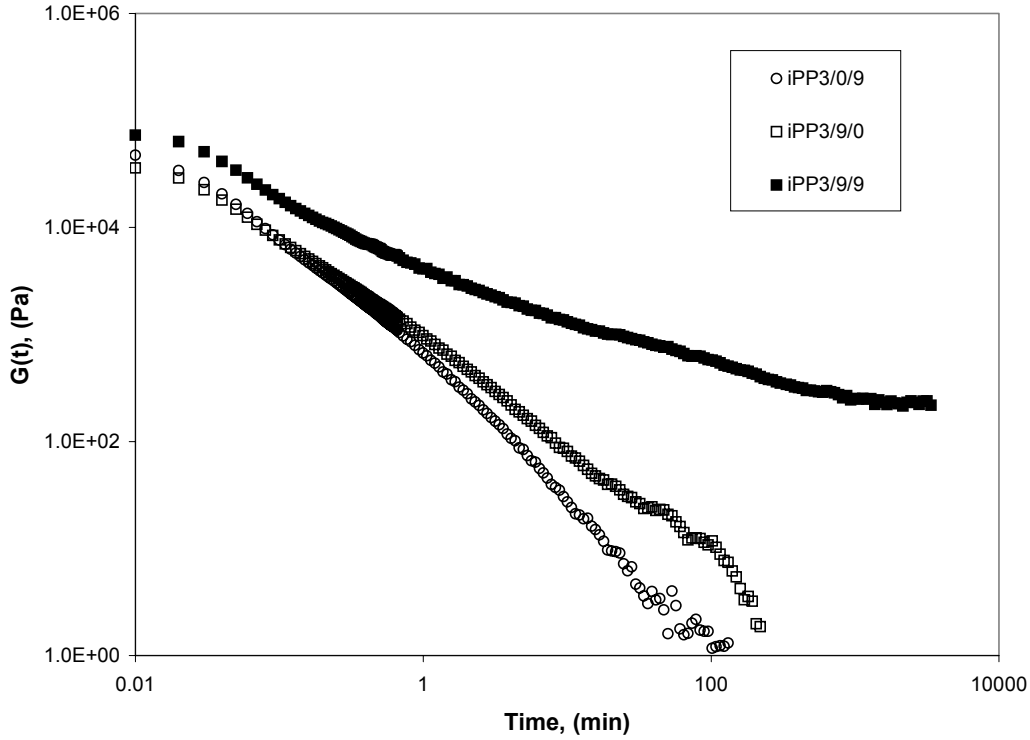

Figure 7.4. Stress relaxation after step strain for matrix polymer (iPP3/0/9), uncompatibilized (iPP3/9/0) and compatibilized (iPP3/9/9) hybrids at T = 200°C, γ_0 = 0.5%

7.1.2. Creep experiments of iPP nanocomposites

Figure 7.5 shows the creep behavior of two representative samples, uncompatibilized (iPP3/9/0) and compatibilized (iPP3/9/9) hybrids. The extruded samples were subjected to creep tests in the stress-controlled Bohlin rheometer at 200°C and creep compliance was recorded for a creep time of 180 s. Creep tests were done with time intervals of 10 min between subsequent tests for a total period of 3 hrs. As seen in Figure 7.5 the long time creep compliance (J_c) of (iPP3/9/0) increases linearly with creep time (t_c). The uncompatibilized hybrid (iPP3/9/0) material flows immediately even under small stress, resembling typical liquid like behavior. However the creep compliance of the extruded compatibilized hybrid (iPP3/9/9) was considerably lower than that of the uncompatibilized (iPP3/9/0) hybrid indicating more solid-like behaviour.

It is important to note that all hybrid samples, including the compatibilized hybrid do creep, which means they have a viscous response at long time. The most prominent difference between the compatibilized and the uncompatibilized hybrids is the significantly lower slope of the long time compliance for the compatibilized hybrid compared to the uncompatibilized hybrid. This indicates that the zero shear viscosity (η_o) of compatibilized hybrid is significantly higher than that of the uncompatibilized hybrid (see e. q. 2.14).

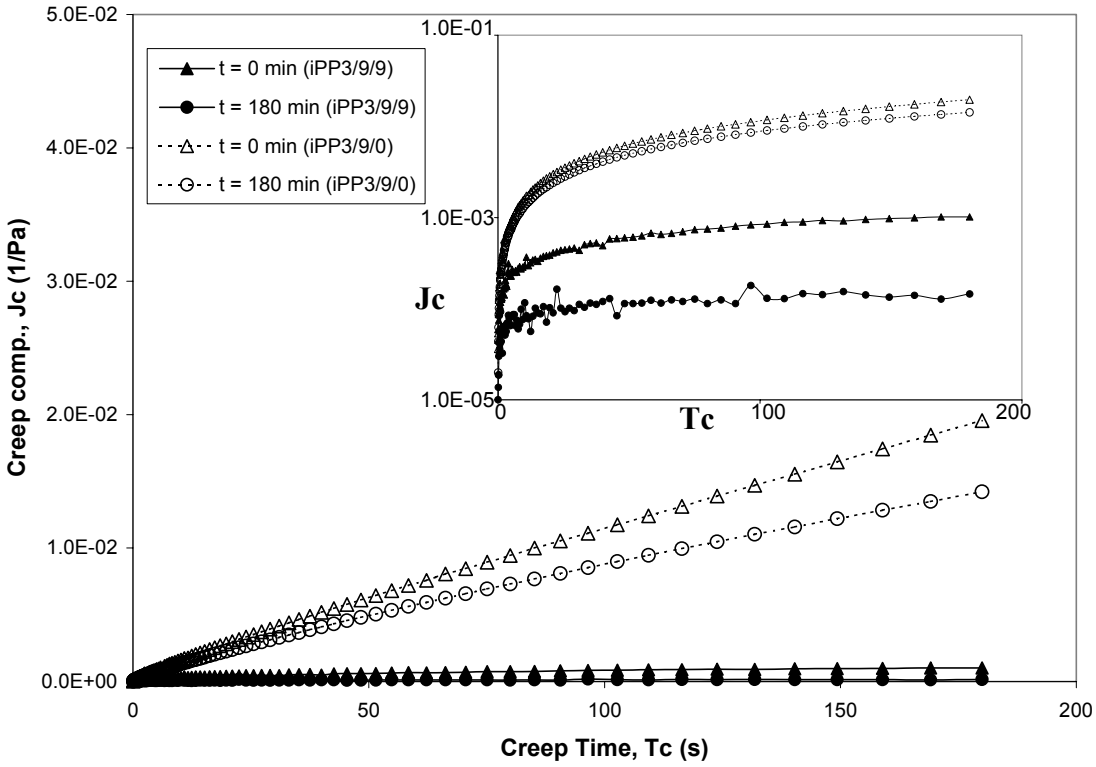

Figure 7.5. Creep data for uncompatibilized (iPP3/9/0) and compatibilized (iPP3/9/9) hybrids at T = 200°C, σ_o = 10 Pa

The inset in Figure 7.5 shows a semi-log plot of the same data. The plot shows two things: First, the creep behaviour of both types of hybrids is viscoelastic, i.e., a rapid jump in strain at short time, which a characteristic elastic behaviour, followed by a slow steady increase in strain with time, which is a viscous response. Second, the long time creep compliance of the compatibilized hybrid changes more significantly after 180 min of annealing compared to the corresponding change in the uncompatibilized hybrid.

The fact that the compatibilized hybrid creeps also agrees with the weak frequency dependence of the G' and G'' observed in the dynamic experiment, as shown in Figure 7.3. The creep behaviour and the weak frequency dependence suggests that at low stresses compatibilized hybrids behave like fluids with very high zero shear viscosity. If these were elastic solids, then G' and G'' would be independent of frequency.

The effect of annealing on creep behaviour is shown in Figure 7.6. It was found that the creep compliance of the compatibilized (iPP3/9/9) and the uncompatibilized (iPP3/9/0) gradually decreased to lower values during annealing period of 3 hrs.

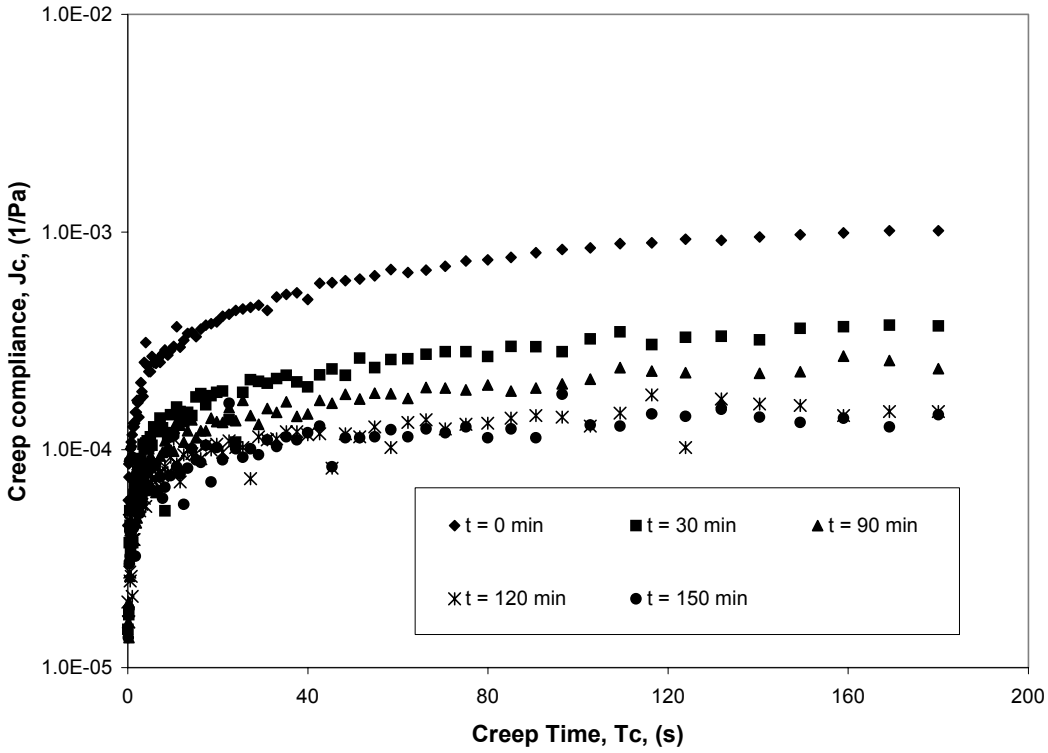

Figure 7.6. Creep compliance of the compatibilized hybrid with annealing time at T = 200°C, σ_o = 10 Pa

This suggests that though most of the microstructural changes have occurred during hybrid formation in the extrusion process, subtle microstructural evolution in the hybrids continues to occur under near-quiescent conditions during annealing. As seen from the Figure 7.6, the creep compliance becomes nearly independent of annealing time after 120 min of annealing.

Creep data also gives valuable information about the zero-shear viscosity. Figure 7.7 shows the zero shear viscosity for various iPP hybrids as a function of annealing time. The zero-shear viscosity of the polymer matrix slightly decreased with annealing times, while the viscosity of iPP hybrids (in the presence or absence of PPMA) increased continuously with annealing time. The viscosity of all hybrids increased more rapidly initially and tended to reach saturation value at longer times (typically in 2 to 3 hrs). Further, the viscosity of the compatibilized hybrids was always significantly higher than that of the uncompatibilized hybrids. The small decrease in the viscosity of the polymer matrix can be attributed to possible thermal degradation under the experimental conditions, while the increase in viscosity of the compatibilized (iPP3/9/9) and the uncompatibilized (iPP3/9/0) hybrids is indicative of the micro-structural changes occurring during annealing.

Figure 7.8 shows the zero shear viscosity (η_o) as a function of clay loading for the compatibilized (iPP3/9/9) and the uncompatibilized (iPP3/9/0) hybrids. It was observed that after a clay concentration of ~ 3-wt% the zero shear viscosity increased exponentially with a slope that is significantly higher for iPP3/9/9 as compared to that for iPP3/9/0.

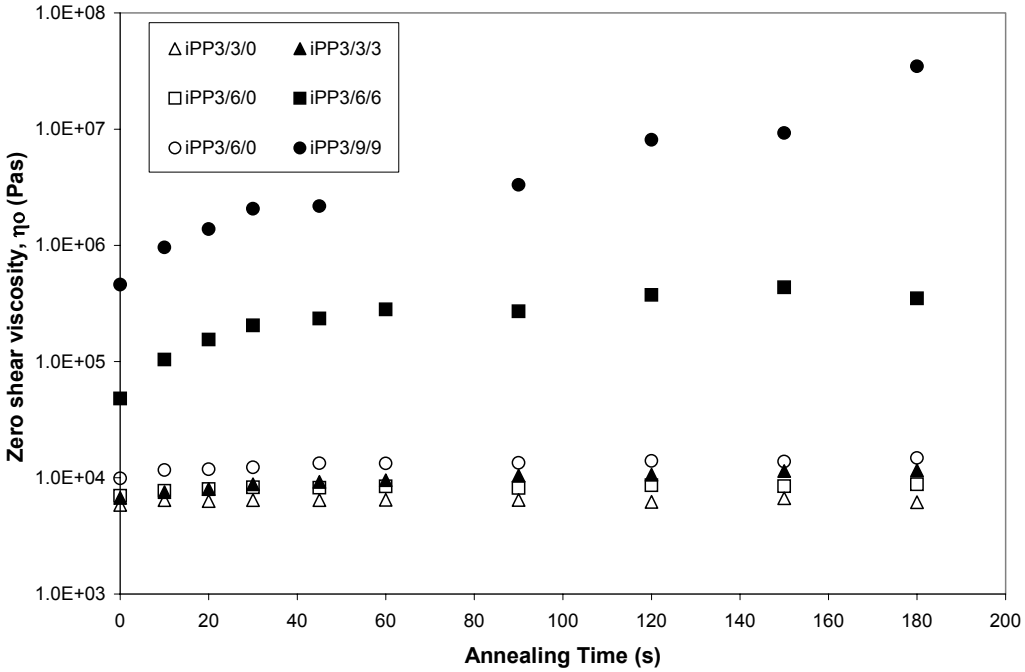

Figure 7.7. Zero shear viscosity as a function of annealing time for iPP hybrids at T = 200°C, σ_o =10 Pa

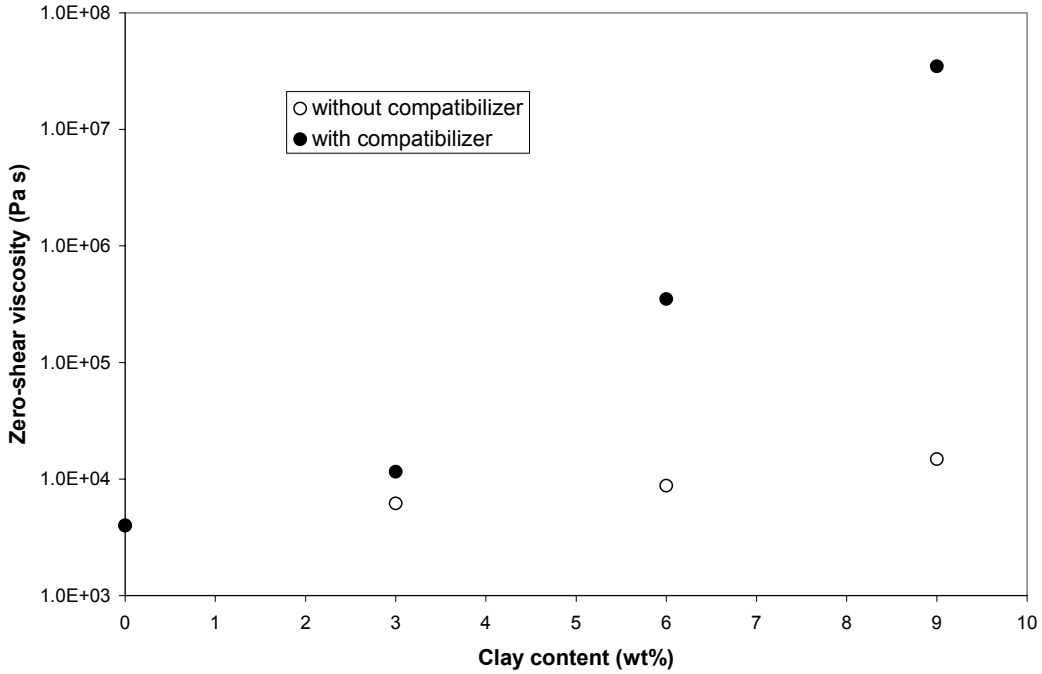

Figure 7.8. Zero shear viscosity as a function of clay loading at T = 200°C

7.1.3. Dynamic experiments during annealing

Figures 7.9 and 7.10 shows the time evolution of the elastic and viscous moduli respectively, for the compatibilized (iPP3/9/9) and the uncompatibilized (iPP3/9/0) hybrids which were subjected to small strain oscillatory shear tests every 10 minutes during their total annealing duration of 3 hrs in the Bohlin rheometer at 200^{o}C.

The low frequency elastic modulus of as-extruded (iPP3/9/9) was always higher than that of (iPP3/9/0). Further, whereas the elastic modulus of the uncompatibilized hybrid (iPP3/9/0) at low frequency decreased with annealing time, that of the compatibilized hybrid (iPP3/9/9) increased initially and then remained more or less unchanged. The viscous modulus also showed similar behavior as shown in Figure 7.10

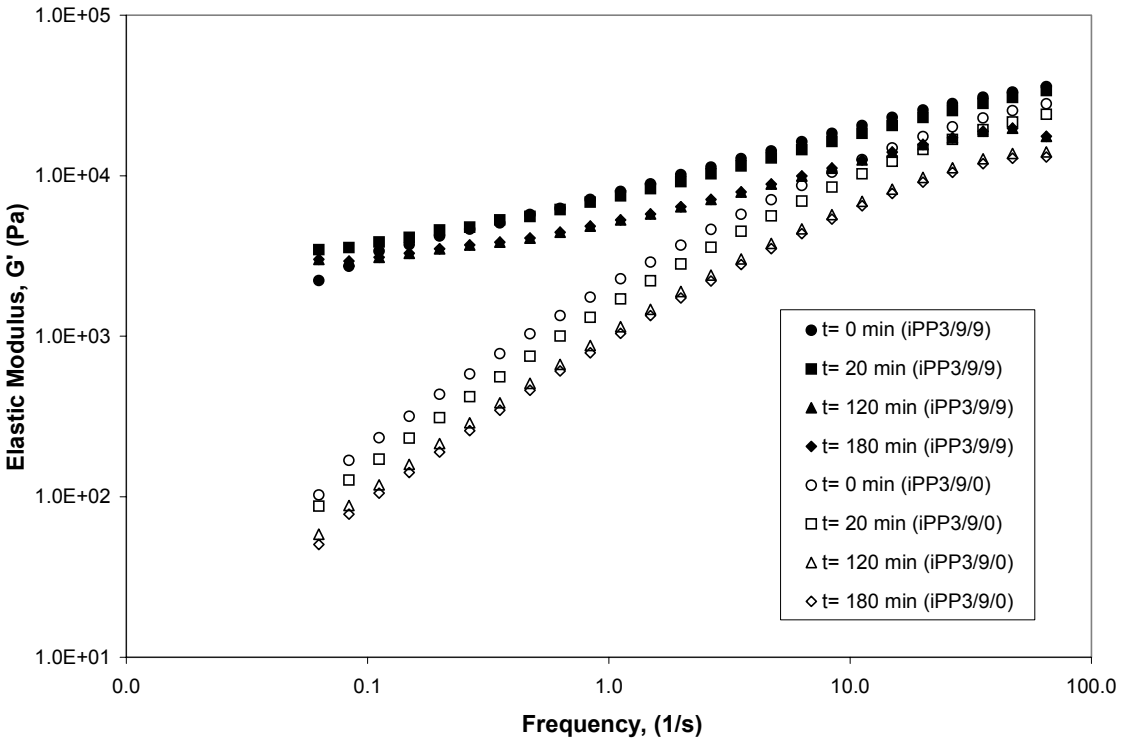

Figure 7.9. Elastic modulus of compatibilized and uncompatibilized iPP hybrids with annealing time at T = 200^{o}C

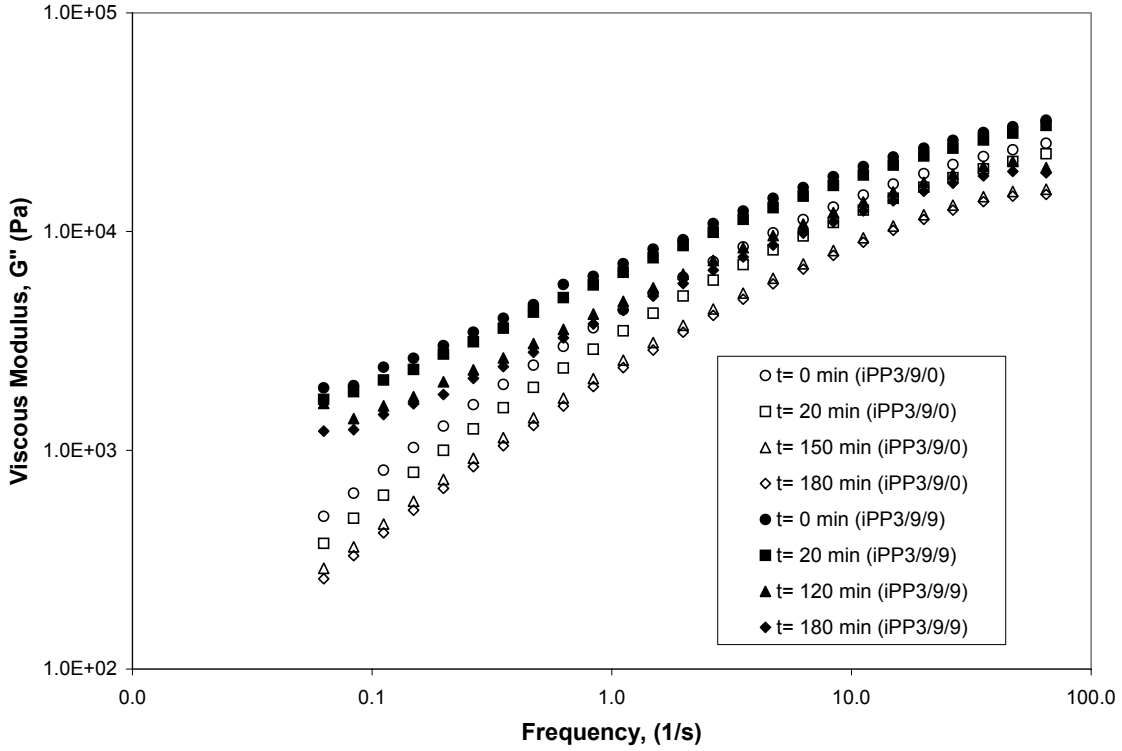

Figure 7.10. Viscous modulus of compatibilized and uncompatibilized iPP hybrids with annealing time at T = 200^{o}C

The elastic modulus of (iPP3/9/0) showed a near-terminal behavior ($G' \sim \omega^2$), while that of (iPP3/9/9) showed a distinct non-terminal response. The terminal slopes of G' and G'' for the different iPP nanocomposite samples are reported in Table 7.1 for the different annealing times. In case of the uncompatibilized hybrids, the slopes of G' and G'' slightly decreased with the increase in the clay content above 6-wt% clay. In the case of the compatibilized hybrids, the slopes of G' and G'' decreased above 3-wt% clay. In summary, the dynamic data compliments the creep data and is indicative of subtle microstructural changes occurring during annealing of the hybrids.

Prima facie it appears that the time evolution of the zero shear viscosity measured by creep experiments during annealing (see Fig.7.7) is different than the evolution of G' and G'' at low frequency (see Fig. 7.9 and 7.10). The zero shear viscosity increases significantly with time to reach a saturation value, while the G' and G'' either seem to remain unchanged or decrease slightly with annealing time. This apparent difference is possibly due to the fact that it has not been possible to probe the G' and G'' at very low

frequencies that are comparable to the low shear rates of the creep experiments. In principle it is possible to probe the response at very low frequencies by performing the dynamic experiments at high temperatures and then using time-temperature superposition (TTS) to shift the data to the desired lower temperature. However, it was found that PP is susceptible to degradation at high temperature and therefore annealing at high temperature was not feasible.

Table 7.1. Terminal slopes of G' and G'' for iPP hybrids

Sample	Time (hrs)	Terminal slope (Elastic modulus)	Terminal slope modulus)
iPP	T=0	1.41	0.89
	T=3	1.45	0.92
(iPP3/3/0)	T=0	1.28	0.85
	T=3	1.03	0.85
(iPP3/3/3)	T=0	1.18	0.82
	T=3	1.30	0.80
(iPP3/6/0)	T=0	1.27	0.83
	T=3	1.25	0.84
(iPP3/6/6)	T=0	0.66	0.64
	T=3	0.44	0.60
(iPP3/9/0)	T=0	1.06	0.77
	T=3	1.04	0.78
(iPP3/9/9)	T=0	0.42	0.48
	T=3	0.19	0.41

7.1.4. Discussion

The wide-angle x-ray diffraction (WAXD) data for the as-extruded uncompatibilized (iPP3/9/0) and the compatibilized (iPP3/9/9) hybrids shows that the clay peak shifts to lower 2θ values compared to the pristine clay (see Fig. 3.2 and Fig. 3.3). This shift is an

indication of intercalation, which must have occurred possibly by the combined effect of shear and diffusion of polymer chains in between the clay galleries. [1]

Interestingly, the amount of peak shift was found to be almost equal for both the compatibilized (iPP3/9/9) and the uncompatibilized (iPP3/9/0) hybrids. Thus the effect of the compatibilizer is not clearly evident in the WAXD. However, the compatibilizer has striking impact on the rheological behaviour of the compatibilized (iPP3/9/9) hybrid, as discussed earlier. Thus the PP-MA acts as an effective stress transfer agent between the matrix iPP and the clay tactoids.

One possibility is that the PP-MA does intercalate in the galleries; however, the gallery spacing of the organoclay is large enough to accommodate the comparatively low molecular weight compatibilizer chains without increasing the intergallery distance further. In the light of the characteristic surface charges of the montmorillonite clay (i.e., negatively charged gallery surfaces and positively charged edge groups), a second possibility is that the anhydride group of PP-MA interacts with the silanol (Si-OH) groups present only on the edges of the clay tactoids. Thus, the use of PP-MA in iPP nanocomposite does not lead to significant increase in the intergallery distance, as evident by the WAXD, but would still facilitate effective stress transfer between the clay and the matrix, as evident by rheology. Thus, in a way, rheology provides for a sensitive tool that can compliment XRD and TEM to understand the microstructure of polymer nanoclay composites.

The high temperature WAXD data for both the compatibilized (iPP3/9/9) and the uncompatibilized (iPP3/9/0) hybrids as a function of annealing time showed a decrease in peak intensity accompanied by slight peak broadening. As it was discussed in chapter 6, a calculation based on the Scherrer's formula (see e. q. 2.5) suggests that 4-5 platelets in the clay tactoid at time (t= 0 min) decreased to about 3, after 3 hrs annealing. This suggests that quiescent annealing of the hybrids perhaps causes platelets from the edges of the tactoids to disperse into the melt. There is no difference in peak positions between the compatibilized (iPP3/9/9) and the uncompatibilized (iPP3/9/0) hybrids as a function of annealing time, and infact, the first peak shifts to the higher 2θ values with annealing. This might be due to the possible degradation of the organic modifier at higher temperatures.

The subtle microstructural changes during annealing as detected by WAXD seem to have large effects on the rheological response of the hybrids. As shown in Figures 7.6 and 7.7, the creep compliance decreases and the zero shear viscosity increases significantly on annealing. As will be discussed later, the slow edge exfoliation of the platelets could possibly cause the large increase in the zero shear viscosity of the hybrids. In summary, the rheological response of the compatibilized hybrid showed large differences from that of the uncompatibilized hybrids. Creep experiments, in particular, were found to be very sensitive to microstructural changes occurring in the melt. The continuous variation of creep compliance with time is distinct and easy to measure.

The rheological data presented earlier suggests a solid–like response or rather a very high viscosity response of the compatibilized hybrids at the lower frequencies, lower stresses and longer times. There can be two different possibilities for explaining the observed solid-like behavior of the PP nanocomposites and indeed of any PLS nanocomposites in general. One hypothesis could be that the solid-like rheological behavior arises from the confinement of polymer chains within the silicate layers. [2-3]

Lugenos et. al. studied the dynamics of polymer melt using Surface Force Apparatus (SFA), in which the melt confined between parallel mica plates, separated by distances ranging from 200 nm–10 nm could be sheared. [4] They reported pseudo-solid like behavior of the polymer melt with increasing confinement of polymer chains from 350 nm to 10 nm as shown in the Figure 7.11. In particularly, the plateau of $G^{'}$ at small gaps (~ 10 nm) looks similar to the low frequency plateau of the $G^{'}$ seen in Figure 7.3.

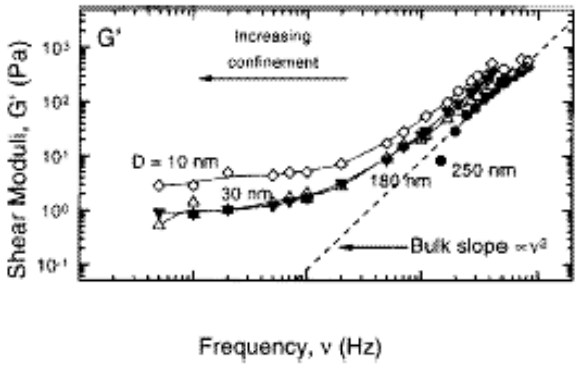

Figure 7.11. Effect of confinement on the modulus of polymer melt (Reprinted with permission from Lugenous et. al. [13] copyright © 97 American chemical society)

It has been also observed that the viscosity of confined polymer melts is greater than that of bulk chains. The large viscosity of confined melts is believed to arise from an "immobilized hydrodynamic layer" near the wall having a thickness of the order of radius of gyration (R_g) of the polymer chain. Similarly, the pseudo solid-like behaviour of PLS nanocomposites might be due the confinement of polymer chains in the silicate layers.

According to a scaling model of Semenov and Doi for shear flow of melts confined between parallel plates separated by a distance $h/a \sim N^{1/2}$, where a is the segment length and N is the number of segments in the polymer chain, the relative zero-shear viscosity of the confined melt (η_o^c) with respect to the bulk viscosity (η_o^b) can be given as

$$\frac{\eta_o^c}{\eta_o^b} \sim \frac{a}{h}\frac{\lambda^c}{\lambda^b} \sim \left(\frac{h}{a}\right)^2 \quad for\ \lambda^c/\lambda^b \sim (h/a)^3 \tag{7.1}$$

Here, λ^c and λ^b are segment relaxation times of the confined and bulk polymer chains, respectively. Thus the scaling model predicts that if $\lambda^c >> \lambda^b$ and if the separation distance were of the order of radius of gyration of the polymer chain (as is typically the situation for exfoliated hybrids), then the zero-shear viscosity of the confined system would scale as N, which is typically of the order of 100 in commercial polypropylene resins. Thus, the viscosity of a confined melt can be several times that of the bulk viscosity.

The underlying physics for the increased viscosity of confined polymers is the slow relaxation of such chains arising from a larger barrier for segmental motions in the confined space, particularly very close to the boundaries. The confinement of polymeric molecules is expected to create an energetic barrier for the reptation motion of chains and this will retard the molecular relaxation process. Thus the confinement may lead to shift of terminal relaxation to very low frequency. Hence, if the observed increase in the zero-shear viscosity of polymeric-layered silicate nanocomposites were a signature of the larger barrier for flow of confined chains, then the flow activation energy for nanocomposites should be significantly higher than that for bulk polymer.

The flow activation energy of iPP nanocomposites from creep data obtained at various temperatures as shown in Figure 7.12.

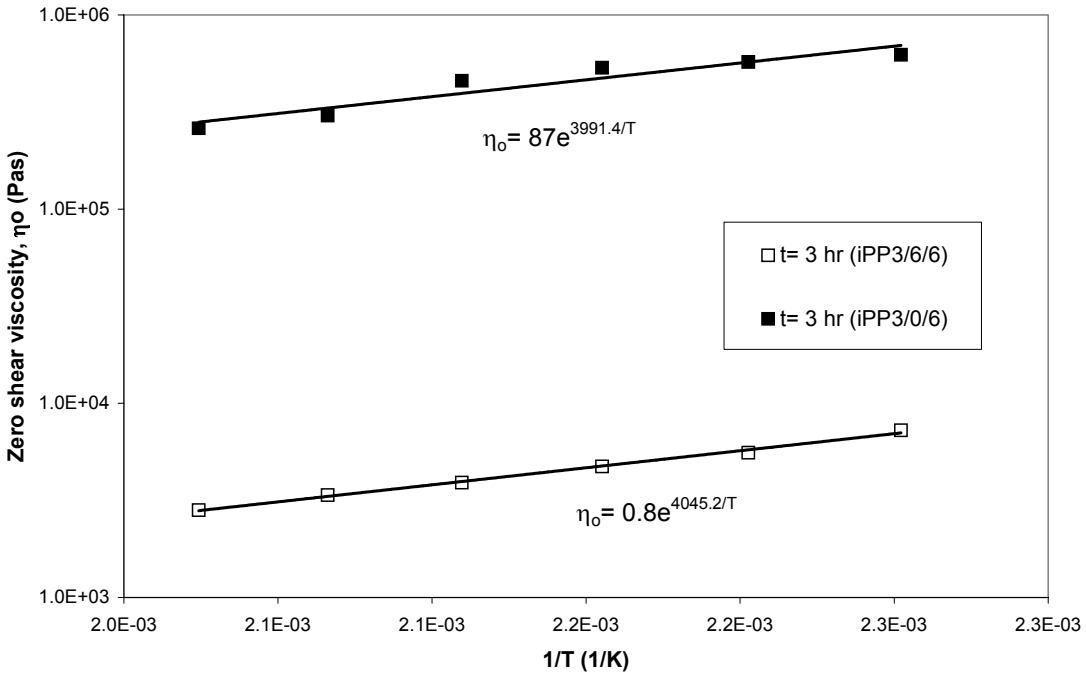

Figure 7.12. Arrhenius plot of zero shear viscosity as a function of temperature

It is seen that the activation energy of the (iPP3/6/6) sample (~ 33 kJ/gmol) is nearly the same as that of the PP/PP-MA matrix or of PP homopolymer (~35 kJ/gmol). [5] This indicates that the highest energy barrier for flow in the nanocomposites is the same as that in the bulk polymer, which is analogous to the finding by Vaia et. al. that the activation energy for diffusion during intercalation was nearly equal to that for self-diffusion in the bulk. [6,7] This suggests that the pseudo solid–like behaviour observed for the compatibilized hybrid does not originate from the confinement of the polymer chains in silicate layers.

The other possibility for the solid-like rheological behavior of the hybrids is that such a response can arise from frictional interactions between the anisotropic clay crystallites. These interactions can become particularly significant at higher clay contents, i.e., above a percolation limit, where the viscosity would depend rather strongly on clay loading. As discussed in chapter 2, the silicate layers are highly asymmetric materials with high aspect ratio (D/t=1000) and hence, can form a percolating network of hydrodynamically interacting silicate layers even at lower clay concentrations. The viscosity of such filled materials scales exponentially with the filler concentration (see e.

q. 2.37 and 2.38). Such a strong dependence of the zero shear viscosity on the clay loading in our materials has been observed, as shown in Figure 7.8.

In summary, two different possibilities namely, the effect of confined melts within clay layers and the effect of frictional interactions between anisotropic clay crystallites, were investigated, both of which could result in a solid-like response of PLS nanocomposite melts. The activation energy data clearly shows that the major influence is due to the frictional interactions of the silicate layers.

The exfoliated silicate layers might induce inter-crystallite frictional interactions during shearing deformations by hydrodynamically 'bridging' different crystallites and thus creating a percolating network that resists flow. The increase in the concentration of such exfoliated platelets could intensify the network structure causing an increase in the zero shear viscosity. In the light of the annealing studies, it is possible to understand the effects of the slow edge exfoliation observed by HT-WAXD on the zero shear viscosity.

Several reports in the literature contemporary to the present work also provide convincing evidence for the presence of a percolating network structure in PLS nanocomposites. [8-11] Ren et. al. have shown using model monodisperse polystyrene-polyisoprene diblock copolymer that the rheology of PLS nanocomposites was affected more by the mesoscopic structure of the hybrid and not by the chemical nature of the polymer. [9] Small amplitude dynamic measurements indicated a solid-like response for time scales of the order of 10^3 s and it was shown that the confined polymer chains within the galleries of the nanoclays did not contribute significantly to the rheological properties of the composite. It was suggested that clay tactoids containing ~ 30 platelets at loadings in excess of 6.7 wt% would form a percolating network as a result of physical jamming, which then offers considerable resistance to deformation and hence nanocomposites are believed to exhibit the solid-like behavior. As seen from Figure 7.8, network formation seems to occur even for 3-wt% loading for the clays used in this work. For 9-wt% compatibilized (iPP3/9/9) hybrid, an average tactoid size calculated by Scherrer's formula is ~ 10 nm, implying a minimum stacking of 3 silicate platelets (3.4 nm is the intergallery spacing). Further, this tactoid size implies, that the effective anisotropy associated with the clay tactoids is ~ 100. Calculations using e. q. 3.1 for iPP3/9/9 suggest that a percolating network can be formed even for a volume fraction (ϕ) ~ 1.5%.

Solomon et. al. reported the transient response of polypropylene nanocomposites in a shear start-up experiment in which a varying rest period was allowed after a large initial pre-shear in the reverse direction. [11] They observed increasing overshoot with annealing time indicating microstructural changes during the quiescent period. Further, the transient stress scaled linearly with the clay loading and with the effective strain, which again suggest a solid-like response due to a percolating non-Brownian network.

Finally, it may be noted that the solid-like response of nanocomposite melts is observed in an equally striking manner for both well defined end-tethered polymer-clay hybrids such as the polycaprolactone nanoclay composites described by Krishnamoorti et. al. [10,12] as well as for the nanoclay composites in which the matrix chains, although not directly end tethered to the clay surface, still interact with the clay via compatibilizing polymer chains, as described in this work.

7.2. Syndiotactic polypropylene (sPP) nanocomposites

7.2.1. Linear rheology of sPP nanocomposites

Nanoclay composites made from syndiotactic polypropylene of different molecular weights and clay concentrations and containing isotactic polypropylene grafted with malefic anhydride (PP-MA), as a compatibilizer were prepared by melt intercalation. Sample nomenclature and compositions are listed in Table 3.3. Kaempfer et. al. have shown that sPP nanocomposites prepared by melt intercalation in the presence of iPP-g-malefic anhydride copolymer (PP-MA) as a compatibilizer have a complex microstructure. [13] The compatibilizer is incompatible with the sPP matrix and forms immiscible domains of the order of 50-100 nm in the blend. In the presence of clay, the PP-MA copolymer intercalates within the silicate galleries and encapsulates the clay tactoids to form nanoparticles of core/shell morphology. These nanoparticles are then dispersed in the sPP matrix to form a nanocomposite. Thus, the microstructure of layered silicate sPP nanocomposites is more complex than that of conventional iPP based nanocomposites. However, the sPP nanocomposites show characteristic rheological

features similar to the intercalated iPP nanocomposites, as shown in Figure 7.13, 7.14 and 7.15.

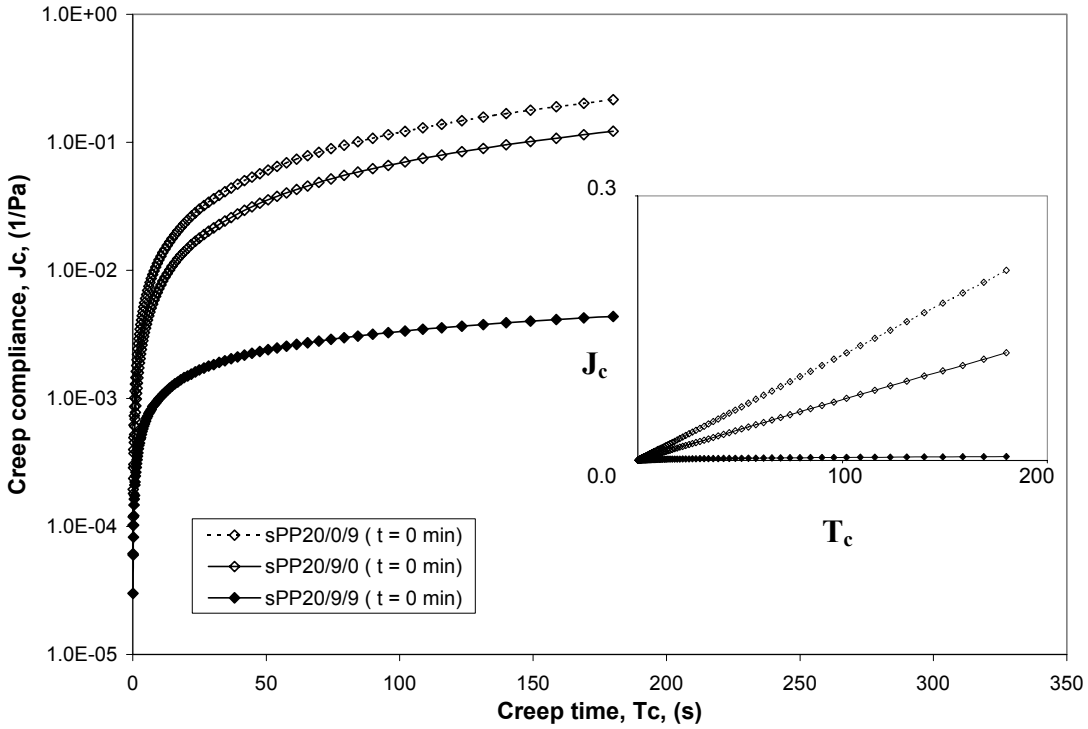

Figure 7.13. Creep compliance of sPP (MFI= 20) nanocomposites at T = 190°C, σ_o = 10 Pa

Figure 7.13 shows characteristic viscoelastic creep response of the matrix polymer (sPP20/0/9), the uncompatibilized (sPP20/9/0) and the compatibilized (sPP20/9/9) samples. The semi log plot of the creep compliance shows rapid initial increase in the creep compliance followed by a slow increase at longer times. The creep compliance of sPP20/9/9 was significantly lower than that of the matrix (sPP20/0/9) and the uncompatibilized (sPP20/9/0) samples suggesting solid like behavior of the compatibilized hybrid. Yet, the small but finite slope of J(t) – time data at long times indicates a viscous behaviour of large zero shear viscosity. The inset shows the same data plotted on linear-linear scale, for which the large differences in the slope of the long time compliance data are more clearly visible.

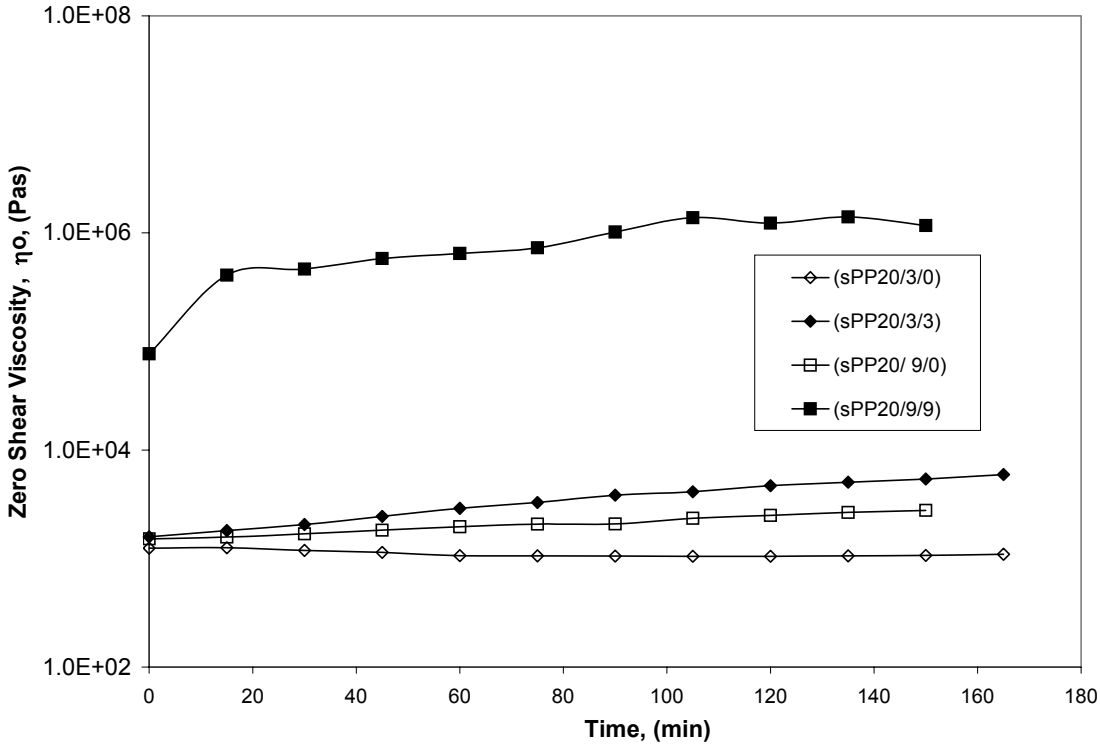

Figure 7.14. Transient creep response of sPP (MFI=20) nanocomposites at T = 190°C, σ_o = 10 Pa

As shown in Figure 7.14 the zero shear viscosity of sPP nanocomposite (sPP20/9/9) increases with annealing time indicating that some microstructural changes are occurring as a function of time during the annealing process. Figure 7.15 shows the plots of η_0 vs clay loading for compatibilized sPP20 nanocomposites of increasing clay loadings (sPP20/0/0, sPP20/3/3, sPP20/6/6, sPP20/9/9 and sPP20/25/25). The data shows that the zero-shear viscosity of the nanocomposites scales exponentially with the silicate loading.

7.2.2. Effect of sPP molecular weight on the zero shear viscosity

We have seen that the compatibilized hybrid shows significantly higher zero shear viscosity compared to the uncompatibilized hybrid and the matrix polymer (see Fig 7.7)

Figure 7.16 shows variation of zero shear viscosity of sPP nanocomposites, of the same clay loading but of different molecular weight sPP resins with annealing time.

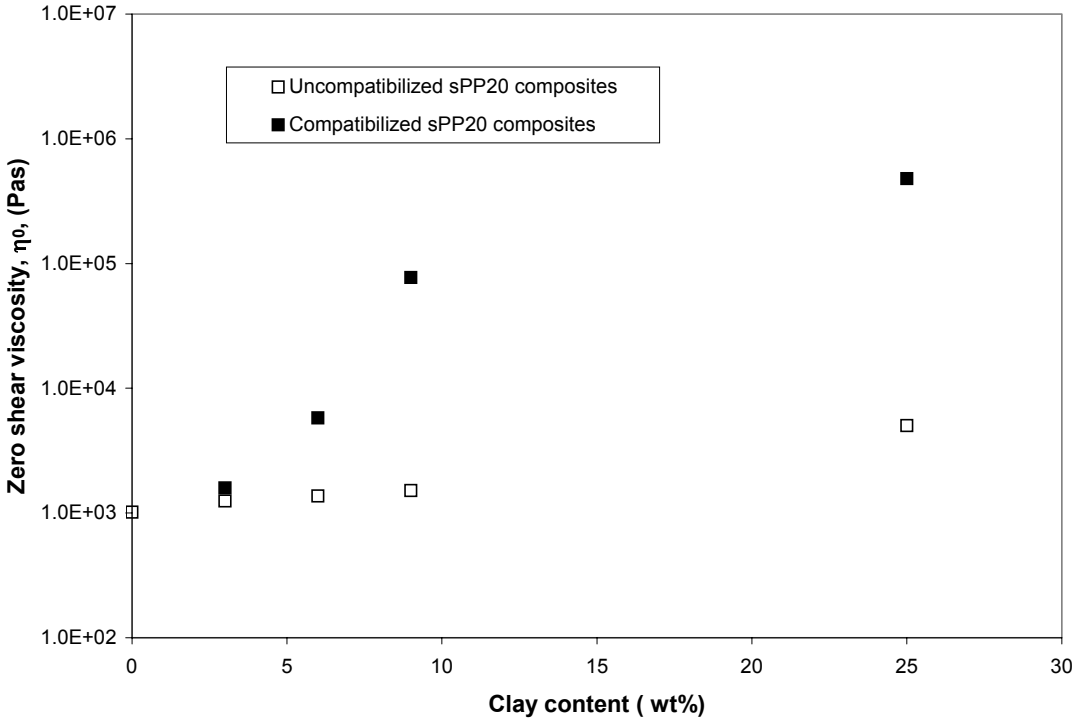

Figure 7.15. Zero shear viscosity of sPP (MFI = 20) nanocomposites as a function of clay concentration variation at T = 190^{o}C

As expected, the polymer matrix of lower molecular weight (sPP20/0/9) shows lower zero shear viscosity compared to the matrix with higher molecular weight (sPP4/0/9). However, the zero shear viscosity (η_o) of the nanocomposite made from the lower the molecular weight resins (sPP20/9/9) was found to be higher than the zero shear viscosity (η_o) of the nanocomposite with higher molecular weight resin (sPP4/9/9). It is possible that the smaller chains of a matrix having lower viscosity would diffuse into the primary particles of the clay at a faster rate, leading to better dispersion and hence higher η_o value. This indicates that the zero shear viscosity (η_o) of the nanocomposites is greatly determined by the microstructure of the percolating network of the clay tactoids and not so much by the zero shear viscosity (η_o) of the matrix.

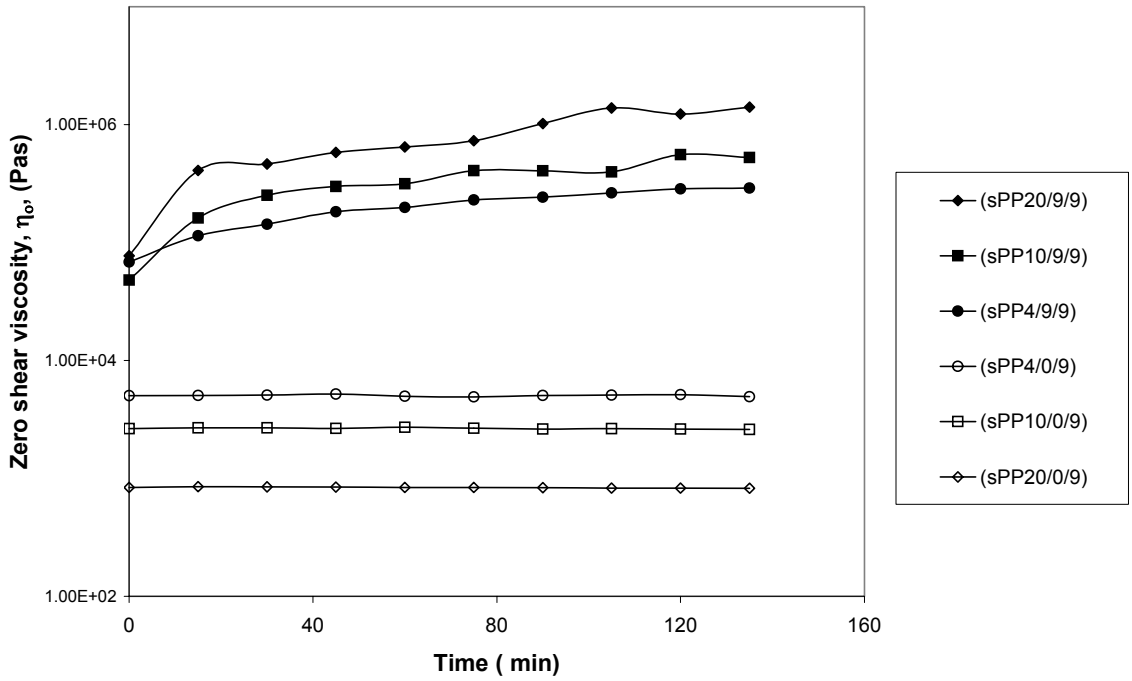

Figure 7.16. Transient creep response of sPP nanocomposites with different molecular weight matrix at T = 190^{o}C

7.2.3. Dynamic experiments

Dynamic strain sweep experiments were performed to identify the frequency over which the material would give a linear response in the dynamic frequency sweep tests. Figure 7.17 shows the storage modulus obtained from strain sweep tests on three samples viz., the matrix polymer (sPP20/0/9), the uncompatibilized hybrid (sPP20/9/0) and compatibilized (sPP20/9/9) hybrid. The transition from the linear to the non-linear regime, as characterized by the rapid decrease in G', occurs at about 60% strain for the matrix polymer and the uncompatibilized hybrid. For the compatibilized hybrid the transition occurs much earlier, at 1% strain. Further, rheological characterizations in the linear regime were done at 0.5% strain for the compatibilized hybrids and at 5% strain for the uncompatibilized and the matrix samples.

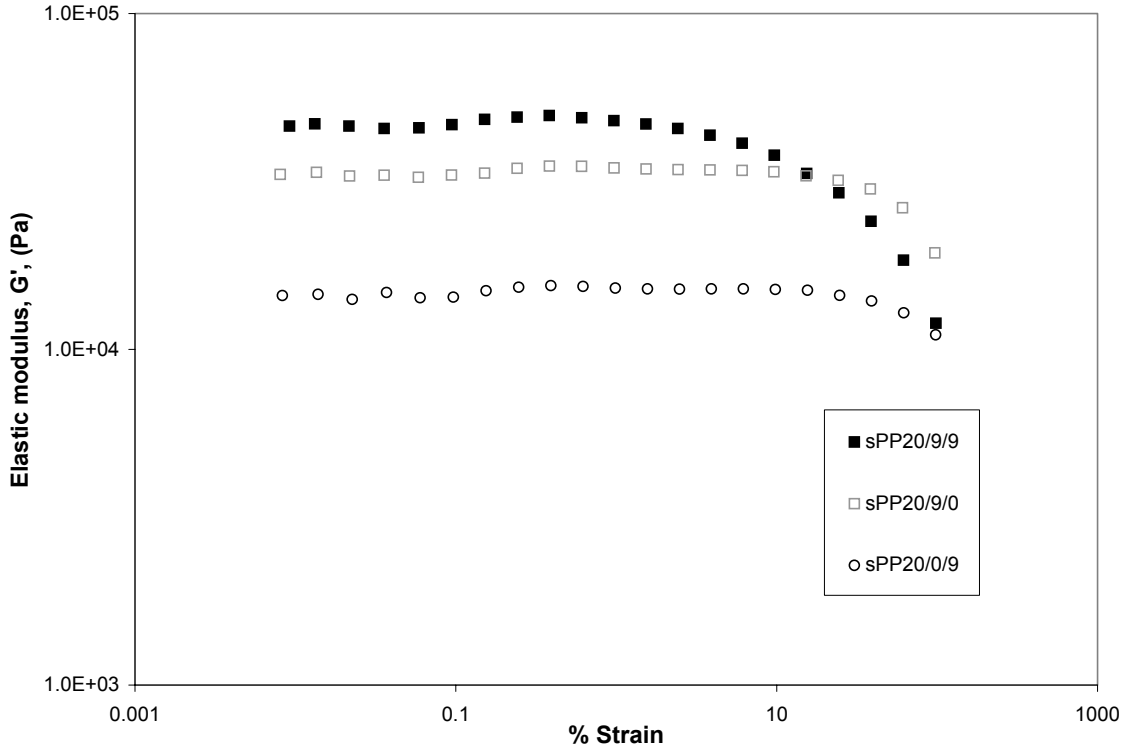

Figure 7.17. Strain sweep data for matrix polymer (sPP20/0/9), uncompatibilized (sPP20/9/0) and compatibilized hybrids (sP20/9/9) at T =170^{o}C

The master curves of small amplitude frequency-sweep dynamic experiments on the three samples are shown in Figure 7.18, 7.19 (a) and (b). The terminal slopes of $G^{'}$ and $G^{"}$ vs. frequency data from the mastercurves in the terminal region are listed in Table 7.2. The matrix polymer shows classical viscoelastic behavior namely, a terminal regime at low frequency ($G"\sim \omega, G^{'} \sim \omega^2$) with $G^{'} < G^{"}$, followed by a crossover at 100 rad/s, after which $G^{'} > G^{"}$. The uncompatibilized hybrid shows a small deviation from the classical behavior in that the slopes of $G^{'}$, $G^{"}$ in the terminal zone are less than 2 and 1, respectively. $G^{'}$ is still less than G'' at lower frequencies and a crossover is observed at 37 rad/s. The behavior of the compatibilized nanocomposite is distinctly different. At low frequency, $G' > G''$ and both $G^{'}$ and $G^{"}$ show a distinct non-terminal plateau-like behaviour. In the intermediate frequency range, there is a crossover at a frequency of 0.2 rad/s into a regime where $G' < G''$, and then there is a crossover again at a frequency of 100 rad/s where $G' > G''$. The non-terminal behaviour of the compatibilized

nanocomposite is similar to that reported earlier for iPP and other intercalated PLS nanocomposites. [9-12] The plateau is suggestive of a solid-like response at time scales longer than at least 1000 s. The first crossover in the intermediate frequency range is an indication of a transition to viscous response. At high frequency, the values of G' for all the three samples are similar indicating that segmental motions of the polymer matrix dictate the material response at short time scale. Thus, the second crossover for the compatibilized sample represents a typical elastic response arising from the matrix polymer.

Table 7.2. Terminal slopes of G' and G'' for sPP hybrids

	Matrix polymer (sPP20/0/9)	**Uncompatibilized hybrid (sPP20/9/0)**	**Compatibilized hybrid (sPP20/9/9)**
G'	1.7	1.2	0.02
G''	0.98	0.96	0.13

The small amplitude frequency-sweep dynamic experiments were performed on the same sample at different temperatures (170-210^{o}C). The master curves were generated by applying only horizontal shifts. The quality of shift is poor for the compatibilized hybrid.

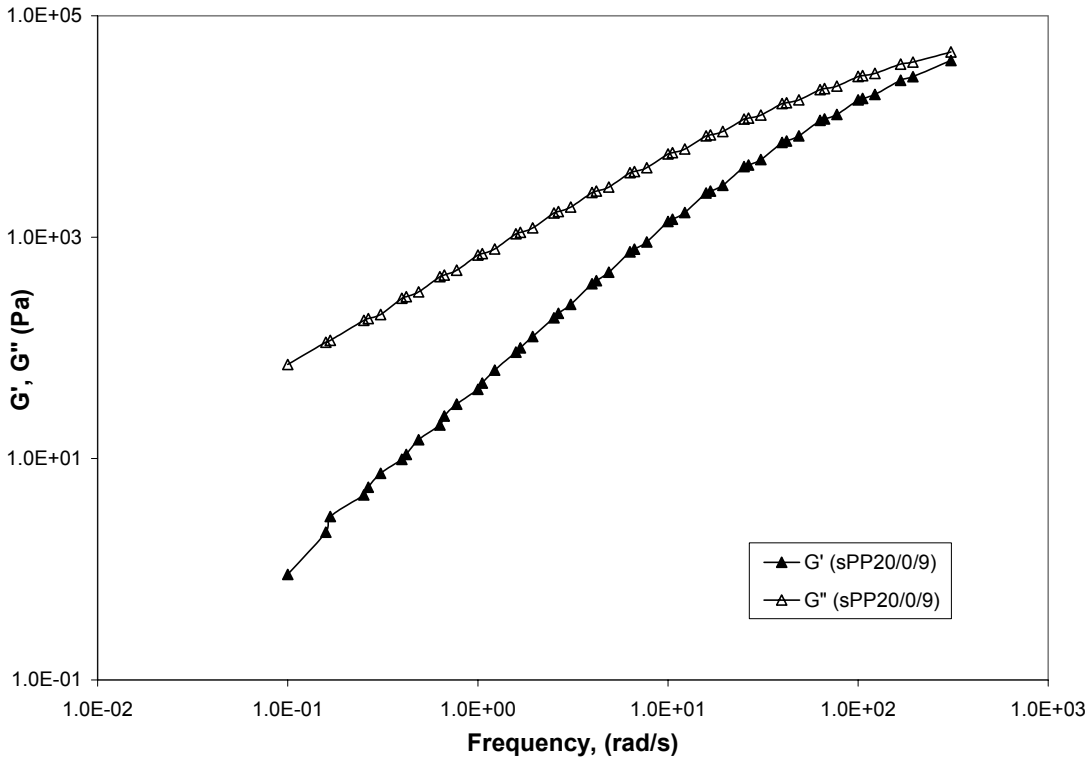

Figure 7.18. Mastercurve of the frequency sweep data for matrix polymer (sPP20/0/9) shifted to T = 170^{o}C

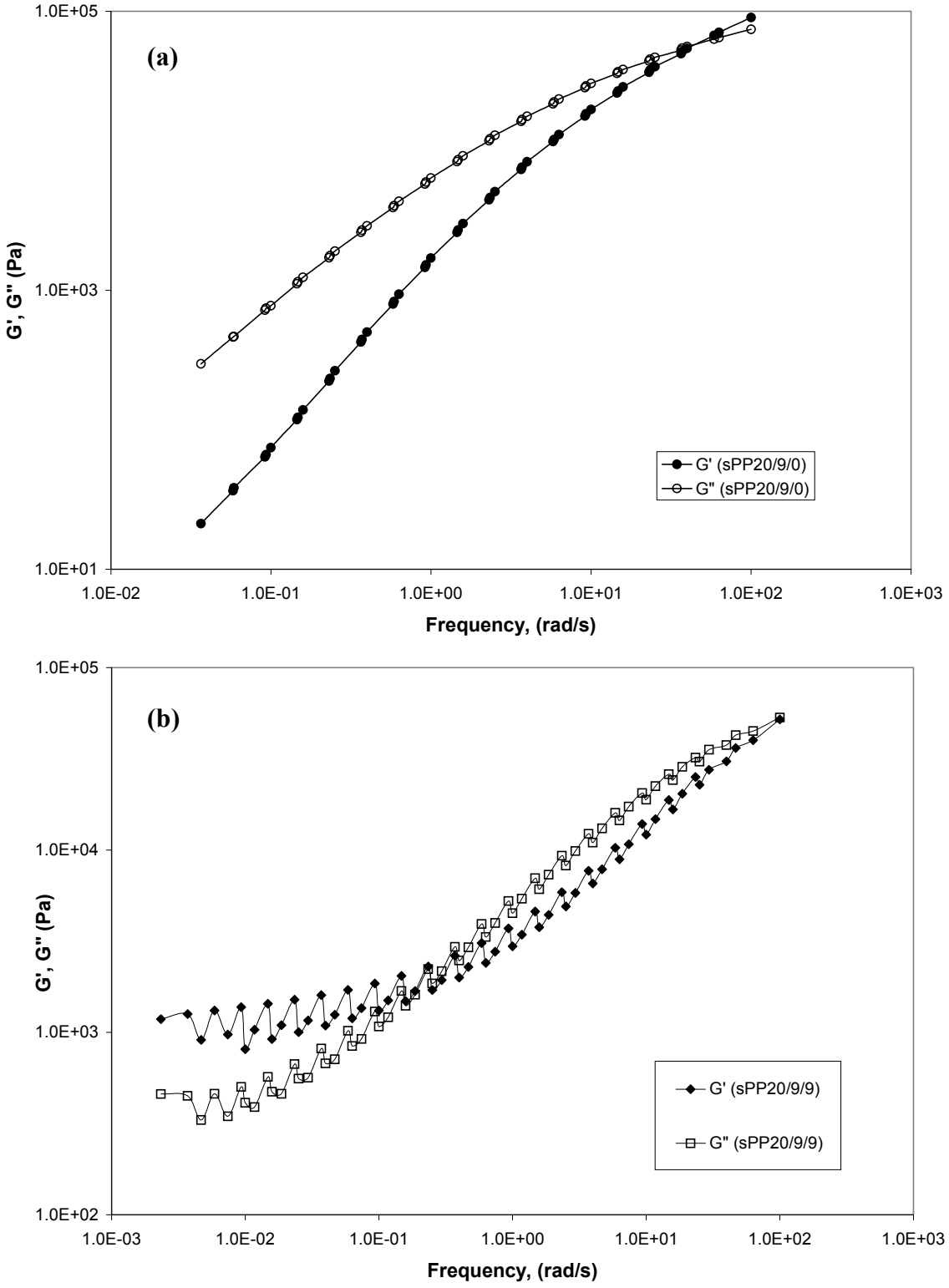

Figure 7.19. Mastercurve of the a) frequency sweep data for uncompatibilized hybrid (sPP20/9/0) b) frequency sweep data for compatibilized hybrid (sPP20/9/9) at T = 170°C

This might be due to the microstructural changes occurring in the sample during the frequency tests even though an initial annealing of 2 hrs was performed on the sample before the tests. This annealing time period was arrived at based on the changes observed in the zero shear viscosity as shown in Figure 7.16. The shift factors a_T are shown in Fig.7.20 as a function of temperature. The activation energy of the compatibilized hybrid (sPP20/9/9), 65 KJ/mole, was found to be slightly higher compared to that for both the uncompatibilized and the matrix samples (45 KJ/mole). Given the quality of the mastercurve it may be concluded that the temperature dependence of a_T is similar for all three samples.

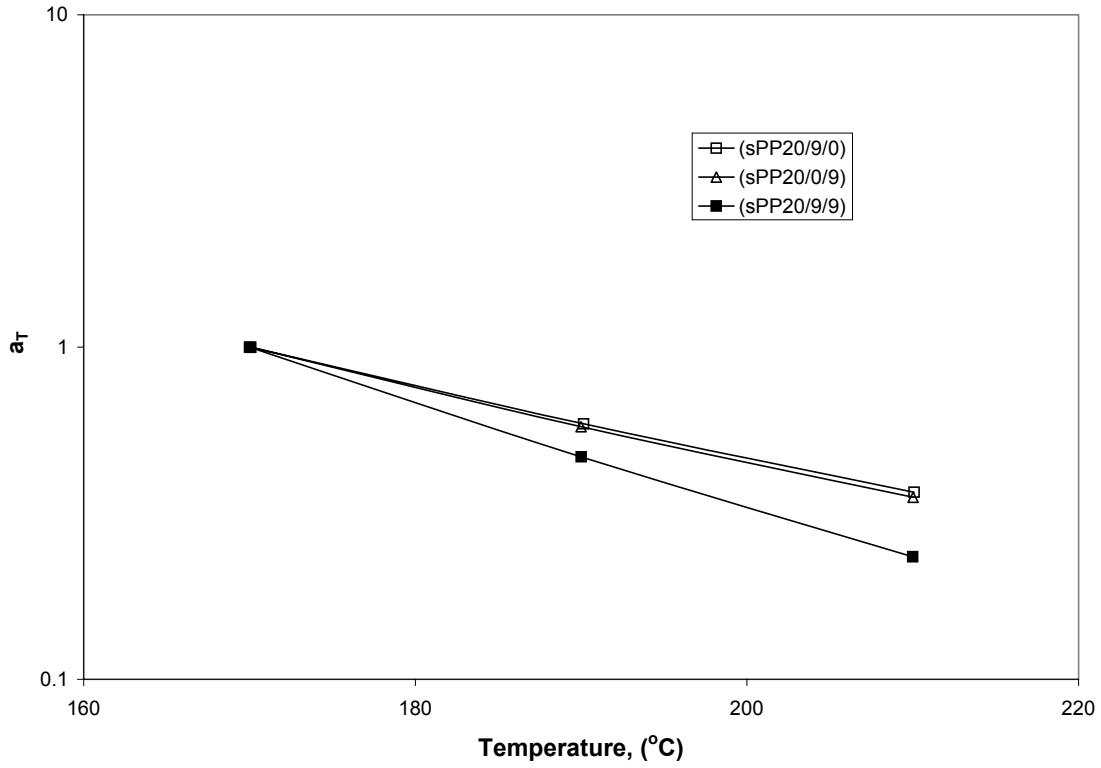

Figure 7.20. Frequency shift factor with temperature for (sPP20/9/9), (sPP20/0/9) and (sPP20/9/0)

7.2.4. Stress relaxation experiments

Stress relaxations after a step strain were performed to measure the responses of the hybrids in the time domain. Fig. 7.21 shows stress relaxation of the three samples after a step strain in the linear regime. Based on the strain sweep data (see Fig. 7.17) a

step strain of 0.5% was used for the matrix polymer (sPP20/0/9), the uncompatibilized hybrid (sPP20/9/0), and the compatibilized hybrid (sPP20/9/9) to ensure linear response.

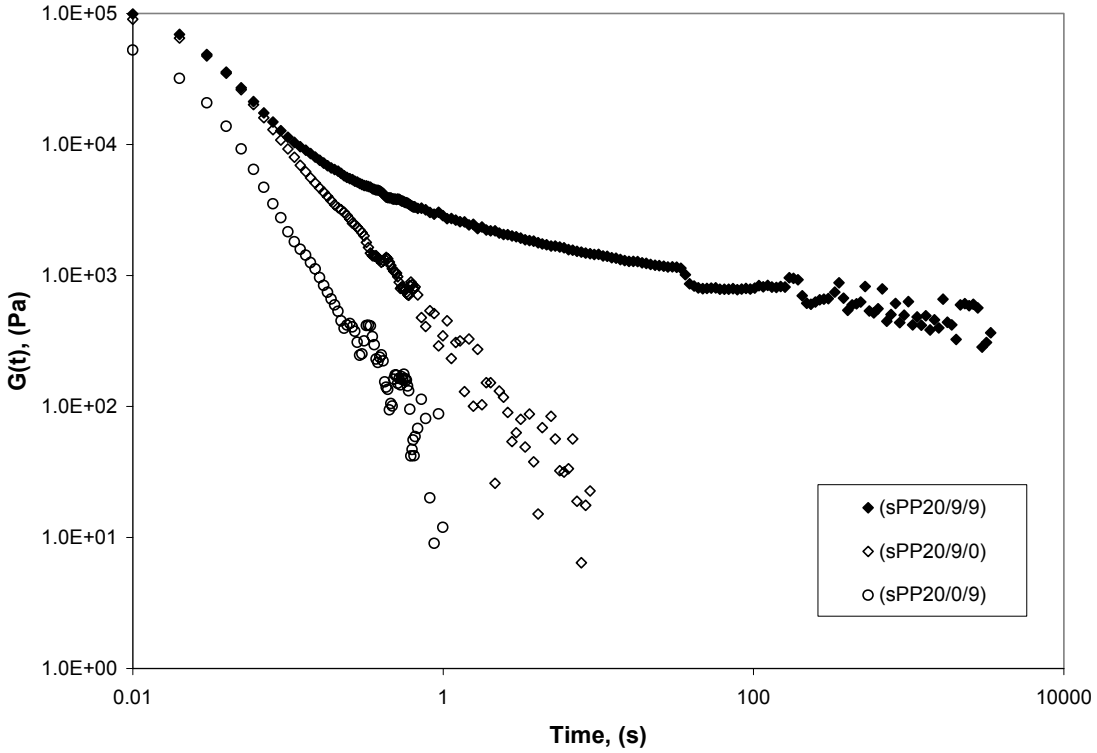

Figure 7.21. Stress relaxation after step strain for matrix polymer (sPP20/0/9), uncompatibilized (sPP20/9/0) and compatibilized (sPP20/9/9) hybrid at T = 190°C, γ_0 = 0.5%

Apart from the slightly higher relaxation modulus of the uncompatibilized sample, the stress relaxation behaviour was qualitatively similar to that of the matrix polymer. For the compatibilized hybrid the relaxation modulus at very short times (< 0.2 s) was similar to that of the uncompatibilized and the matrix polymers. However the stress relaxed very slowly after this and reached a plateau at very long times of ~1000 s. Thus, it may be inferred that the short time stress relaxation corresponded to the response of the matrix polymer while the long time response originated from the dispersed clay microstructure that did not relax further over the experimentally probed time scale.

7.3. Diffusional kinetics of sPP and iPP nanocomposites

The transient creep response of the PP nanocomposites reported earlier (see Fig. 7.14 and 7.16) shows that the zero shear viscosity (η_o) increases with annealing. It was suggested that this increase might due to an evolution of the microstructure on annealing. Specifically, polymer chains can diffuse into the primary clay particles (see Fig. 6.9) and then into the intergallery distances to cause possibly edge exfoliation (as suggested by the peak broadening in XRD patterns of Fig. 6.3). Vaia et. al. reported by using x-ray diffraction studies that the rate of hybrid formation is limited by the diffusion of the polymer chains into the primary clay particles rather than by the diffusion in the interlayer gallery distance. [14] Thus it may be hypothised that the increase in the zero shear viscosity (η_o) with time is related to the diffusion of polymer chains into the primary clay particles. In other words, the evolution of the zero shear viscosity (η_o) could offer a rheological method for measuring the rate of intercalation.

A qualitative support for this hypothesis is seen in Figure 7.16, which shows that, the zero shear viscosity (η_o) of the nanocomposite made with lower molecular weight resins is higher than the zero shear viscosity (η_o) of nanocomposite made using resins of higher molecular weight. Smaller chains of the low molecular weight resin would more rapidly diffuse into the primary particles, compared to the high molecular weight polymers. If this hypothesis were correct, then the relative increase in the zero shear viscosity (η_o) of hybrids made form resins with comparable diffusion rates should be similar.

In order to test the hypothesis, the evolution of the zero shear viscosity (η_o) made from different metallocene catalyzed syndiotactic and isotactic polypropylene was investigated. The PP reins were selected such that the self diffusion coefficient of only one of the pairs matched. Figure 7.22 shows the zero shear viscosity of the matrix resins and their hybrids (sPP4/9/9), (sPP10/9/9), (sPP20/9/9) and (iPP27/9/9).

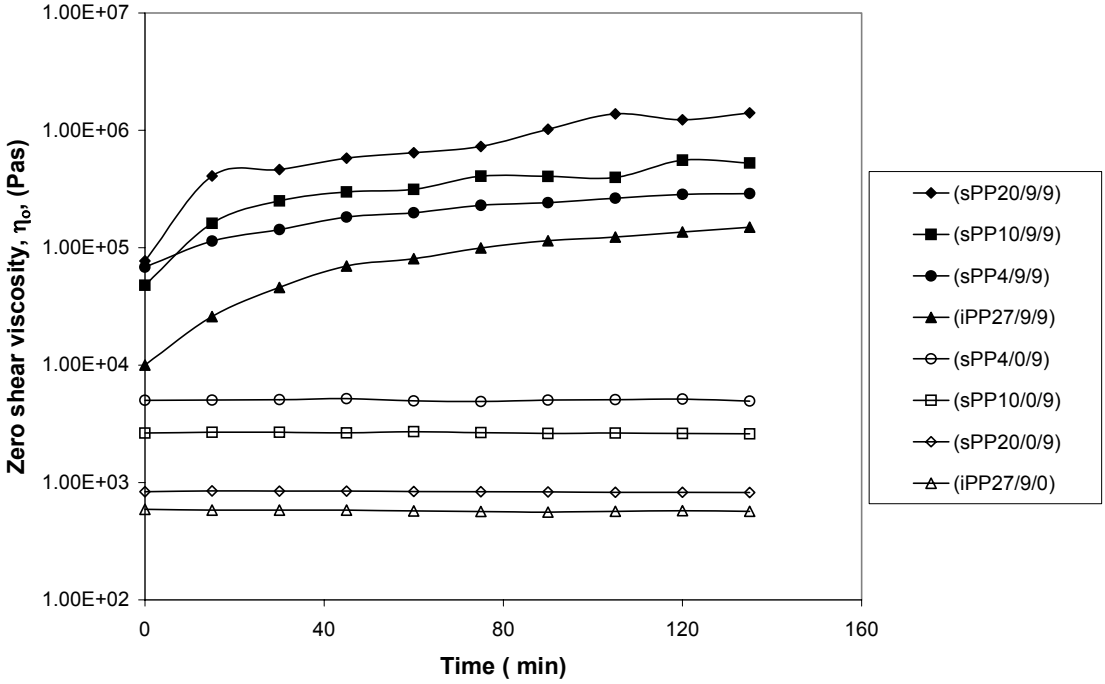

Figure 7.22. Transient creep response of sPP and iPP matrix resins and their hybrids at T = 190°C, σ_o = 10 Pa

According to the reptation theory, the self diffusion constant (D_G) is related to the molecular weight (M) as [15]

$$D_G = \frac{1}{135}\left(\frac{\overline{R}_M^2}{M}\right)\frac{M_e}{M}\frac{\rho RT}{\eta_o^{(R)} M} = \left(\frac{\overline{R}_M^2}{M}\right) G_N^o \frac{M}{\eta_o} \tag{7.1}$$

where $\overline{R}_M^2$ = root mean square end to end distance, M_e = entanglement molecular weight, ρ = density, R = gas constant, T = absolute temperature, $\eta_o^{(R)}$ = Rouse viscosity and G_N^o is plateau modulus. Also, $\frac{\overline{R}_M^2}{M}$ scales with G_N^o as [16]

$$\frac{\overline{R}_M^2}{M} \sim \left(G_N^o\right)^{1/3} \tag{7.2}$$

From e. q. 7.1 and 7.2 we have

$$\frac{D_{sPP}}{D_{iPP}} = \frac{(G_N^o)_{sPP}^{1..33}}{(G_N^o)_{iPP}^{1..33}} \frac{(M)_{sPP}}{(M)_{iPP}} \frac{(\eta_0)_{iPP}}{(\eta_0)_{sPP}} \tag{7.3}$$

The values of plateau modulus for sPP and iPP are reported to be $(G_N^0)_{sPP}$ = 1.35 MPa, $(G_N^0)_{iPP}$ = 0.42 MPa [17]

Assuming M = M_w from table 5.3 and using the experimentally determined values of zero shear viscosity (η_0) at 190°C for sPP4, sPP10 and sPP20 resins, which are 5000, 2600, 830 respectively, in e. q. 7.3, we get, values of $\frac{D_{sPP}}{D_{iPP}}$ as 0.56, 0.77 and 1.8 for sPP resins of MFI= 4, 10 and 20 respectively. The $\frac{D_{sPP}}{D_{iPP}}$ for sPP (MFI= 10) and iPP (MFI= 27) is close to one. Thus, $D_{sPP(MFI=10)} \cong D_{iPP(MFI=27)}$. Thus the hypothesis suggests that the evolution in time of the relative viscosity of these two resins should be similar. Figure 7.23 shows the relative increase in the zero shear viscosity of the hybrid to the matrix. It is seen clearly that the increase in the relative viscosity for the sPP10 and iPP27 hybrids with time is nearly identical. For the sPP20 hybrid the rise is much faster, as expected due to its low $\overline{M}_w$ and for sPP4 the rise is slower due of its high $\overline{M}_w$. Thus it may be concluded that the rise in the zero shear viscosity of the hybrids on annealing indeed gives information on the diffusion of polymer chains from the matrix into the primary particles of the clay.

7.4. Summary

The linear viscoelastic rheology of compatibilized intercalated polypropylene nanoclay composite melt indicates that at low stresses the microstructure consists of a hydrodynamically percolating three-dimensional network of dispersed clay tactoids. Such a network exhibits a solid-like rheological response as demonstrated by the plateau behaviour of the G' and G'', which is actually a weak frequency dependence. Also, the compatibilized hybrids do creep albeit with a low compliance, or alternatively, with a high zero shear viscosity. The zero shear viscosity depends strongly on the clay loading, which further reinforces the existence of the network structure.

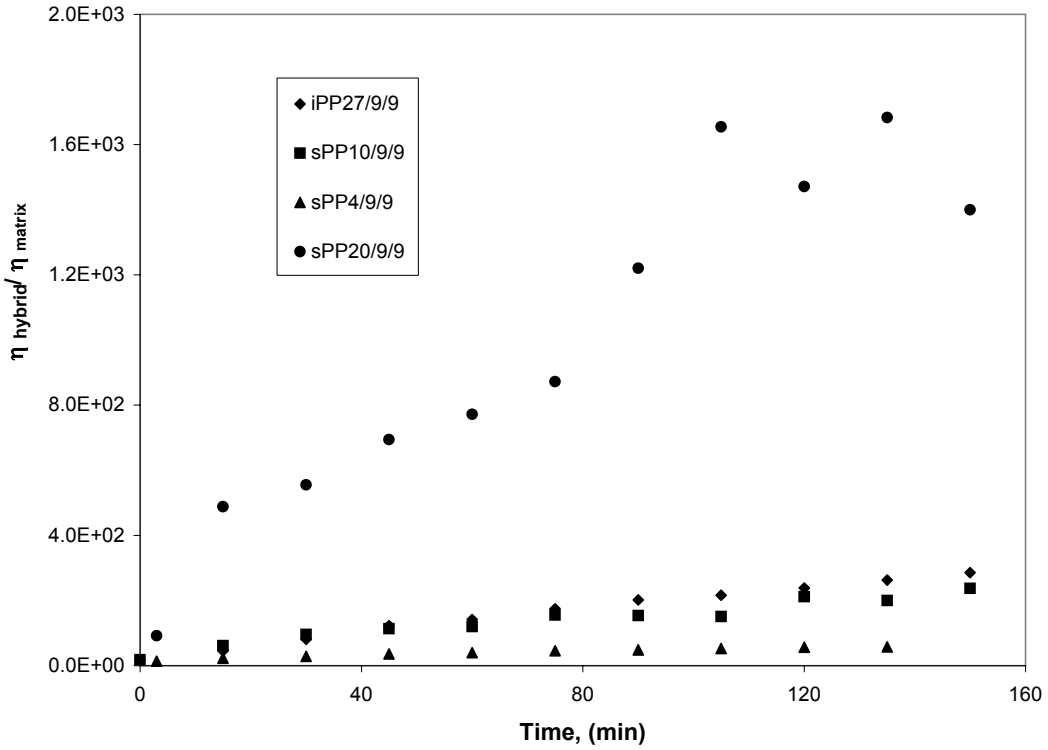

Figure 7.23. Relative increase in the zero shear viscosity of the compatibilized hybrids (sPP4/9/9), (sPP10/9/9), (sPP20/9/9) and (iPP27/9/9) at T = 190°C, σ_o = 10 Pa

The solid-like rheological response is independent of the finer structure of the nanocomposites, i.e., whether they are end-tethered or melt intercalated. The temperature dependence of the zero shear viscosity (η_o) and of the horizontal shift factor (a_T) indicate that the typical rheological response of layered silicate nanocomposites arises from frictional interactions between the silicate layers and not due to immobilization of confined polymer chains between the silicate layers. Specifically, the large rise in the viscosity does not arise from a high activation energy barrier, which might be expected for a confined chain. Further, it has been shown that the creep behavior is very sensitive to the micro-structural changes occurring in the nanocomposites. The creep data together with the XRD suggests that some of the silicate layers from the edges of the crystallites possibly exfoliate into the matrix during annealing of the hybrid. The possibility of exfoliation is greatly enhanced by the presence of a compatibilizer. The exfoliated layers can bridge different silicate crystallites to form a percolating network that strongly resists

deformation. The evolution of the zero shear viscosity (η_o) with time seems to be controlled by the diffusion of polymer from the matrix into the primary clay particles.

Finally, the combined evidence of a weak dependence of G' and G'', the long-time plateau of G(t) and the high zero shear viscosity (η_o) suggests that such materials might have an apparent yield stress. This feature and other non-linear phenomenon are described in the next chapter.

Reference List:

1. Fornes, T. D.; Yoon, P. J.; Keskkula, H.; Paul, D. R. *Polymer* **2001,** *42*(25), 9929-9940.
2. Khare, R.; de Pablo, J. J.; Yethiraj, A. *Macromolecules* **1996,** *29*(24), 7910-7918.
3. Subbotin, A.; Semenov, A.; Doi, M. *Phys. Rev. E: Stat. Phys.* **1997,** *56*(1), 623-630.
4. Luengous, G.; Schmitt, F. J.; Hill, R.; Israelachvili, J. *Macromolecules* **1997,** *30*(8), 2482-2494.
5. Barakos, G.; Mitsoulis, E.; Tzoganakis, C.; Kajiwara, T. *J. Appl. Polym. Sci.* **1996,** *59*(3), 543-556.
6. Vaia, R. A.; Jandt, K. D.; Kramer, E. J.; Giannelis, E. P. *Chem. Mater.* **1996,** *8*(11), 2628-2635.
7. Vaia, R. A.; Jandt, K. D.; Kramer, E. J.; Giannelis, E. P. *Macromolecules* **1995,** *28*(24), 8080-8085.
8. Krishanmoorti, R.; Silva, A. S. *Polymer-Clay Nanocomposites*. Pinnavaia, T. J. Beall, G. W. Eds. John Wiley and Sons. N.Y. **2000**.
9. Ren, J.; Silva, A. S.; Krishnamoorti, R. *Macromolecules* **2000,** *33*(10), 3739-3746.
10. Giannelis, E. P.; Krishnamoorti, R.; Manias, E. *Adv. Polym. Sci*. **1999**, *138*, 107-147.
11. Solomon, M. J.; Almusallam, A. S.; Seefeldt, K. F.; Somwangthanaroj, A.; Varadan, P. *Macromolecules* **2001**, 34(6), 1864-1872.
12. Krishnamoorti, R.; Giannelis, E. P. *Macromolecules* **1997,** *30(14)*, 4097-4102.
13. Kaempfer, D.; Thomann, R.; Mulhaupt, R. *Polymer* **2002**, *43(10),* 2909-2913.
14. Vaia, R. A.; Jandt, K. D.; Kramer, E. J.; Giannelis, E. P. *Macromolecules* **1995,** *28*(24), 8080-8085.

15. Doi, M.; Edwards, S. F. *The Theory of Polymer Dynamics* The international series of monographs on physics 73 Birmann, J.; Edwards, S. F.; Llewellyn, C. H; Rees, M. Eds. Oxford Science Publications, U.K. **1995**.
16. Fetters, L. J.; Lohse, D. J.; Richter, D.; Witten, T. A.; Zirkel, A. *Macromolecules* **1995**, 27(17), 4639-4647.
17. Eckstein, A.; Suhn, J.; Friedrich, C.; Mulhaupt, R. *Macromolecules* **1998**, *31*(4), 1335-1340.

Chapter 8 Non-linear rheology of PP nanocomposites

This chapter describes the non-linear viscoelastic behaviour of isotactic and syndiotactic PP nanocomposites in stress ramp and steady shear experiments. It presents experimental results on the apparent yield like behaviour observed in these hybrid materials and discusses them in the context of visco-plastic models. The microstructural origins of the non-linear behaviour are investigated by the in–situ measurements on the orientations of clay tactoids under shear and the relaxation of these orientated tactoids on cessation of shear using a novel rheo x-ray technique.

8.1. Isotactic polypropylene (iPP) nanocomposite

8.1.1. Non-linear rheology of iPP nanocomposites

The steady shear viscosity as a function of shear rate for the compatibilized hybrids with varying clay loading, viz., (iPP3/25/10), (iPP3/9/9), and the pristine polypropylene (iPP3/0/0) was investigated.

The sample was subjected to steady shear using parallel plates at 200^{o}C in the ARES rheometer. As seen from Figure 7.1, the pristine polymers and all the hybrids exhibit shear thinning at higher shear rates. The hybrids shear thin to a greater extent with the matrix viscosity, the shear thinning sets in at comparatively lower shear rates for increasing clay loading. Further, when compared with the matrix viscosity, the viscosity of the hybrids at low shear rates divergently increased with increasing clay loading. This divergence is in agreement with, the previously discussed pseudo solid-like behaviour for the compatibilized hybrids at long times or under near quiescent conditions.

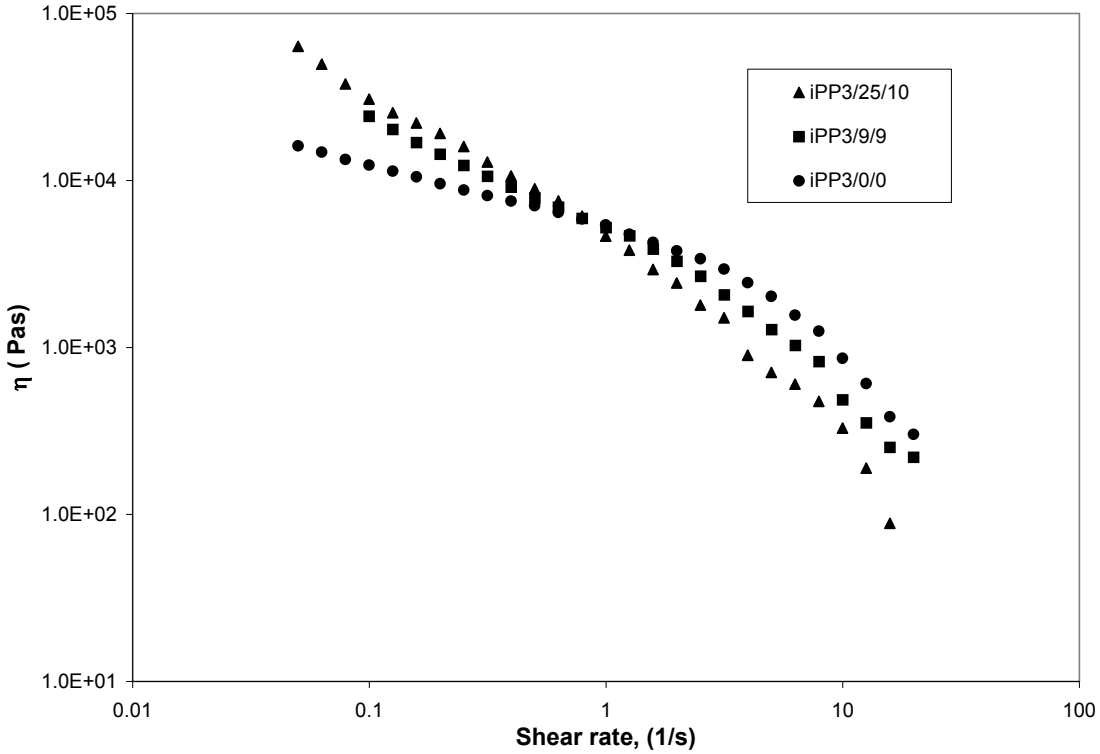

Figure 8.1. Steady shear viscosity as a function of shear rate for iPP-nanocomposites at T = 200^{o}C

The effect of a pre-shear on the linear viscoelastic properties was also investigated. Figure 8.2 shows small amplitude frequency sweep data for the compatibilized hybrid (iPP3/9/9) before and after a steady pre-shear of 1 s^{-1} was applied for 60 s. As seen from the Figure 8.2, the $G^{'}$ and $G^{''}$ of the pre-sheared sample is lower than those for the initial unsheared sample.

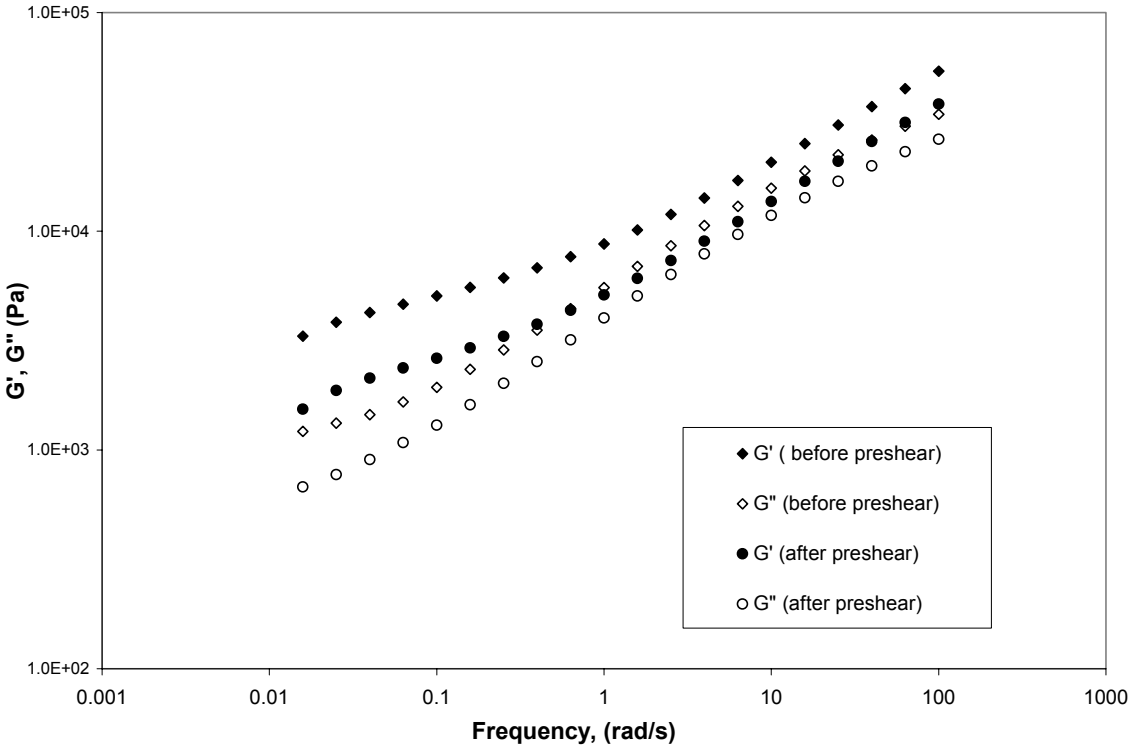

Figure 8.2. Small amplitude oscillatory frequency sweep for (iPP3/9/9) before and after applying large amplitude pre-shear at T = 200^{o}C

The effect of pre-shear on the zero shear viscosity (η_o) of the compatibilized hybrid (iPP3/9/9) was also investigated by performing creep measurements using the Bohlin rheometer. The sample was pre-sheared at 200^{o}C at a steady shear stress of 1000 Pa. The pre-shearing time of the sample was measured in terms of the number of rotations of the upper plate in the parallel plate geometry. It can be seen from the Figure 8.3 that the zero shear viscosity decreased rapidly with pre-shearing, and then reached a plateau value that was more than an order of magnitude smaller than the initial value.

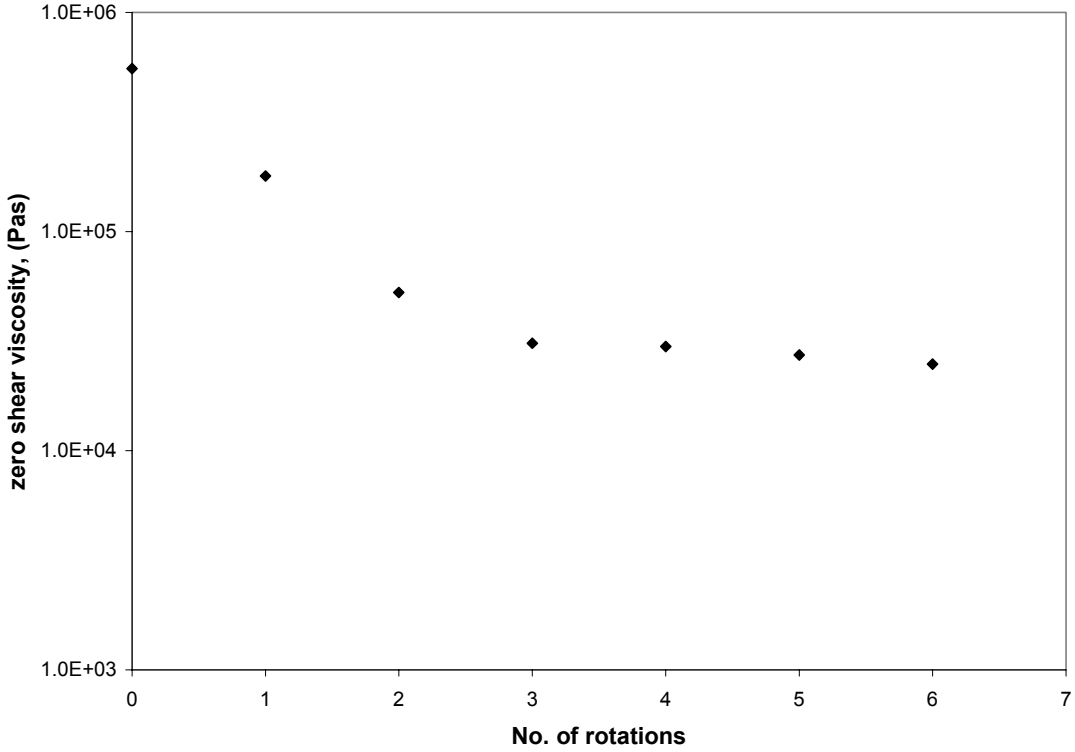

Figure 8.3. Zero shear viscosity of (iPP3/9/9) as a function of pre shear at T = 200^{o}C

8.1.2. Yielding phenomenon in iPP nanocomposites

An important property of filled materials above the percolation limit of filler content is the apparent 'yielding' after a critical stress. The so-called yield stress of a material is a useful engineering parameter to describe the flow behavior of several non-Newtonian fluids, however, a true yield stress is a myth since all materials 'flow' at all stresses given sufficient time. [1] A yielding fluid typically shows a high Newtonian viscosity at low stresses, i.e., it creeps at low stresses, following which there is a sharp drop in viscosity over a narrow range of higher stresses. This is termed as the apparent yielding behavior and the stress at the onset of yielding is called an 'engineering yield stress' (σ_y).

The viscosity at increasing stresses was probed by performing stress ramp experiments on the Bohlin rheometer. Figure 8.4 shows the viscosity of (iPP3/9/9) as a function of shear stresses. The material creeps at low stresses in a Newtonian manner with a high zero shear viscosity followed by an apparent yielding starting at about 200 Pa

in which the viscosity drops by more than three orders of magnitude in a relatively narrow range of shear stresses. That the drop in viscosity is not a slip artifact was confirmed by performing gap dependence studies. Wall-slip did occur at much higher stresses, which is not included in the figure.

As discussed in chapter 7, the very high zero shear viscosity observed at low stresses for the compatibilized hybrid is the response of a hydrodynamically interacting percolating network. At shear stresses greater than the apparent yield stress the network structure must break down causing the large reduction in the viscosity of the sample.

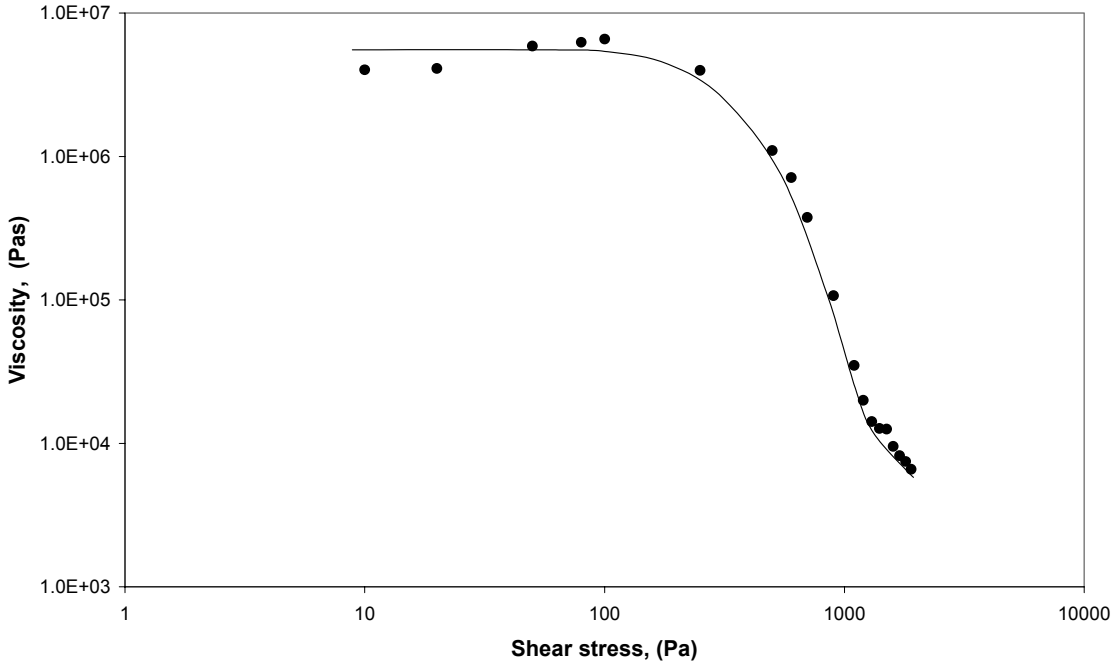

Figure 8.4. Viscosity of (iPP3/9/9) as a function of shearing stress at T = 200^{o}C

It has already reported that a possible cause for the breakdown of the network structure is a large scale alignment of the clay tactoids (or platelets), due to shear flow. [2.3] Because of the highly anisotropic nature of the tactoids, the flow-induced alignment of these tactoids should be relatively easy. The greater shear thinning of the hybrids and the lowering of the continual decrease G' and G'' with pre-shear also suggestive of the flow alignment of the clay tactoids. Other rheological evidences have been provided in the literature suggesting flow alignment. Krishnamoorti et. al. observed that the G' and

G'' decreased continuously with application of large amplitude of oscillatory shear, to reach a plateau value. [2]

Similarly, Krishnamoorti et. al. reported the strong shear thinning character of the hybrids under steady shear, which was attributed to the ability of the steady shear to orient the anisotropic clay in shear direction. [3]

Figure 8.5 shows a combined plot of shear stress versus shear rate and complex modulus versus frequency for the compatibilized hybrid (iPP3/9/9). The shear rates were measured in the stress ramp experiments in which the shear stress was increased in a step-wise manner. The complex modulus was obtained from the dynamic data (see Fig. 7.9, 7.10). The complex modulus does not seem to match with the shear stress value in the yield region, thereby indicating that the Cox-Merz rule is not valid for the compatibilized hybrids. As we have discussed in chapter 2, similar failures of Cox-Merz rule for PS-PI and nylon nanocomposites by Krishnamoorti et. al. [3] and Fornes et. al. [4], respectively.

Thus, the complex viscosity (η^*) measured by the dynamic experiments in the linear viscoelastic regime, exceeds the viscosity measured by the steady shear stress ramp experiment. The possibility of flow-induced alignment of the clay tactoids can explain the failure of the Cox-Merz rule in a straightforward manner. For instance it can be easily argued that the microstructural changes in the material during the two types of tests could be very different and therefore these tests do not probe the same microstructure. For instance, the stress ramp experiment imposes a large strain on the sample with increasing stress, which could result in the orientation of the clay tactoids in the nanocomposites, (i.e., yielding), and these oriented clay tactoids contribute negligibly to the hybrid viscosity and hence a reduction in the frictional resistance to flow. In the small amplitude oscillatory shear experiment, on the other hand, the microstructure probably does not change significantly due to the small-imposed strain and as a result the frictional resistance remains higher. On the other hand, large amplitude oscillatory shear experiments (not shown here) have indeed shown a decrease in the complex modulus and a better matching with the steady shear data.

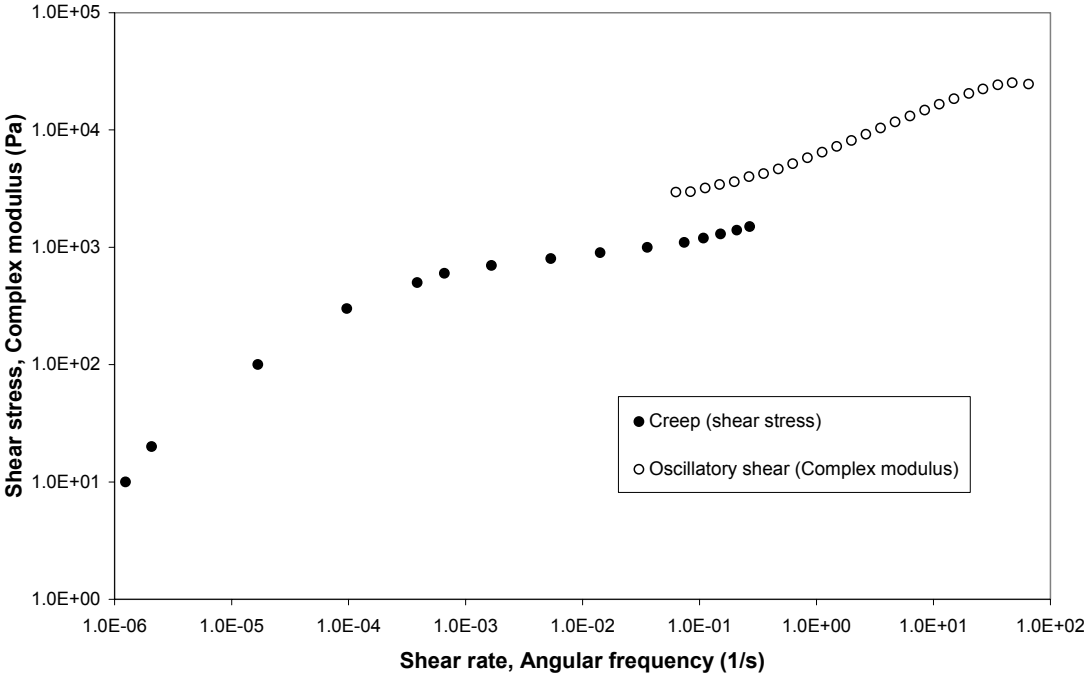

Figure 8.5. Shear stress and complex modulus of (iPP3/9/9) as a function of shear rate and frequency at T = 200^{o}C

8.2. Syndiotactic polypropylene (sPP)

8.2.1. Effect of molecular weight and clay content on yielding

Figure 8.6 shows data from stress ramp experiments for the compatibilized and the uncompatibilized sPP nanocomposites of different matrix molecular weights. The matrix polymers (not shown in Fig. 8.6, to avoid cluttering) showed a Newtonian behaviour over the entire range of stress probed experimentally, while the uncompatibilized nanocomposites showed a slightly higher zero-shear viscosity followed by a small decrease in the viscosity at higher stress. The compatibilized samples showed a significantly higher zero-shear viscosity followed by a large decrease in the viscosity over a narrow range of shear stress. Thus, the compatibilized hybrids showed distinct yield behaviour, and after yielding, the hybrid viscosity rapidly decreased to match the matrix viscosity. Similar to the iPP nanocomposites, it has been independently confirmed that the drop in viscosity is not an artifact of wall-slip.

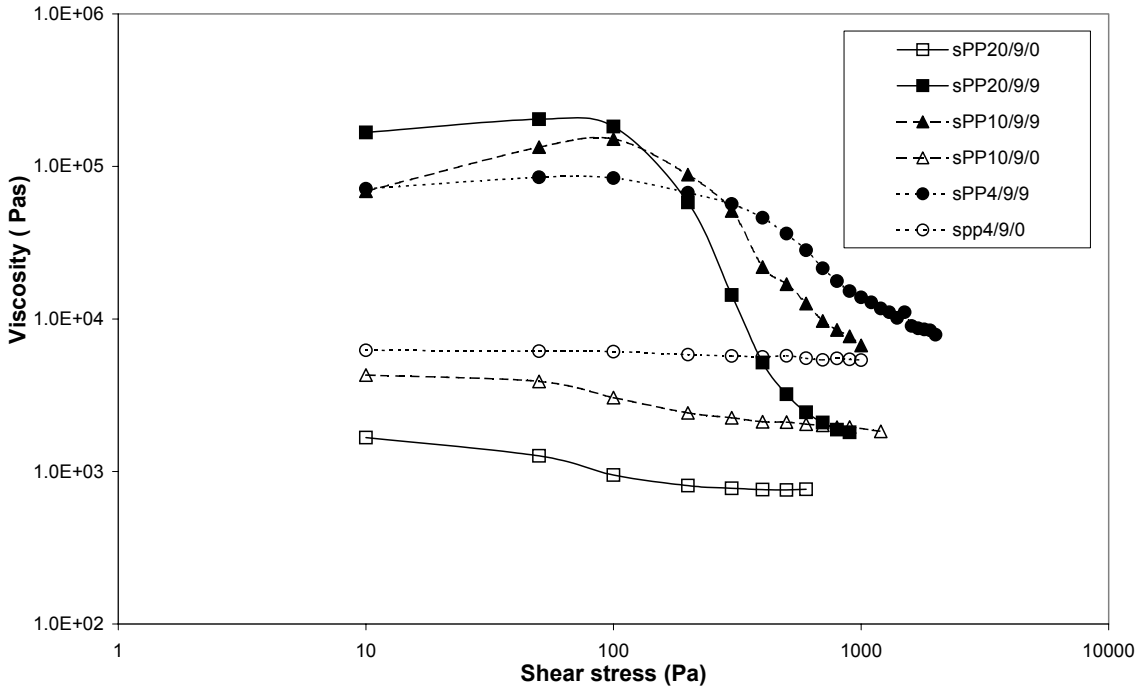

Figure 8.6. Viscosity of compatibilized and uncompatibilized sPP nanocomposites of different molecular weight at T = 190^{o}C

The above data once again highlights the crucial role of the compatibilizer(PP-MA) in the rheological response of the hybrid. Apparently, only in the presence of the compatibilizer the clay tactoids were able to form a percolating network, which is destroyed at higher shear stresses.

As discussed in chapter 7, the zero shear viscosity (η_o) of the low molecular weight compatibilized hybrid (sPP20/9/9) was found to be greater than that of the high molecular weight matrix (sPP4/9/9). After yielding however, the matrix properties dominate, and in this regime the viscosity of (sPP4/9/9) is greater than that of (sPP20/9/9). This phenomenon will be discussed in more detail later.

Figure 8.7 shows the plots of η_0 vs. clay loading and σ_y vs. clay loading for compatibilized sPP20 nanocomposites of increasing clay loadings (sPP20/0/0, sPP20/3/3, sPP20/6/6, sPP20/9/9 and sPP20/25/25). η_0 was obtained from transient creep measurements after 3 hrs of annealing (see Fig. 7.22) and the σ_y values were read from the stress ramp experiments (see Fig. 8.6). As discussed in chapter 7, the data shows that

the zero-shear viscosity of the nanocomposites scales exponentially with silicate loading, which supports the hypothesis of a percolating network microstructure formed by well-dispersed clay tactoids at low shear stresses. On the other hand, the yield stress scales linearly with silicate loading, which suggests a non-cooperative resistance from the clay tactoids in contrast to the highly cooperative effects of the percolating network at low stresses. Thus, the yielding process corresponds to a destruction of the hydrodynamically interacting network of clay tactoids. The yield stress is therefore governed by the population of individual tactoids rather than by their cooperative frictional interactions.

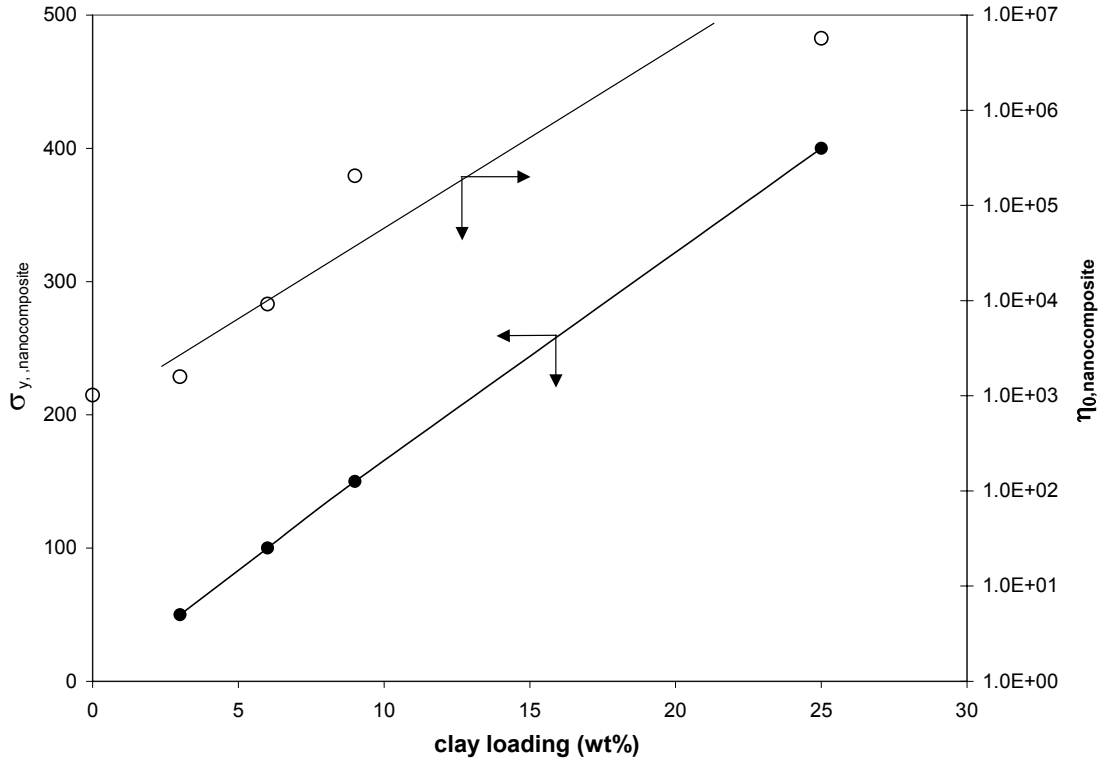

Figure 8.7. Zero shear viscosity and yield stress of compatibilized hybrids containing different clay loadings (sPP20/0/0, sPP20/3/3, sPP20/6/6 and sPP20/9/9) at T = 190°C

Figure 8.8 shows the plots of $\eta_{0,nanocomposite}$ vs. $\eta_{0,matrix}$ and $\sigma_{y,nanocomposite}$ vs. $\eta_{0,matrix}$ for compatibilized sPP-nanocomposites of same clay loading but of different molecular weight sPP resins sPP4/9/9, sPP10/9/9, and sPP20/9/9. Contrary to the zero-shear viscosity, the yield stress of the compatibilized hybrids increased linearly with the matrix viscosity. This is not surprising since yielding corresponds to the destruction of the

percolated network of clay tactoids, and once the network is destroyed the yield stress should then be governed by the matrix properties. The decrease in $\eta_{0,nanocomposite}$ with increasing $\eta_{0,matrix}$ was discussed in the chapter 7.

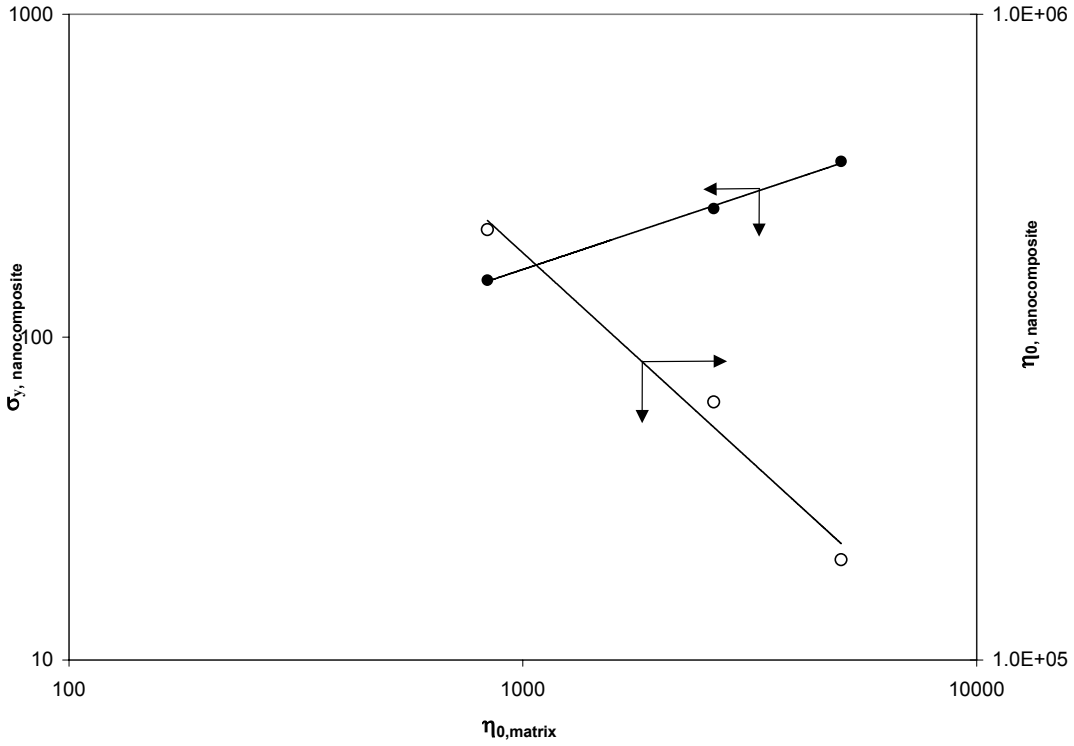

Figure 8.8. Zero shear viscosity and yield stress of compatibilized hybrids prepared using matrix polymers of different molecular weights (sPP4/9/9, sPP10/9/9, sPP20/9/9) as a function of matrix zero-shear viscosity at T = 190°C

8.3. Material functions

The rheology of a PLS nanocomposite melt can be described by three material functions: (a) the zero-shear viscosity η_0, which provides insight into the microstructure of the material under near-quiescent conditions, (b) the yield stress, σ_y which suggests breakage of the microstructure, and (c) a characteristic time scale $\lambda = \eta_0 / \sigma_y$.

The dependence of zero shear viscosity (η_o) and the yield stress (σ_y) on material and state variables like clay content, matrix molecular weight and temperature have been

discussed in earlier sections. From η_o and σ_y a characteristic relaxation time for the sPP20/9/9 material can be estimated as $\lambda = \eta_0 / \sigma_y \sim 2 \times 10^5/200 = 10^3$ s. Note that this agrees approximately with the inverse of the shear rate at which yielding begins (see Fig. 8.11) and suggests that below this shear rate the material has sufficient time to relax and maintain the percolated microstructure, while above this shear rate the network breaks down. Stress relaxation experiment described previously (see Fig. 7.20) also showed that for the compatibilized hybrid (sPP20/9/9), the relaxing stress reached a plateau value at very long times of ~ 1000 s, which matches with the characteristic relaxation time scale. Thus, different rheological experiments indirectly suggest that a characteristic relaxation time associated with the clay microstructure is of the order of 1000 s.

8.4. Modelling of the yield behaviour in PLS nanocomposites

Concentrated suspension of solid particles in Newtonian liquids often show a yield stress followed by nearly Newtonian flow. Such materials are called viscoplastic or Bingham plastics. They show very little or no deformation up to a certain level of stress, i.e., the yield stress, after which materials flow readily. [5]

The application of inelastic viscoplastic models viz., Bingham, Herschel–Bulkley, and Papanatasiou models for the compatibilized hybrids were investigated in this study.

A simple model, which describes viscoplasticity, is the Bingham constitutive equation (see e. q. 2.28). The Bingham model assumes a Hookean response below the yield stress and a Newtonian behaviour above the yield stress. The Herschel-Bulkley model also assumes a Hookean response below the yield stress, but proposes a power law behaviour yielding to capture the non-Newtonian shear thinning response at high shear rates. Several studies covering a wide range of shear rates indicate that in the very low shear rate regime, the material actually exhibits a Newtonian response rather than Hookean behaviour. Such behaviour is more clearly captured by the two-viscosity model (see e. q. 2.29). Papanatasiou proposed a modification to the viscoplastic fluid models to avoid the discontinuity in the flow curve due to the incorporation of the yield criterion (see e. q. 2.30). Figure 8.9 shows predictions of the inelastic viscoplastic models described above, fitted to experimental data of the compatibilized hybrid (sPP20/9/9).

The values of yield stress (σ_y) = 350 Pa, high shear viscosity (η) = 1069 Pas and the constants m = 2218 and n = 0.56 were estimated from the experimental data. These values were used to fit the models to the experimental data. The symbols show the experimental data, while the various lines points represent the model fits.

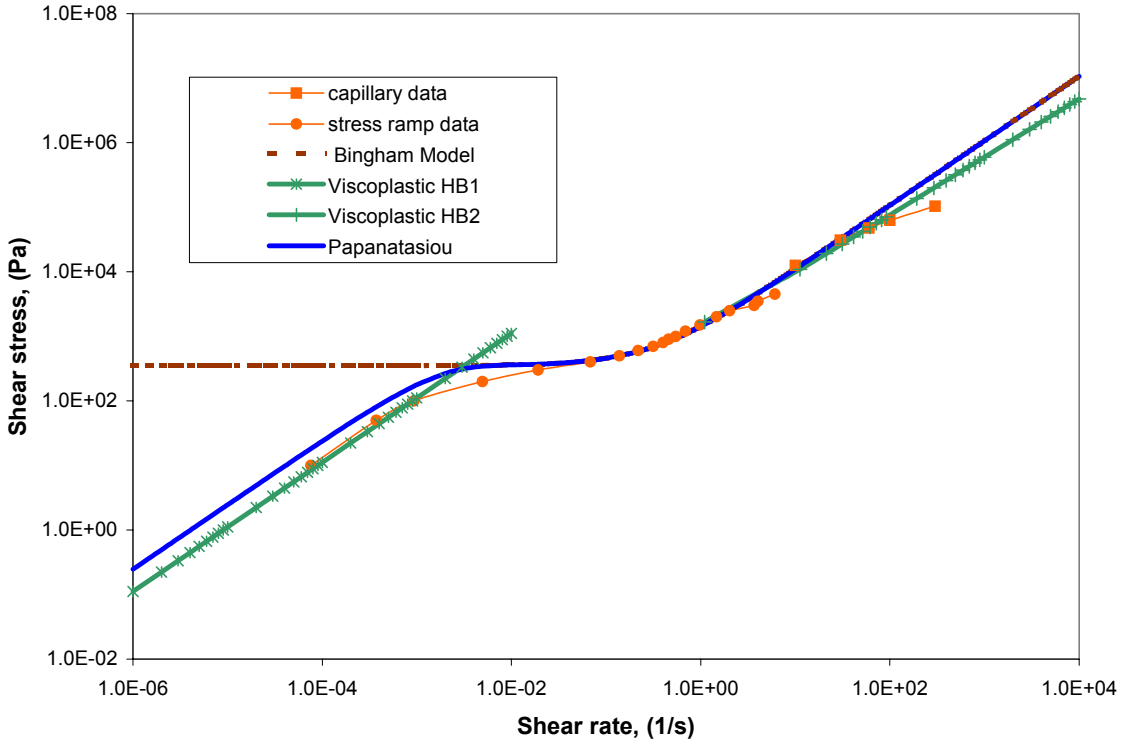

Figure 8.9. Inelastic models fitted to compatibilized hybrid (sPP20/9/9)

8.5. Rheo-x-ray analysis

The different rheological experiments described so far give consistent and complementary information about the flow behaviour of sPP nanocomposites under near-quiescent and high shear flow conditions. However, rheology in itself is an indirect tool to probe the microstructure of the materials. Direct evidence of the microstructural changes would be desirable to confirm rheological analysis. In particular, the observations of the clay orientation under shear would be desirable to quantify the structure - rheology links. Rheological characterization with simultaneous x-ray analysis was carried out using the Cambridge Multi Pass Rheometer (MPR).

Two types of experiments were performed in the rheo-XRD MPR apparatus. In the first experiment the samples were subjected to steady shear in a multipass mode in which the pistons were reciprocated at a set velocity with a short rest time of 1s between each of the strokes. The piston movement and the corresponding pressure difference data during one cycle of a typical test for a (sPP20/9/9) are shown in Figure 8.10.

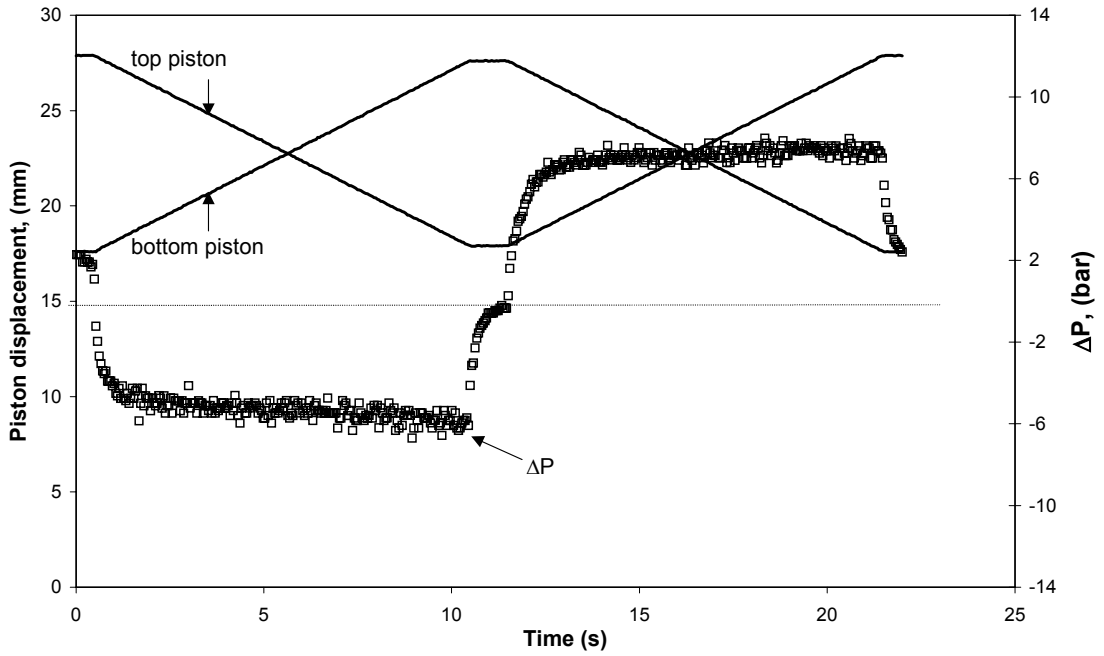

Figure 8.10. Typical rheological data from a Multi Pass Rheometer (MPR)

As seen in the Figure 8.10, when the pistons start moving the pressure difference rapidly increases and reaches a steady state value. The wall shear stress can then be calculated from e. q. 3.1. When the pistons stop, the pressure difference decreases rapidly but before it can relax completely the next cycle begins after the short rest time. The wall shear stress calculated using e. q. 3.1 from the measured pressure difference at different piston speeds is plotted in Figure 8.11. A complete picture of the rheological response of sPP20/9/9 over a wide range of shear rates (or stresses) is shown in Figure 8.11. Data from different rheological experiments viz., small amplitude oscillatory shear, stress ramp and capillary rheometry, are included in the figure. At shear rates lower than 10^{-3} 1/s the nanocomposite behaved as a Newtonian liquid of very high viscosity (~$2x10^5$ Pas). The non-linear regime began when the material yielded, i.e., deformed significantly

for a relatively small increase in stress in the range of approximately σ_y ~200–500 Pa. After the apparent yielding process the shear stress increased again with shear rate as shown by the Multi Pass Rheometer data and the Ceast Rheovis 2100 capillary rheometer data. The high shear data matched well with the stress ramp data obtained from the Bohlin rheometer at the low shear rate range and also with the dynamic data obtained from the RDS-II rheometer at the high shear rate range. Interestingly, at low frequency the complex viscosity calculated from the small amplitude oscillatory data did not match with the steady shear data. This implies that similar to the compatibilized iPP hybrids, the sPP compatibilized hybrids too did not follow the empirical Cox-Merz rule.

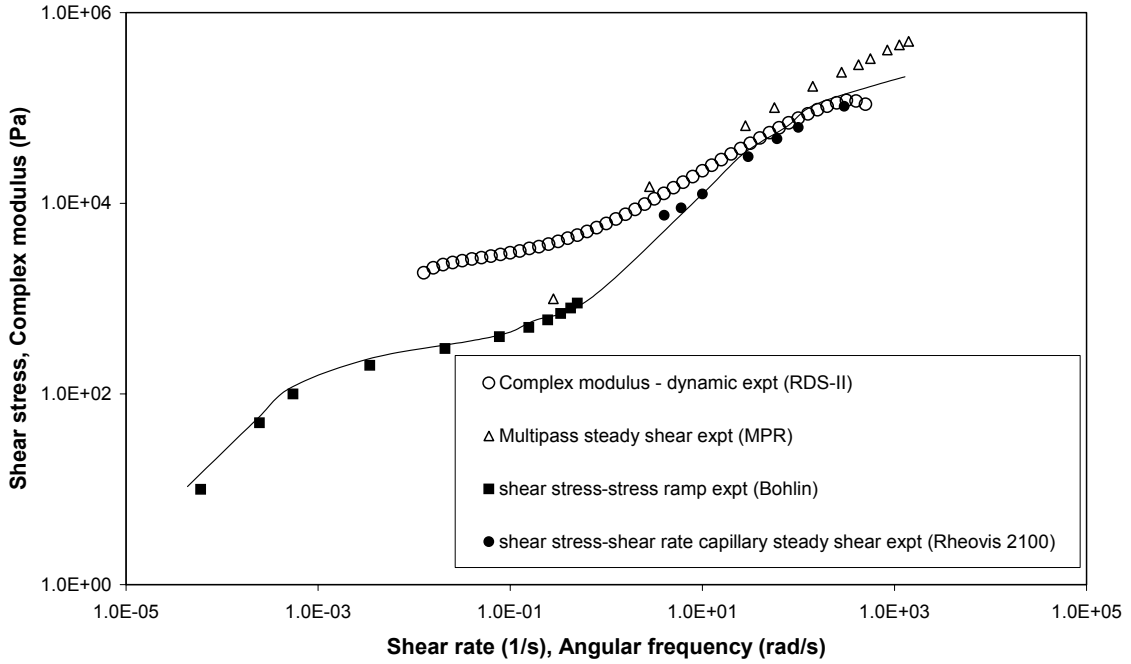

Figure 8.11. Overlay of flow curves obtained from stress-ramp, frequency sweep and MultiPass experiments for sPP20/9/9 at T = 190^{o}C

The XRD data was collected simultaneously during steady shear multipass runs, as shown in Figure 8.10. Data collection time was set to 4 minutes to allow for sufficient signal intensity. The diffraction patterns for the compatibilized hybrid sPP20/9/9 at different piston velocities are shown in Figure 8.12 and the corresponding integrated intensity along the azimuthal direction is plotted alongside. When the pistons were at rest, the diffraction pattern was an almost uniform ring (see Fig.2.7), which corresponds to the

Braggs diffraction by the clay platelets that stack up to form the clay tactoids. At the smallest achievable piston speed of 0.01 mm/s in the MPR (corresponding to an apparent wall shear rate of $\dot{\gamma}_a = 0.28\,s^{-1}$) there was already an increase in scattered intensity near the equator of the ring. With increasing piston speeds the full diffraction ring disappeared and a distinct equatorial band of high intensity was seen. The integrated intensity patterns show two corresponding sharp peaks at the azimuthal angles of $\chi = 90^o$ and 270^o (where, $\chi = 0^o$ at 12 O' clock position on the diffraction pattern). Above 10 mm/s piston speed ($\dot{\gamma}_a = 280\,s^{-1}$) the equatorial diffraction pattern remained almost unchanged. The appearance of equatorial diffraction pattern is a clear indication of shear-induced alignment of the clay tactoids along the flow direction with their faces normal to the gradient and x-ray beam direction as shown schematically in Figure 8.12. Further, the appearance of a band rather than spots suggests the presence of a series of long-range order generated by the shear. It is possible that platelets from the edges of the tactoids exfoliate due to shear and thus increase the gallery spacing. Alternatively, the clay tactoids could align relative to each other and create a long-range order.

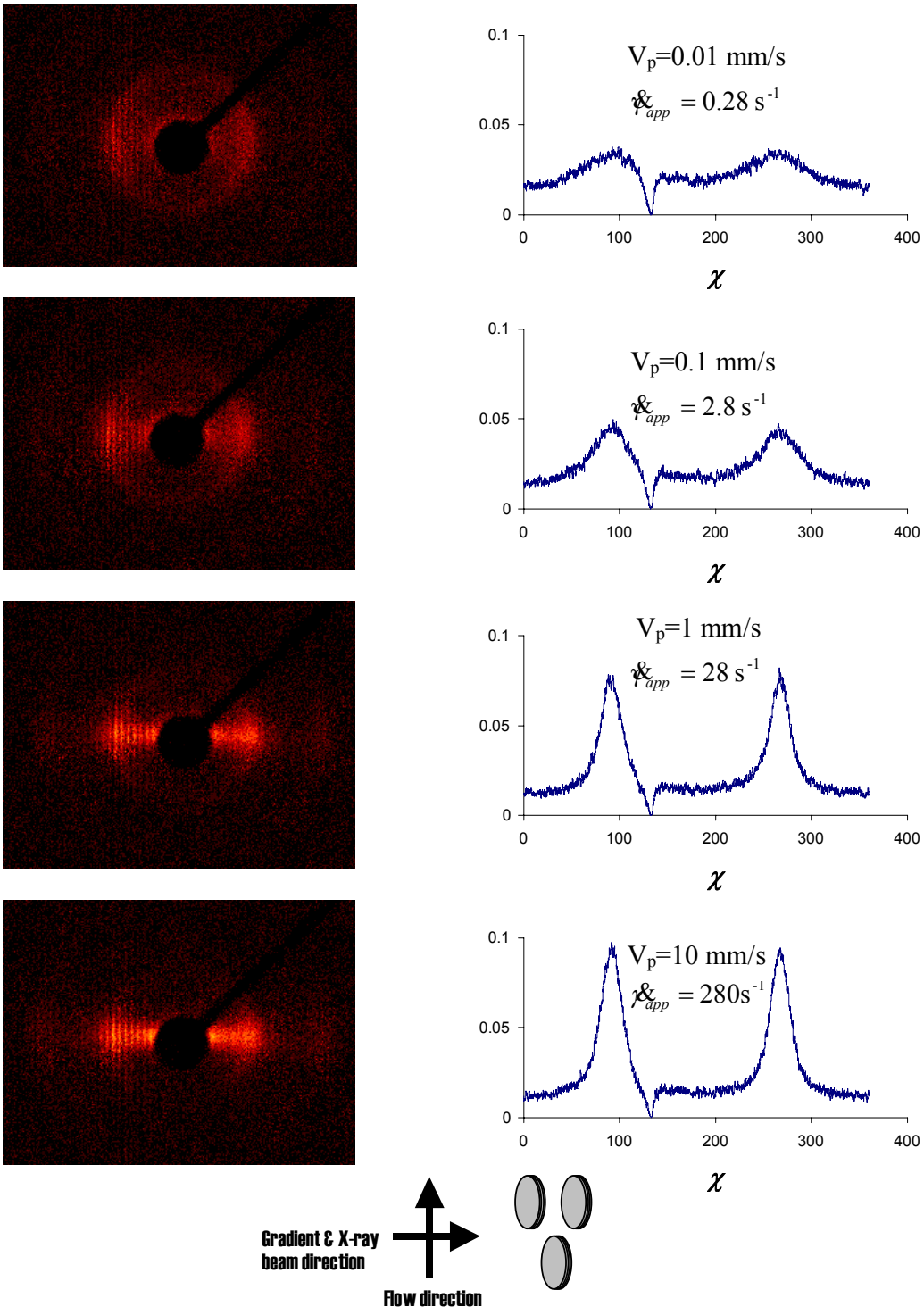

Figure 8.12. X-ray diffraction patterns of the compatibilized hybrid (sPP20/9/9) at different piston velocities at T= 190°C and schematic of the orientation of the clay tactoids

The uncompatibilized hybrid (sPP20/9/0) was orientated to a smaller extent at comparable piston speeds as shown in the inset in Figure 8.13 for a speed of 10 mm/s. Figure 8.13 also shows the diffraction patterns of the compatibilized hybrid (sPP20/9/9) and the uncompatibilized (sPP20/9/0) hybrids at a piston speed of V_p=10 mm/s. In case of the uncompatibilized samples, the absence of a distinct equatorial band is notable instead of which equatorial alignment along the diffraction ring was seen. This is clearly seen as a flat peak in the intensity-2θ plot for the compatibilized sample and a sharp peak for the uncompatibilized sample.

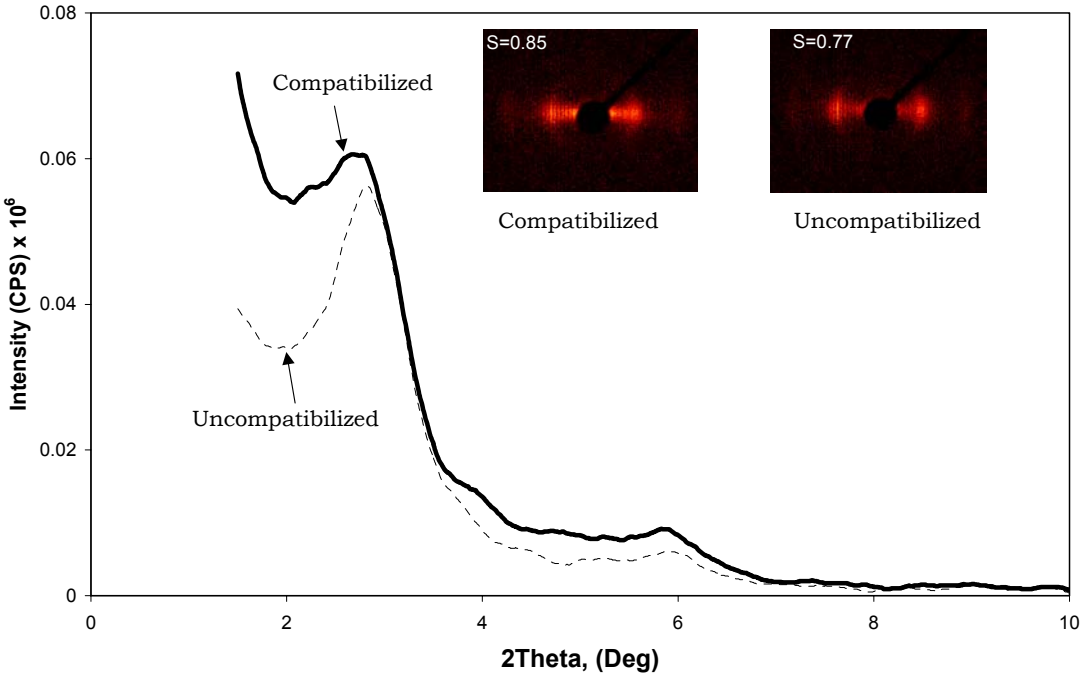

Figure 8.13. Comparison between the diffraction patterns of compatibilized (sPP20/9/9) and uncompatibilized (sPP20/9/0) hybrids at T = 190°C

The degree of orientation can be quantified by an average orientation function defined as [6]

$$S = \frac{-2\int_0^{\pi/2} I(\chi)P(\chi)\sin\chi\, d\chi}{\int_0^{\pi/2} I(\chi)\sin\chi\, d\chi} \qquad (8.1)$$

Here $I(\chi)$ is the intensity at the azimuthal angle χ and $P(\chi)=\frac{3\cos^2\chi-1}{2}$ is the Herman orientation function. The orientation function takes the values of zero and unity for random orientation and perfect uniaxial orientation, respectively. Figure 8.13 shows the orientation function plotted against the wall shear stress that is calculated from the measured pressure drop at each piston velocity.

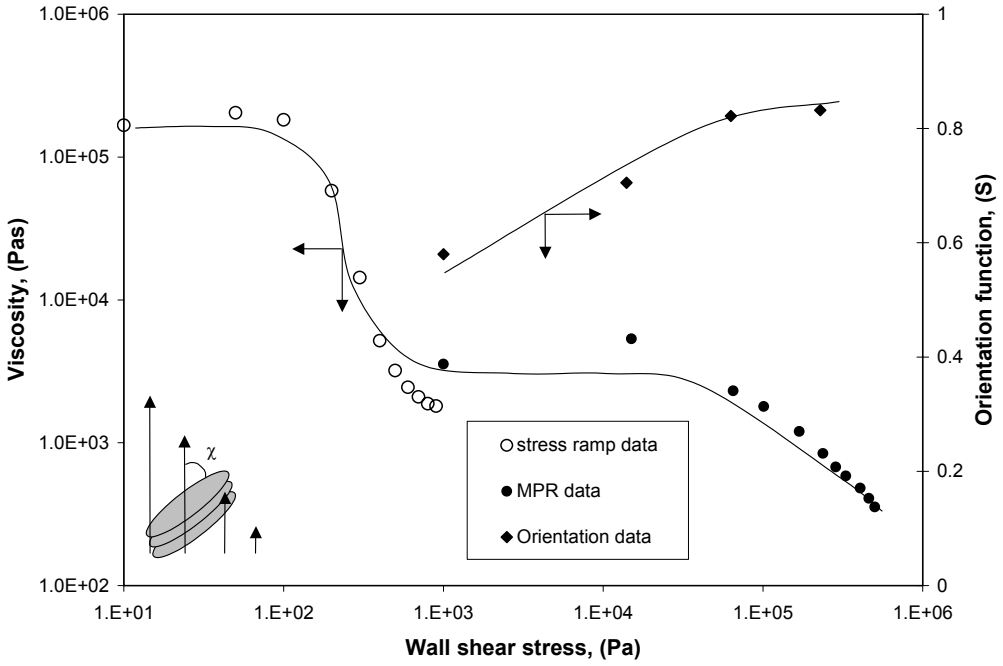

Figure 8.14. Orientation function and viscosity of the compatibilized hybrid (sPP20/9/9) as a function of wall shear stress at T = 190^{o}C

The orientation increased with shear stress and reached a saturation value of approximately 0.85. An orientation function of 0.85 is slightly higher than that obtained in typical thermotropic LCP melts under high shear [7,8]. However, it is less than that seen in uniaxially oriented fibers. Figure 8.14 also shows the yielding behaviour of the same sample as obtained from the stress ramp experiment in the controlled stress Bohlin rheometer. While the MPR experiments could not reach the low level of shear stress that were achievable in the stress ramp experiment, it is clear that the apparent yielding behaviour is connected with the orientation of the clay layers. It should be noted that in the rheo-XRD experiment only a small volume of sample near the capillary wall

experiences the shear stress plotted in Figure 8.14. The remaining sample experiences linearly decreasing stress down to zero at the centre. Accordingly, the orientation function could be plotted against a volume average stress, $\overline{\sigma} = 2\sigma_w / 3$, however, this does not distinctly change the nature of the rheology-microstructure link shown in the Figure 8.14.

There are several contemporary reports of rheological characterization coupled with in-situ and ex-situ techniques like SAXS, SANS and XRD describing flow orientation of polymer nanoclay composites, as we have discussed in chapter 3. [9-11] The effect of high strain on the crystallization of end-tethered nylon-6 nanocomposite was studied by Medellin-Rodriguez et. al. using rheo-SAXS analysis. [9] They found that the silicate layers and the polymer chains are orientated in the flow direction even at relatively low shear and at temperatures just above the melting point. Schmidt et. al. studied shear orientation in aqueous solutions of PEO nanocomposites using flow birefringence and SANS. [10] It was found that the clay platelets were oriented in the flow direction with their surface normal perpendicular to in the flow direction.

Okamoto et. al. reported ex–situ measurements of the elongation flow–induced orientation of clay particles in polypropylene nanocomposites using TEM. [11] The TEM analysis showed that, the biaxial flow-induced alignment of clay particles along the cell boundries, enhances the modulus of the foam.

In the second type of rheo-XRD experiment done in this work the relaxation of orientation after cessation of shear was investigated for the uncompatibilized (sPP20/9/0) and the compatibilized (sPP20/9/9) hybrids. Orientation relaxation of individual colloidal particles under quiescent conditions is expected occur by Brownian motion, which can be described by the simple equation [12]

$$\frac{\partial f}{\partial t} = \Theta \frac{\partial^2 f}{\partial \phi^2} \tag{8.2}$$

where $f(\phi,t)$ is the fraction of particles oriented at angle ϕ at a time t and Θ is the rotational diffusion coefficient. The orientation relaxation can be expected to follow an exponential decay function starting from an initial condition f_0 corresponding to the pre-shear orientation. Thus

$$f \approx f_0 e^{-t\Theta} \tag{8.3}$$

For an ellipsoidal particle the rotational diffusivity is related to the particle dimensions and to the matrix viscosity by [12]

$$\Theta = \frac{3kT}{16\pi\eta_{matrix}a^3}\left[2\ln\left(\frac{2a}{b}\right)-1\right] \tag{8.4}$$

Here, a and b are the dimensions of an ellipsoidal particle along the major and minor axes, η_{matrix} is the matrix viscosity, k is the Boltzmann constant and T is the absolute temperature. The clay tactoids can be approximated as disk-like particles having approximate dimensions of $a = 500\,\text{nm}$ (diameter) and $b = 30\,\text{nm}$ (thickness). [13] For sPP20/9/9 the matrix has a zero-shear viscosity of about 833 Pa s at 190^{o}C. Substituting these values in e. q. 8.4 gives a rotation diffusivity of $\Theta \sim 10^{-6}$ 1/s. Thus, individual, non-interacting clay tactoids can be expected to relax very slowly due to the high aspect ratio and the high viscosity of the polymer melt matrix.

The orientation relaxation experiments were conducted by pre-shearing the samples for about 10 minutes in a multipass mode and then stopping the piston motion suddenly while continuing to record the scattered intensity at regular intervals of time after cessation of shear. Data was collected for 4 minutes each at 0, 10, 20 and 30 minutes after cessation of shear. Owing to the finite compressibility of the polymer melt, it continues to flow in the capillary for a short time of approximately 10 s immediately after stopping the piston motion [14]. However, this time is small compared to the XRD data collection time of 4 min so that the first data point can be assumed to be a true representation of the initial orientation relaxation after cessation of shear. The orientation function was calculated from e. q. 8.1.

Figure 8.15 shows the relaxation of orientation for the compatibilized (sPP20/9/9) and the uncompatibilized (sPP20/9/0) samples that were pre-sheared at 1 mm/s piston speed. The lines show the theoretically expected decay of orientation of individual tactoids as per e. q. 8.3; the dashed line is for the uncompatibilized hybrid and the full line is for the compatibilized hybrid. The initial orientation of the uncompatibilized hybrid is lower than that of the compatibilized hybrid and also relaxes very slowly in agreement with the theoretical prediction at least during the experimental timescale

explored here. In contrast, the initial orientation of the compatibilized hybrid relaxes more rapidly over the first 10^3 s as compared to the theoretical prediction. After this time, the orientation remains constant at about $S = 0.56$. Experimental data for nanocomposites of lower clay loading of approximately 7-wt% also showed a similar trend of rapid initial relaxation followed by a slower relaxation to a value of about $S = 0.4$. Experiments at very low clay loading (such as 3-wt%) were not possible due to the reduced scattering intensity. It appears therefore that the rapid initial relaxation is caused by factors other than simple Brownian motion. One possible reason could be the attractive forces between clay tactoids that act like a body force for relaxation. However, the much slower relaxation of the clay tactoids in the uncompatibilized hybrids of similar clay loading suggests that attractive forces may not be the cause of the rapid relaxation. As we have discussed in the chapter 7, it is also possible that the anhydride group of the PPMA is interacting with the silanol (Si-OH) groups present on the edges of the tactoids. It is therefore possible that, if the polymer chains of the matrix are coupled with the clay tactoids via compatibilizer, then the stress relaxation of the matrix polymer might accelerate the orientation relaxation of the clay tactoids. The absence of such a coupling (via compatibilizer) in the uncompatibilized hybrid could explain the much slower relaxation as well as the smaller initial orientation of the clay in this sample.

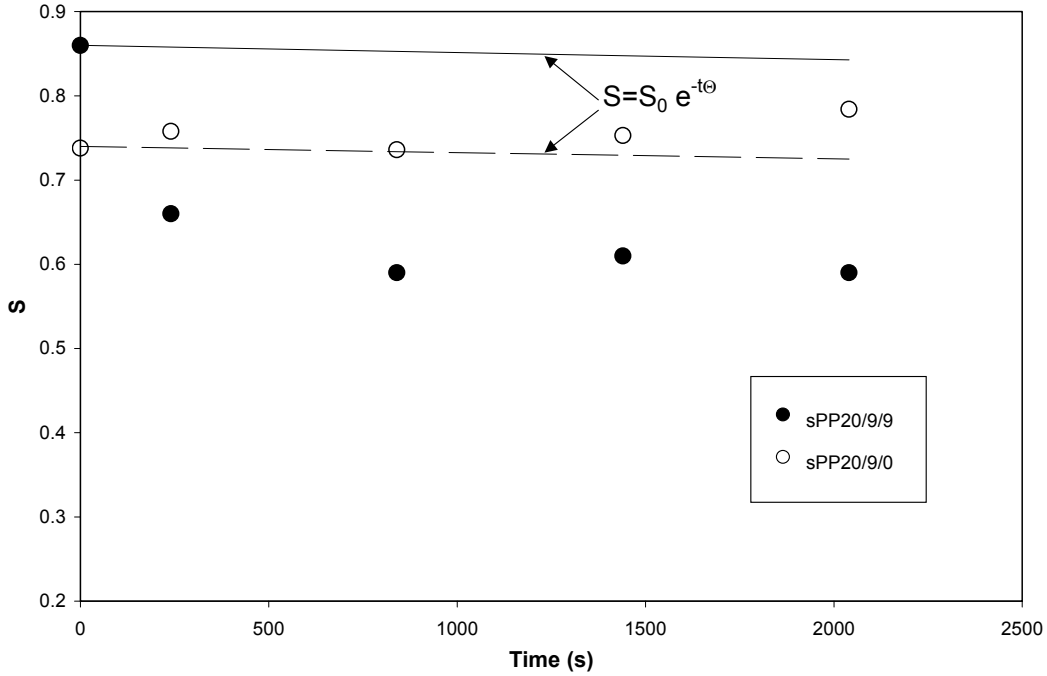

Figure 8.15. Relaxation of orientation after the cessation of steady shear at T = 190°C

8.6. Summary

The linear rheology of compatibilized intercalated polypropylene nanocomposite indicates that under quiescent conditions, the microstructure of the nanocomposites consists of a percolating three-dimensional network of hydrodynamically interacting clay tactoids. However, at higher stresses (or shear rates), the asymmetric clay tactoids might be oriented in the flow direction, leading to the breakage of this network. Once the network breaks, the viscosity drops down by orders of magnitude over very small range of stress and the hybrid shows yield-like behaviour.

The characteristic microstructural relaxation time estimated to be about 10^3 s from the stress ramp data matches with long time saturation of the $G(t)$ at 1000 s. Thus the non-linear rheological experiments are indicative of an apparent yielding process that might be linked to orientation of the clay tactoids.

The rheological experiments were methods of probing the microstructure indirectly. A direct technique namely, in-situ rheo-XRD, was also used to quantify the flow induced microstructural changes. High degree of orientation was observed at shear stresses greater than the yield stress. Extrapolation of the orientation data to low stresses suggests that yielding is associated with a small amount of orientation that is perhaps just enough to break the percolating network structure. The rheological data for the uncompatibilized hybrid showed a much smaller zero shear viscosity and a much less pronounced yield-like behaviour and the corresponding rheo-XRD data showed a lesser orientation of the clay.

Another rheology-microstructure link was obtained from the transient experiments. The orientation relaxation experiments after cessation of shear showed that the clay tactoids relax their orientation incompletely in approximately 1000 s after which the orientation remains frozen in. Correspondingly, the stress relaxation data shows relaxation in 1000 s followed by a plateau in the modulus. The orientation relaxation time from the rheo-XRD measurements matched with the characteristic microstructural relaxation time scale estimated from the rheological data. Since the Brownian relaxation time scale is expected to be much longer, it is possible that the stress relaxation of the matrix chains, which are compatibilized with the clay platelets, drives the orientation relaxation in about 10^3 s. After this time scale the clay tactoids are jammed to produce a percolating network that has a residual orientation and a residual relaxation modulus. The stress relaxation data for the uncompatibilized hybrid indicates that the relaxation of matrix polymer is decoupled with that of the weak structure formed by the clay. Thus, most of the stress in a step-strain experiment is bourn by the polymer matrix, which then relaxes in a manner similar to the pure polymer melt. The corresponding rheo-XRD data also suggests that the orientation is smaller during pre-shear and relaxes extremely slowly and independently of the matrix polymer. In the case of a steady shear experiment, at shear rates of below 10^{-3} s^{-1} the clay tactoids would have sufficient time to relax their orientation and hence give a response corresponding to that of a percolating network. At shear rates above 10^{-3} s^{-1} the clay tactoids will have insufficient time to relax their orientation, which will trigger a destruction of the network causing a yield-like response. The results presented in chapter 7 and 8 described the interlinks between the

microstructure of the hybrids and their flow behaviour. The relatively slow relaxation of clay orientation compared to the melt processing time scales suggests the possibility of trapping residual orientation from the melt state into the solid state after processing operations. The solid-state properties of the hybrids would be expected to depend on the trapped clay orientation. Studies on the modulus of hybrids in the solid state are described in chapter 9.

References List:

1. Barnes, H. A. *J. Non-Newtonian Fluid Mech.* **1999,** *81,* 133-178.
2. Krishnamoorti, R.; Giannelis, E. P. *Macromolecules* **1997,** *30*(14), 4097-4102.
3. Krishnamoorti, R.; Ren, J.; Silva, A. S. *J. Chem. Phy.* **2001,** *114*(11), 4968-4973.
4. Fornes, T. D.; Yoon, P. J.; Keskkula, H.; Paul, D. R. *Polymer* **2001,** *42*(25), 9929-9940.
5. Macosko, C. W. *Rheology principles, Measurements, and Applications;* Wiley-VCH Inc.: N.Y., **1994**.
6. Ugaz, V. M.; Burghardt, W. R. *Macromolecules* **1998**, *31*(24), 8474-8484.
7. Gervat, L.; Mackley, M. R.; Nicholson T. M.; Windle, A. H. *Phil. Trans. R. Soc. Lond.* A **1995**, 350, 1-27.
8. Ugaz, V. M.; Burghardt, W. R.; Zhou, W.; Kornfield, J. A. *J. Rheol*. **2001** *45*(5), 1029-1063.
9. Medellin-Rodriguez, F. J.; Burger, C.; Hsiao, B. S.; Chu, B.; Vaia, R.; Phillips, S. *Polymer* **2001,** *42*(21), 9015-9023.
10. Schmidt, G.; Nakatani, A. I.; Butler, P. D.; Karim, A.; Han, C. C. *Macromolecules* **2000,** *33*(20), 7219-7222.
11. Okamoto, M.; Nam, P. H.; Maiti, P.; Kotaka, T.; Nakayama, T.; Takada, M.; Ohshima, M.; Usuki, A.; Hasegawa, N.; Okamoto, H. *Nano Letters* **2001,** *1*(9), 503-505.
12. Alexander, A. E.; Johnson, P. *Colloid Science*; Oxford University Press, U.K., **1949**.
13. Ren, J.; Silva, A. S.; Krishnamoorti, R. *Macromolecules* **2000,** *33*(10), 3739-3746.
14. Ranganathan, M.; Mackley, M. R.; Spiteller, P. J. H. *J. Rheol*. **1999**, *43*(2), 443-451.

Chapter 9 Solid state properties of sPP nanocomposites

The flow behaviour of melt processed, intercalated polypropylene nanoclay composites and the linkages between the rheology and microstructure in the nanocomposite melts was discussed in chapters 7 and 8. This chapter describes the links between flow-induced orientation of clay and the solid-state properties, in particular the tensile modulus, of syndiotactic polypropylene nanoclay composites in a semi quantitative manner. The aim is to use the experimentally measured clay orientation to predict the tensile modulus of nanocomposites using micromechanical models.

9.1. Solid state microstructural characterization of sPP nanocomposites

Melt intercalated sPP nanocomposites (see Table 5.5) were extruded into tapes using the Rheovis 2100 capillary rheometer equipped with a slit die, as described in chapter 5. The compatibilized hybrids (sPP20/9/9), the uncompatibilized hybrids (sPP20/9/0) hybrids and the polymer matrix (sPP20/0/9) were chosen as the representative samples to study the effect of melt processing on the Youngs modulus of the hybrid. Figure 9.1 shows data on the viscosity and clay orientation vs. wall shear stress (σ_w) for the compatibilized hybrid (sPP20/9/9), as was discussed in chapter 8 (see Fig. 8.13). The five values of σ_w at which the tapes were extruded are marked by arrows in Figure 9.1. The piston speed range spanned from the minimum achievable speed in the capillary rheometer to a high wall shear stress value, where the clay orientation in the melt state had reached a saturation value. The corresponding wall shear stress values of these extruded tapes are tabulated in the Table 9.1.

In addition to the extruded tapes, one film of compatibilized hybrid (sPP20/9/9) was prepared by compression molding at 190^{o}C.

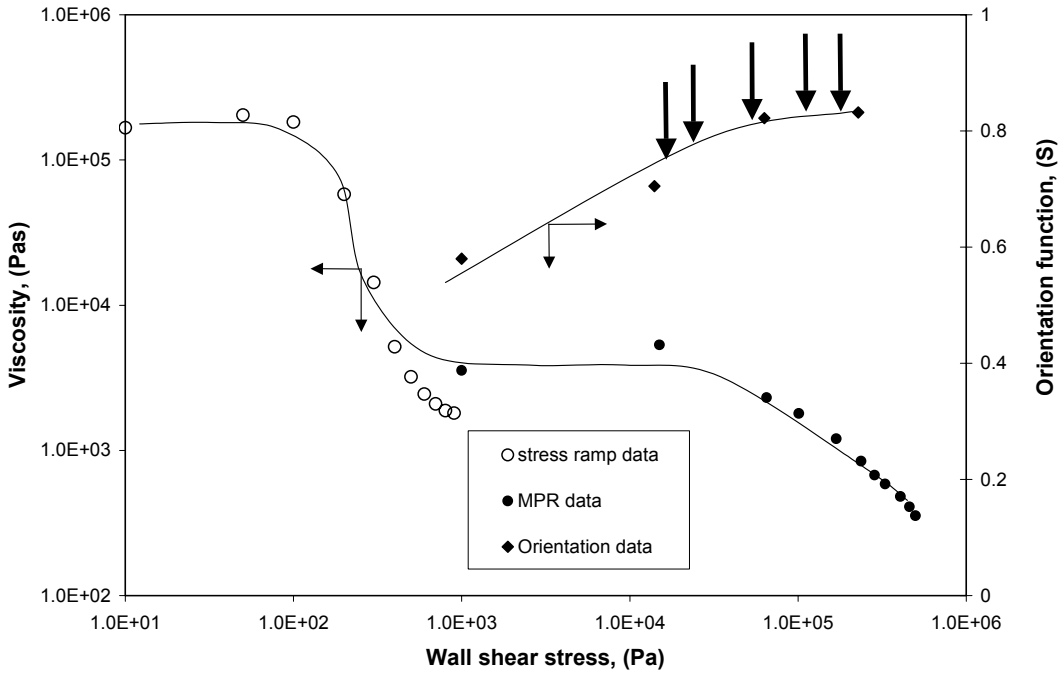

Figure 9.1. Orientation function and viscosity of the compatibilized hybrid (sPP20/9/9) as a function of wall shear stress at T= 190^{o}C. The arrows indicate the wall shear stress used for the tape extrusions

Table 9.1. Wall shear stress for the tape extrusion at the corresponding piston speed

Piston speed (mm/s)	Wall shear stress (x 10 ^{4}Pa)
0.01	1.05
0.05	4.77
0.5	74.6
0.9	97.5
1.5	123.0

The microstructural characterization of the extruded tapes of (sPP20/9/9), (sPP20/9/0) hybrid, and the polymer matrix (sPP20/0/9) were done using three different x-ray machines, as described in the chapter 5. 1-D x-ray diffraction patterns were obtained from Rigaku dmax 2500 diffractometer. The pristine polymer was scanned in the 2θ range of 5 - 45 deg at a scan speed of 1 deg/min, while the clay and the hybrids

were scanned in the 2θ range of 2 - 45 deg. The sPP and the PP-MA do not give any peak in 2θ range of 2 - 10 deg.

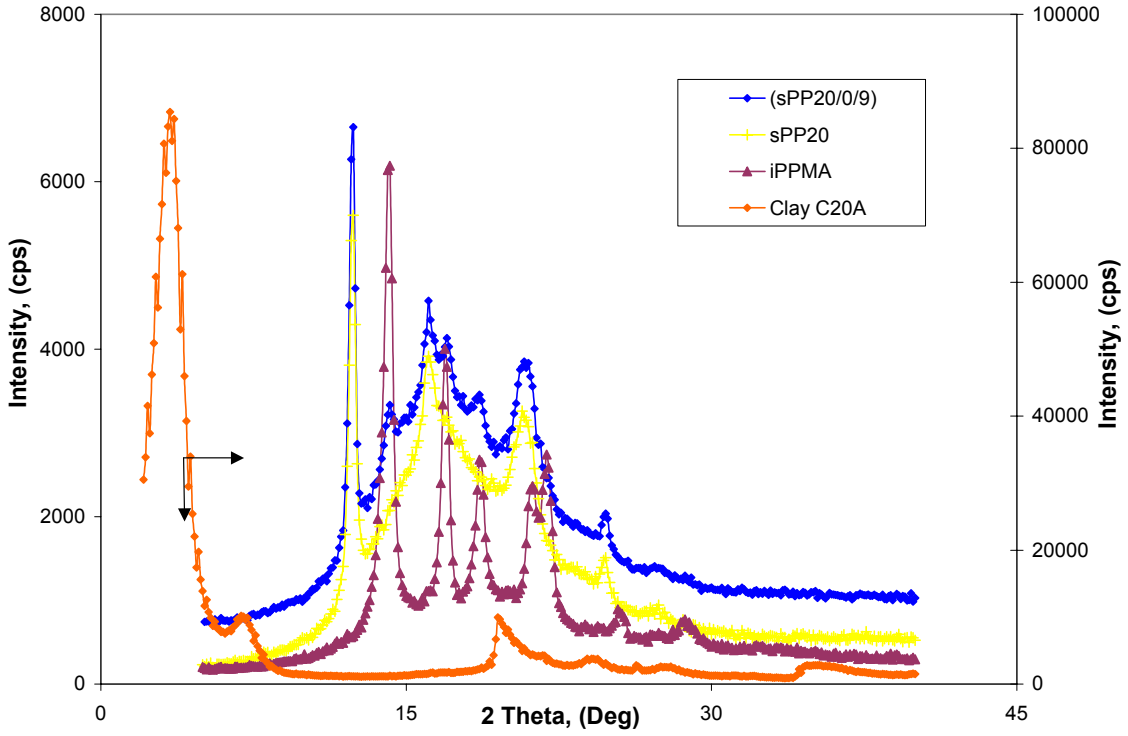

Figure 9.2. X-ray diffraction patterns of polymer matrix (sPP20/0/9), pristine clay (C20A), sPP20 and PP-MA

Figure 9.2 shows the 1-D XRD patterns of the clay (C20A), pristine sPP, PP-MA and the polymer matrix (sPP20/0/9). Figure 9.3 shows the XRD patterns of the uncompatibilized (sPP20/9/0) and the compatibilized (sPP20/9/9) hybrid. The assignment of the various peaks is tabulated in the Table 9.2.

As seen from the Figure 9.2 and 9.3, the polymer matrix (sPP20/0/9) shows peaks of both polymers, i.e., sPP and PP-MA, which is perhaps due to the fact that sPP and PP-MA form an immiscible, micorphase, separated blend. [1-3] The sPP matrix gives strong peak at 7.13 Å (2θ = 12.4 deg) in the polymer matrix and hybrids, while other peaks are broad and weak. The first clay peak for the compatibilized (sPP20/9/9) hybrid is shifted to lower 2θ values compared to the uncompatibilized (sPP20/9/0) hybrid.

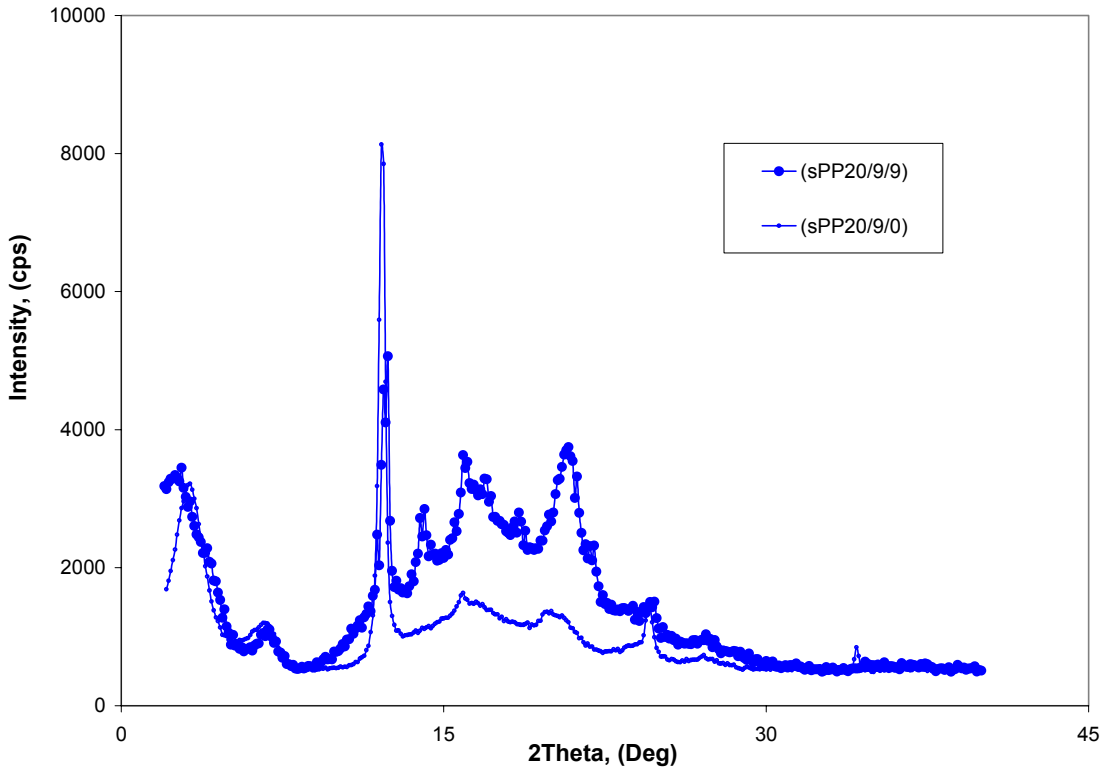

Figure 9.3. X-ray diffraction patterns of uncompatibilized (sPP20/9/0) and compatibilized (sPP20/9/9) hybrids

The clay orientation was measured using a Rigaku x-ray machine having a 'RUH3R' rotating anode x-ray generator with 'RAXIS IV^{++}' image plate detector, which recorded a 2-D x-ray diffraction pattern from the sample. The orientation of the clay tactoids can be described by an orthogonal coordinate system identified by the flow direction, gradient direction and vorticity direction. Clay orientation data for the compatibilized hybrid (sPP20/9/9) at the highest piston speed of 1.5 mm/s along all three directions with respect to the incident x-rays is shown in Figure 9.4 a, b, c. The schematic of the sample orientation is plotted alongside.

As discussed in chapter 8, after yielding the highly asymmetric clay tactoids can be easily oriented in the flow direction. As indicated in Figure 9.1, the tapes were extruded at shear stresses much higher than the yield stress. The melt state investigations showed that the clay tactoids are highly oriented at the corresponding shear rates. It was also shown in chapter 8 that the clay tactoids have a long relaxation time of ~ 1000 s. It may therefore be anticipated that the oriented clay may not be able to relax completely

after extrusion and before solidification. Thus some of the residual orientation in the melt state might get trapped in the solid state.

Table 9.2. Peak positions of clay, polymers and hybrids

2 Theta (Deg)					
sPP	**PP-MA**	**Clay**	**sPP20/0/9**	**sPP20/9/9**	**sPP20/9/0**
		3.40		2.6	3.2
		7.0		6.7	6.8
		19.60			
12.4			12.4	12.3	12.1
	14.2		14.2	14.1	
16.1			16.1	16.0	15.9
	16.9		17.0	16.9	
	18.6		18.6	18.5	
20.8			20.9	20.8	20.7
	21.9		21.7	21.7	
24.7			24.8	24.7	24.6

Figure 9.4 shows the XRD patterns of the compatibilized (sPP20/9/9) hybrid at the highest piston speed, collected along the three mutually perpendicular directions. The diffraction patterns collected along the flow direction (Fig. 9.4A) and vorticity direction (Fig. 9.4B) show distinct axial and equatorial bands, respectively, The appearance of these bands indicates orientation of clay tactoids under the flow with the major axis parallel to the flow direction.

The diffraction pattern along the gradient direction (Fig. 9.4A) shows a ring like pattern indicating no such preferred orientation about the gradient direction. Figure 9.4 A, B, C clearly indicates that the clay platelets are oriented along the flow direction with their major axis along the flow direction and with their surface normal parallel to the gradient direction (or in other words, perpendicular to the plane of flow and vorticity

direction). Thus, the angle ϕ between the surface normal and the flow direction is nearly equal to 90^{o}.

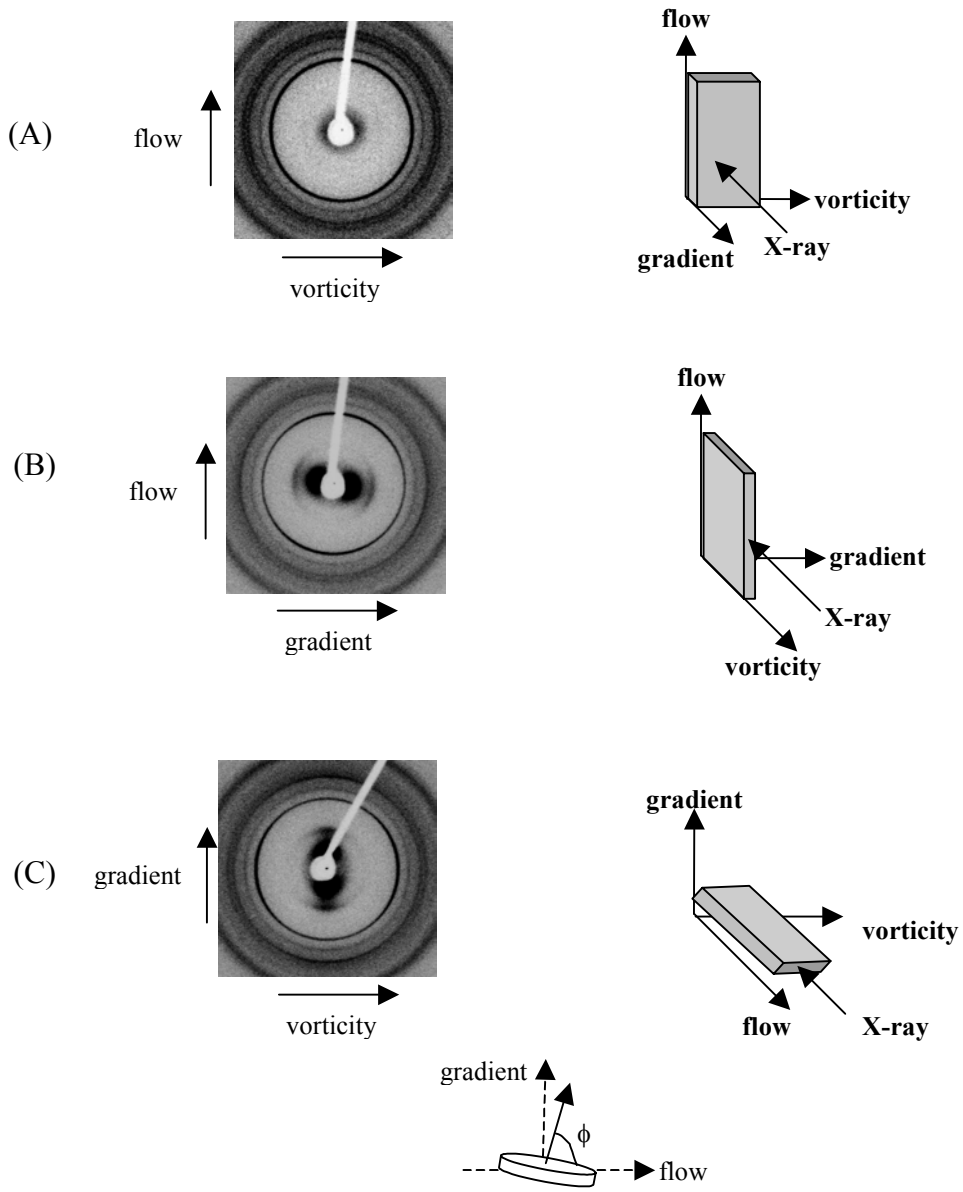

Figure 9.4. 2D-XRD patterns for compatibilized hybrid (sPP20/9/9) a) along gradient axis b) along vorticity axis and c) along flow direction

Bafna et. al. recently reported the 3-D orientation of clay tactoids in blown films of polyethylene nanocomposites. Their results also showed that the clay tactoids were

oriented with their surface normal nearly perpendicular to the machine and transverse directions (i.e., parallel to the film thickness direction). [4]

In the time required to collect the clay data, the polymer diffraction patterns were found to be saturated. In order to look more closely at the orientation of polymer crystalline unit cells, if any, the Bruker Smart Apex CCD single crystal diffractometer was used. The source being Mo target (λ = 0.8 Å), it was possible only to look at the polymer unit cell signals, which appear at higher 2θ values. The clay peaks appearing at lower 2θ were submerged into the beam stop. A comparison of data collected from different x-ray machines for the (sPP20/9/9) sample is tabulated in Table 9.3.

Table 9.3. Comparison of d spacing (Å) obtained from different machines for sPP20/9/9

	1-D R XRD	2-D Ri XRD	2-D Brucker XRD
Clay peaks	33.0	31.2	
	13.1	12.6	
Polymer Peaks	7.2	7.2	7.3
	6.23	6.3	6.28
	5.5	5.5	5.4
	4.4	4.3	4.2
	3.6	3.6	3.6

As shown in Table 9.3, the d-values obtained from all three x-ray machines for all the polymers and clay signals matched well. The PP-MA peaks were not as distinctly visible as the strong sPP signals in both the 2-D XRD machine because of the much smaller content of PP-MA in the sample.

Figure 9.5 A, B, C shows the diffraction patterns for the extruded tapes of the polymer matrix, the uncompatibilized hybrid (sPP20/9/0), and the compatibilized hybrid (sPP20/9/9) respectively, extruded at piston speeds of 0.01 and 1.5 mm/s. As it can be seen from Figure 9.4 A, there is no orientation of polymer crystallites at any of the speeds for the polymer matrix, which is expected from the fact that the relaxation time for the

polymer chains in the melt (as estimated from the crossover frequency in the dynamic frequency sweep at 190^{o}C) is ~ 0.01 s (see Fig 7.18 in chapter 7). Thus the polymer chains relax rapidly after extrusion and before solidification and thereby do not show any orientation.

Figure 9.4 B, C shows the diffraction patterns for the extruded tapes of the uncompatibilized (sPP20/9/0) and the compatibilized (sPP20/9/9) hybrids, respectively, at the same piston speeds of 0.01 and 1.5 mm/s. Clearly, the unit cell of sPP crystallites seems to have some orientation along the flow direction especially at the higher piston speeds. This is in contrast to the behaviour of the polymer matrix and suggests that the clay orientation induces oriented crystallization of sPP matrix.

Orientation of silicates and polymers has also been observed in nylon, [5-10] and PP nanoclay composites. [11] Kojima et. al. have characterized the orientation of silicate layers in nylon-6 nanocomposites using XRD and TEM. [8,9] They reported three different regions of orientations as a function of depth in an injection molded sample. Near the center of the sample, where the shear forces are minimal, the silicate layers and the polymer crystallites were found to be randomly oriented with the chain axes of the polymer crystallites oriented perpendicular to the silicate layers. Near the surface, where the shear stress would be very high, the silicate layers and chain axes of the polymer crystallites were found to be parallel to the bar surface. In the intermediate shear region, the clay layers, due to their asymmetric nature, were still oriented parallel to the bar surface, but the chain axes of the polymer crystallites was perpendicular to the silicate layers. [9] Varlot et. al. also demonstrated that the γ phase was induced in the nylon matrix due to orientation, and the polymer lamellae grew on the silicate sheet with chain axes parallel to the silicate layer. [7,10]

Given the fact that the sPP chains are not tethered to the clay surface and that they are compatibilized with the clay only via the PP-MA, it is somewhat surprising that they crystallize in oriented structures. The slow stress relaxation seems to support the presence of residual orientation as the melt cools down thereby resulting in the formation of oriented crystallites. Further, the formation of oriented crystallites was observed even for the uncompatibilized hybrids, indicating that the orientation of the clay is driving the formation of oriented crystallites. [10-12]

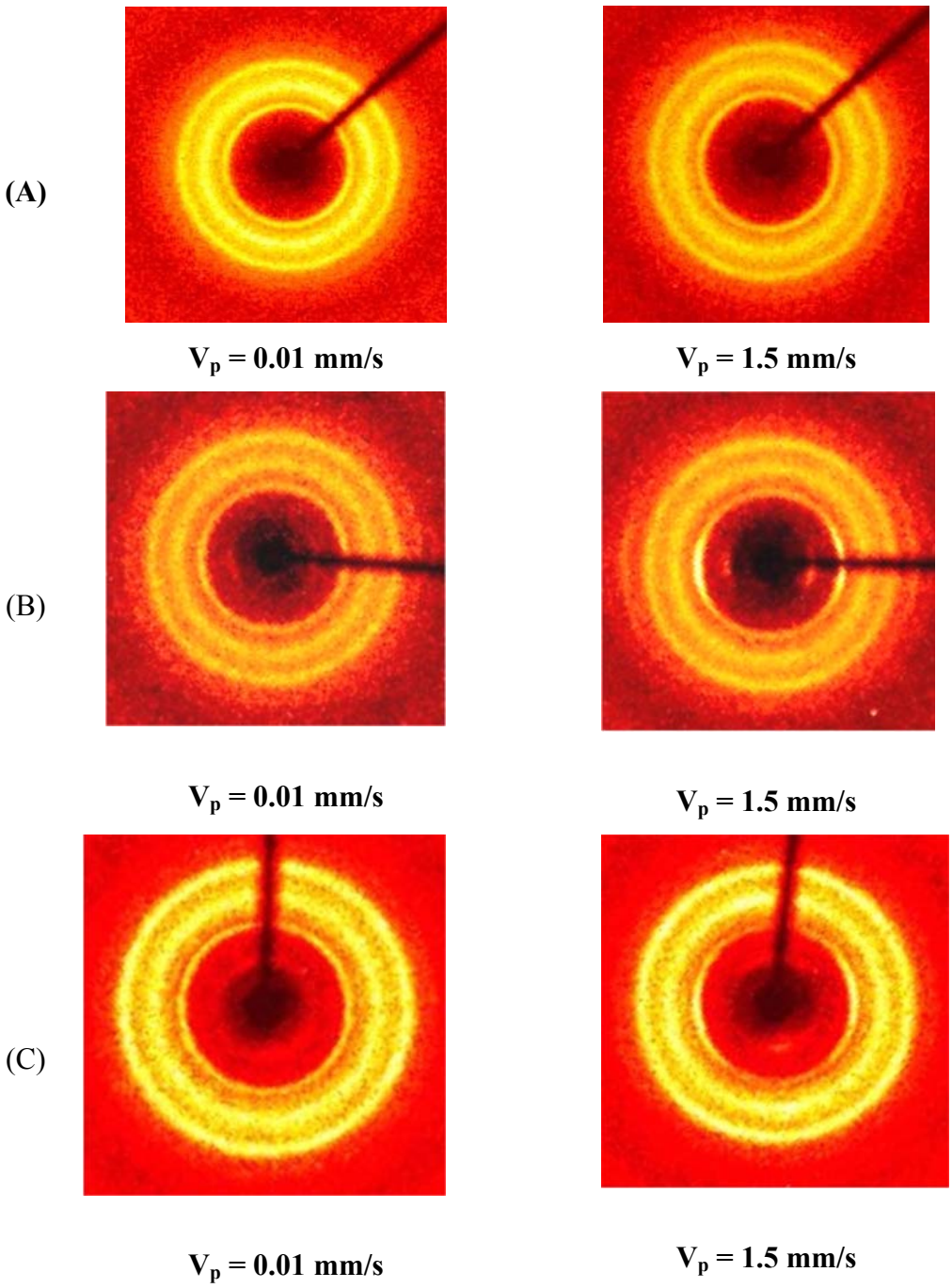

Figure 9.5. X-ray diffraction patterns for a) polymer matrix (sPP20/0/9) b) uncompatibilized hybrid (sPP20/9/0) and c) compatibilized hybrid (sPP20/9/9)

Figure 9.6 (A)-(D) shows the orientation of the clay tactoids, when the x-rays are incident along the vorticity direction, for piston speeds of 0.01, 0.05, 0.9 and 1.5 mm/s,

respectively. The graph on the right shows the azimuthal variation of intensity for the second clay peak (2θ = 12.8°). The processing of data from the main diffraction peak of the clay was not possible since the peak has a $2\theta \sim 2.6°$ (see Fig. 9.3), which is very close to the beam stop. Therefore, all the calculations for clay orientation were done on the peak (2θ= 12.8°) by converting the image plate data into TIFF files, which are then processed using an image processing IMAGE-PROPLUS software. In any case, it is clear from Figure 9.6 that the clay orientation increases with piston speed. At the lower piston speed of V_p= 0.01 mm/s a circular ring-like pattern is seen, while the pattern becomes increasingly elliptical with increasing piston speeds. A distinct equatorial band is seen at the highest piston speed of V_p= 1.5 mm/s. The clay orientation can be quantified by an average orientation function (S) calculated by using e. q. 8.1. The average clay orientation calculated from the data in Figure 9.5 is shown in Table 9.4 for the compatibilized (sPP20/9/9) and the uncompatibilized (sPP20/9/0) hybrids. Also, orientation values calculated for the compression-molded sample are reported. For the compatibilized hybrid the orientation function was found to be minimum for the compression molded sample, whereas it increased with the piston speeds for the extruded tape samples.

Table 9.4. Orientation function of compatibilized and uncompatibilized hybrids

Piston speeds (mm/s)	Orientation Function (S)	
	Compatibilized hybrid (sPP20/9/9)	Uncompatibilized hybrid (sPP20/9/0)
Compression molded hybrid	0.12	-
0.01	0.15	0.25
0.05	0.16	0.27
0.5	0.28	0.26
0.9	0.31	0.27
1.5	0.32	0.26

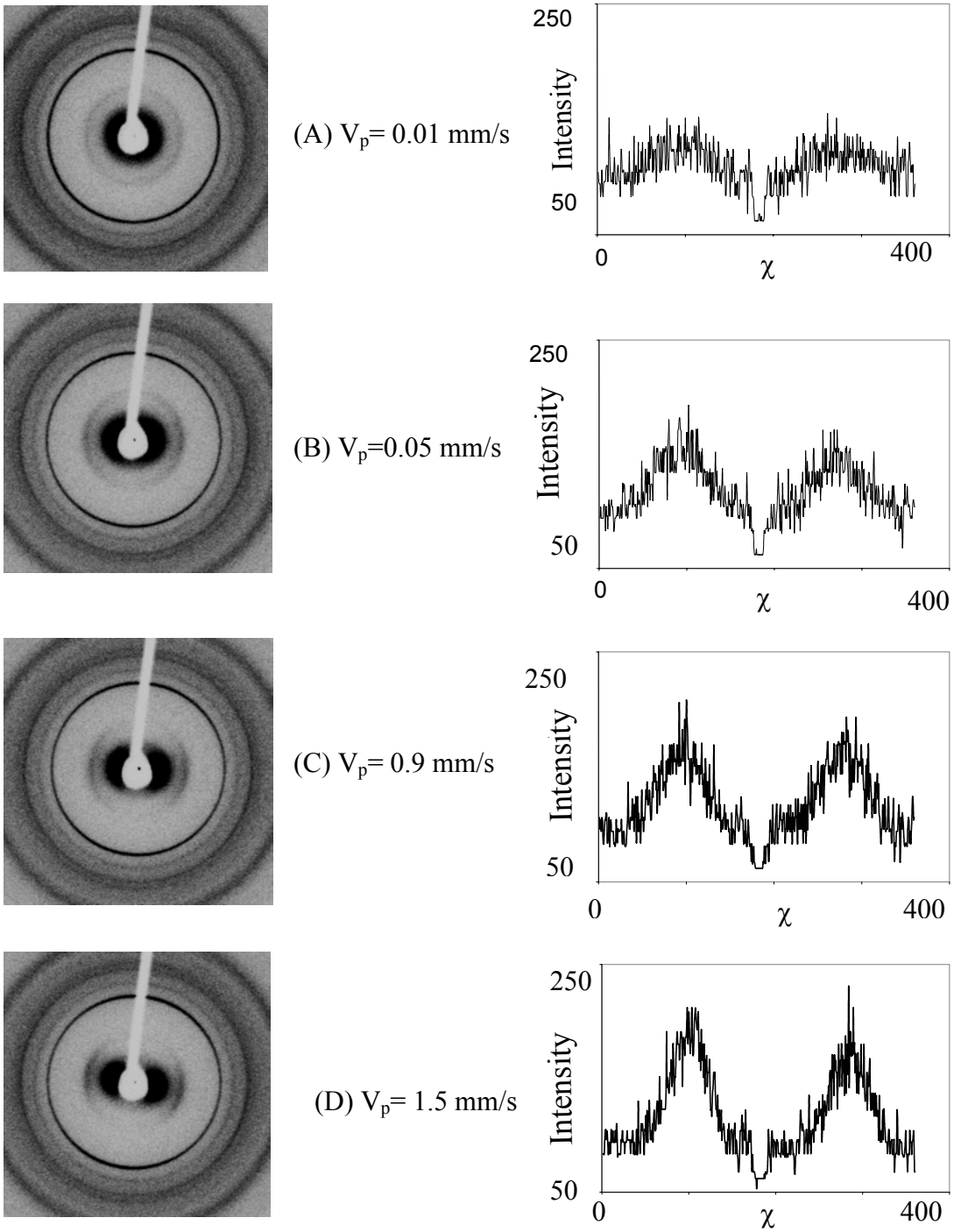

Figure 9.6. X-ray diffraction patterns of the compatibilized hybrid (sPP20/9/9) at different piston speeds along the vorticity direction

Interestingly for the uncompatibilized (sPP20/9/0) tape samples, the orientation values are nearly independent of piston speeds. They were slightly higher for the lower

piston speeds and lower at the high piston speeds compared to those for the compatibilized samples, at the corresponding piston speeds. The high aspect ratio (diameter/thickness) of the clay tactoids combined with the high matrix viscosity means that the Peclet numbers are high even for the low shear rates. Thus clay tactoids can be easily oriented by flow. As discussed in chapter 8, the orientation relaxes relatively faster for the compatibilized hybrid (sPP20/9/9) than for the uncompatibilized hybrid (sPP20/9/0). It is therefore possible that at low piston speeds, the clay orientation relaxes more for the compatibilized tape samples before the solidification. Hence it is not surprising that the orientation values are lower at low piston speeds for the compatibilized tape samples. Further, it is also not surprising that at high piston speeds the clay orientation is higher in the compatibilized tape samples, since the orientation in the melt state itself is higher than for the uncompatibilized hybrids (see Fig. 8.11)

Finally, it is noteworthy that the orientation values reported in Table 9.4 are much lower than the corresponding values in the melt state (see Fig. 9.1). Given that the orientation relaxation for the clay tactoids in the melt is slow, the significantly lower orientation in the tapes could be due to randomization process driven by the crystallization of polymer during cooling.

9.2. Tensile properties of sPP nanocomposites

The ambient temperature tensile properties of the extruded tapes were tested using an Instron 4204 Universal Testing Machine at a crosshead speed of 25 mm/min.

The tensile modulus of the polymer nanoclay composites would depend on the modulus of the polymer matrix, the modulus of the clay platelets, the dispersion of the clay, the clay loading, the degree of crystallinity, the orientation of the clay, the orientation of polymer crystallites and the interfacial stress transfer mechanisms. The compatibilizer determines the dispersion of the clay and the stress transfer between the polymer matrix and the clay, while, the orientation of the clay and polymer crystallites are determined by the deformation history during processing. For the compatibilized (sPP20/9/9) and the uncompatiblized (sPP20/9/0) hybrids, the degree of crystallinity, measured by DSC was found to be similar ~ 8 – 8.5 J/g. Thus, for the given polymer and

clay type and for given clay loading, (sPP, Closite 20A and 9 wt% in the present case) the modulus of the nanocomposite would be determined by the presence of the compatibilizer and the deformation history.

9.2.1. Effect of compatibilizer and clay orientation

Figure 9.7 shows the modulus of the extruded tape samples of both the compatibilized (sPP20/9/9) and the uncompatibilized (sPP20/9/0) hybrids as a function of the piston speed. From the orientation studies described above, it is clear that for the compatibilized tape samples the orientation of the clay and polymer crystallites increases with piston speeds. For the uncompatibilized tape samples the clay orientation remains more or less independent of shear stress. For the compatibilized hybrids, the modulus increased with the piston speed and reached a saturation value at high piston speeds in a manner that follows the clay orientation trend. Similarly, the modulus of the uncompatibilized tape samples remained independent of piston speed, again following the same trend as the clay orientation values. However, unlike the orientation values, the modulus of the uncompatibilized samples is always lower than that for the compatibilized samples. This is possibly due to the absence of an effective stress transfer between the matrix and clay without the compatibilizer.

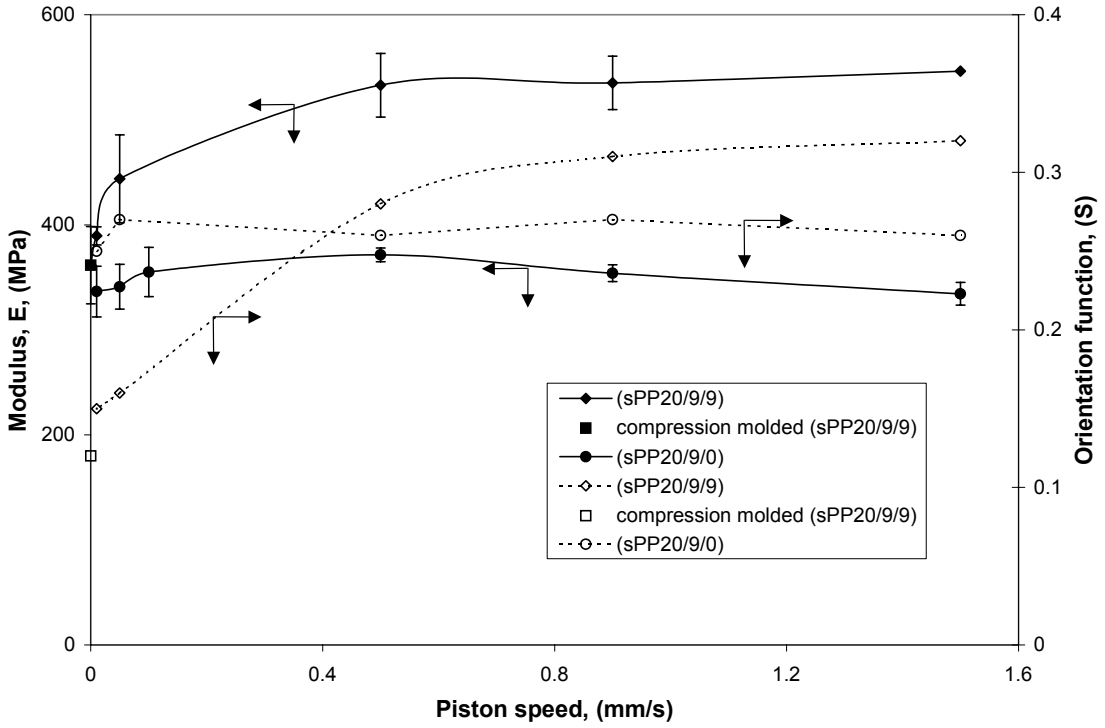

Figure 9.7. Modulus and orientation function at different piston speeds for compatibilized (sPP20/9/9) and uncompatibilized (sPP20/9/0) hybrids

9.2.2. Effect of matrix molecular weight

Figure 9.8 shows the variation of the modulus for the compatibilized hybrids with 9 wt% clay concentration, made from the different molecular weight resins, viz., (sPP4/9/9), (sPP10/9/9) and (sPP20/9/9). A couple of interesting observations can be made in Figure 9.8. First, the modulus of all hybrids increased with the piston speed. The extent of increase was higher for the lowest molecular weight hybrid and smaller for the highest molecular weight hybrid. Second, at the lower piston speeds of 0.01 and 0.05 mm/s the modulus of the hybrid goes through a maximum as a function of the resin molecular weight. Thus, the modulus of sPP10/9/9 was higher than those of sPP4/9/9 and sPP20/9/9. However, at higher piston speeds the modulus of the sPP20/9/9 becomes comparable to that for sPP10/9/9, as shown in Figure 9.8 and 9.9.

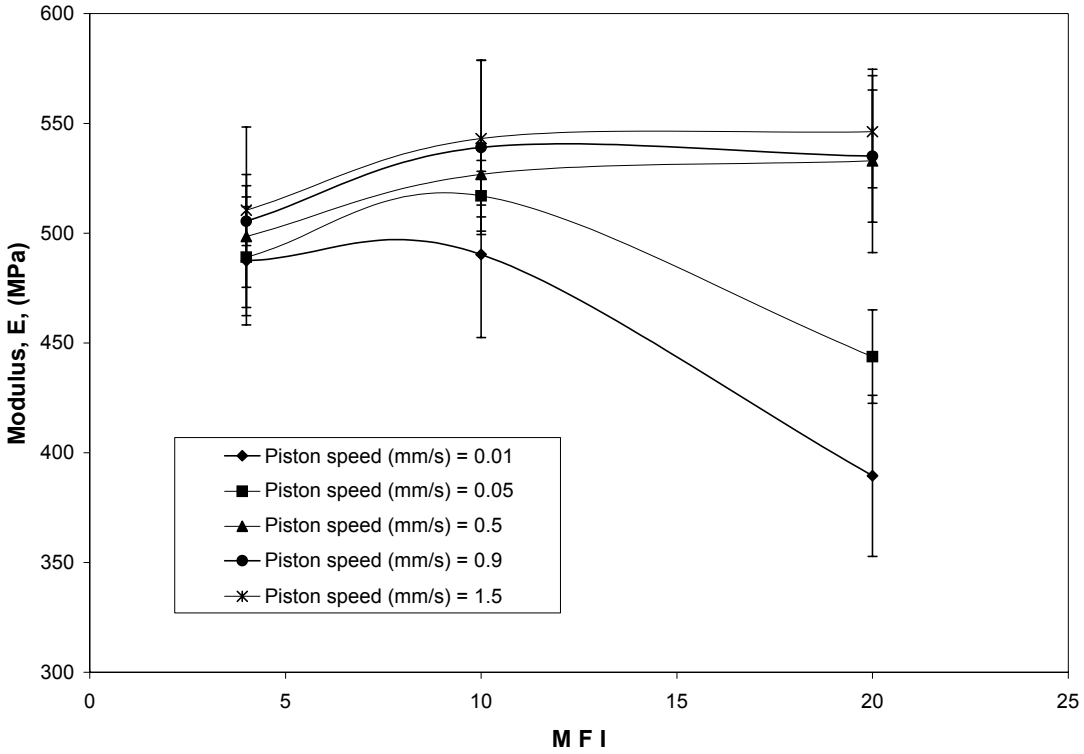

Figure 9.8. Modulus of the compatibilized hybrids (sPP20/9/9), (sPP10/9/9) and (sPP4/9/9) at different piston speeds

As discussed in chapter 8, the zero shear viscosity of the (sPP20/9/9) > (sPP10/9/9) > (sPP20/9/9), which suggests that the dispersion of clay is better in the (sPP20/9/9) compared to (sPP10/9/9) and is the least in (sPP4/9/9). It was suggested that the small chains of the lower molecular weight resin may be able to diffuse more rapidly in the primary clay particles compared to the large chains of the higher molecular weight resins, leading to the higher intercalation and/or better dispersion in lower molecular weight resin hybrids. It may therefore be expected that the extent of reinforcement due to the clay would be the highest for sPP20/9/9 compared to sPP4/9/9 and sPP10/9/9. Hence modulus of sPP20/9/9 would be higher.

On the other hand, the modulus of the matrix resin itself decreases with the decrease in the molecular weight as seen in the Figure 9.9. Thus, there are two competing effects viz., the modulus of the hybrid increases with the resin molecular weight due to the increase in modulus of the matrix resin with molecular weight and the modulus of the

hybrid decreases with resin molecular weight, due to the decrease in the extent of dispersion of the reinforcing clay with increase in the resin molecular weight.

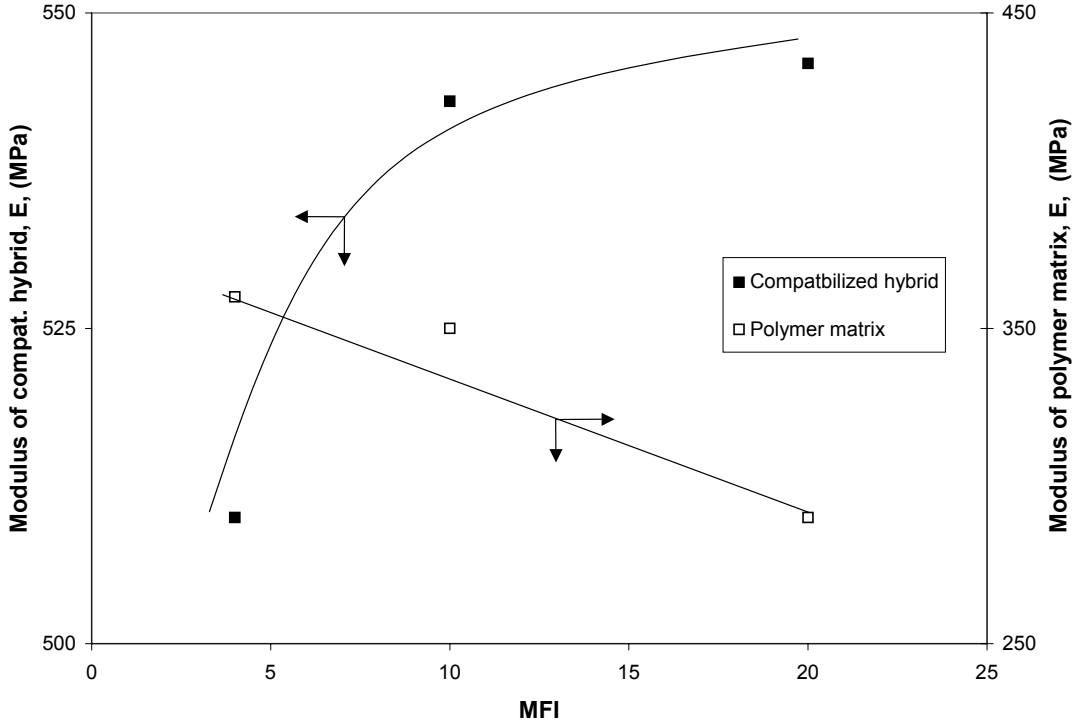

Figure 9.9. Modulus of the polymer matrix and the compatibilized hybrid at piston speed (V_p= 1.5 mm/s)

At low piston speeds the interplay between these competing influences may result in a maximum modulus for the intermediate molecular weight resin. However, at high piston speeds, the orientation of the clay perhaps dominates the modulus of the hybrids. The ratio of wall shear stress (σ_w) / yield stress (σ_y) was found to be 1.23 x 10^3, 0.6 x 10^3 and 0.8 x10^3 for (sPP20/9/9), (sPP10/9/9) and (sPP4/9/9) respectively, for the piston speed (V_p=1.5 mm/s). Thus, for the given piston speed the (sPP20/9/9) hybrid was subjected to a relatively higher wall shear stress with respect to its yield stress, compared to the (sPP10/9/9) and (sPP4/9/9). Thus the orientation in sPP20/9/9 could be higher at higher piston speeds and hence its modulus increases to become nearly equal to that of the sPP10/9/9 composite.

9.3. Micromechanical model

It can be seen from the previous sections that the modulus of the hybrid is related to the orientation of the clay and the polymer produced due to the melt processing operations. In this section an attempt is made to quantify these links using a micromechanical model. Recently, Brune et. al. proposed such a model based on the Halpin-Tsai model to show that the reinforcement efficiency decreases even with small off-plane deviation from perfect in-plane orientation. [13]

In the present work, a simplified version of the micromechanical model of Brune et. al. is used to predict the tensile modulus of extruded tapes of intercalated sPP-nanoclay composites. [13] Orientation in the extruded tapes was measured as described in 9.1 and fed to the micromechanical model to predict the modulus, which was then compared with the experimental tensile test data.

For a compatibilized nanoclay composite the tensile modulus may be estimated from the micromechanical model in a manner analogous to that for a conventional composite. [14,15] Brune et. al. have shown that for the intercalated (or incompletely exfoliated) nanocomposites having perfectly aligned silicate layers along the flow direction the tensile modulus may be calculated from the Halpin-Tsai equation as [16,17]

$$E_A = \frac{E_{composite}}{E_{matrix}} = \frac{1 + 2A_f^{'}\eta'\phi'}{1 - \eta'\phi'} \tag{9.1}$$

where $A_f^{'}$ is the aspect ratio of the tactoids given by

$$A_f^{'} = \frac{A_f}{\hat{N}}\left(\frac{1}{1 + (1 - 1/\hat{N})\frac{s}{t}}\right) \tag{9.2}$$

Here A_f is the aspect ratio of a single platelet (ratio of diameter to thickness). The corrected volume fraction of clay tactoids (i.e., for the incomplete exfoliation) (ϕ') in the e. q. 9.1 is given by

$$\phi' = \phi\left[1 + \left(1 - 1/\hat{N}\right)\frac{s}{t}\right] \tag{9.3}$$

Here ϕ is the volume fraction of clay assuming complete exfoliation.

And η' in the e. q. 9.1 is given as,

$$\eta' = \frac{E_r' - 1}{E_r' + 2A_f'} \tag{9.4}$$

where E_r' is the ratio of the modulus of the platelet stack to the matrix, in the e. q.9.1and is given as

$$E_r' = E_r \left(\frac{1}{1 + (1 - \hat{N}) \frac{s}{t}} \right) + \frac{(1 - 1/\hat{N}) \frac{s}{t}}{1 + (1 - 1/\hat{N}) \frac{s}{t}} \tag{9.5}$$

where, E_r is the ratio of the platelet to the matrix modulus and

$$\hat{N} = N + (1 - N)\left(\frac{s}{t}\right)\left(\frac{\phi}{1 - \phi}\right) \tag{9.6}$$

where N is the number of platelets in a stack. The ratio $\frac{s}{t}$ represents the ratio of the distance between the platelets in a stack to the platelet thickness.

Equation 9.1 gives the modulus of hybrids for the case of perfect alignment of the reinforcing filler. On the other hand, Figure 9.6 shows that the clay tactoids have a distribution of orientation around perfect alignment. Following Krenchel's approach, the modulus of a composite in which the reinforcement is aligned at an angle θ to the tensile load can be estimated as [18]

$$E = E_A \cos^4 \theta \tag{9.7}$$

For a distribution of orientation we assume that the modulus may be estimated as

$$E = E_A \left\langle \cos^4 \theta \right\rangle \tag{9.8}$$

where, the average orientation can be calculated from the 2-D x-ray diffraction data as

$$\left\langle \cos^4 \theta \right\rangle = \frac{\int_0^{2\pi} I(\theta) \cos^4 \theta d\theta}{\int_0^{2\pi} I(\theta) d\theta} \tag{9.9}$$

where, θ is the angle between the normal to the clay tactoids and the gradient direction ($\theta = 90 - \phi$, in Fig. 9.4) and $I(\theta)$ is the azimuthal intensity measured when the x-rays are incident along the vorticity direction (see e. q. 9.7).

Figure 9.10 shows a comparison between the modulus predicted from e. q. (9.1)-(9.9) and the experimentally measured values. The model requires the values of the modulus for the matrix, which is 300 MPa for the matrix polymer (sPP20/0/9) and the modulus of the clay platelets, which is reported to be 1.72 GPa. [19-22] The predicted values are in the range of the experimentally measured values and qualitatively follow the experimentally measured values of modulus, indicating that the micromechanical model can be used to estimate the mechanical properties of polymer nanoclay composites from independently measured orientation of the clay. It is indeed a bit surprising that the modulus of the hybrids can be predicted only from the clay orientation given that the polymer crystallites also orient in the compatibilized and uncompatibilized hybrids. More accurate predictions of the modulus of the hybrid may be obtained by considering the effects of polymer orientation and by solving the full tensorial constitutive equation for the composite as suggested by Brune et. al.

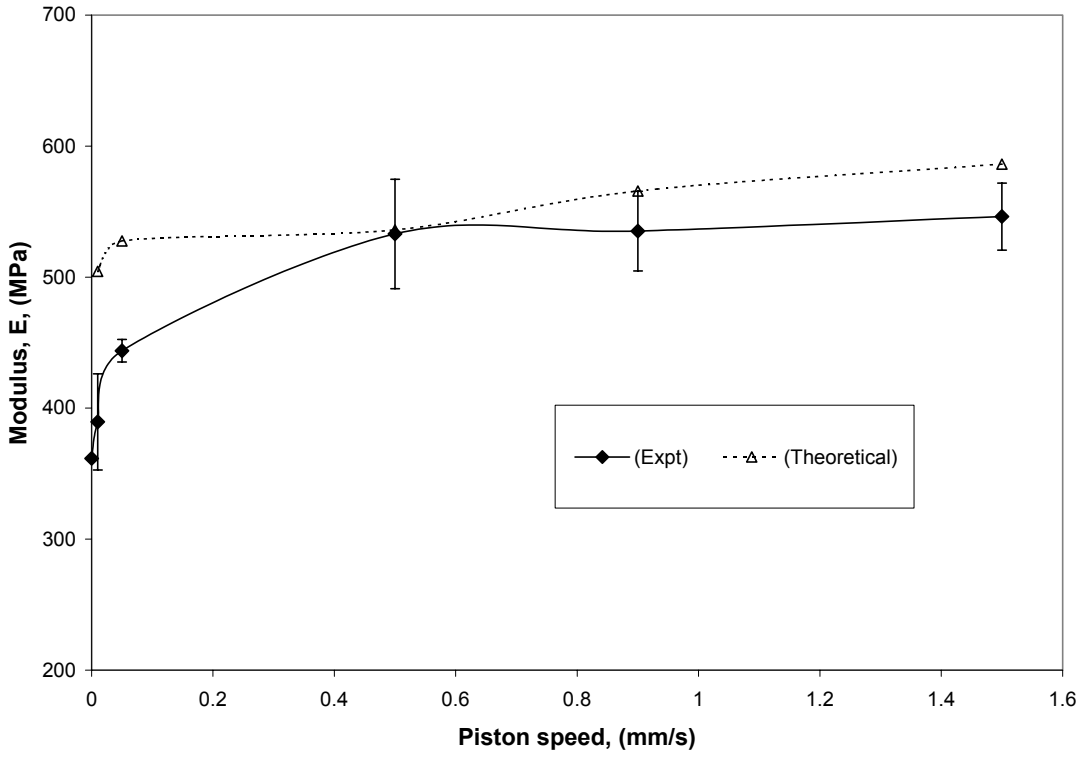

Figure 9.10. Comparison of experimental modulus and theoretical modulus at different piston speed for compatibilized (sPP20/9/9) hybrids

9.4. Summary of structure-processing-property relations in intercalated PP nanocomposites

The linear rheological analysis in chapter 7 shows that in the compatibilized intercalated polypropylene nanocomposite under quiescent conditions, the microstructure consists of a percolating three-dimensional network of hydrodynamically interacting clay tactoids. However, at higher stresses (or shear rates), the asymmetric clay tactoids might be oriented in the flow direction, leading to the breakage of this network. Once the network breaks, the viscosity drops down by several orders of magnitude over very small range of stress and thus the hybrid shows yield-like behaviour.

The rheological experiments provided methods of probing the microstructure indirectly. A direct technique namely, in-situ rheo-XRD, was also used to quantify the flow-induced microstructural changes, as discussed in chapter 8. A high degree of orientation was observed at shear stresses greater than the yield stress. Extrapolation of the orientation data to low stresses suggests that yielding is associated with a small amount of orientation that is perhaps just enough to break the percolating network structure. The rheological data for the uncompatibilized hybrid showed a much smaller zero shear viscosity and a much less pronounced yield-like behaviour and the corresponding rheo-XRD data showed a smaller orientation of the clay.

It was found from the rheological studies that the microstructure at low stresses had a characteristic relaxation time, which was seen to be 1000 s for the compatibilized sPP nanocomposite. The rheo-XRD data showed that this time corresponded to one over crossover frequency, which the oriented tactoids managed to relax some of their orientation. Thus, at shear rates of below 10^{-3} s^{-1} the clay tactoids would have sufficient time to relax their orientation and hence give a response corresponding to that of a percolating network. At shear rates above 10^{-3} s^{-1} the clay tactoids will have insufficient time to relax their orientation, which will trigger a destruction of the network causing a yield-like response. The results presented in chapter 7 and 8 described the interlinks between the microstructure of the hybrids and their flow behaviour. The relatively slow relaxation of clay orientation compared to the melt processing time scales suggested the possibility of trapping residual orientation from the melt state into the solid state after

processing operations. The solid-state properties of the hybrids would be expected to depend on the trapped clay orientation. The effect of clay orientation on the tensile modulus of hybrids was described in chapter 9.

After yielding, the anisotropic clay tactoids are found to orient in the flow direction, with their surface normal perpendicular to the flow direction. The orientation of the clay tactoids, increased with increasing shear rate and reached a plateau value. The tensile modulus of the compatibilized hybrid (sPP20/9/9) was found to increase with increasing orientation of clay tactoids and in analogy to the clay orientation, reached a plateau value. However, in the case of the uncompatibilized hybrid (sPP20/9/0) the increase in the orientation of the clay tactoids did not result in the corresponding increase in the tensile modulus. This is attributed to the absence of effective stress transfer agent like PP-MA between the polymer matrix and the reinforcing clay tactoids. Besides the clay orientation, the increase in the tensile modulus was found to be dependent mainly on the extent of dispersion and the molecular weight of the resin. The discussion in chapter 8 shows that the molecular weight and extent of intercalation are inversely proportional. The modulus of the hybrid increased with the resin molecular weight due to the increase in modulus of the matrix resin and it decreased with resin molecular weight, due to the decrease in the extent of interaction with increase in the resin molecular weight. Finally, a simplified micromechanical model, which was originally developed for the conventional composites, was found to predict the modulus of the PP nanocomposites in a semi quantitative manner. The clay orientation data was used as an input to the model.

Reference List:

1. Thomann, R.; Wang, C.; Kressler, J.; Juengling, S.; Mulhaupt, R. *Polymer* **1995,** *36*(20), 3795-3801.
2. Thomann, R.; Kressler, J.; Setz, S.; Wang, C.; Mulhaupt, R. *Polymer* **1996,** *37*(13), 2627-2634.
3. Thomann, R.; Kressler, J.; Rudolf, B.; Mulhaupt, R. *Polymer* **1996,** *37*(13), 2635-2640.
4. Bafna, A.; Beaucage, G.; Mirabella, F.; Mehta, S. *Polymer*, **2003**, *44*(4), 1103-1115.

5. Kojima, Y.; Usuki, A.; Kawasumi, M.; Okada, A.; Fukushima, Y.; Kurauchi, T.; Kamigaito, O. *J. Mater. Res.* **1993**, *8*(5), 1185-1189.
6. Usuki, A.; Koiwai, A.; Kojima, Y.; Kawasumi, M.; Okada, A.; Kurauchi, T.; Kamigaito, O. *J. Appl. Polym. Sci.* **1995,** *55*(1), 119-123.
7. Varlot, K.; Reynaud, E.; Klopper, M.; Vigier, G.; Varlet, J. *J. Polym. Sci. Part. B: Polym. Phys*. **2001**, *39*(12), 1360-1370.
8. Kojima, Y.; Usuki, A.; Kawasumi, M.; Okada, A.; Kurauchi, T.; Kamigaito, O.; Kaji, K. *J. Polym Sci. Part. B: Polym Phys* **1994**, *32*(4), 625-630.
9. Kojima, Y.; Usuki, A.; Kawasumi, M.; Okada, A.; Kurauchi, T.; Kamigaito, O.; Kaji, K. *J. Polym Sci. Part B: Polym Phys.* **1995**, *33*(7), 1039-1045.
10. Varlot, K.; Reynaud, E.; Vigier, G.; Varlet, J. *J. Polym. Sci. Part B: Polym. Phys*. **2002**, *40*(2), 272-283.
11. Okomoto, M.; Nam, P.; Maiti, P.; Kotaka, T.; Nakayama, T.; Takada, M.; Ohshima, M.; Usuki, A.; Hasegawa, N.; Okomoto, H. *Nanoletters* **2001**, *1*(9), 503-505.
12. Medellin-Rodriguez, F. J.; Burger, C.; Hsiao, B. S.; Chu, B.; Vaia, R.; Phillips, S. *Polymer* **2001,** *42*(21), 9015-9023.
13. Brune, D. A.; Bicerano J. *Polymer* **2002**, *43*(2), 369-387.
14. Nielson, L. *Mechanical properties of polymers and composites* vol. 2 Marcel Dekkar, Inc.; **1974**.
15. Mccrum, N. G.; Buckley, C. P.; Bucknall, C. B. *Principles of Polymer Engineering*, second Ed.; Oxford science publications.
16. Halpin, J. C.*, Primer on composite materials analysis*, second Ed., Lancaster, PA: Technomic publishing, **1992**.
17. Halpin, J. C.; Kardos, J.L.; *Polym Engg. Sci* **1976**, *16*, 344-352.
18. Folkes, M. J. *Short Fibre reinforced thermoplastics;* Research Studies Press, John Wiley and Sons, U.K.**1982**.
19. Yoon, P. J.; Fornes, T. D.; Paul, D. R. *Polymer* **2002**, *43*(25), 6727-6741.
20. Van E. S.; Xiqiao, F.; Vanturnhout. J.; Van der Giessen E. In: *Comparing polymer-clay nanocomposites with conventional composites using composite modeling,*

Specialty polymer additives: Al Malakia S., Golovoy A., Wilkie C. A., Eds.; Oxford: Blackwell, **2001**.

21. Lusis, J.; Woodhams, B. T.; Xanthos, M. *Polym. Engg. Sci***. 1973**, 13, 139-145.

22. Utracki, L. A., Vu Khanh T., In: *Filled Polymers. Multicomponent polymer systems* Miles I. S., Rostami, S. Eds., Essex: Longman **1992**.

Chapter 10 Polyethylene nanocomposites

This chapter describes the rheological behaviour of polyethylene nanocomposites (PENC) synthesized by in-situ polymerization of ethylene in the presence of clay. The PE nanocomposites were synthesized with and without the heterogenization of the catalyst on the clay surface. Rheological responses of such nanocomposites are discussed.

10.1. Transient creep experiments of PE nanocomposites

Figure 10.1 shows the transient creep response of the representative samples, PENC-1 (600), PENC-1 (1000) and PENC-3 (600) of PE nanocomposites at 170^{o}C for an annealing period of 7.5 hrs. Similar to the PP nanocomposites, the zero shear viscosity (η_o) of the PE nanocomposites increased with annealing period, rapidly initially and then reached a plateau after an annealing period of 1 hr. However, contrary to PP nanocomposites, the overall rise in zero shear viscosity (η_o) for the PE nanocomposites was much smaller. As discussed in chapter 6 (see Fig. 6.11 and 6.12) the PE hybrids were nearly exfoliated, as determined by WAXD. Further microstructural evolution seemingly stopped after 1 hr of annealing.

Also, it is seen that the high molecular weight PE hybrids with 1-wt% clay were stable over an annealing period of 7.5 hrs. However, the zero shear viscosity (η_o) of the PE hybrids containing 5-wt% clay, which are of lower molecular weight and higher polydispersity compared to the (PENC-1 series), decreased at longer annealing time periods. This can be attributed to the degradation of lower molecular weight fraction of the PE. Based on the creep data, the dynamic experiments discussed in the next section, for all samples were performed after an initial annealing of 1 hr.

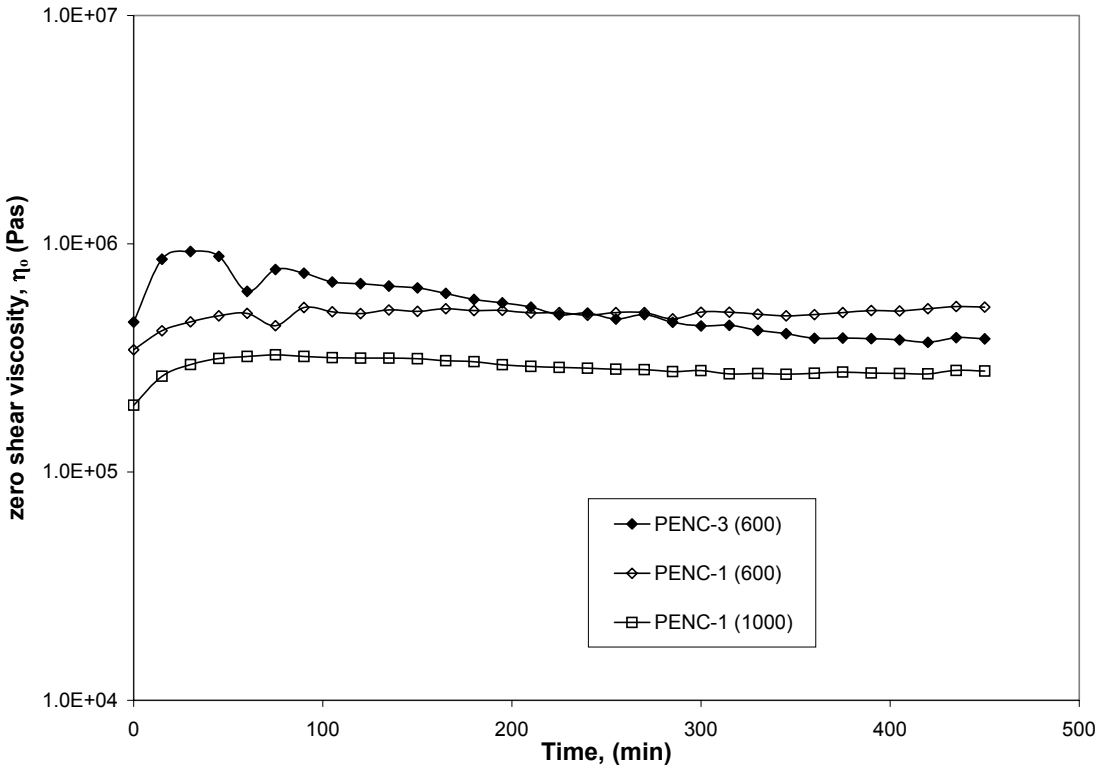

Figure 10.1. Zero shear viscosity as function of annealing time for PE hybrids at T = 170°C, σ_o = 50 Pa

10.2. Dynamic experiments on PE nanocomposites

The linear and nonlinear viscoelastic regions of the PE nanocomposites of PENC-1 (200), PENC-2 (200) and PENC-3 (200) samples were delineated by dynamic strain sweep at 150°C without any pre annealing. As seen in the Figure 10.2, the non-linear region starts at 60%, 8%, 0.7% strains for PENC-1 (100), PENC-3 (1600) and PENC-2 (1600) respectively. As it would be expected, the non-linear region for the higher clay loading sample PENC-3 (1600) starts at lower strain compared to that for the PENC-1 (1600) sample. Interestingly, the non- linear region starts at much lower strain for the PENC-2 (1600) compared to the PENC-1 (1600) even though the clay loading is almost same. Also, the elastic modulus for the PENC-2 (1600) is lower than that for the PENC-1 (1600). Thus, PENC-1 (1600) is more elastic but less non-linear than PENC-1 (1600). This indicates that whether or not the catalyst is heterogenized on the clay has significant impact on the rheological behaviour of the PE nanocomposites. Further dynamic

frequency sweep experiments were performed below non-linear limits of strains to ensure linear response. The dynamic frequency sweep tests were performed in the temperature range of 150-230^{o}C and over frequency range of 0.1-100 rad/s.

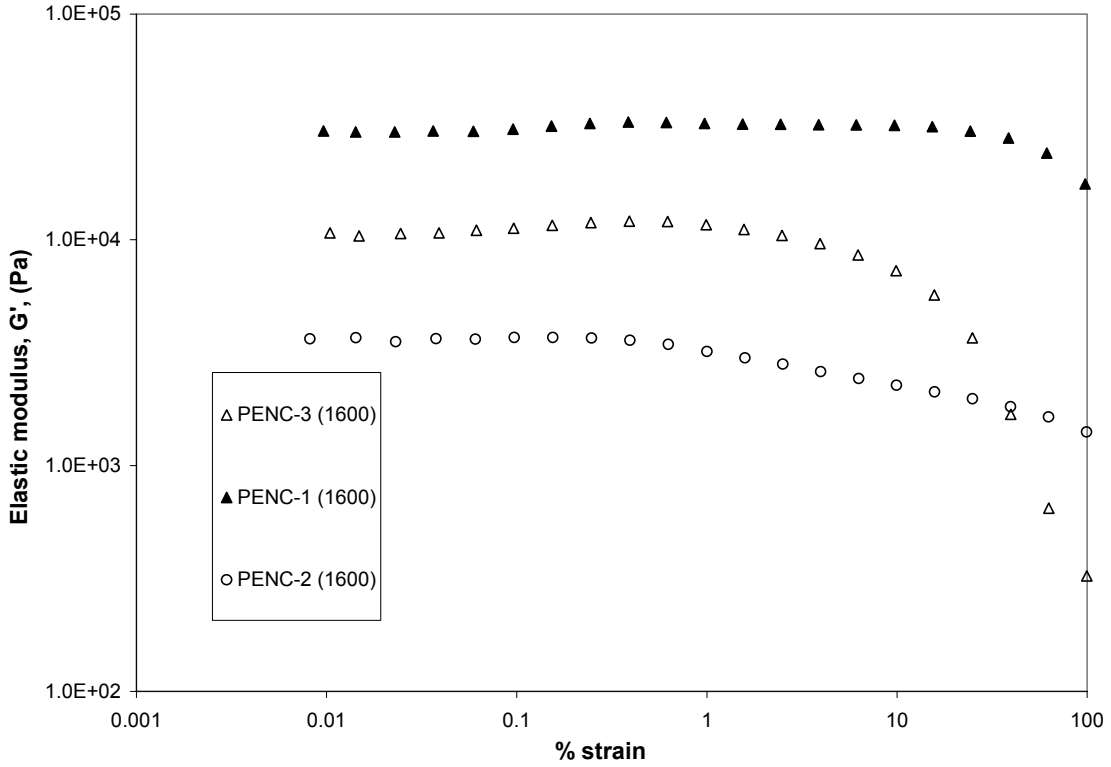

Figure 10.2. Dynamic strain sweep for the PE hybrids at T = 150^{o}C

Figure 10.3 and Figure 10.4 (a), (b) show the dynamic data for these samples viz., pristine PE (1000), PENC-1 (1000) and PENC-3 (1000) all of which were prepared using co-catalyst: catalyst ratio of 1000. The M_w and MWD of these samples are however different as discussed in chapter 5. [1] The mastercurves were obtained by shifting the frequency sweep data to a reference temperature of 150^{o}C. Figure 10.3 shows the mastercurve of dynamic frequency sweep data for the pristine PE. It can be seen that $G'' > G'$ for pristine PE over the entire range of frequencies scanned. A crossover to a highly elastic regime is observed at a frequency of ~ 100 rad/s. The slopes of G' and G'' in terminal region are 0.5 and 0.7 respectively, which are much less than the classical values of 2 and 1 for monodisperse samples. The greatly reduced terminal slopes can be attributed to the very high polydispersity of the PE samples synthesized by late transition metal catalyst (see Table 5.6). Figure 10.4 (a) and (b) shows the mastercurves for the

PENC-1 (1000) and PENC-3 (1000). It can be seen that for the PENC-1 (1000) hybrid, $G'' > G'$ for only very low frequencies followed immediately by a crossover at a frequency ~ 0.04 rad/s, at frequencies higher than 0.04 rad/s again $G' > G''$. For the PENC-3 (1000) hybrid the $G' > G''$ at all frequencies probed in this experiment. The crossover frequency, if any must have shifted to very lower frequencies (<< 0.01 rad/s).

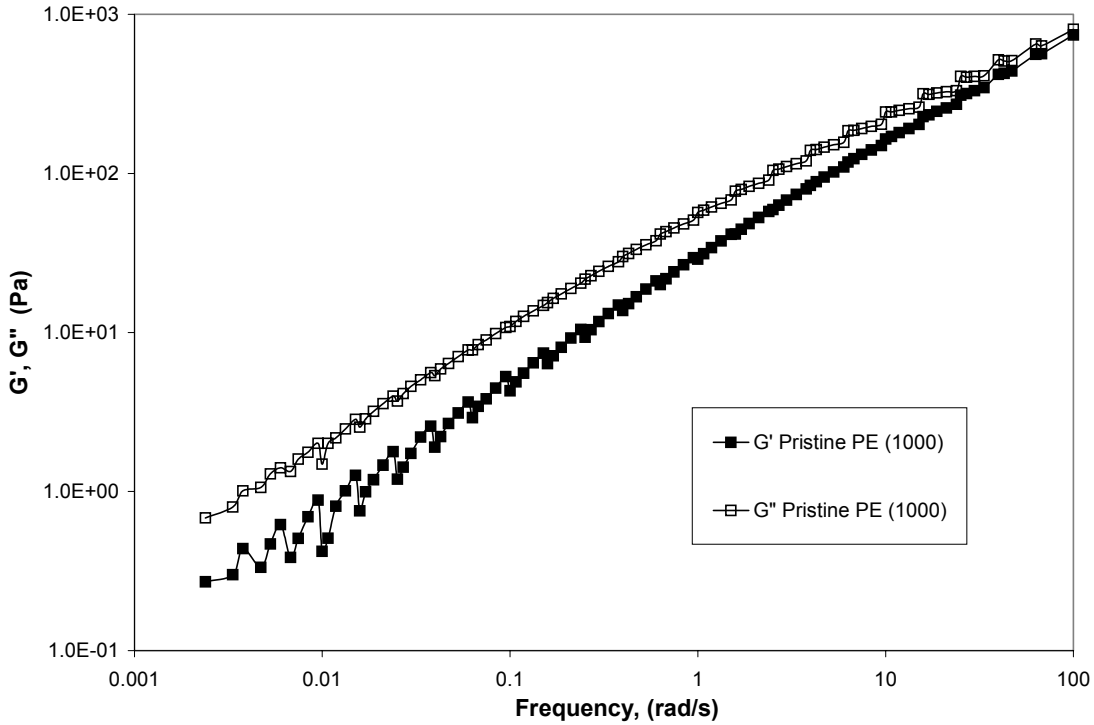

Figure 10.3. Mastercurve of dynamic frequency sweep data for pristine polyethylene at T = 150^{o}C

At 150^{o}C, the pristine PE relaxes very fast in ~ 0.01 s as gauged by the crossover frequency. However, the characteristic relaxation time was found to be much higher for PENC-1 (1000) i.e., ~ 25 s. The relaxation time for the PENC-3 (1000) must be even higher. Thus the presence of a small amount of exfoliated clay seems to strongly influence the relaxation of polymer chains. For the PENC-3 (1000) hybrid the G' exhibits a plateau in the terminal region, which is indicative of the formation of a percolating network of hydrodynamically interacting silicate layers, formed, as discussed in chapter 7 and 8. [2,3] No such response was observed for the PENC-1 (1000) sample.

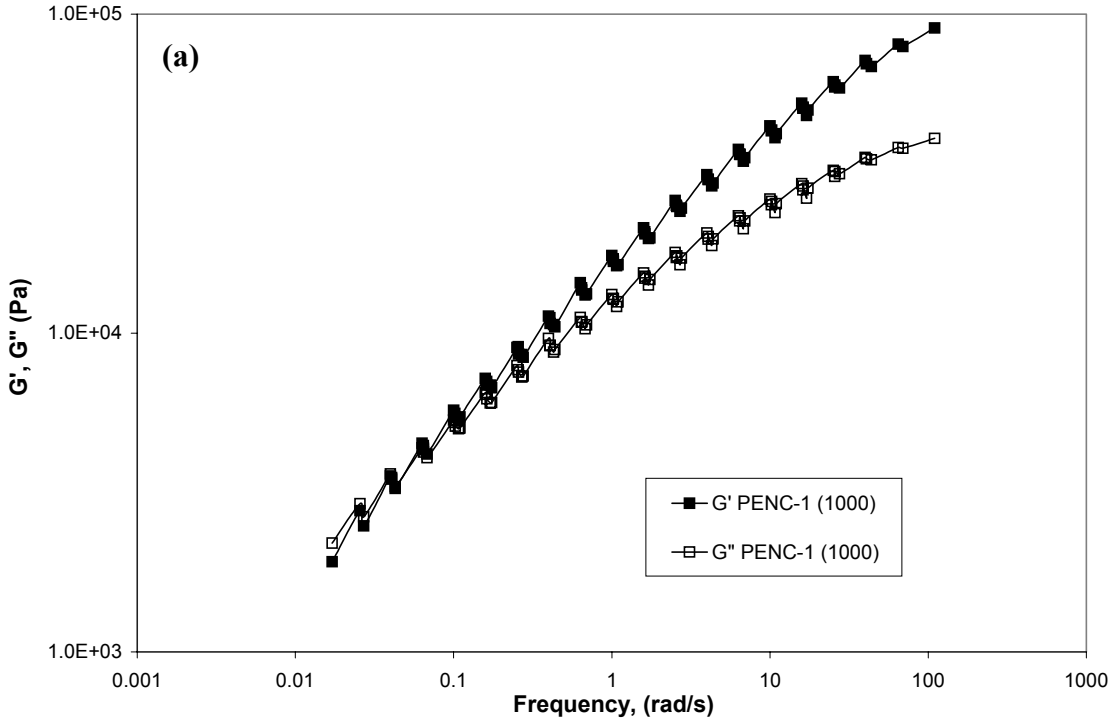

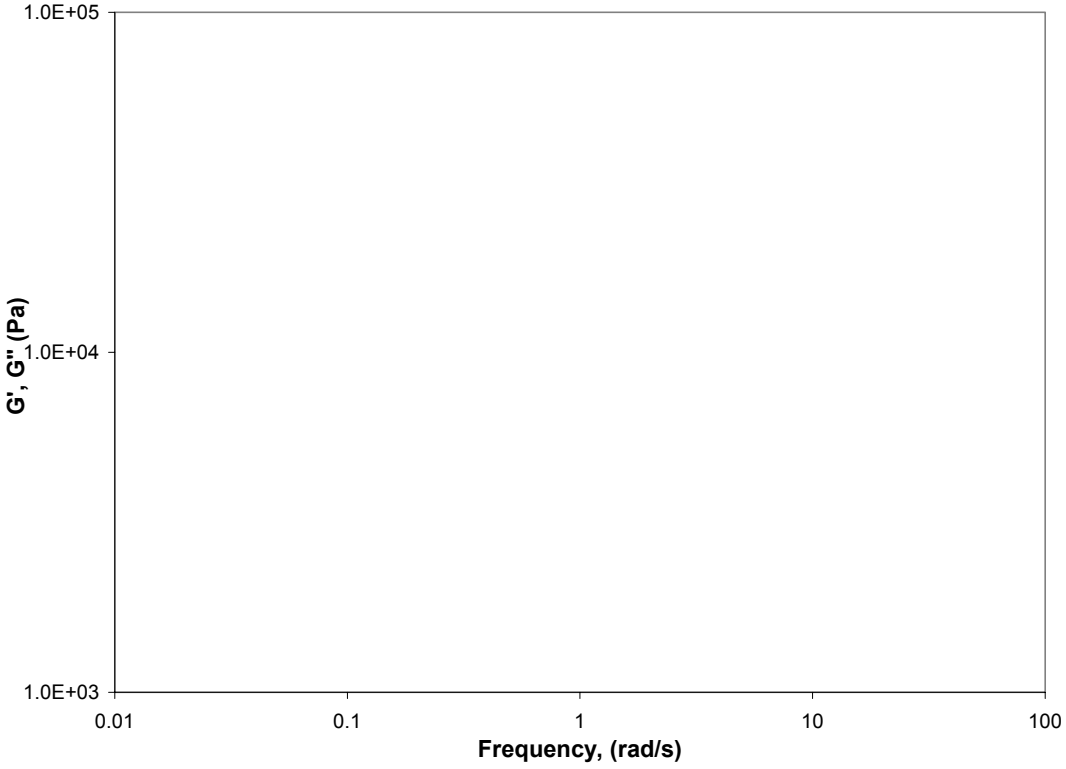

Figure 10.4. Mastercurve of dynamic frequency sweep data for a) PENC-1 (1000) b) PENC-3 (1000) at T = 150^{o}C

This suggests that a network microstructure is probably not formed for a clay loading as low as 1-wt%. It also may be noted that while M_w increase in the order of PENC-3 (1000) < PENC-1 (1000) < Pristine PE, the elastic modulus decreases in the order PENC-3 (1000) > PENC-1 (1000) > Pristine PE.

10.2.1. Effect of molecular weight

Figure 10.5 shows the mastercurves of the elastic modulus (G') of PENC-3 (1600), PENC-3 (1000) and PENC-3 (200) at T= 150^{o}C. These three PE hybrids have the same clay content i.e., 5.6-5.9 wt% clay, however the co-catalyst: catalyst ratios are different. The molecular weight of the resin decreases with increasing co-catalyst: catalyst ratio. The molecular weight of the PENC-3 (200) > PENC-3 (1000) > PENC-3 (1600) as shown in Table 5.6. However, as seen in the Figure 10.5, the elastic modulus (G') shows exactly the opposite trend PENC-3 (200) < PENC-3 (1000) < PENC-3 (1600).

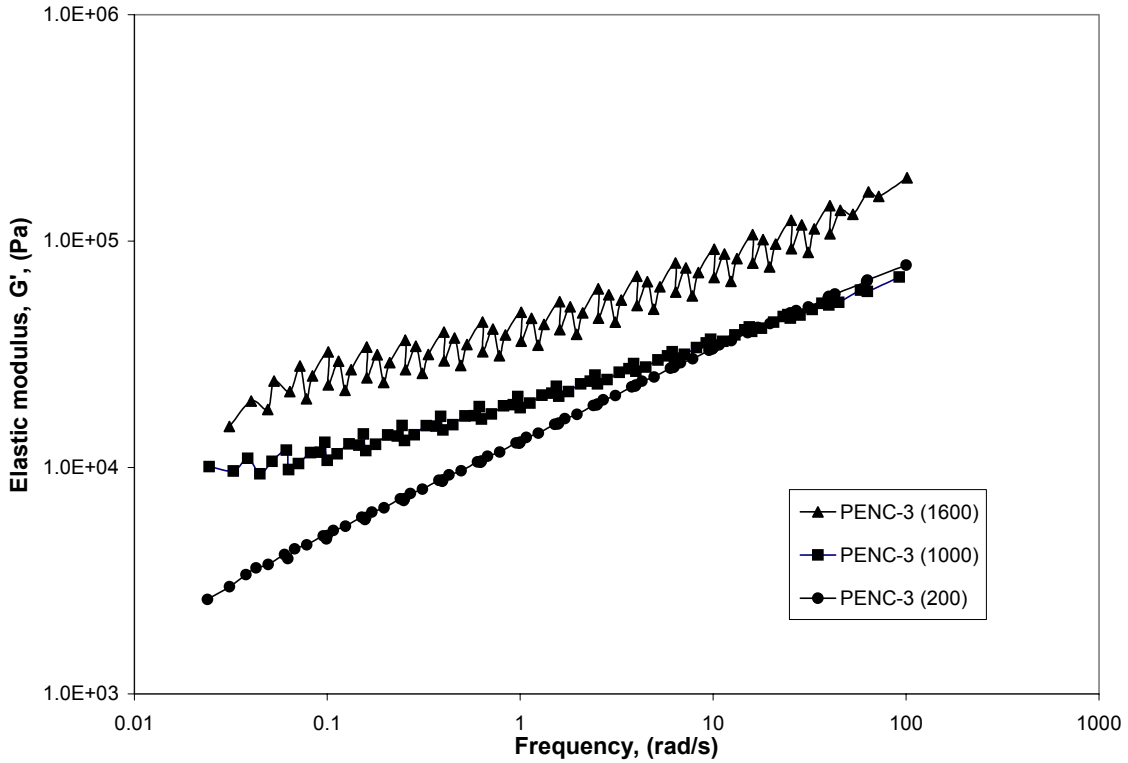

Figure 10.5. Mastercurves of elastic modulus for (PENC-3) series at T= 150^{o}C

Thus, the elastic modulus of the lowest molecular weight hybrid was found to be higher than that of highest molecular weight hybrid. The data in Figure 10.4 (a) and (b) and Figure 10.5 suggests that the viscoelastic response of the PE nanocomposites is dictated by the microstructure of the hybrid rather than the molecular weight of the matrix resin. As evidenced from the XRD data of the Figure 6.12, the PENC-3 (200) probably has a greater fraction of intercalated microstructure, while the PENC-3 (1600) has a greater fraction of exfoliated microstructure. Therefore, the network density is probably the highest for PENC-3 (1600), which reflects in the highest G' for this sample.

10.3. Effect of heterogenization of the catalyst

As discussed in chapter 6, the XRD patterns of PENC-1 series and PENC-2 series (see Fig. 6.12) indicate that PENC-2 hybrids are of an intercalated type, as evident by the presence of the clay peak, while PENC-1 hybrids are nearly exfoliated hybrids. Figure 10.5 shows the mastercurves of the frequency sweep data for the PENC-1 (1600) and PENC-2 (1600).

It can be seen from the Figure 10.5 that the rheological response of hybrids synthesized with catalyst heterogenized on the clay surface i.e., PENC-1 (1600) and the one synthesized with catalyst added as such, i.e., without heterogenization on the clay PENC-2 (1600), are qualitatively different. The G' and G'' crossover at frequency ~ 0.5 rad/s i.e., the material relaxes in 2 s for PENC-1 (1600), while there seems to be no crossover for the PENC-2 (1600) hybrid. Further, for the PENC-2 (1600), the $G' > G''$ and plateau of G' in the terminal region suggests solid-like relaxation mechanism. Further, even though the molecular weight of the PENC-1 (1600) is slightly less than the PENC-2 (1600), the elastic modulus of the PENC-1 (1600) hybrid was found to be higher than the PENC-2 (1600).

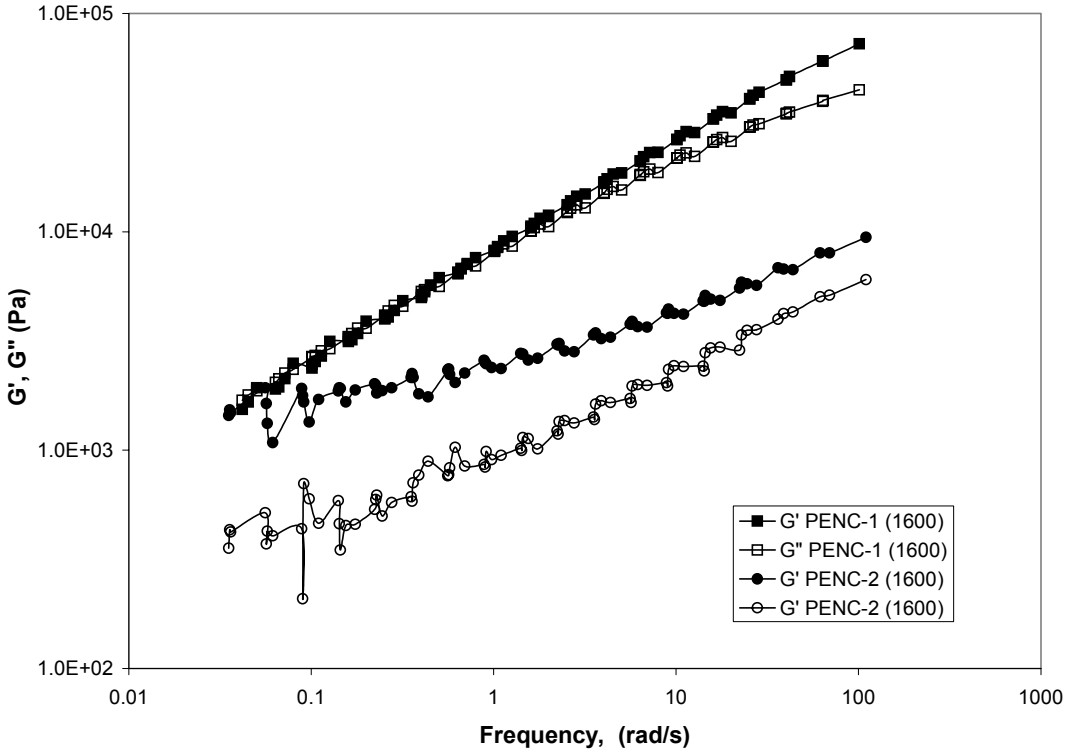

Figure 10.6. Mastercurve of dynamic frequency sweep data for PENC-2 (1600) and PENC-1 (1600)

10.4. Summary

The studies reported in chapter 7, 8 were for intercalated nanocomposites. The purpose of the work reported in this chapter was two fold: first to see if the rheology of exfoliated nanocomposites, particularly those for which there is a high probability of chains end – tethered to the silicate surfaces, is different than that of the intercalated nanoclay composites, and second to study how subtle changes in the nearly exfoliated microstructure might affect rheological response of such hybrids. Towards meeting the second objective, two types of PE nanoclay composites were tested. One synthesized using a catalyst heterogenized on the clay surface and the other synthesized with catalyst added as such without heterogenization.

The data reported in this chapter suggests that the nearly exfoliated PE nanocomposite melt containing as low as 1-wt% clay is significantly more elastic than the pristine PE. However, intercalated PP nanocomposite melt having 3-wt% clay does

not exhibit any significant differences compared to the matrix PP resin, as discussed in chapter 7.

The PENC-1 series showed a high G' and much lower crossover frequency that the pristine PE. However no plateau was observed at low frequencies. The PENC-3 series showed even higher G', probably a much lower crossover frequency and plateau region at low frequency. Thus, a percolating network response is evident at 5-wt% clay loading, which is similar to what was observed for the intercalated PP nanocomposite in chapter 7. The PENC-2 series showed non-linear rheological behaviour at lower strains than, the PENC-1 hybrids, however their elasticity as measured by G' was lower than the PENC-1 series nanocomposites.

Also, the PENC-2 showed a tendency to form network structure as evidenced by G' plateau at low frequencies. This is surprising since PENC-1 series might be expected to form a network structure more easily than PENC-2 given that it is more exfoliated than PENC-2.

Finally, in contrast to the strain hardening tendency observed for the end–tethered polycparolactone nanocomposite observed by Krishnamoorti et. al. [4], the PE nanocomposites reported here show a strain softening behaviour although there is strong possibility of having PE chains tethered to the clay surface because of the heterogenization of the catalyst on the clay.

Reference List:

1. Saptarshi Ray Ph. D thesis to be submitted to University of Pune (Dept. of chemistry) 2003.
2. Krishnamoorti, R.; Giannelis, E. P. *Macromolecules* **1997,** *30*(14), 4097-4102.
3. Krishnamoorti, R., Yurekli, K. *Current Opinion in Colloid & Interface Science* **2001,** *6*(5,6), 464-470.
4. Krishnamoorti, R.; Giannelis, E. P. *Langmuir* **2001,** *17*(5), 1448-1452.

Chapter 11 Conclusion and Future work

11.1. Conclusions

The objective of this work as illustrated in Fig 4.1 was to develop an understanding of the structure-processing-property relationships in polyolefin nanocomposites. Chapters 7-10 describe in detail the work done towards meeting this goal. The structure-property linkages are summarized in Figure 11.1 along with the salient contributions of the work done in this study. The main conclusions have already been summarized in chapter 9. The study reported in this thesis showed that the rheological data, particularly creep data, is sensitive to the microstructure of the PLS nanocomposites. Under quiescent conditions, the microstructure of compatibilized PLS nanocomposites consists of 3D percolating network of clay tactoids, which is responsible for the very high viscosity exhibited by these hybrids. At higher stresses the clay tactoids get oriented in the flow direction, leading to the breakage of this network. Once the network breaks down, the viscosity drops down by orders of magnitude. Thus, these hybrids exhibit the yield–like behaviour. Further, the orientation of clay tactoids, under flow conditions was quantitatively studied by a novel in-situ rheo XRD technique. Both rheological and rheo-XRD studies showed that the yielding corresponded to the orientation of clay in the flow direction. The effect of clay orientation on the solid-state properties was also reported. The tensile modulus was found to increase with the increasing clay orientation. This thesis also reported on the rheological analysis of exfoliated and possibly end tethered PE nanocomposites. The PE nanocomposites were found to be significantly more elastic than the matrix resin, even at very low (1-wt%) clay loading. A percolating network was evidenced at 5-wt% clay loading.

11.2. Future work

The work reported in this thesis suggests that the final product properties of PLS nanocomposites will be dependent on the subtleties of the clay microstructure. For

instance, in the case of PP nanocomposites although the XRD did not reveal significant differences between the microstructures of the compatibilized and the uncompatibilized hybrids, large differences were seen for the rheological and the tensile properties of these two hybrids. Such differences could only result from the presence of the PP-MA compatibilizer. Thus, the interactions between the PP-MA and the silanol groups (Si-OH) on the clay are critical to the successful development of a nanocomposite.

There are many reports in the literature about PP nanocomposites synthesized by using different types of clay and the consequent improvements in properties achieved, but the understanding of the exact interaction between the polymer matrix, modified or pristine, and the clay via the PP-MA compatibilizer, remains elusive. For instance, PP nanocomposites can be prepared by using different types of synthetic clays: such as those having silanol groups present only the edges and others having silanol groups present both on the edges and on the surface of platelets. The properties of the hybrids prepared under similar conditions, but using clays, which are different in terms of the locations of silanol groups would be a dependent on the nature and extent of interactions of the clay and the polymer. This kind of study will help to tailor the clay-matrix interactions and to optimize the hybrid properties.

Further, it was shown in this work that rheological experiments, in particular the creep measurements are sensitive to the diffusion of the polymer chains into the primary clay particles. The effect of molecular weight of the resin on the diffusion of polymer chains into the primary particles and the resultant extent of intercalation was reported in this thesis. It was suggested that creep measurements could potentially offer a rheological method to probe the diffusion of polymer chains into the primary clay particles. However, rheology in itself is an indirect tool to probe the diffusion studies. For example, as reported in this study, the rheologically probed yield–like behaviour in the polymer nanocomposites, was attributed to the orientation of clay tactoids. This was then quantitatively measured and proved by in-situ XRD analysis. Similarly, the diffusion of polymer chains probed indirectly by the rheological studies can be quantitatively understood by using coupled techniques like rheo-NMR or in-situ fluorescent spectroscopic techniques.

It was shown in this work that the tensile modulus increased with increasing clay orientation. The hybrid modulus was predicted only from the clay orientation in a semi quantitative manner even though polymer crystallites were slightly oriented. More accurate predictions of the hybrid modulus may be possible with model polymer systems which orient at very high shear rates and by solving the full tensorial constitutive equation for the composite as suggested by Brune et. al. [1]

Studies reported in this thesis were focused only on the tensile modulus. But other properties like the barrier properties of the nanocomposites are also strongly dependent on the orientation of the clay. Bhardwaj et. al. have proposed a simple model for relating the clay orientation with the barrier properties. [2] It would be interesting to quantify the effects of clay orientation on the barrier properties of polyolefin nanocomposite films.

This thesis also reported preliminary studies on the rheology of PE nanocomposites synthesized by in situ polymerization of ethylene. The purpose of this study was to investigate the difference in the rheological behaviour of the intercalated and exfoliated nanocomposites. The rheological response of nanocomposites is sensitive to both the polydispersity and the clay dispersion in the polymer matrix. The PE nanocomposites studied in this work were highly polydisperse, which made it difficult to separate out the effects of molecular weight distribution and clay dispersion on the rheology of the PE nanocomposites. The rheological response of the clay dispersion would be more clearly seen for a model monodisperse material.

A lot more obviously remains to be done to quantify the structure-property relations in PLS nanocomposites. The study reported in this thesis has provided new insights and has raised new questions in this scientifically interesting and industrially relevant class of materials.

Reference List:

1. Brune, D. A.; Bicerano J. *Polymer* **2002**, *43*(2), 369-387.
2. Bharadwaj, R. K. *Macromolecules* **2001,** *34*(26), 9189-9192.

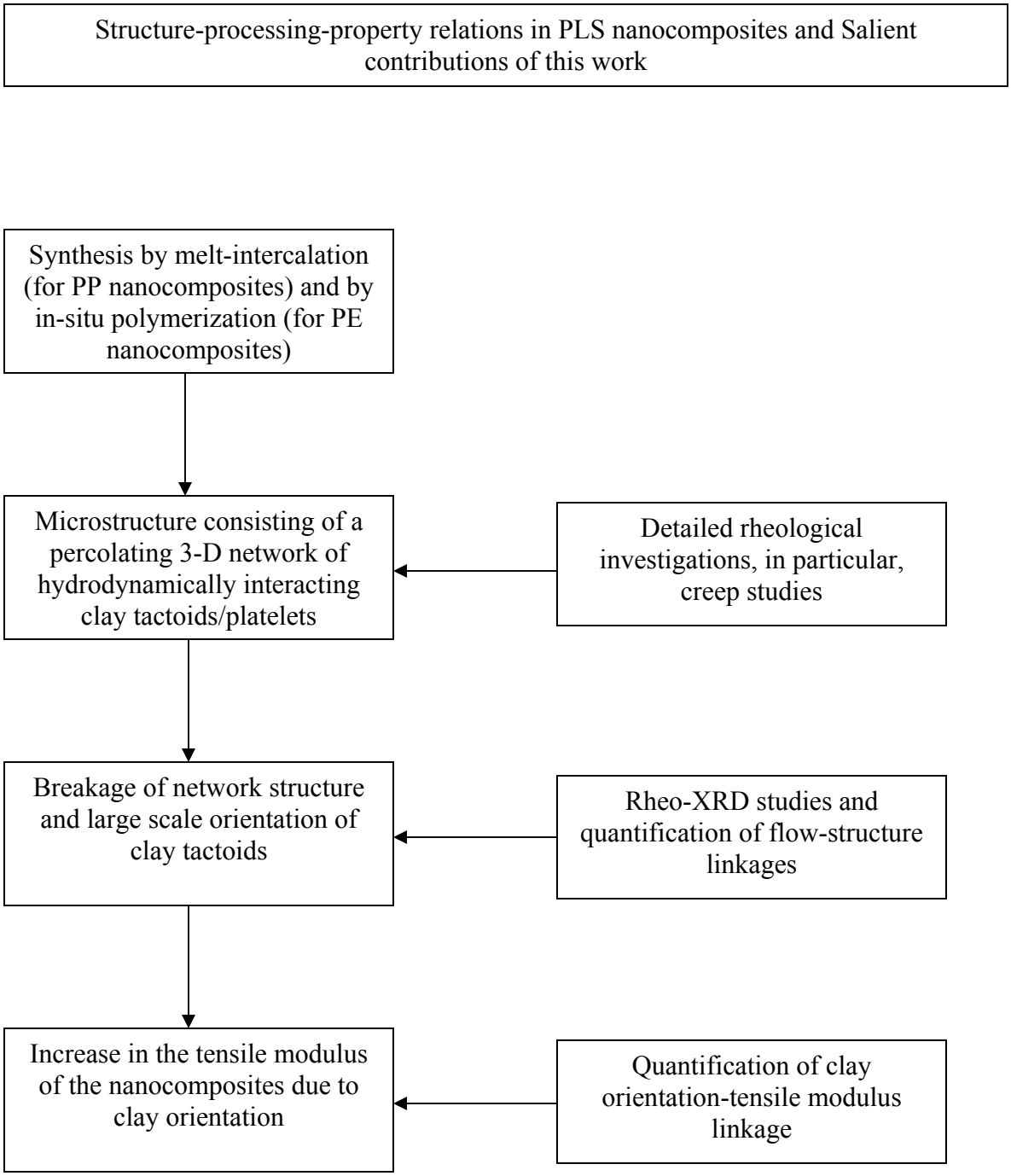

Figure 11.1. Schematic of the objectives of this thesis and salient contribution of this work